

Dynamics of Lightweight Tensegrity-Inspired Metamaterials Fabricated with 3D-Printing

Thesis by
Kirsti Mari Pajunen

In Partial Fulfillment of the Requirements for the
Degree of
Doctor of Philosophy in Space Engineering

The logo for the California Institute of Technology (Caltech), featuring the word "Caltech" in a bold, orange, sans-serif font.

CALIFORNIA INSTITUTE OF TECHNOLOGY
Pasadena, California

2020
Defended March 24, 2020

© 2020

Kirsti Mari Pajunen
ORCID: 0000-0002-5366-1190

All rights reserved

ACKNOWLEDGEMENTS

A PhD is an immense undertaking that often is attributed to independent work. However, the ability to produce independent research is truly the product of the support, insight, and contributions of many individuals. Thus, it would be ungracious to present the work in this thesis without acknowledging so many who have helped me in countless ways over the last six years.

First, I would like to thank my adviser, Chiara Daraio. I would like to thank her for taking me on as her first student when she came back to Caltech after ETH. I'm forever thankful for this, because she enabled me to pursue an exciting research path that fit my interests perfectly and challenged me in amazing ways. Her remarkable insight, intellect, and passion for novel research shines through in all her mentees' work. I especially thank her for being an incredible role model in so many ways, including not only how to thrive as a leader and woman in this field, but more importantly how to be a person with immense integrity, patience, and kindness. I am so grateful she was my adviser through this time in my life.

I also would like to thank the Chair of my thesis committee, Professor Guruswami Ravichandran. Ravi is a wonderful person and professor that I had the pleasure of working with for my first year of research at Caltech. He helped me forge professional and personal connections through my time at Caltech, and he always pushed me to grow as a researcher. I would also like to thank Professor Sergio Pellegrino and Dr. Doug Hofmann for serving on my candidacy and thesis committees, where they were always excited about my research and provided very useful insight and suggestions for my work.

I likely would not have done research in the area of tensegrities if not for Professor Julian Rimoli, my collaborator at Georgia Tech. I still remember the first meeting he and I had where he introduced me to tensegrities, and his excitement about these structures and their potential rubbed off on me. That excitement didn't diminish for me for the rest of my time at Caltech. Julian's constant willingness to provide code (along with the help of his postdoc, Raj Kumar Pal, who I also thank), ideas, and techniques was extremely helpful, as was his sincere interest in my work.

Another person I am very grateful for is Paul Johanns, who I mentored when he was a six-month master's student from ETH in 2017. Apprehensive at first to take on a mentee only a few months after I started with Chiara, I quickly realized how

well we worked as a team to push this project forward. Paul was an immense help, such as designing and building most of the drop weight setup. It was wonderful to see both of us learning so much and bouncing ideas back and forth. Those six months were among the most productive and enjoyable times during my PhD.

The Daraio group was truly a great group of people to work with. I challenge any group that I work with in the future to be as enjoyable and helpful as they were. Paolo, for helping me immensely with experiments, teaching me so much about dispersion curves, and being incredibly patient and helpful. Eleftheria, for always being a smiling face and being willing to lend an ear about anything research and non-research. Brian R., for helping me with drop tests. Alex O., Sharan, Jag, Chris, and Gunho for getting me through the last few exhausting months of my PhD with support and some seriously useful advice. And also so many others for making my time at Caltech in this group so wonderful.

My PhD work would not have been possible without the financial support of the National Defense Science and Engineering Graduate Fellowship (32 CFR 168a) through the Department of Defense Air Force Office of Scientific Research.

First year was not only made bearable but also, dare I say it, enjoyable because of the great friendships I made with my cohort. I am so glad that ten of us made it to this point of getting our PhDs. I will always treasure our time together at Caltech, from the torturous problem sets to all the amazing memories we made along the way. Most importantly, I would not have made it to this point if not for my best Caltech friends Serena and Matt, whose undying support and belief in me pulled me through way more often than they know. I'm so thankful they are in my life for the rest of my life.

Surrounding the PhD, these last six years were full of immense changes in so many areas of my life, and I could not have gotten through it all without my best friends, Sherri and Elizabeth, and my mom, dad, and sister Anna. The love I have for all of you is beyond words. Thank you for the countless calls, texts, vacations, mournings, and celebrations that filled the last 6 years and got me through to the other side.

Almost lastly, I need to thank Kenny. He has been there in everything, and I mean everything, throughout all this. He probably knows more about my research than anyone at Caltech. Every step of the way he has supported me, pushed me, consoled me, been excited with me, and even stayed up till 3 am doing experiments with me

on a Sunday night. I am so glad you chose me to do life with.

Finally, I thank God for being my rock, and for being with me and for me throughout everything. I thank him for giving me these gifts and for instilling in me perseverance to use them to their fullest. And I thank him for letting me discover through my research just a little bit more about the unknowns of the universe, but which have been known to him all along.

ABSTRACT

Tensegrity structures and lattices have been of interest in engineering applications for decades, with their dynamics becoming a thriving field of study. Tensegrities consist of structural members under purely axial loading, either tension or compression, and obtain their stability from prestress. They possess unique characteristics such as high strength-to-weight ratio, nonlinear behavior, and elastic response under severe deformation. Tensegrity lattices (or metamaterials) have been shown to exhibit appealing dynamic attributes such as continuous tunability with prestress, impact mitigation, energy trapping and lensing, and nonlinear wave propagation, to name a few. However, their pin-jointed and prestressed nature presents significant manufacturing limitations, especially in the formation of lattices with large numbers of tessellated unit cells. Therefore, experimental validation of the dynamics of tensegrity metamaterials has remained elusive. For lattices with tensegrity-like characteristics to be manifested for real-world applications, a method for producing tensegrity-like metamaterials at multiple length scales is needed.

In this thesis, we present a design for a 3D-printable tensegrity-inspired structure with the equivalent strain energy capacity and stress-strain response as a pin-jointed tensegrity. Using this structure as a building block for multidimensional lattices, we subject them to a range of dynamic loading conditions to study their response. First, we perform experiments and simulations to obtain the dispersion relations for 1D and 3D lattices. We demonstrate the lattices' ability to continuously tune the dispersion characteristics (e.g., band gap and wave speed) under precompression. This trait shows potential for acoustic lensing and dispersive wave propagation. In 3D, we show that the lattice shows the same type of unique properties, such as faster shear speed than longitudinal speed, as pin-jointed tensegrity lattices. Next, we study the lattices under impact loading. Long-duration impact experiments on baseline unit cells and 1D lattices show their resilience to repeated deformation, elasticity, and load limitation behaviors. Short-duration impulse experiments and simulations exhibit a wealth of desirable properties, such as high force transmission reduction, highly dispersive wave propagation, tunable wave speeds, energy trapping, and redirection of energy. We demonstrate that these tensegrity-inspired metamaterials not only exhibit and experimentally demonstrate tensegrity-like characteristics, but open a new range of lightweight metamaterials with unprecedented dynamic properties.

PUBLISHED CONTENT AND CONTRIBUTIONS

- [1] K. Pajunen, P. Celli, and C. Daraio. “Experimental evidence of analog prestrain-induced bandgap tuning in 3D-printed tensegrity-inspired lattices”. In: *Extreme Mechanics Letters* (2020). In Press.
K.P. participated in the conception of the project, designed and analyzed the structures, prepared the data, and participated in the writing of the manuscript.
- [2] K. Pajunen et al. “Design and impact response of 3D-printable tensegrity-inspired structures”. In: *Materials & Design* 182 (2019), p. 107966. DOI: [10.1016/j.matdes.2019.107966](https://doi.org/10.1016/j.matdes.2019.107966).
K.P. participated in the conception of the project, designed and analyzed the structures, prepared the data, and participated in the writing of the manuscript.

TABLE OF CONTENTS

Acknowledgements	iii
Abstract	vi
Published Content and Contributions	vii
Table of Contents	vii
List of Illustrations	x
List of Tables	xxiv
Chapter I: Introduction	1
1.1 Background and Motivation	1
1.1.1 Introduction to Tensegrity Structures	1
1.1.2 Dynamics of Tensegrity Structures and Lattices	3
1.2 Goals and Organization	6
Chapter II: Methods	9
2.1 Numerical Methods	9
2.1.1 ABAQUS Finite Element Modeling	9
Material Model	10
3D Solid Model	12
Beam Element Model	14
2.1.2 COMSOL Finite Element Modeling	19
Dispersion	19
Transmission	21
2.2 Experimental Methods	23
2.2.1 Sample Fabrication	23
2.2.2 Static Compression Tests	23
2.2.3 Dynamic Impact Testing	23
Drop Weight: Baseline Unit Cell	24
Drop Weight: 1D Lattice	26
Sample Drop Tests	27
2.2.4 Frequency Transmission Experiments	29
Chapter III: Design of Tensegrity-Inspired Structures	33
3.1 Design Methodology	33
3.1.1 Target Baseline Tensegrity and Initial Design Iteration	33
3.1.2 Conversion Method Between the Fixed and Pin-jointed Structure	37
3.1.3 Examples of the Design With Alternate Materials and Length Scales	45
3.2 Fundamental Comparison of the Fixed and Pin-Jointed Structures	47
3.3 Representative Volume Elements for Tensegrity-Inspired Lattices	50
3.4 Chapter Summary	52
Chapter IV: Dynamics: Frequency Response	54

4.1	Introduction to Dynamic Frequency Analysis	54
4.2	Unstrained Lattice	55
4.2.1	Dispersion Results	55
4.2.2	Wave Speed Analysis and Comparison with Other Lattices	61
4.3	Tunability with Compression	64
4.4	3D RVE Dispersion Characteristics	73
4.5	Chapter Summary	78
Chapter V: Dynamics: Impact		80
5.1	Introduction of Impact Studies	80
5.2	Drop Weight: Long-Duration Impact	82
5.2.1	Baseline Unit Cell	82
	Force Response and Observation of Load Limitation	82
	Analysis of Energy Loss During Impact	91
	Energy Absorption Comparison	93
5.2.2	1D Lattices	96
	Force Response	96
	Deformation Behavior and Wave Characteristics	100
5.3	Sample Drop Tests	108
5.3.1	Experimental Results	109
5.3.2	Wave Characteristics	116
	Energy Localization	116
	Dispersive and Asymmetric Wave Propagation	121
	Comparison Between Lattice Types	123
5.4	Flatten the Curve: Short Duration Impulse by a Falling Mass	125
5.4.1	Wave Propagation	126
5.4.2	Force Transmission Reduction	133
5.5	Chapter Summary	134
Chapter VI: Conclusions and Future Directions		135
6.1	Summary	135
6.2	Future Directions	136
Bibliography		139
Appendix A: Appendices for Chapter 2		151
A.1	MATLAB Codes for Dispersion Experiments	151
A.2	MATLAB Code for Drop Weight Experiments	160
Appendix B: Appendices for Chapter 3		171
B.1	Relaxation Tests for Two Materials	171
B.2	Intermediate Geometry Design Iterations	172
Appendix C: Appendix for Chapter 5		174
C.1	Distribution of Kinetic and Strain Energy in a Lattice Under Impact	174

LIST OF ILLUSTRATIONS

<i>Number</i>	<i>Page</i>
1.1 An example of a tensegrity structure, held by Buckminster Fuller who coined the term “tensegrity.”	2
1.2 A rendering of a tensegrity planetary lander impacting the ground, suspending a protected payload (e.g., a camera) in the center [32, 36].	3
1.3 Load displacement plot for a titanium strut with density of 4480 kg/m^3 , Young’s modulus of 91 GPa , external diameter of 19 mm, and thickness of 1 mm. The results are shown for the elastic continuum solution and the discrete buckling model developed in [23].	5
2.1 Stress-strain response of the EOS PA2200 polyamide material used for the structures in this thesis. The results at three strain rates (0.2, 1.1, and 5 mm/min) are shown. The 5 mm/min test follows ASTM standards for strain rate and was thus used to obtain the material properties. For this test, the sample ruptures at about 0.19 strain. The hyperelastic Marlow model requires strictly increasing values of stress and strain, so for the model we input only the region from 0 to 0.13 strain. The slope of the initial region gives the Young’s Modulus, E . This slope is equivalent for all three strains rates tested.	10
2.2 A 3D rendering of the tensegrity-inspired structure in ABAQUS. Boundary conditions are placed on top (displacement only in y -direction) and bottom (fixed) reference points (blue circles), which are located along the vertical y -axis and each centered on the plane of the top and bottom face nodes. The top and bottom face nodes (orange dots) are kinematically coupled to the top and bottom reference points (orange lines), such that they are vertically constrained like the reference points, but are able to rotate freely around the vertical axis.	13
2.3 Beam element rendering of the tensegrity-inspired baseline unit cell with (a) wire elements and (b) beam element cross sections visualized. The struts are displayed as the gold members, the cables are the blue members, and the edges (4 of which together simulate a sphere at each node) are the green members.	16

2.4	Example ABAQUS renderings of (a) 1D, (b) 3D1D, and (c) 3D bulk lattices with top and bottom analytical rigid surfaces used for impact simulations.	17
2.5	A rendering of the solid model of a 1D RVE in COMSOL. We make a cut through the top and bottom faces on the horizontal planes that intersect the center axes of the cables, creating flat surfaces to apply the Bloch boundary conditions. The RVE has a total height of 96.6 <i>mm</i> in the <i>y</i> -direction.	20
2.6	A rendering of the solid model of a 3D RVE in COMSOL. We make a cut through the 24 external faces to create flat surfaces on which to apply the Bloch boundary conditions.	21
2.7	A finite 3 RVE 1D lattice is modeled in COMSOL to find the longitudinal frequency transmission response. Displacement amplitudes are extracted from the input and output locations (orange and green circles, respectively) to find the transmissibility ratio at approximately the same locations as in the experiments.	22
2.8	Quasistatic compression tests were performed on baseline unit cell samples using an Instron E3000 [®] . The bottom plate remains fixed, while the top plate displaces the structure vertically using displacement control. The structure faces are allowed to rotate during the compression.	24
2.9	Dynamic drop weight test setup for a baseline unit cell. A schematic is shown in (a), and a picture of the physical setup is shown in (b). . .	25
2.10	Dynamic drop weight test setup for a 5 baseline unit cell 1D lattice. . .	26
2.11	Schematic showing the sample drop test of a 3D1D lattice, with displacement tracking points shown.	28
2.12	Picture taken of the entire sample drop test setup, with the total height seen in the left panel and the zoomed-in image of the lights, sample, ruler, etc. in the right panel.	29
2.13	Schematic of the experimental setup used to study the spectro-spatial wave characteristics of a tensegrity-inspired 1D lattice.	30

- 2.14 (a) Global buckling is apparent in the 3 RVE lattice even at low compression levels. Thus, we devised an apparatus using strings and rods (b) to hold the structure in its axis and prevent first mode buckling. The transmissibility is calculated by dividing the velocity amplitude at the output (green dot) by the velocity amplitude at the input (orange dot), as in the simulations. 32
- 3.1 (a) Pin-jointed truncated octahedron tensegrity with 6 orthogonal faces, which we refer to as shown in the image. This is the baseline tensegrity structure we model after in this thesis. (b) The initial iteration for a 3D-printable structure, which is fixed-jointed structure overlapping members at the nodes. 34
- 3.2 Global compressive stress-strain curves showing the 3D stress ABAQUS simulation and representative experimental responses of the 3D-printable, fixed-jointed structure, as well as the response of the corresponding pin-jointed structure. All member diameters correspond to Geometry #1. The pin-jointed structure exhibits a clear buckling point around 0.3 longitudinal strain, whereas the fixed-jointed structure does not exhibit a buckling point, but ruptures around 0.3 strain. The stiffness of the fixed-jointed structure is much higher than the pin-jointed stiffness. This fixed-jointed structure is thus inadequate to represent the pin-jointed response. 36
- 3.3 (a) Pin-jointed truncated octahedron tensegrity with 6 faces. (b) 3D-printable, fixed-jointed structure with overlapping members. In the updated design, nodal locations and cable lengths are maintained by (c) scaling up the structure while keeping cable lengths constant and (d) inserting spheres at the nodes. 38
- 3.4 (a) Spherically-jointed structure compressed during an experiment. (b) ABAQUS rendering of compression of the spherically-jointed structure. (c) Representation of the mechanical deformation modes exerted on the members of the spherically-jointed structure. (d) ABAQUS beam element rendering of the compression of the spherically-jointed structure. 39

3.5	Global compressive stress-strain curves showing responses of the 3D stress simulation, beam simulation, corresponding pin-jointed tensegrity simulation, and representative experiment. All four show comparable behavior, indicating the spherically-jointed structure's equivalence to a corresponding pin-jointed tensegrity structure. <i>This is the final geometry design chosen for the studies in this thesis.</i> . . .	41
3.6	Maximum principal elastic strain within the structure at a global strain level of 0.4. The blue-to-red rainbow colorplot ranges from the lowest strains in blue to the highest strains in red. A magnification of one of the the highest local strain locations is shown in the inset red box.	42
3.7	Pin-jointed tensegrity structure, zoomed in at the top face leftmost node. Here, we show the forces acting on this node. This enables us to solve for the diameter of the strut needed to achieve a buckling load equal to that of the spherically-jointed tensegrity-inspired structure. .	43
3.8	Microscale samples with a height of $120\ \mu m$ were fabricated with the Nanoscribe [®] printing system. (a) A scanning electron microscope photograph of a sample is shown. (b) Photograph of a compression test on a sample using the FemtoTools [™] testing system. The sample on the lower right is being compressed by the force sensor tip, which is lowered by displacement control.	45
3.9	Global compressive stress-strain results of compression tests on microscale samples with a height of $120\ \mu m$ and d_s/d_c of 1.44. The results of four samples are shown. The results show behavior similar to the $48.3\ mm$ samples printed with the Shapeways PA2200 material and same d_s/d_c value.	46
3.10	Global compressive stress-strain responses of a linear elastic spherically-jointed structure and its corresponding pin-jointed tensegrity structure found using our design method.	47
3.11	Representative volume element of the baseline spherically-jointed, tensegrity-inspired structure. This is used for calculating the relative density of our structure and subsequent lattices.	48
3.12	The force in a representative strut (F) normalized by its buckling load (F_b) for both the spherically-jointed tensegrity-inspired structure and the corresponding pin-jointed structure, as a function of global compressive strain.	49

3.13	The baseline tensegrity-inspired structure has a left-handed and right-handed configuration, and both must be used to tessellate the structure into multidimensional lattices. The representative volume elements and their number of baseline cells are shown.	51
3.14	Global compressive stress-strain curves from ABAQUS beam element simulations of the baseline, 1D, and 3D RVEs.	52
4.1	Setup of the 1D RVE in COMSOL for eigenfrequency analysis of an infinite 1D lattice. Periodic Bloch boundary conditions are applied on the top and bottom faces.	56
4.2	Numerical dispersion relation for the unstrained 1D lattice response. The dispersion relation is plotted in real space, from $k = 0$ to $1/(2a)$ m^{-1} , where $a = 0.0966m$. The red circular markers are longitudinal modes, the green ones are combined longitudinal and rotational modes, the purple ones are rotational modes, and the blue stars indicate flexural modes and modes that do not clearly belong to any of the above categories. The red shaded region indicates a frequency region where there are no longitudinal modes present; this is a longitudinal bandgap.	57
4.3	The vertical displacement magnitudes are extracted from locations (a), (b), and (c), and the curl magnitude around the vertical axis is extracted for the volume average of the RVE (d). From these magnitudes, we establish quantitative thresholds of these values to distinguish between mode shapes of the dispersion curve. We also show two examples of longitudinal modes where (e) the middle of the RVE stays stationary, but the vertical displacement is large, and (f) the middle and top of the RVE stay stationary, but the vertical displacement of the baseline mid-cell locations is large.	58
4.4	Mode shapes for the 1D RVE are shown. (a) Longitudinal, (b) rotational, (c) flexural, (d) combined rotational and longitudinal, where both rotation along the vertical axis and motion vertically are prevalent.	59

4.5 The colormap shows the experimentally-reconstructed dispersion plot for longitudinal wave motion of the 5-RVE 1D lattice. We expect the dispersion branches to follow the maxima of the colormap [121]. We see a frequency region of very low amplitude on the colormap from about 350 to 430 Hz, indicating a bandgap. The red circles indicate the “unwrapped” longitudinal wave mode locations from the numerical COMSOL simulations. 60

4.6 A position-time (x-t) diagram showing how the velocity amplitude measurements from the laser vibrometer (given by the grayscale colormap) vary with measurement location and time. This provides an experimental estimate of the long-wavelength, low frequency wave speed. The inset plot zooms in on the first propagated wave through the lattice, where we find the times at the first and last locations where the same feature of the wave packet has a maximum (red lines). The physical distance between these locations divided by the time difference gives the wave speed. 62

4.7 The global compressive stress-strain curve of the 1D RVE under compression, as outputted from the ABAQUS 3D stress element simulation. This best indicates how the lattice we are working with in this section behaves under compression. A visual depiction of the deformation in the structure is shown at 0, 0.2, and 0.4 global compressive strain. 65

4.8 Linear perturbation buckling analysis of the 5-RVE lattice in ABAQUS to show the loads and global strains for the (a) first and (b) second buckling modes. 66

4.9 Precompression-induced tunability. The left panel of each subfigure represents the experimentally-reconstructed dispersion curve (gray colormap), with overlapped circular markers corresponding to the numerical dispersion relation. The right panel is the transmissibility plot, where the experimental curves are black and the numerical ones are red. The dashed vertical line indicates a transmissibility of 1. The shaded gray and red regions serve as a guide to the eye and indicate what we identify as bandgaps for the experimental and numerical curves, respectively. (a) Lattice compressed to 0% global strain, (b) 5% global strain, and (c) 10% global strain. 67

4.10	The longitudinal dispersion plots of both numerics and experiments for prestrain levels from 0% to 20%. The prestrain levels are given in the lower right-hand corner of each plot.	69
4.11	(a) Experimental and numerical longitudinal wave speeds at varying levels of global precompression. (b) Evolution of the bandgap width, in Hz , based on the numerical dispersion curve. The bandgap region is shaded for strains up to 0.2.	70
4.12	F. Fabbrocino and G. Carpentieri demonstrated this example of a tensegrity focusing lens [77]. The acoustic lens (1) consists of an array of tensegrity and lumped mass chains, each subject to different prestress levels (2). The incident wave signal (3) creates multiple waves with different phase velocities (4) within the array. These waves come together at a focal point (5) in the adjacent medium (6) [77]. A similar concept could be applied to the tensegrity-inspired lattices in this thesis.	71
4.13	Complete COMSOL dispersion results for each level of compressive prestrain (shown in bottom right-hand corner of each panel). Again, red circles are longitudinal modes, purple circles are rotational modes, green circles are combined rotational and longitudinal modes, and the blue stars are flexural and all other mode types.	72
4.14	The first Brillouin zone of a simple cubic 3D RVE is shown in reciprocal space. The path is given below the diagram. [131]	75
4.15	The 3D RVE dispersion relation is shown for all 7 regions of the first Brillouin zone. Red dotted lines are longitudinal pressure modes and blue stars are all other modes, including shear modes. The frequencies are normalized as described in the text. We see that in the first longitudinal region, ΓX , the low frequency shear mode has a speed of 176 m/s , which is about twice as fast as the longitudinal speed (89.6 m/s), unlike in natural solid materials. Also, the diagonal wave speed in region ΓR (334 m/s) is about twice that of the shear speed in region ΓX	76
4.16	The 3D RVE dispersion relation for a buckling truncated octahedron tensegrity lattice as given in [87].	78
5.1	Classification of mechanical specimen testing according to strain rate. [137]	81

- 5.2 Force-time curves for the four baseline unit cell samples at an impact velocity of 1.15 m/s , corresponding to an impact energy ratio, E_i/E_m , of 0.4. This shows the variance in the sample responses due to manufacturing differences. 83
- 5.3 An experimental result for Sample 3 at an impact velocity of 0.8 m/s , corresponding to an impact energy ratio, E_i/E_m , of 0.18. (a) The applied force on the top of unit cell derived from accelerometer measurements is shown by the dashed-dotted line, and transmitted force measured by the force sensor on the bottom of the unit cell is shown by the solid line. (b) The discrete Fourier transform of the applied force. 85
- 5.4 Beam element and 3D tetrahedral element ABAQUS dynamic implicit simulation results, which show the force-time response on the bottom of the structure for an impact velocity of 0.8 m/s ($E_i/E_m = 0.18$). The lag time, the time for the wave to pass through the structure initially, is the same for both simulations. 86
- 5.5 The force-time response of the structure (Sample 4) at varying impact energies, as a ratio of the impact energy to the maximum strain energy of the structure before densification. Impacting velocities are also shown, corresponding to the impact energy ratios. The solid lines are experimental curves and the dashed lines are results of the ABAQUS beam element simulation. The force plateaus to the structure's buckling force as the impact energy increases. 87
- 5.6 Dynamic results of the quasistatically equivalent pin-jointed baseline unit cell and the beam element simulation of the spherically-jointed structure. (a) Comparison of the pin-jointed structure simulation (dotted lines) and the spherically-jointed ABAQUS beam element simulation (dashed lines) for two impact energies. (b) Deformation of the structure from the beam element simulation at maximum compression during a 1.8 m/s impact. (c) Deformation of the structure from the pin-jointed simulation at maximum compression during a 1.8 m/s impact. 89

- 5.7 The maximum force exhibited by the tensegrity-inspired structure as a function of both the impact energy ratio and impacting velocity. The experimental results of 4 samples are shown with error bars. The ABAQUS beam element simulation results and the pin-jointed simulation results are also shown for comparison. In the inset plot, the force and impact energy ratio are given to the origin in order to observe the significant plateau of the maximum force. The plateau begins at energies well below the maximum energy capacity of the structure ($E_i/E_m = 1$). 90
- 5.8 Experimental dynamic stress-strain curve during impact of the test structure (Sample 4). Stress and strain here are the effective global stress and strain in the direction of vertical impact. The energy dissipated as a percentage of the impact energy is listed for each impact energy ratio. 91
- 5.9 To evaluate the effect of the test setup on energy loss, the force-time results of two experiments with a constant impacting momentum of $0.23Ns$ are given. The area under the curves gives the total momentum absorbed during impact. 92
- 5.10 A series of images from a drop weight test with an E_i/E_m of 1. The images are shown at increasing times, from 0 to t_{imp} , which is the total impact time of the structure. The initial height of the structure is nearly recovered after impact. 94

- 5.11 Energy absorption efficiency (W_{min}) by relative density for the spherically-jointed structure and counterpart pin-jointed structure, as well as for several lattice, foam, and solid materials. The energy absorption efficiency is given by the cushion factor multiplied by the relative density of the material. The target region is defined by a W_{min} less than 0.21 and relative density less than 0.1 (reasons explained in the text). Solid materials all have a relative density of 1 and their W_{min} extend well beyond the range of this plot, as indicated by the truncated gray oval. The structures presented in this work lie within the target region, with the spherically-jointed structure exhibiting the best energy absorption efficiency of all presented materials, along with a very low relative density. The lattice, foam, and solid material data was obtained from the following sources: solid materials [40], CNT Foams [40], porous auxetic microlattices [40], SLS octet truss lattices [142], highly-stretchable soft lattices [138], SLA octet truss lattices [139], SLM Ti-6Al-4V truss lattices [143]. 95
- 5.12 The reaction force measured by the force sensor from three experimental tests on the lattice structure with the impacting mass falling from the same drop height. The transmission time is zeroed out. The impacting velocity for each test is shown in the legend. The results agree considerably, showing high repeatability for the experiments. . 97
- 5.13 Reaction force of the rigid plate at the bottom of the lattice over time for several impacting velocities. (a) Experimental response for four impacting velocities. (b) ABAQUS beam element simulation results for five impacting velocities. The plateau in the force is seen clearly in the 2.9 m/s response. (c) Comparison of response of the numerical and experimental results for two impacting velocities. 98
- 5.14 The global compressive stress-strain curve of the quasistatic compression experiment on the baseline unit cell. We identify two regions: a linear region from 0 to 0.15 strain, and a nonlinear/buckling region from 0.15 to 0.48 strain. Densification, where contact begins between the struts, occurs at 0.48 strain. 101

- 5.15 (a) The 5 unit cells in the lattice are labeled with colored numbers, with the color corresponding to its effective longitudinal strain-time curve in (b)-(f). The longitudinal strain of each unit cell over time for a 1.05 m/s impact is shown for experiment (b) and ABAQUS simulation (c). The strain of each unit cell over time for a 2.3 m/s impact is shown for experiment (d) and ABAQUS simulation (e). (f) The ABAQUS simulation result of unit cell strain over time for a 2.9 m/s impact. 102
- 5.16 Frames from an experimental video of the lattice compression for a 2.3 m/s impact velocity. The frames are given at various stages of compression up to total impact time, $t = t_{imp}$. The red line is placed on the top nodes of the structure in the $t = 0$ image. The red line extends to $t = t_{imp}$, showing that the structure visibly fully recovers its original height after impact. 104
- 5.17 (a) An image of the lattice is given, with velocity measurement locations labeled by number and by color. The colors correspond to the appropriate curve in the plots. (b) Experimental velocity results at unit cell intersection points for an impact of 0.75 m/s . Numerical ABAQUS velocity results at unit cell intersection points for an impact of (c) 0.75 m/s , (d) 1.7 m/s , and (e) 2.9 m/s 106
- 5.18 The discrete Fourier transform of the applied force pulse on the lattice's bottom nodes in a sample drop test of a 3D1D 3 RVE lattice. 108
- 5.19 A 3D1D lattice is shown with measurement locations for wave propagation analysis. The colored lines at the cell intersections indicate where velocity measurements are taken, and the shaded cells are where cell longitudinal strain measurements are taken. The longitudinal strains are defined as indicated by the inset equations. The colored numbers are a numerical reference to each corresponding measurement location. 110
- 5.20 Strain development in a 1D lattice drop test for various impact velocities. The colors of the curves correspond to the cell locations in Figure 5.19. The dashed lines for locations 1 and 6 are ABAQUS simulation results, and the solid lines for all locations are the experimental results. 111

- 5.21 Snapshots of the experimental (left photo) and numerical ABAQUS (right snapshot) deformation of the lattice for a 6.5 m/s sample drop test. The bottom unit cell compresses the most, and the top unit cell compresses significantly less. 112
- 5.22 The sample drop results are shown for a 3D1D lattice. The dashed lines are simulations and the solid lines are experiments. The strains in each cell location are shown for a 2.8 m/s impact in (a) and a 5.4 m/s impact in (b). The velocities at each location are shown for a 2.8 m/s impact in (c) and a 5.4 m/s impact in (d). 113
- 5.23 Images of sample drop test with a glass ornament sitting on top of the lattice. Sample best for the test with the ornament is shown on the left. A high speed video image of the sample and ornament at maximum compression during a 5.4 m/s impact is shown in the center. The ornament after this test is shown on the top right, and an ornament after a drop test without a lattice is shown on the bottom right (broken areas circled in red). 117
- 5.24 ABAQUS velocity profiles for a single point at each cell location in the 3D1D lattice for an impact speed of 8.5 m/s 118
- 5.25 The time evolution of the 8.5 m/s impact of a 3D bulk lattice ($4\times 4\times 4$ RVEs). The colormap shows the vertical component of the velocity, with deep blue indicating the impact velocity and red indicating the opposite of the impact velocity. We zoom in on the regions in black boxes for the first three timestamps to show localization within the struts. 119
- 5.26 For an 8.5 m/s impact, the velocity magnitude at the center of two struts is shown. The inset indicates the locations in the lattice where the strut velocities are measured. 121
- 5.27 Vertical velocity propagation through the lattice by vertical position for the 3D bulk 8.5 m/s impact. The velocity profiles for 9 timestamps are shown. The impact begins on the left of the velocity-position plot at 8.5 m/s 122
- 5.28 ϵ_6/ϵ_1 is the maximum strain at the top cell location divided by the maximum strain at the bottom cell location in a lattice. Here, we show simulation results of ϵ_6/ϵ_1 as a function of impact velocity for 1D, 3D1D, and bulk 3D tensegrity-inspired lattices. 123

5.29	Vertical velocity propagation over time for a 3D1D lattice with 10 RVEs, 18 m/s impact. The colormap ranges from 0 (blue) to v_{imp} (red). The mass separates at 0.0047s.	126
5.30	Space-time (x-t) diagrams for a 10 RVE (20 baseline cell locations) 1D lattice. The colorbar plots the normalized Kinetic Energy, KE/KE_{max} , where KE_{max} is the maximum kinetic energy at the first cell location (location of impact). The top three panels show this for a colorbar scale from 0 to 1, and the bottom three show this for a scale from 0 to 0.5.	128
5.31	Leading wave speeds as a function of impact velocity for 1D and 3D1D lattices, both 5 and 10 RVEs long.	129
5.32	The impact response of a 3D bulk (4x4x4 RVE) lattice under a 12 m/s impact. The colorbar in all plots indicates the vertical velocity normalized by the impacting velocity, on a scale of 0 to 0.5. On the left, we show the bulk lattice at three steps in time, when the wave reaches a peak at the three locations indicated by the black cut regions. On the right, for each timestamp, we show a plot of the normalized velocity over the horizontal cut region indicated in the transverse directions (X and Z).	131
5.33	The force of impact and the transmitted reaction force for various lattices and impact velocities, as indicated on the plots. F/F_c is the force normalized by F_c , which is the force capacity of the bottom layer unit cells. The black line indicates where $F/F_c = 1$	132
6.1	Tensegrity-inspired 3D lattice printed with the Nanoscribe printer.	137
B.1	Relaxation tests performed on the Shapeways PA2200 polyamide nylon material and the Formlabs “Tough” material. ASTM D638 Type IV specimens are loaded in tension, and the strain is held constant at 0.03. The reduction in stress is then measured over time. The magnitude of stress reduction is indicated by the colored arrows next to the vertical axis.	171
B.2	Experimental stress-strain responses of four member diameter geometries of the spherically-jointed structure. The parameter d_s/d_c is the strut-to-cable diameter ratio. The stress is normalized by the maximum stress of the chosen final design (d_s/d_c of 1.44) for comparison.	172

C.1	Strain energy (SE) and kinetic energy (KE) in all cables and all struts in a 10 RVE 3D1D lattice under impact by a 10 g impactor traveling at 18 <i>m/s</i>	174
-----	---	-----

LIST OF TABLES

<i>Number</i>	<i>Page</i>
2.1 The final parameters used in the beam element simulation for the edge members. Four edge members at each node model a sphere in the full 3D structure, as seen in Figure 2.2. The total moment of inertia and total mass given in this table are the combined values for 4 edge members and match that of the real sphere.	15
4.1 Longitudinal low frequency wave speeds for other lattice types with the same relative density and material properties as our tensegrity-inspired lattice. All but the Kelvin lattice wave speeds are calculated from dispersion diagrams [127], and the Kelvin wave speed is calculated from Equation 4.2 [126].	63
5.1 Wave speed measurements for each sample from baseline unit cell drop weight tests. For each sample and impact speed, the average wave speed from 3 tests is given. The wave speeds are averaged for all samples at each impact speed, and the standard deviation of the values is given. All units are m/s	84
5.2 The total remaining strain after 24 impacts for each sample, and the average remaining strain after each impact. The structure undergoes little plastic deformation, even after many impacts, showing the resilience and reusability of the structure.	93
5.3 Leading wave speed measurements for 1D lattice long-duration impact experiments and simulations for multiple impact speeds. All values are in m/s . The experimental values are averaged for multiple tests at each impact speed. We calculate the transmission time for the wave front as the time from when the top nodes of the lattice begin to move to when the top nodes of the bottom unit cell reach a velocity that is 1% of the impact velocity.	105
5.4 Coefficients of restitution for common objects under impact. [147, 148]	115
5.5 Observed leading wave speeds in 1D and 3D1D lattices for both experiments and simulations. The results are averaged for all sample drop tests. All units are in m/s	116

Chapter 1

INTRODUCTION

This thesis presents the design and dynamic investigation of a new type of lightweight, 3D-printable, periodic lattice, which we term “tensegrity-inspired metamaterials.” Tensegrity structures are a type of structural system where the structural members carry pure axial loads and the system derives its stability from member prestress. They have been shown to be very appealing for both static and dynamic applications due to their unique properties. The structures’ geometric complexities make them difficult to manufacture, so using them in a range of real-world applications has remained either complex or infeasible. In this work, we present the design of a 3D-printable structure that exhibits the desirable characteristics and mechanical behaviors of tensegrity structures. Then we examine the dynamics of multidimensional periodic lattices with tensegrity-inspired building blocks, exhibiting their extraordinary tensegrity-like properties that present themselves, experimentally and numerically, in both vibration and impact scenarios. In this introduction, we give an overview of tensegrity structures and their use in dynamic applications, the motivation to develop 3D-printable lattices with tensegrity characteristics, and an overview of the goals and organization of this thesis.

1.1 Background and Motivation**1.1.1 Introduction to Tensegrity Structures**

The term “tensegrity,” coined by Buckminster Fuller, is acquired from the combination of “tension + integrity.” This indicates that the structural integrity of a tensegrity structure is derived from the balance of its tensile members [1], which, under prestress, hold the compressive members stable. Thus, tensegrity structures have been described as islands of compression among a sea of tension [2]. An example of a tensegrity structure is shown in Figure 1.1. They consist of two types of axially-loaded, pin-jointed members: isolated, rigid struts in compression and a continuous arrangement of cables in tension. Tensegrity structures appear similar to truss structures, but have the important difference that they must carry prestress in the members to carry external load [3].

In the 1960’s, Kenneth Snelson created several new art sculptures that employed the tensegrity concept, and it took off as an art form [4]. New types of civil

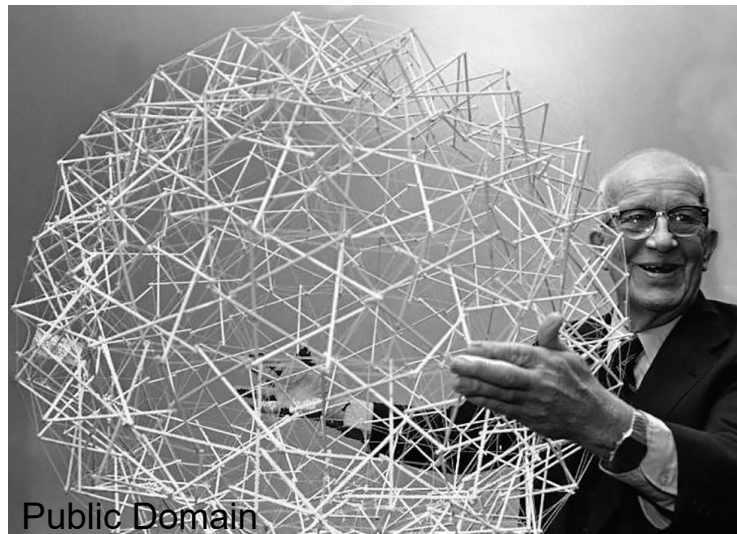


Figure 1.1: An example of a tensegrity structure, held by Buckminster Fuller who coined the term “tensegrity.”

engineering structures such as bridges began being built with tensegrity members instead of traditional truss members. It soon became recognized that the tensegrity concept was a good model of several biological systems, such as bones and tendons in the body, as well as biological cellular structures [5–7]. In fact, tensegrity has been called the “architecture of life,” as its set of structural rules seem to guide the design of organic structures, ranging from carbon compounds to large scale biological structural components [8]. Why, then, did nature choose tensegrity structures as its structural basis for life? Studies of these structures for the last several decades have continued to show their advantages: they are self-stable, extremely lightweight (very important for space applications), energy and mass efficient, can store strain energy for deployment, robust to failure, can undergo multiple loading cycles, and able to withstand large deformations while remaining elastic [9–22]. It is clear, then, that tensegrity structures have been very appealing for mechanical structural applications for several decades.

Tensegrities used as load-bearing structures can achieve high load capacity with a minimal amount of building materials [8, 11, 23]. Their quasistatic response naturally exhibits nonlinearity; this is due to rigid rotation of the struts and effects from prestress [16]. This nonlinearity leads to unusual properties, like extreme softening/stiffening, high tunability with prestress, and even locomotion [16, 24–29]. Until the last decade or so, tensegrity structures remained in the realm of load-bearing and quasistatic mechanical systems. However, in recent years the

unique characteristics of tensegrities have greatly increased the interest and study of tensegrity structures for dynamic applications, which we describe next.

1.1.2 Dynamics of Tensegrity Structures and Lattices

In the arena of dynamics, structures and materials are called upon to protect sensitive objects from damaging loads, be it vibrational or impact loads. Tensegrity structures have a unique capacity to achieve this end by means of their nonlinearity, low densities, reusability, and other exceptional properties. A straightforward example of their use in this area is for planetary landers. For the last few years, significant studies of tensegrity structures as potential landers for extra-terrestrial applications has been of great interest [23, 30–35]. Tensegrity landers present significant advantages over other lander systems (e.g., balloons, parachutes) because they are robust to failure, carry distributed load throughout the structure (characteristic of tensegrities), are tunable, can impact at any angle, are lightweight, and are deployable [36]. For an impact landing, the kinetic energy from impact is stored as elastic strain energy, instead of inducing plasticity or damage [23]. Thus, if an object, such as a camera, was suspended in the center of the tensegrity, it could be protected, as well as being able to “see” out of the tensegrity [36]. An example of this is seen in Figure 1.2: a tensegrity lander impacts the ground with a protected payload at the center. Because of the high stored elastic strain energy, the tensegrity bounces several times before stopping, allowing it to not only withstand impact, but also traverse terrain passively.

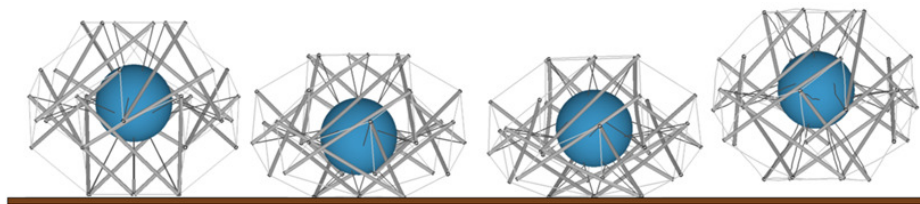


Figure 1.2: A rendering of a tensegrity planetary lander impacting the ground, suspending a protected payload (e.g., a camera) in the center [32, 36].

Tensegrity structures have been of interest in the dynamic regime not only as single structures but also as periodic lattices. Lattices are lightweight structural systems featuring architected assemblies of simple structural elements [37]. Metamaterials refer to structural systems/materials that exhibit properties not found in natural materials or structures. Thus, if they exhibit such properties, periodic lattices are often referred to as metamaterials. Structured metamaterials composed of periodic

arrays of architected building blocks have been recently explored as alternatives to stochastic foams in energy absorption and impact mitigation applications [38–41]. Metamaterial building blocks exploit local deformations, like buckling of members, to convey unique global properties to the bulk lattice. Metamaterials are of interest for the aim of creating mechanical material-like devices that exhibit tunable acoustic band gaps, shock protection, energy lensing/focusing, impact mitigation, and energy trapping for a wide range of applications [42–47]. The selection of appropriate building block geometries allows tailoring the mechanical properties to achieve desired characteristics.

Periodic metamaterials also present interesting elastic wave dispersion characteristics. For example, they can be engineered to propagate elastic waves at desired direction-dependent wave speeds [48–52], and they can be designed to feature bandgaps, i.e., frequency ranges of strong wave attenuation [48, 49, 53–55]. In classical periodic lattices, bandgaps are predominantly of the Bragg scattering type [48]: when lattices feature additional/auxiliary structural elements located within each unit cell, they also feature locally-resonant bandgaps at the resonance frequencies of said auxiliary microstructures [54, 56, 57]. Typically, the wave properties of lattices are set in stone after fabrication. This limitation can be lifted for specific lattice structures, typically made of soft materials, that display buckling-induced phase transitions and therefore can change shape in response to external mechanical forces [58–62]. These lattices typically feature a discrete degree of tunability, since they can only transform into a finite number of geometrical configurations. Moreover, their soft nature makes practical realizations challenging [61], since damping tends to dominate these systems' wave response [63]. Continuous tunability, whereby the wave properties can be swept within a geometry-dependent interval, is usually not attainable in lattice structures, unless they are soft [64], or endowed with multifunctional capabilities and the tunability is induced by an external stimulus such as an electric field [65, 66], temperature [67, 68] or a magnetic field [69, 70].

The unique static and dynamic behavior of tensegrity structures make them appealing as metamaterial building blocks, and so they are gaining increasing attention in this area [23, 71, 72]. Tensegrity structures can be tessellated into lattices that are extremely lightweight, featuring unique characteristics such as the ability to support large global prestrains [17], and to function as effective energy absorbers [73]. They have also been shown to exhibit load-limiting, non-linear characteristics when the bars are designed to elastically buckle [23]. This greatly influences the dynamic

characteristics of lattices formed with these tensegrity unit cells. One-dimensional chains of tensegrity unit cells have been shown to possess unique nonlinear wave propagation, such as highly localized solitary waves [74–77]. Under dynamic loading, tensegrity lattices have been shown to be impact tolerant and possess unique nonlinear responses [23, 78–84].

Tensegrity lattices also display phononic characteristics and Bragg scattering bandgaps. Most importantly, they present extra-ordinary tunability attributes: their dispersion characteristics can be altered by varying the degree of pre-tension of the cables [72, 85–87], or by applying a global prestrain to the whole lattice [86]. With respect to other lattice architectures that feature mechanically-tunable bandgaps, tensegrity lattices are particularly appealing for their large degree of tunability, stemming from the fact that they can sustain large prestrains, and for their continuous tuning attributes.

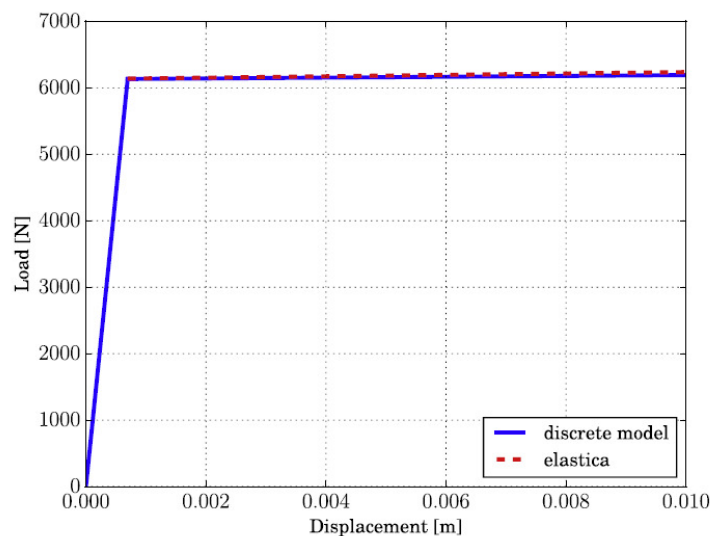


Figure 1.3: Load displacement plot for a titanium strut with density of 4480 kg/m^3 , Young’s modulus of 91 GPa , external diameter of 19 mm , and thickness of 1 mm . The results are shown for the elastic continuum solution and the discrete buckling model developed in [23].

The traditional definition of a tensegrity structure assumes that the struts are rigid, are not free to buckle, and do not store energy [35, 88–95]. Tensegrity structures with elastically buckling struts have been recently studied using physics-based reduced-order models, and their mechanical response has been characterized under static and dynamic loads [23]. In this case, the struts undergo large deformation due to buckling, contributing to the strain energy of the structure. There are many

advantageous properties associated with this. First, the load is distributed among all the members in the structure, increasing structural efficiency. Second, the strain energy capacity of the structure (the area under the stress-strain curve) is dramatically increased because the stress-strain curve plateaus due to buckling in the struts. Finally, the structure can undergo severe deformation and recover its initial configuration upon unloading due to elastic buckling in the struts [23].

Lattices formed by tessellating these buckling tensegrity structures in 1, 2, and 3 dimensions have been shown to possess superior static and dynamic mechanical properties [71, 87]. Under impact loading, wave propagation is highly dispersive and asymmetric in these lattices, and show potential for stress-wave management and energy mitigation [71]. Multidimensional lattices formed with these buckling tensegrity unit cells also exhibit unique dispersion characteristics, which are continuously tunable with prestress [87]. Such characteristics include very low wave speeds, sharp phase transitions, existence of flat bands and zero energy modes, and faster shear wave speeds than longitudinal speeds.

Despite these sought-after dynamic characteristics, experimental studies on the dynamic behavior of tensegrity metamaterials are virtually nonexistent. This originates from the fact that (i) they are difficult to fabricate and assemble due to their pin-jointed and prestressed nature, (ii) assembled systems can introduce spurious propagation modes if cables and bars are not properly bonded, (iii) accurately applying local or global prestrains without affecting the quality of the measurements can be challenging. A way to manufacture such lattices for applications and experimentally corroborate existing theoretical studies on these structures has thus remained elusive. Most work has relied on manual prestress and assembly [18, 35, 80, 96]. However, in multidimensional lattices, especially at decreasing length scales and with potentially thousands of members, this approach quickly becomes impractical.

1.2 Goals and Organization

We recognize the great potential that tensegrity metamaterials hold for dynamic applications, but, from what we can find in the literature, studies have almost exclusively remained in the realm of numerical and theoretical studies to this point. If tensegrity-like characteristics are to be manifested for real-world applications, and the research has indicated this desire, a method for producing tensegrity-like structures as multidimensional lattices at multiple lengths scales is required. It may be possible to mimic pin-jointed behavior and control prestress using multiple

materials [27], shape memory materials [97], differential thermal expansion from multiple materials [98], or induced residual stresses from varying laser intensity [99]. However, all these options require some type of post-processing or a certain manufacturing method. An ideal solution to this manufacturing issue would rely on 3D-printing with a single material and no post-processing, which would enable the production of lattices with a variety of fabrication methods at a large range of length scales.

The goal of this research was to develop a method to obtain an “equivalent” 3D-printable, fixed-jointed structure as a pin-jointed, buckling tensegrity, tessellate the structure into multidimensional lattices, and investigate their dynamic characteristics under both vibration and impact loads. When we refer to the 3D-printed structure being “equivalent” to a pin-jointed tensegrity, this means that the two structures have equivalent strain energy capacity and compressive response. By doing this, we fill the gap in the literature and provide an experimental manifestation of the unique characteristics of tensegrity structures and lattices that have been discovered in recent years. We note here that although the 3D-printed lattices we design are inspired by tensegrity structures and exhibit remarkable tensegrity-like characteristics, our lattices can best be thought of as a new type of extremely lightweight, nonlinear, energy absorbing metamaterial in its own right. This is because the structure is fundamentally different (bending dominated) and shows desirable characteristics that tensegrity structures do not. Tensegrities provide the jumping-off point for obtaining a new class of 3D-printable periodic lattices with properties not yet obtained by traditional designs. In this thesis, we refer to the 3D-printable, tensegrity equivalent lattices as “tensegrity-inspired” lattices.

This thesis is organized such that it progresses systematically from building block design and quasistatic response to increasingly complex lattices and their response to various dynamic loads. To begin, Chapter 2 provides a toolset for understanding this range of studies we performed on the tensegrity-inspired structures. We give a detailed description of all numerical and experimental methods we used throughout the thesis. The majority of studies are performed and validated with both experiments and simulations, except for the most complex dynamic loading case. In that case, the validated simulations are used to infer the behavior of the lattices.

In Chapter 3, we provide a detailed description of the design methodology we developed to produce 3D-printable tensegrity-inspired baseline unit cell structures. We find the equivalent buckling tensegrity response using a reduced-order model

for these structures, developed by our collaborators at Georgia Tech [23]. ABAQUS simulations are used to find the quasistatic response of the structure; simulations are validated with quasistatic compression experiments on the 3D-printed structures. We give a description of the process used to form representative volume elements (RVEs) that tessellate the tensegrity-inspired structure into multidimensional lattices, and provide the quasistatic characteristics of each RVE type.

In Chapter 4, we begin the dynamic investigation of these structures by examining them under frequency excitation. Dispersion curves are obtained for 1D and 3D lattices using both COMSOL frequency simulations and experiments. Since continuous tunability of metamaterials is a desirable characteristics, we study the tunability of 1D lattice dispersion characteristics under global precompression. The band gap and wave speed vary significantly with precompression level. The COMSOL simulations provide insight into the evolution of non-longitudinal mode shapes with precompression for a complete understanding of the dynamics. Finally, we obtain the dispersion characteristics of a 3D lattice in COMSOL. We see the unique result that diagonal and shear waves travel faster than longitudinal waves, as also observed for buckling tensegrity lattices [87]. These results give a foundation for understanding the subsequent behaviors of the lattices under impact loading.

In Chapter 5, we dive into the dynamics of the tensegrity-inspired structures by studying their response under impact. We begin with experiments and simulations of long-duration drop weight tests on single baseline unit cells. We demonstrate the resilience of the structure to repeated loading, its load-limiting ability, slow wave speed, elastic response, and high energy absorption ability. We increase the structure size to a 1D lattice and perform drop weight impact tests on these. Since these long-duration tests are decoupled from the dynamic effects of high-frequency/high-impulse loading, we can observe how the wave propagation is affected solely by the nonlinearity in the structure's response. Next, we perform sample drop tests and short-duration impulse tests on 1D, 3D1D, and 3D bulk lattices. The lattices are loaded by a high-frequency pulse that induces a highly dispersive response in the lattice. We observe significant energy trapping, wave guiding, and force reduction abilities in the tensegrity-inspired lattices.

Finally, in Chapter 6, we provide a summary of the results of this thesis and give a perspective outlining potential extensions of this work as well as future directions for tensegrity-inspired lattices.

Chapter 2

METHODS

We used several numerical and experimental tools in this thesis to study tensegrity-inspired 3D-printable metamaterials. Both types of tools were vital in different ways. The numerical methods provided two main outcomes: (i) preliminary estimates to narrow the range of parameters and variables before experiments were performed, and (ii) detailed exploration of underlying physics and extrapolation of cases beyond the results attainable from the experiments. The experiments provided validation for the simulations, as well as gave insight into how the 3D-printed structures actually behave under the loading conditions explored. This is important in applying our structures to real-world applications, where all systems inherently deviate from nominal conditions. Since a significant contribution of this thesis is the assertion that tensegrity-like structures with desirable characteristics can be fabricated and employed in physical systems, experimental tests are paramount. In this chapter, we explain both the numerical and experimental methods used throughout this thesis.

Some content of this chapter has been partially adapted from:

K. Pajunen, P. Celli, and C. Daraio. “Experimental evidence of analog prestrain-induced bandgap tuning in 3D-printed tensegrity-inspired lattices”. In: *Extreme Mechanics Letters* (2020). In Press.

K. Pajunen et al. “Design and impact response of 3D-printable tensegrity-inspired structures”. In: *Materials & Design* 182 (2019), p. 107966.

2.1 Numerical Methods

2.1.1 ABAQUS Finite Element Modeling

We used the commercial finite element software ABAQUS for all quasistatic and impact simulations. For both cases, we employed ABAQUS/Standard, which uses an implicit integration scheme. ABAQUS/Explicit is well suited for highly transient dynamic problems, problems at high strain rates, and rapidly evolving contact problems [100]. Since our simulations do not exhibit these characteristics, ABAQUS/Standard was the computationally efficient choice and allowed straightforward transition from quasistatic to dynamic modeling.

Material Model

As we explain in Chapter 3, we chose to fabricate all our samples with the polyamide EOS PA2200 material from Shapeways.com[®]. The manufacturer's published properties [101] include only the basic material properties useful for our simulations (i.e., Young's modulus, density, and tensile strength). To form a more complete material model for our simulations, we characterized the polyamide material via ASTM D638 tensile tests on ASTM D638 Type IV test specimens. We performed the tests at various strain rates using an Instron E3000[®]. The results of three representative tests are given in Figure 2.1.

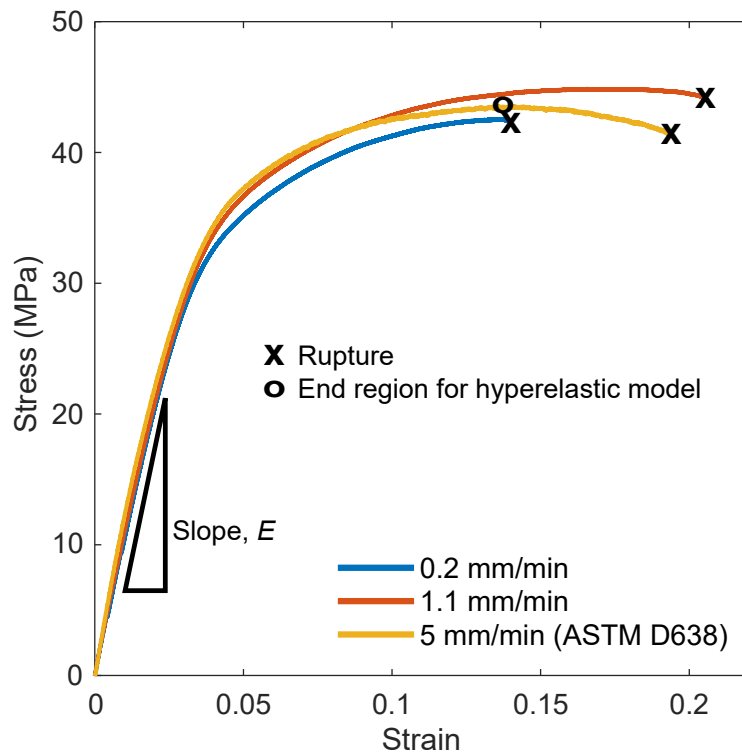


Figure 2.1: Stress-strain response of the EOS PA2200 polyamide material used for the structures in this thesis. The results at three strain rates (0.2, 1.1, and 5 mm/min) are shown. The 5 mm/min test follows ASTM standards for strain rate and was thus used to obtain the material properties. For this test, the sample ruptures at about 0.19 strain. The hyperelastic Marlow model requires strictly increasing values of stress and strain, so for the model we input only the region from 0 to 0.13 strain. The slope of the initial region gives the Young's Modulus, E . This slope is equivalent for all three strains rates tested.

Testing the material at three strain rates gives insight into the viscoelasticity of the material. For a viscoelastic material, the initial slope (Young's modulus), maximum strength, and rupture strain can change considerably with strain rate [102, 103].

We see in Figure 2.1 that for the PA2200 polyamide material, the rupture strain is lower for the lowest strain rate ($0.2 \text{ mm}/\text{min}$), which is observed in viscoelastic materials [102, 103]. However, the initial slope remains constant for the three strain rates tested, and the maximum strength varies by only about 2 MPa . We observe that the material does exhibit some viscoelasticity, but it is not significantly prominent in the material's stress-strain response.

The $5 \text{ mm}/\text{min}$ test follows the ASTM D638 standards, and thus it was used to determine the material properties. The Young's modulus (E), given by the initial slope in Figure 2.1, is 1.29 GPa . The Poisson's ratio was found to be 0.3 using a laser extensometer which tracked transverse and axial reflective strips during the tensile test.

We use the hyperelastic Marlow model to represent the constitutive material in ABAQUS. The Marlow model strain energy potential is given by [100]:

$$U = U_{\text{dev}}(\bar{I}_1) + U_{\text{vol}}(J_{el}) \quad (2.1)$$

where U is the strain energy per unit reference volume, U_{dev} is the deviatoric part, U_{vol} is the volumetric part, \bar{I}_1 is the first deviatoric strain invariant, and J_{el} is the elastic volume ratio. \bar{I}_1 is defined as [100]:

$$\bar{I}_1 = \bar{\lambda}_1^2 + \bar{\lambda}_2^2 + \bar{\lambda}_3^2 \quad (2.2)$$

where $\bar{\lambda}_i = J^{-\frac{1}{3}} \lambda_i$. J is the total volume ratio, and λ_i are the principal stretches. U_{dev} is defined by providing test data, either uniaxial, biaxial, or planar. U_{vol} is defined by the Poisson's ratio, volumetric test data, or lateral strains coupled with the test data.

The Marlow model is unlike other hyperelastic models because it has no material coefficients. Instead of determining coefficients to define the deviatoric part of the strain energy potential, it must be defined with test data. The strain energy potential is constructed within ABAQUS to exactly reproduce the test data and provide reasonable behavior in all deformation modes [100]. For our material, we provide the uniaxial tensile test data shown in Figure 2.1 for the deviatoric part and Poisson's ratio of 0.3 for the volumetric part of the strain energy potential. The tensile test data provided is from 0 to 0.13 strain because the Marlow model requires monotonically increasing test data.

In summary, the material properties implemented in ABAQUS are a hyperelastic Marlow model with the uniaxial stress-strain data, a Poisson's ratio of 0.3, and a

density of 930 kg/m^3 . Simulations using these properties provide well-matching results with experiments throughout this thesis. In addition, for the purpose of calculating strut diameters in the elastically buckling range (Chapter 3), we need a value for yield strength (σ_y). Since yield strength is not well-defined for hyperelastic materials, we estimate a value of 29.1 MPa using the linear elastic 0.5% offset rule.

It is useful to note that we compared the results of this hyperelastic model with an elastic-plastic model. We found that the elastic-plastic model consistently gave results with characteristics not seen in the experiments, such as much too low stiffness and showing permanent plastic deformation when no plasticity was observed in experiments. So, we chose to use the hyperelastic model. A downside of the hyperelastic model is that it is not able to model hysteresis simultaneously in ABAQUS with beam elements. Since the material is viscoelastic, hysteresis is a factor in the dynamic experiments. We see in Chapter 5 that even with awareness of this assumption, the hyperelastic model still gives the best numerical result for our studies.

3D Solid Model

Before we arrived at the final design of our tensegrity-inspired baseline structure, we went through iterations of the design which required full 3D modeling in ABAQUS. Thus, we developed a model which was then used for both quasistatic and dynamic analyses of the baseline tensegrity-inspired structure. A 3D rendering was constructed in Solidworks, imported into ABAQUS, and meshed using about 100,000 3D stress quadratic tetrahedral elements (element type C3D10) which captured the response well with minimal runtime. Tetrahedral elements best conformed to the geometry, while quadratic elements produced better resolution of the bending within the structure with less elements than linear elements. A rendering of the solid model and boundary conditions is shown in Figure 2.2. We henceforth refer to this structure as the *baseline unit cell* or *baseline structure*, which is the basic building block for all subsequent lattice structures.

The baseline structure is 48.3 mm from top to bottom nodes with cable diameters of 1.2 mm , strut diameters of 1.73 mm , and sphere diameters of 5.7 mm . This choice of design and dimensions will be explained in Chapter 3. *Note:* The terms “cables” and “struts” describe the tensile and compressive members of pin-jointed tensegrity structures, respectively. However, the members in our fixed-jointed structure undergo bending and are not under pure tension and compression. For sake of

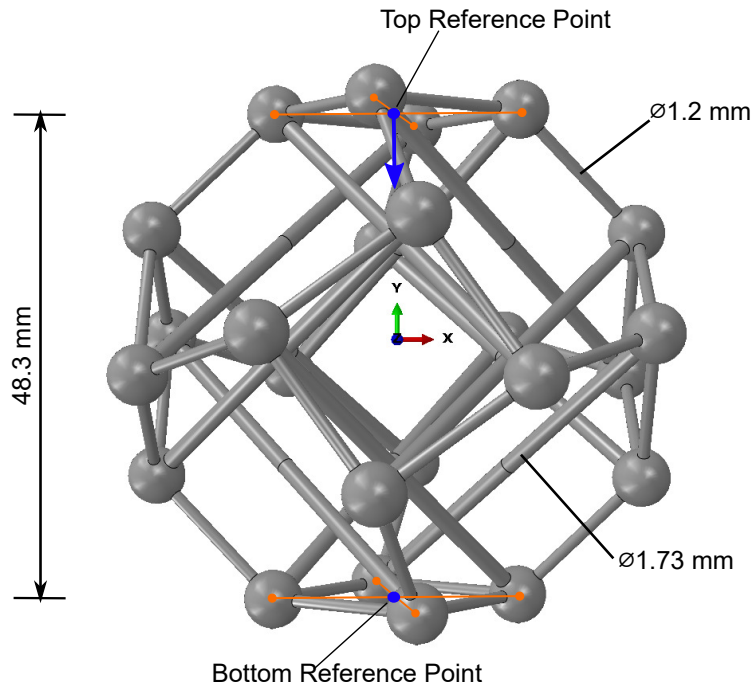


Figure 2.2: A 3D rendering of the tensegrity-inspired structure in ABAQUS. Boundary conditions are placed on top (displacement only in y-direction) and bottom (fixed) reference points (blue circles), which are located along the vertical y-axis and each centered on the plane of the top and bottom face nodes. The top and bottom face nodes (orange dots) are kinematically coupled to the top and bottom reference points (orange lines), such that they are vertically constrained like the reference points, but are able to rotate freely around the vertical axis.

simplicity and easy comparison with the corresponding tensegrity, in this thesis we also refer to the members of our fixed-jointed structure as cables and struts.

To allow rotation of the top and bottom nodes as the structure is compressed (like in the experiments), two reference points, each located at the center of the top and bottom face nodes, are kinematically coupled to their respective face nodes. The top reference point moves downward only, and the bottom reference point is fixed. The coupling constrains the vertical displacement of the 4 top face nodes to the displacement of the reference node, and keeps the 4 bottom face nodes fixed vertically. At the same time, the face nodes are allowed to rotate around their reference points, so they rotate freely around the vertical axis like in the experiment. Nonlinear geometry is used in the full Newton solver to capture the large deformation buckling response.

For quasistatic simulations, a “Static, general” solution step ramps linearly over a certain vertical compressive displacement of the top reference point. For dynamic

drop weight simulations, a “Dynamic, implicit” step is used with “moderate dissipation” activated, which is recommended for impact problems. The top reference point is assigned a point mass and a predefined negative vertical velocity. It can still only displace in the vertical direction.

Beam Element Model

A beam element model was also developed in ABAQUS for static and dynamic analyses of these structures. The deformation of each member in the baseline structure can be modeled as a beam with constant cross section that undergoes only simple bending, torsion, and tension/compression. Also, since using beam elements greatly simplifies the physics problem being solved, the beam element simulations are computationally much more inexpensive than the full 3D model (20x’s less runtime for the beam element simulation). We compared the results of the beam element simulation and the full 3D simulation for quasistatic compression of the baseline unit cell, as well as for a drop weight impact of the baseline cell. With the results matching considerably well, and full 3D modeling being unnecessary and impractical for lattice simulations, the beam element model was used for all subsequent dynamic analyses. The beam element simulation was thus employed for: baseline unit cell drop weight, 1D lattice drop weight, 1D lattice sample fall, 3D1D lattice sample fall, 3D bulk sample fall, 1D lattice short duration impulse, 3D1D lattice short duration impulse, and 3D bulk short duration impulse simulations. Renderings of these different lattice types are shown later in this section.

Beam elements in ABAQUS are one-dimensional line elements with a certain length and an assigned constant cross section. In our case, all cross sections are circular. It is clear that the cables and struts can thus be modeled simply with beam elements. They are given a circular cross-section matching the 3D model and modeled using the Shapeways polyamide material. However, the spheres require some extra thought to be modeled correctly.

As can be seen in Figure 2.2, each spherical joint at each node connects four members (3 cables, and 1 strut). The spheres are essentially rigid and deform insignificantly during deformation of the structure. Because of this trait, we model each sphere as 4 “edges,” each the length of the radius of the sphere, and each connecting the end of each member to the node. Each edge is given a single element, and the material assigned to this element has a Young’s modulus (stiffness) of 291 GPa (approximately that of aluminum, and two orders of magnitude larger

Edge Member Parameters for Beam Model	
Young's Modulus	291 <i>GPa</i>
Poisson's Ratio	0.3
Density	456.6 <i>kg/m³</i>
Total Moment of Inertia	4.04 x 10 ⁻¹⁰ <i>kg · m²</i>
Total Mass	0.096 <i>g</i>
Radius of Each Edge Member	2.4 <i>mm</i>

Table 2.1: The final parameters used in the beam element simulation for the edge members. Four edge members at each node model a sphere in the full 3D structure, as seen in Figure 2.2. The total moment of inertia and total mass given in this table are the combined values for 4 edge members and match that of the real sphere.

than the stiffness of the constitutive material). By doing so, the edges do not deform during deformation of the structure. Additionally, we must assign a circular cross-section to the edges, which must be carefully chosen to match the physics of the spheres. The spheres have a certain mass and moment of inertia, both of which significantly influence their dynamic response. The mass of each sphere is 0.096 *g*, and its moment of inertia is $4.04 \times 10^{-10} \text{ kg} \cdot \text{m}^2$ (given by $I = \frac{1}{2} m_{\text{sphere}} r_{\text{sphere}}^2$). Thus, the combined edge members at each node in the beam simulation must have this mass and moment of inertia. Solidworks was used to calculate the moment of inertia of the combined edge members: a total mass of 0.096 *g* was assigned, and the member radius was adjusted until the combined moment of inertia matched that of the sphere. Then, the material density required was calculated by dividing the total mass by the total volume of the combined edge members. The final edge member parameters are given in Table 2.1. Also, a rendering of the beam element model is given in Figure 2.3, where (a) shows the wire rendering and (b) shows the rendering with the cross-sectional areas shown. The gold members are the struts, blue members are the cables, and green members are the edges.

The beam element type we use is B32, a 3-node quadratic Timoshenko beam element. These allow for transverse shear deformation and large strains, so they are chosen over Euler-Bernoulli elements. Due to the simple nature of the beam element simulation, only 540 elements are needed (less than 1% of the number of elements used for the 3D model). We used a mesh refinement study to choose a number of elements that appropriately weighed the accuracy of the solution with the computational cost. For the baseline quasistatic and dynamic drop weight simulations, the same boundary conditions, coupling constraints, and step parameters

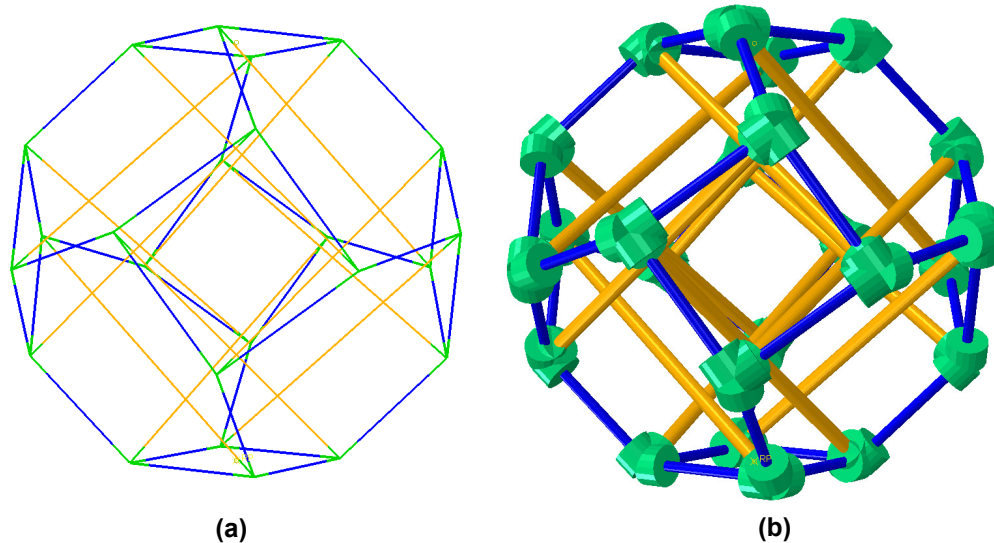


Figure 2.3: Beam element rendering of the tensegrity-inspired baseline unit cell with (a) wire elements and (b) beam element cross sections visualized. The struts are displayed as the gold members, the cables are the blue members, and the edges (4 of which together simulate a sphere at each node) are the green members.

were used that were employed in the 3D simulation (see Figure 2.2).

Lattice simulations are easily set up in ABAQUS using the beam element modeling method described. The baseline cell is simply tessellated in space appropriately for each lattice case. However, for lattice simulations, the boundary conditions are slightly altered. Instead of top and bottom reference points that couple with the top and bottom face nodes, we model analytical rigid plates that interface with the top and bottom face nodes. We do this because of two reasons: (i) for short duration impact, separation of the top rigid surface occurs early in the simulation, and (ii) as the number of top and bottom face nodes moves beyond 4, as is the case for higher dimensional lattices, kinematic coupling with a reference point is no longer physically valid. We set up node-to-surface contact interactions between the top and bottom plates and the top and bottom face nodes that they interact with. The interaction property models frictionless tangential behavior and hard contact and allows separation of the rigid surfaces after contact.

Both analytical rigid surfaces have reference points at their center (corresponding to the center of the top or bottom face nodes) where boundary conditions are applied. Again, the bottom reference point is fixed. The top reference point is assigned a point mass and a predefined negative vertical velocity. It can only displace in the vertical direction. For sample drop simulations, the lattice itself is assigned a predefined

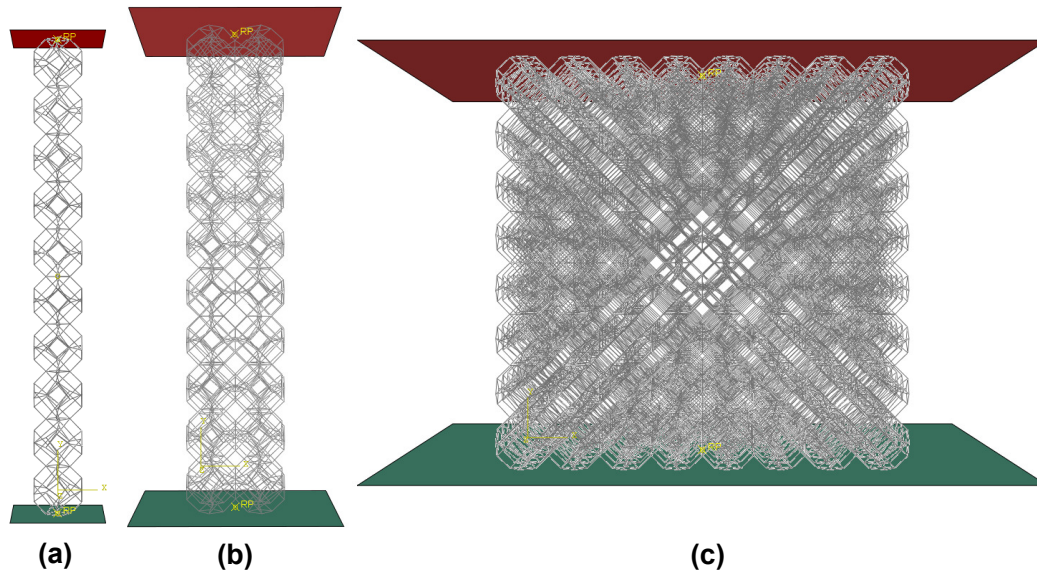


Figure 2.4: Example ABAQUS renderings of (a) 1D, (b) 3D1D, and (c) 3D bulk lattices with top and bottom analytical rigid surfaces used for impact simulations.

negative vertical velocity, and there is no top analytical rigid surface. In that case, the bottom rigid surface remains fixed. As explained in Chapter 3, different lattice types have representative volume elements (RVEs) that have different numbers of baseline unit cells. A 1D lattice RVE has 2 baseline unit cells and a 3D RVE has 8 baseline unit cells. We define a 3D1D lattice as a lattice that tessellates 3D RVEs in only one direction. Example renderings of 1D, 3D1D, and 3D bulk lattices with the analytical rigid surfaces are shown in Figure 2.4.

As the lattices and strain rates become larger, the computational cost of the simulations greatly increases, but also convergence of the solution steps become more difficult due to the complexity of the deformation. This manifested most particularly in the 3D bulk simulations. To overcome this, we had to use hybrid elements and a quasi-Newton solver for the 3D bulk models. The hybrid formulation for beam elements overcomes the difficulty of computing axial and shear forces in geometrically nonlinear analyses by using a more general finite element formulation that treats these forces as primary variables [100]. Hybrid elements are best used in cases with very slender beams ($D/L < 1/15$) and very rigid axial and transverse shear deformation (bending deformation dominant) [100]. It is true that bending deformation is dominant in our structures, but axial and transverse shear still play a role, especially in the cables which have a length-to-diameter ratio of 0.1 (the struts have an D/L of 0.04). When we compared 1D lattice results with hybrid

vs. non-hybrid elements, the non-hybrid elements provided better resolution of complexities in the response at smaller time steps, but the hybrid elements still captured the overall response well.

The quasi-Newton solver in ABAQUS employs an inexpensive stiffness matrix update for most solver iterations rather than factorizing a new stiffness matrix for every iteration, as is done in the full Newton solver. In large models, stiffness matrix factorization is complex and can dominate the solution time, so the quasi-Newton solver is recommended for large models, especially for nonlinear dynamic situations (as is the case for us). We found that without employing hybrid elements or the quasi-Newton solver, 3D bulk simulations did not converge. But with their addition, the simulations ran successfully. We believe that the physics are still captured well for the 3D bulk simulations even with these alterations.

Pin-Jointed Tensegrity Model

As a complement to the ABAQUS simulations and experiments of baseline unit cells, we also find the response of corresponding pin-jointed tensegrities. To do this, we use a numerical model developed at Georgia Tech by the Rimoli group to generate quasistatic and dynamic responses of pin-jointed tensegrity baseline unit cells [23, 71, 87, 104]. The numerical model is patented [104] and the MATLAB files are available on the Rimoli group website (as of 3/10/2020) at: http://rimoli.gatech.edu/docs/pal_rimoli_code.zip.

Although any tensegrity structure configuration can be implemented in this model for the single unit cell case, the truncated octahedron tensegrity unit cell is the default (and patented) configuration due to its ability to be tessellated into 3D lattices. The form-finding for this structure was performed in [23] using the method described in [105]. We base our tensegrity-inspired structure off of this truncated octahedron tensegrity configuration.

The model uses a reduced-order approach to modeling the response of tensegrity structures with buckling struts. The struts are discretized as a set of four masses, three linear springs, and two angular springs (which capture the buckling of the strut). The cables are discretized as a set of four masses, three linear springs, and no angular springs, since the cables undergo pure tension [23]. The dynamic response is found through an explicit, second order accurate, central-difference time integration scheme. Contact is modeled through a penalty approach, and friction forces are neglected [23]. Both the dynamic and quasistatic responses of a tensegrity structure are captured well with this model. We use this code to find

a corresponding tensegrity structure to our tensegrity-inspired structure. We then perform both quasistatic and drop weight simulations on that structure to compare with our ABAQUS and experimental results in this work.

2.1.2 COMSOL Finite Element Modeling

COMSOL was used to simulate the frequency dynamics of 1D and 3D RVEs, consisting of 2 and 8 baseline unit cells, respectively. Within its Solid Mechanics module, COMSOL has readily available tools to find dispersion curves and transmission characteristics in the frequency domain. ABAQUS does not contain such tools; calculating dispersion curves can only be found using complex user-defined scripts. COMSOL contained all that was necessary to perform dispersion and transmission analyses on our unstressed as well as prestressed (using a quasistatic compression step before the frequency step) tensegrity-inspired structures. Therefore, we chose to use COMSOL for this portion of the thesis.

Dispersion

First, we construct a COMSOL model which simulates an infinite lattice to extract the dispersion curve. We build a 3D model of a 1D RVE in Solidworks, import it into COMSOL, and mesh it with quadratic tetrahedral volume elements. Although we know that the polyamide material behaves as a hyperelastic material, only the linear elastic material model was available to us in COMSOL. For low amplitude waves, the structure deforms only slightly corresponding to oscillations around a small area of the stress-strain curve. Thus, for low levels of precompression, the linear elastic model is a good assumption. Deviance from the linear elastic model only becomes an issue at higher levels of precompression (10%–20% global strain levels). We see this deviance in the simulations, but as we will see in Chapter 4, the simulation captures the experimental response fairly well even with this assumption. Thus, we use a linear elastic material with Young's Modulus of 1.29 GPa , Poisson's ratio of 0.3, and density of 930 kg/m^3 for the polyamide material that the samples are fabricated from.

To calculate the dispersion relation of the 1D lattice, we use an eigenfrequency step with Bloch periodic boundary conditions, thus simulating the response of an infinite lattice. The Bloch theorem states that for a travelling wave $\mathbf{u}(\vec{\mathbf{r}})$, there exists a wave vector $\vec{\mathbf{k}}$, such that translating it by the lattice vector $\vec{\mathbf{R}}$ is the same as

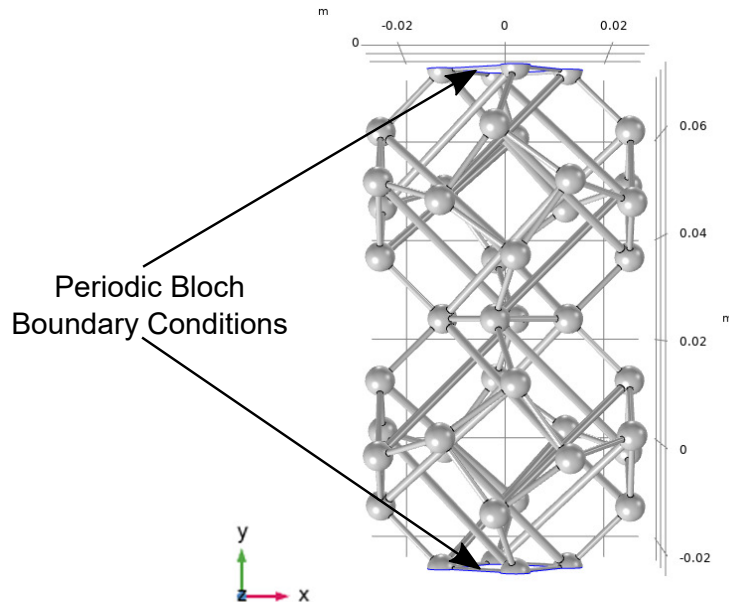


Figure 2.5: A rendering of the solid model of a 1D RVE in COMSOL. We make a cut through the top and bottom faces on the horizontal planes that intersect the center axes of the cables, creating flat surfaces to apply the Bloch boundary conditions. The RVE has a total height of 96.6 mm in the y-direction.

multiplying the wave by a phase factor [106]:

$$\mathbf{u}(\vec{\mathbf{r}} + \vec{\mathbf{R}}) = e^{i\vec{\mathbf{k}} \cdot \vec{\mathbf{R}}} \mathbf{u}(\vec{\mathbf{r}}). \quad (2.3)$$

For our 1D case, tessellating in the vertical (y) direction, this reduces to $u_{top} = u_{bottom} e^{ika}$, where k is the wavenumber and a is the length of the RVE. To create a tessellatable unit, we make a cut through the top and bottom faces on the horizontal planes that intersect the center axes of the cables. In this way, we create flat surfaces on which to apply the periodic boundary conditions in the vertical direction. The 1D RVE has a total height of two baseline cells (96.6 mm). A rendering of the solid model in COMSOL is shown in Figure 2.5.

To produce the dispersion curves, we implement a linear eigenfrequency step where the software solves an eigenvalue problem for the first 20 eigenvalues at each wavenumber value k in the first Brillouin zone $(0, \pi/a \text{ rad/m})$, where a is the length of the RVE. To calculate the dispersion curves for varying levels of precompression, we first use a stationary step to solve for the quasistatic compressive response with geometric nonlinearity taken into account. In this step, a quasistatic periodic boundary condition is applied to the top and bottom face surfaces. The bottom surface remains fixed, and the top surface undergoes vertical compression,

as in the experiment. Then, the final conditions from the stationary step (including the stresses arising from precompression) are set as the initial conditions for the subsequent linear eigenfrequency step, and the boundary conditions are switched to those of the eigenfrequency step. This small-on-large approach is standard procedure when modeling bandgap tunability due to mechanical forces [58, 62, 66].

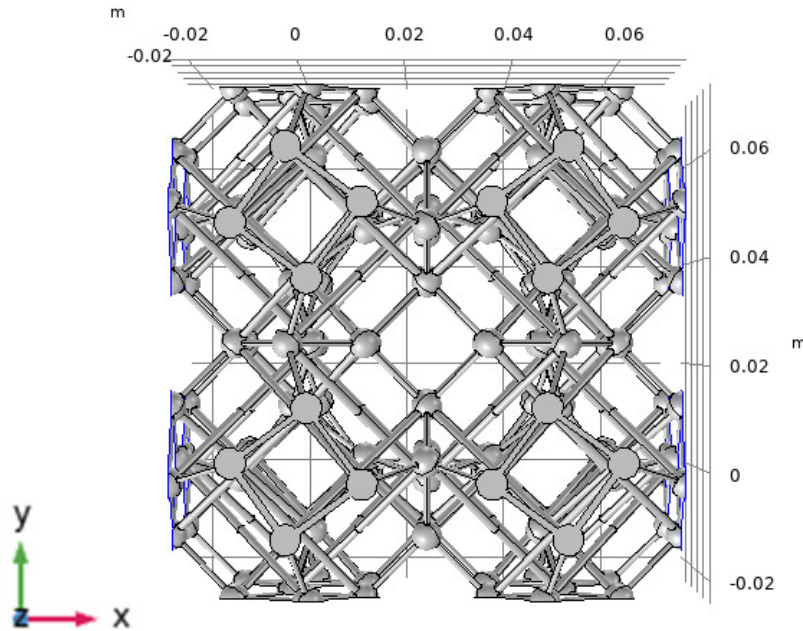


Figure 2.6: A rendering of the solid model of a 3D RVE in COMSOL. We make a cut through the 24 external faces to create flat surfaces on which to apply the Bloch boundary conditions.

We also perform a dispersion analysis on a 3D RVE, but only for the unstrained case. In this case, we make a cut through all right and left (x -axis), top and bottom (y -axis), and front and back (z -axis) faces, for a total of 24 faces, in the same way as for the 1D case. Bloch boundary conditions in each dimension are applied on these faces. An eigenvalue problem is solved for the first 20 eigenvalues at each wave vector combination in the first Brillouin zone for a simple cubic lattice. This wave vector sweep is described in detail in Chapter 4.

Transmission

Finally, a finite lattice with 3 RVEs (289.8 mm height) is simulated in COMSOL in order to find the longitudinal frequency transmission response to compare with experiments (see Figure 2.7). Since this simulation takes into account the finite size

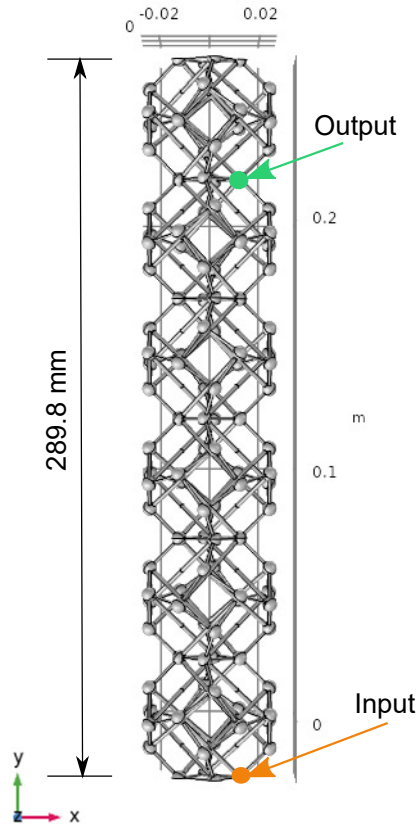


Figure 2.7: A finite 3 RVE 1D lattice is modeled in COMSOL to find the longitudinal frequency transmission response. Displacement amplitudes are extracted from the input and output locations (orange and green circles, respectively) to find the transmissibility ratio at approximately the same locations as in the experiments.

and boundaries of the experiment, we expect it to capture the experimental response better than the numerical dispersion curves. In this case, the lattice with 3 RVEs is modeled with the same element type as the unit cell model. We then perform a harmonic analysis (from 0 to 500 Hz) by applying a base excitation with amplitude of 1 mm to the bottom face surface, while the top face surface is kept fixed as in the experiment. The input and output vertical displacement amplitudes are extracted at approximately the same locations as the first and last measurement points in the experiment. In the simulations with precompression, the nonlinear quasistatic step is performed before the harmonic analysis.

2.2 Experimental Methods

2.2.1 Sample Fabrication

We designed several experiments in order to study the response of 3D-printed tensegrity-inspired structures under both static and dynamic loading. In all experiments, samples were 3D-printed using the EOS PA2200 nylon polyamide material from Shapeways.com[©]. The manufacturing process used is Selective Laser Sintering, or SLS. With this method, a high-powered laser selectively fuses small particles of polymer powder together, layer by layer. The part being constructed is surrounded by powder at all times, eliminating the need for support structure. This manufacturing method was chosen for several reasons. With SLS, this structure is manufacturable with relative ease, having no support structure and no post-curing processes. The lack of post-curing also produces consistent structures with the desired constitutive material properties and mechanical responses. The chosen member diameters and aspect ratios fit well within the manufacturable limits of the SLS manufacturing method for the chosen material. We note that other 3D manufacturing approaches may also be suitable for fabrication, e.g. stereolithography (SLA), material jetting (MJ), fused deposition modeling (FDM), digital light processing (DLP), and 2-photon polymerization. We have also successfully printed this structure with SLA and 2-photon polymerization.

2.2.2 Static Compression Tests

To characterize the mechanical response of the tensegrity-inspired 3D-printed baseline structure, we performed quasistatic compression experiments using an Instron E3000[©] with a 500 N load cell. The chosen structure height of 48.3 mm was a practical size for the compression experiments. The samples were loaded on the top face and compression was applied using displacement control at 1.1 mm/min. The test was stopped when densification (inner struts begin to touch) occurred. The top and bottom faces were allowed to rotate during compression, which naturally occurs due to asymmetry of the face nodes. The experimental setup is shown in Figure 2.8.

2.2.3 Dynamic Impact Testing

Several types of impact experiments were performed on the tensegrity-inspired structures. All of them used the same basic setup, where a high-speed camera tracks nodal displacements and a force sensor measures the reaction force on the bottom of the structure during an impact. The setup and its variations were designed and built



Figure 2.8: Quasistatic compression tests were performed on baseline unit cell samples using an Instron E3000[®]. The bottom plate remains fixed, while the top plate displaces the structure vertically using displacement control. The structure faces are allowed to rotate during the compression.

for this thesis. It was used to test baseline unit cells, 1D lattices, and 3D1D lattices.

Drop Weight: Baseline Unit Cell

To examine the dynamic response of a baseline unit cell, we designed and built a drop weight testing system, shown schematically in Figure 2.9(a) and physically in Figure 2.9(b). A low-friction, stiff vertical rod guides a free-falling striker mass with a flat bottom surface that impacts the 3D-printed samples. The mass is custom-made from steel, with the outer diameter chosen to be large enough to impact all top face nodes of the structure, but narrow enough to minimize the transverse moment of inertia. We fabricated two different strikers with masses of 100 g (exact: 109.0 g) and 200 g (exact: 197.54 g). The impact velocity of the mass is controlled varying the height of the striker above the sample. An accelerometer is placed on top of the mass to record when it first touches the structure as well as the deceleration of the mass during impact. It is a triaxial ceramic shear ICP[®] accelerometer with a sensitivity of $0.47 \text{ mV}/(m/s^2)$. The voltage is recorded with an oscilloscope. Since the accelerometer has a mass of 1.0 g, a counterweight is placed opposite on the mass surface. To allow the natural rotation of the sample, the guiding metal rod runs through the center of the structure.

The structure sits on top of a glass sheet, which serves as a stiff surface extension

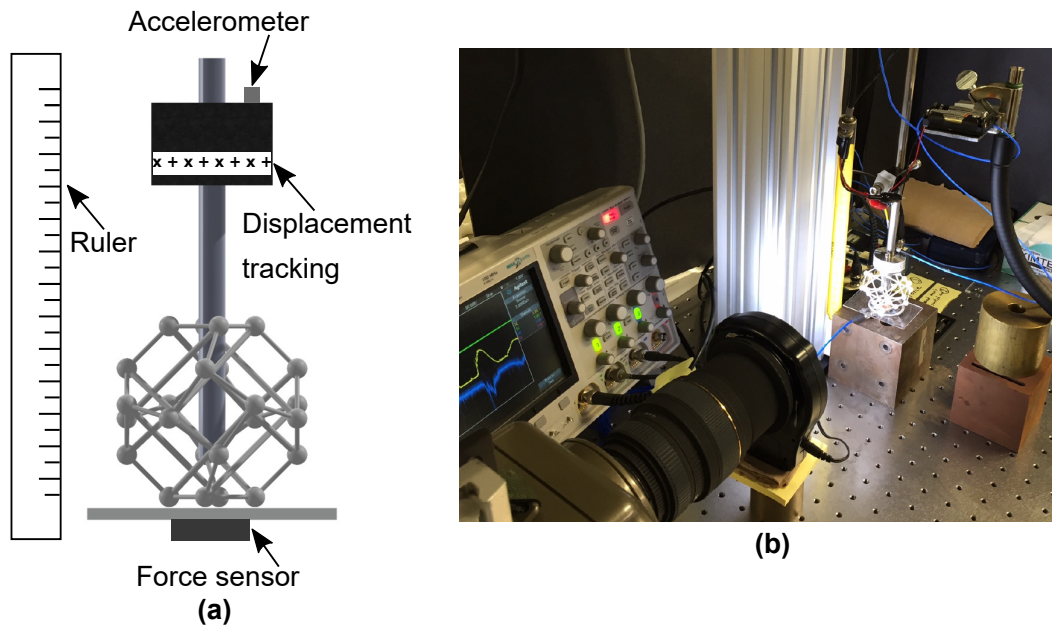


Figure 2.9: Dynamic drop weight test setup for a baseline unit cell. A schematic is shown in (a), and a picture of the physical setup is shown in (b).

for the force sensor under it. The metal rod is suspended just above the glass plate, so it does not affect the force, but also does not allow the structure to slip out of its vertical axis. The force sensor measures the reaction force on the bottom face. It is an Impact ICP[®] quartz force sensor with a sensitivity of 11241 mV/kN . To reduce friction between the structure and the glass sheet, a thin liquid layer of acetone is dispensed on the glass sheet shortly before the test.

A PHANTOM[®] high-speed camera with a framerate of 1000 fps is used to capture the displacement of the falling mass, and thus the top face nodes of the structure. The camera can be seen on the lower left of Figure 2.9(b). A macro flashlight is used to achieve suitable exposure of light. Sufficient light is needed in order to track the markers (black markers of a white background) fixed on the weight during the fall using the Phantom Camera Control (PCC) software. Calibration of the displacement data in the PCC Software is done using a ruler placed in the same focal plane as the markers. Finally, to ensure synchronized time measurement between the camera and oscilloscope data, a switch is triggered when the mass begins to fall, zeroing the time for the oscilloscope and camera.

We developed a customized MATLAB code to process the data from the oscilloscope and camera. Only the first impact is analyzed for each test. Data from the force sensor has a sampling frequency of 4000 Hz and is smoothed using moving

average filter with a span of 5. The force on the top spheres is calculated from the accelerometer data and the impacting mass. Since the accelerometer data was inherently very noisy, we apply a 3rd order digital lowpass Butterworth filter with a normalized cutoff frequency of 0.5. A high cutoff frequency of 1000 Hz is used to filter high frequencies while retaining the desired data representing the physical response. These MATLAB codes are provided in Appendix A.

Drop Weight: 1D Lattice

The drop weight testing system was readily adaptable for 1D lattices. The setup is shown in Figure 2.10. For drop weight experiments on 1D lattices, we use samples

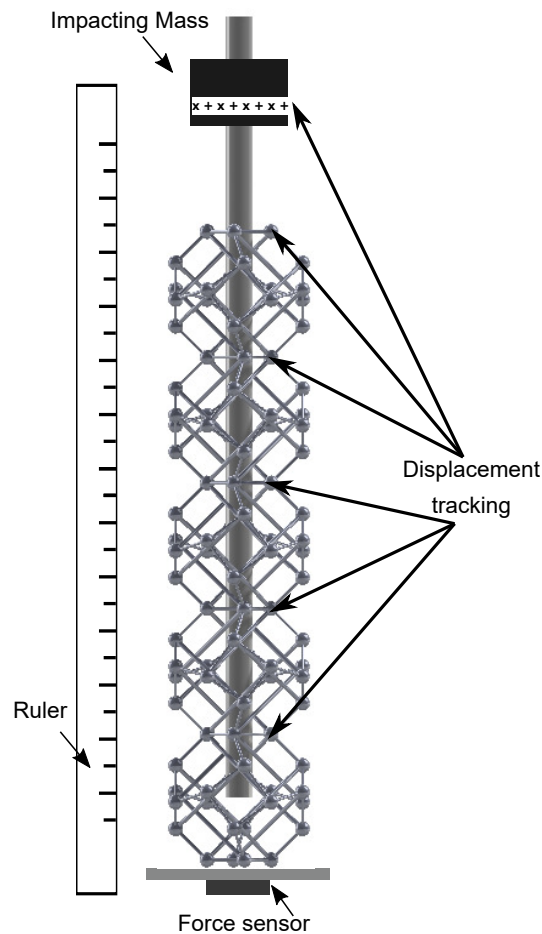


Figure 2.10: Dynamic drop weight test setup for a 5 baseline unit cell 1D lattice.

with 5 baseline unit cells, for which we are able to capture the wave propagation characteristics. A few adjustments had to be made to the test setup. First, the PHANTOM[®] camera frame rate needed to be increased to 3000 fps in order to

sufficiently capture the wave propagation dynamics. To do this, more light was needed to increase exposure, so we added two LED lights on either side of the camera and pointing toward the sample. An even higher frame rate was desired but was not achievable due to lighting constraints.

Also, we track the displacement of not just the impacting mass, but also nodes at each intersection of the unit cells and the top of the lattice (see Figure 2.10). By doing this, we obtain displacement data for each unit cell and can readily differentiate this to obtain the velocity of each unit cell. The accelerometer is, thus, not used for these tests because the wave speed is easily calculated from just the displacement tracking. Even with a frame rate of 3000 *fps*, when we differentiate the displacement data, the velocity data is very noisy. So, we employ the same type of Butterworth filter as was used for the accelerometer to smooth the displacement data before differentiating. Finally, we note that the rod through the center of the lattice and mass is important for these tests for another reason: to keep the lattice straight and from buckling out-of-axis during impact. All other setup details and the data processing are the same as for the baseline unit cell.

Sample Drop Tests

The final type of impact experiments performed were sample drop tests. For these tests, the impacting mass is not used, but the lattices themselves are dropped from a height to achieve a certain impact velocity as it hits the glass plate. We tested both 1D and 3D1D lattices with 3 RVEs. Because the 3D1D lattice had a bottom contact face with a significantly larger area than the 1D lattice, a larger glass plate was obtained from MacMaster Carr. It is a borosilicate glass sheet, 7" x 7" and 3/16" thick with a very smooth finish. As in the 1D drop weight setup, we track multiple locations on the lattice with the camera. A schematic of the setup and displacement tracking points are shown for the 3D1D lattice in Figure 2.11. Two points are tracked at each horizontal section, one inner point and one outer point, and these two points are averaged to get a good estimate of the displacement and velocity at each horizontal intersection location. After averaging, 7 “effective” points are tracked. For the 1D lattice, 7 points are directly tracked: at the top, bottom, and intersection of each baseline unit cell. Wave propagation information through the lattice is obtained through these measurements.

As in the drop weight tests, a rod also must be run through the center of the lattice. As in the drop weight case, it keeps the 1D sample from buckling during

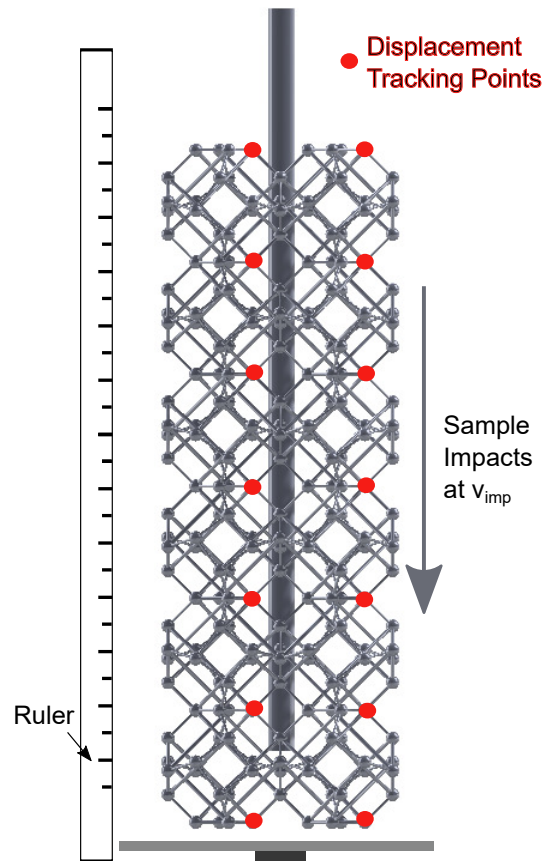


Figure 2.11: Schematic showing the sample drop test of a 3D1D lattice, with displacement tracking points shown.

impact (the 3D1D lattice is too thick to have buckling problems). However, it is also imperative to keep the lattice falling on a straight path during its descent. Since we drop the samples from up to a height of 12 ft (i.e., an impact velocity of 8.5 m/s), without the rod, the sample would easily topple out-of-axis from drag and impact velocities would not be consistent. It was difficult to find a rod long enough and sturdy enough to meet the requirements of the experiment, while still hovering over the force sensor, but we found one: a 16-foot long tent pole. The tent pole was heavy enough to not sway much and also stay relatively straight (although some error unavoidably occurred from these factors). Also, intersections between the tent pole sections were very smooth, and the tension rope within the pole kept the pole together very well. A picture of the entire test setup, capturing the height of the setup as well as a zoomed-in picture is shown in Figure 2.12. Again, all else remains the same from the previously described drop weight testing setup.



Figure 2.12: Picture taken of the entire sample drop test setup, with the total height seen in the left panel and the zoomed-in image of the lights, sample, ruler, etc. in the right panel.

2.2.4 Frequency Transmission Experiments

The final type of experiments we performed were frequency transmission tests on 1D lattices to reconstruct the dispersion curves, measure wave speeds, and determine the transmissibility characteristics of the lattice. Tests were performed at varying levels of compressive longitudinal prestrain to observe the tunability of the lattice response.

We use two one-dimensional lattice specimens, with 5 and 3 RVEs, fabricated with the same polyamide material and same baseline unit cell dimensions as all other experiments. Assessing the dispersion properties of the lattice required us to measure the response at multiple locations along the direction of wave propagation at each RVE. A theoretical dispersion curve is a representation of an infinite medium; thus, when reconstructing a dispersion curve from experimental data, it is desirable to have as many unit cells as possible to avoid truncation-induced features and to

minimize the influence of the boundaries. Also, the wavenumber resolution of the experimental dispersion curve directly relates to the number of RVEs. Due to fabrication limitations, a lattice with 5 RVEs (10 baseline cells) was the largest we could produce reliably. We fabricated the lattice with a plate on the bottom face, intersecting the four spherical nodes, to secure its attachment to the wave source transducer. The 5 RVE lattice was used for the case with no precompression, and the 3 RVE lattice was used for the tests where precompression was applied.

To study the dynamic frequency response of the tensegrity-inspired structure, we use the experimental setup shown in Figure 2.13. To experimentally reconstruct the

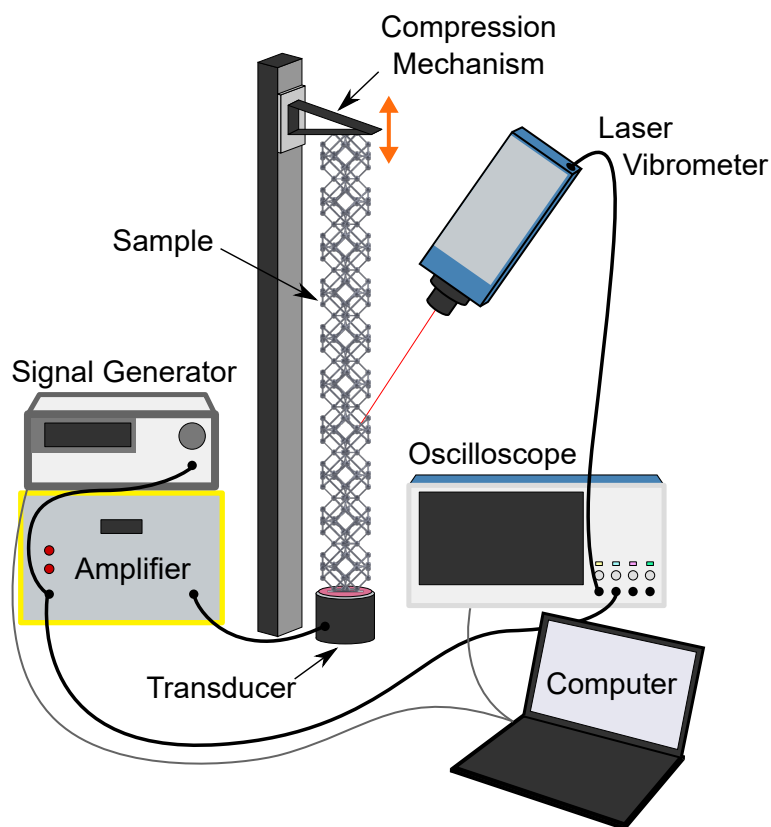


Figure 2.13: Schematic of the experimental setup used to study the spectro-spatial wave characteristics of a tensegrity-inspired 1D lattice.

dispersion characteristics of the lattice, the plate on the bottom of the sample is fixed to a piezoelectric transducer (Panametrics V1011). We excite the bottom plate of the specimen with a one-cycle burst having carrier frequency of 200 Hz and a wide frequency bandwidth (to test a large frequency range with a compact signal). Small strips of retro-reflective tape are placed on top of the nodes at the intersection of each

baseline cell and on the bottom plate, for a total of 10 strips on the 5-RVE lattice and 6 strips on the 3-RVE cell lattice. The single-point Laser Doppler Vibrometer (LDV, Polytec CLV-2534) records the velocity time history at each of the reflective tape locations, repeating the measurement 128 times at each location and averaging to improve the signal-to-noise ratio. Note that the vibrometer is reoriented after each measurement to point it towards another measurement location. We also employ a high-pass filter to eliminate all ambient noise at frequencies lower than 100 Hz . These filtering steps are required since the waves imparted by the transducer onto the specimen are weak, owing to the fact that we are operating the transducer very far from its peak frequency (100 kHz). Once we collect the measured data into a time-space matrix, we obtain a frequency-wavenumber data matrix by using a 2D Discrete Fourier transform (2D-DFT); we zero-pad the data prior to performing the 2D-DFT operation, to interpolate along the wavenumber direction and improve results visualization despite having only few spatial samples.

We devised a compression apparatus to study the effect of global longitudinal prestrain on the dynamic response of the structure. A 90-degree metal bracket moves continuously in the vertical direction on a manually-operated linear stage (Velmex MN10). The flat surface of the bracket compresses the top face of the structure. We can thus directly control the applied longitudinal strain. Our samples are long and slender. For example, the 5-RVE lattice has a slenderness ratio of about 0.1 and a low lateral stiffness of about 58 kPa. When compressing them, we can expect them to undergo global lateral buckling. An analysis of this is given in Chapter 4. To prevent this undesired behavior and to compress the structure to high longitudinal strains, we can only compress 3-RVE-long specimens.

Even with the shorter specimen, global buckling was an issue (see Figure 2.14(a)). So, we constructed an apparatus that can hold the structure in its axis. We tie four strings onto four vertical, stiff rods equidistant from each other and from the structure, as illustrated in Fig. 2.14(b). The other extremity of each string is tied onto the structure at the nearest node at the intersection between the third and fourth baseline unit cells (at approximately half the overall length of the structure). The strings are tensioned so that they are parallel to the top compression plate. Note that we move the strings vertically along the rod as compression changes, to keep them horizontal. The four strings hold the center of the structure in-axis, preventing the first global buckling mode to take place. Four strings are needed so that there is no direction out-of-axis for the structure to move without being held in place by

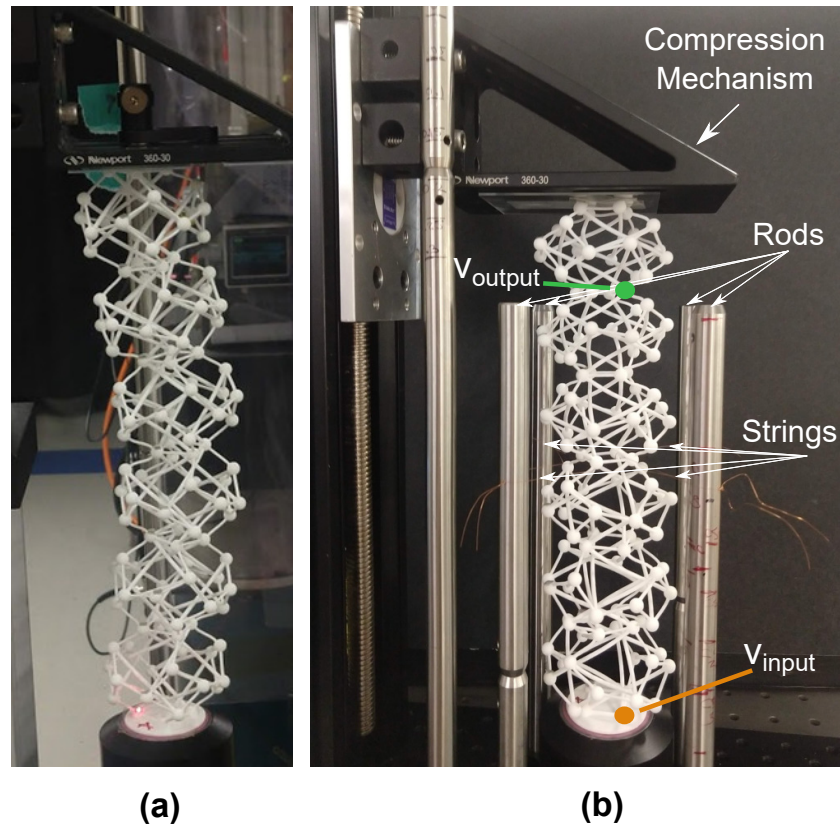


Figure 2.14: (a) Global buckling is apparent in the 3 RVE lattice even at low compression levels. Thus, we devised an apparatus using strings and rods (b) to hold the structure in its axis and prevent first mode buckling. The transmissibility is calculated by dividing the velocity amplitude at the output (green dot) by the velocity amplitude at the input (orange dot), as in the simulations.

another string. The strings only prevent movement out-of-axis, and do not provide resistance vertically. Thus, the strings only minimally influence waves propagating longitudinally along the structure's axis.

We note that the transmissibility through the structure is readily calculated by dividing the velocity amplitude at the output location (green dot in Figure 2.14(b)) by the velocity amplitude at the input location (orange dot in Figure 2.14(b)). Also, dispersion curves (frequency vs. wavenumber), frequency transmission data, and space-time diagrams are obtained through post-processing of the output velocity data in MATLAB; these codes are provided in Appendix A.

Chapter 3

DESIGN OF TENSEGRITY-INSPIRED STRUCTURES

In this chapter, we describe the method we developed to obtain a 3D-printable tensegrity-inspired structure with the equivalent strain energy capacity and global longitudinal stress-strain quasistatic response as a buckling pin-jointed tensegrity. A truncated octahedron tensegrity is used as the baseline, but we infer that the method can be applied to other types of tensegrity structures as well. We obtain a structure which possesses several desirable and unique characteristics of buckling tensegrity structures that make them appealing for dynamic applications. The structure is 3D-printable with a single material, and its quasistatic nonlinear response is geometrically-driven, thus allowing it to be manufactured at multiple length scales with a variety of printing methods. We also show how this structure is tessellated into three dimensions to form multidimensional architected lattices, creating a new type of lightweight, energy absorbing metamaterial.

Some content of this chapter has been partially adapted from:

K. Pajunen et al. “Design and impact response of 3D-printable tensegrity-inspired structures”. In: *Materials & Design* 182 (2019), p. 107966.

3.1 Design Methodology

3.1.1 Target Baseline Tensegrity and Initial Design Iteration

The tensegrity structure described in [23] was used as the baseline pin-jointed tensegrity for this work. The structure’s geometry, which is based on a truncated regular octahedron, was derived using the form-finding method described in [107]. We chose this specific architecture because it has 6 square, orthogonal “faces,” which, with certain reflections required to accommodate asymmetry of the faces, allows tessellation in three-dimensional lattices [71]. We initially use the geometry of the un-prestressed tensegrity, noting that the geometric configuration changes based on the level of prestress applied to the cables.

The tensegrity structure is shown in Figure 3.1(a). The structure has 12 struts and 36 cables. There are no strut-to-strut connections, defining the structure as a “class 1” tensegrity [108]. In choosing the size of the baseline tensegrity, we kept in mind

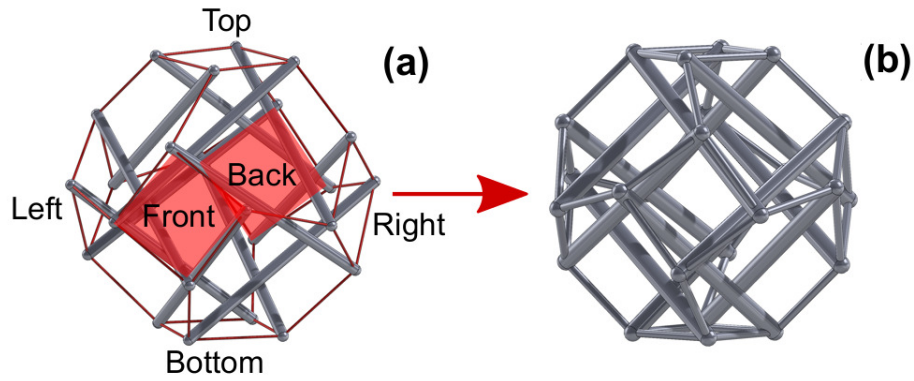


Figure 3.1: (a) Pin-jointed truncated octahedron tensegrity with 6 orthogonal faces, which we refer to as shown in the image. This is the baseline tensegrity structure we model after in this thesis. (b) The initial iteration for a 3D-printable structure, which is fixed-jointed structure overlapping members at the nodes.

the manufacturing and testing constraints of the structure that we would 3D-print using the tensegrity’s geometry, as described later in this section. We chose a height of 48.3 mm from the “top face” nodes to the “bottom face” nodes, which gives a cable length of 17.4 mm and a strut length of 44.2 mm . We chose the cables to have a diameter of 1.37 mm and the struts a diameter of 3.05 mm , giving a strut-to-cable diameter ratio (d_s/d_c) of 2.23. We ensure that the chosen strut diameter allows elastic buckling by using the Euler-Johnson relation [109]:

$$\frac{L}{\rho} \geq \sqrt{\frac{2\pi E}{\sigma_y}} \quad (3.1)$$

where L is the length of the strut, ρ is the strut’s radius of gyration, E is the Young’s modulus of the material, and σ_y is the yield strength of the material. L is 44.2 mm , E is 1.29 GPa , and σ_y is 29.1 MPa . The material we chose for the structures in this thesis was described in Chapter 2.

At this point, we note that this initial pin-jointed geometry was chosen due to manufacturing constraints and to provide elastically buckling struts, not to obtain a “target” mechanical response. Because of this, the member diameters are altered throughout the design process as defined by the ratio d_s/d_c . For clarity, we refer to this initial member geometry as Geometry #1, which as stated has a d_s/d_c of 2.23.

To find an analogous 3D-printable structure, we initially fabricated Geometry #1 with rigidly overlapped members at the nodes, as shown in Figure 3.1(b). The

samples were printed with the polyamide PA2200 material from Shapeways.com[©] using selective laser sintering (SLS). All experimental samples in this thesis use this material. As described in Chapter 2, this manufacturing method and material is appealing for this application because it requires no support structure and no post-curing, with consistent mechanical properties. Also, the slenderness of the structural members fit well within manufacturing limits for this method. Before deciding on this material, we iterated on a few other materials and manufacturing methods, most notably the “Tough” photopolymer from Formlabs[©], which is a stereolithography (SLA) printing system. This material required both a support structure and post-curing, which added difficulties such as accidentally cutting a cable and inconsistent curing. The Shapeways material also was much less viscoelastic compared to the Formlabs material, which made the Shapeways material more appealing for our dynamic applications. In Appendix B, we compare these two materials and provide results of relaxation tests we performed on them to study their viscoelasticity.

To characterize the mechanical response of the fixed-jointed structure, we performed quasistatic longitudinal compression experiments using an Instron E3000[©]. The chosen structure height of about 2 inches was a practical size for the compression experiments. The samples were loaded on the top face and compression was applied using displacement control. The top and bottom faces were allowed to rotate during compression, which naturally occurs (also for the pin-jointed tensegrity structure) due to asymmetry of the face nodes.

We developed a quasistatic model to simulate the experiment using the finite element software ABAQUS/STANDARD, which uses full 3D stress tetrahedral elements. We described this in detail in Chapter 2. We iterated through a few material models to describe the response of the structure, and found that a hyperelastic Marlow model best represented the response of the polyamide material. Since there is no clear yield stress for elastic polymer materials, it is often defined as the peak stress [110], which in this case is well past the linear region of the stress-strain curve (see Chapter 2). An elastic-plastic model in ABAQUS showed too low stresses as well as nonphysical permanent plastic deformation, which would greatly influence the wave propagation characteristics in subsequent dynamic analyses. Thus, the hyperelastic material provided a continuously elastic response that still followed the stress-strain path of the constitutive polymer material.

Note: Henceforth in this thesis, unless otherwise stated, “stress” and “strain” refer to the effective longitudinal global stress and strain in the given struc-

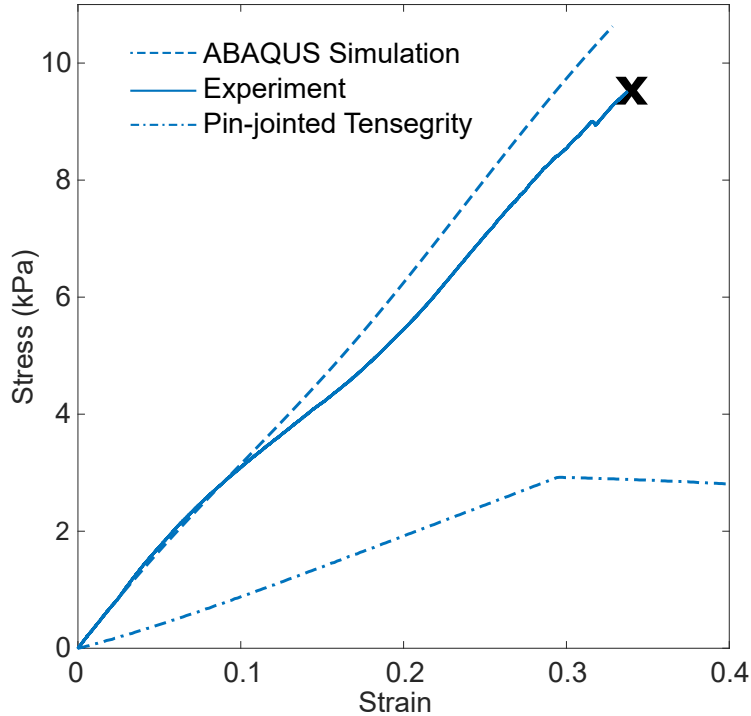


Figure 3.2: Global compressive stress-strain curves showing the 3D stress ABAQUS simulation and representative experimental responses of the 3D-printable, fixed-jointed structure, as well as the response of the corresponding pin-jointed structure. All member diameters correspond to Geometry #1. The pin-jointed structure exhibits a clear buckling point around 0.3 longitudinal strain, whereas the fixed-jointed structure does not exhibit a buckling point, but ruptures around 0.3 strain. The stiffness of the fixed-jointed structure is much higher than the pin-jointed stiffness. This fixed-jointed structure is thus inadequate to represent the pin-jointed response.

ture. That is, stress is defined as the applied compressive load divided by the structure’s projected square cross-sectional area that intersects the face nodes. Strain is defined as the vertical displacement, Δh , divided by the original height, h , of the structure from the bottom to the top face nodes.

The longitudinal stress-strain results of the ABAQUS simulation, the pin-jointed model, and a representative experiment are shown in Figure 3.2. The effective compressive stress-strain responses of the pin-jointed structure was found using a reduced-order model described in [23] that allows the struts to buckle and captures its nonlinear quasistatic and dynamic responses. The ABAQUS simulation and experiment are in good agreement. Both curves show a slightly nonlinear behavior, due to the relative rotation of the top and bottom faces during compression. The structures rupture at 0.3 strain, before reaching buckling, because of the high local

strains at the joints.

The pin-jointed response differs significantly from the fixed-jointed structure. Without member prestress, the pin-jointed structure behaves as a rigid body mechanism until reaching a critical strain (in this case, 0.25), where the members begin to carry force and deform. We subtracted this onset longitudinal strain from the strain values in order to obtain the compressive stress-strain curve reported in Figure 3.2. The pin-jointed response has a much lower stiffness than the printed structure, and distinctly buckles at around 0.3 strain. One important difference between the fixed-jointed and the pin-jointed structures is the distribution of load. The fixed-jointed structure has complex local material stress states that affect the stiffness and prevent the onset of buckling. On the contrary, the members of the pin-jointed structure are loaded purely axially and hence buckle more easily. To capture the buckling response exhibited by the pin-jointed structure, a different design approach for the 3D-printable structures was needed.

3.1.2 Conversion Method Between the Fixed and Pin-jointed Structure

To find a design for a 3D-printable structure with a comparable global compressive stress-strain response as the pin-jointed structure, we took note of a few key characteristics of tensegrity structures and attempted to maintain those characteristics in our 3D-printable structure design. We noted that in pin-jointed tensegrity structures, the nodal locations, member lengths, and independence of the members at the nodes are key characteristics that determine the response. In the initial fixed-jointed structure design (Figure 3.3(b)), these characteristics are not maintained. The effective lengths of all the members are shorter than in the pin-jointed counterpart due to the overlap of the members at the nodes. The cables intersect the struts at different angles, producing varying cable lengths and large stress concentrations. The effective buckling length of the struts is thus significantly shorter than in the pin-jointed counterpart. This greatly increases the buckling load of each strut. These attributes produce the structure's high stiffness and non-buckling behavior compared to the pin-jointed counterpart.

Therefore, we redesigned the 3D-printable structure in the following way. First, we scale the nodal coordinates up by 1.5 times while still maintaining the cable lengths (Figure 3.3(c)). Then, at each node we insert spheres that rigidly connect all of the corresponding members at the node (Figure 3.3(d)). The spheres have a diameter of 8.7 *mm*, sized such that the original cable lengths (17.4 *mm*) are

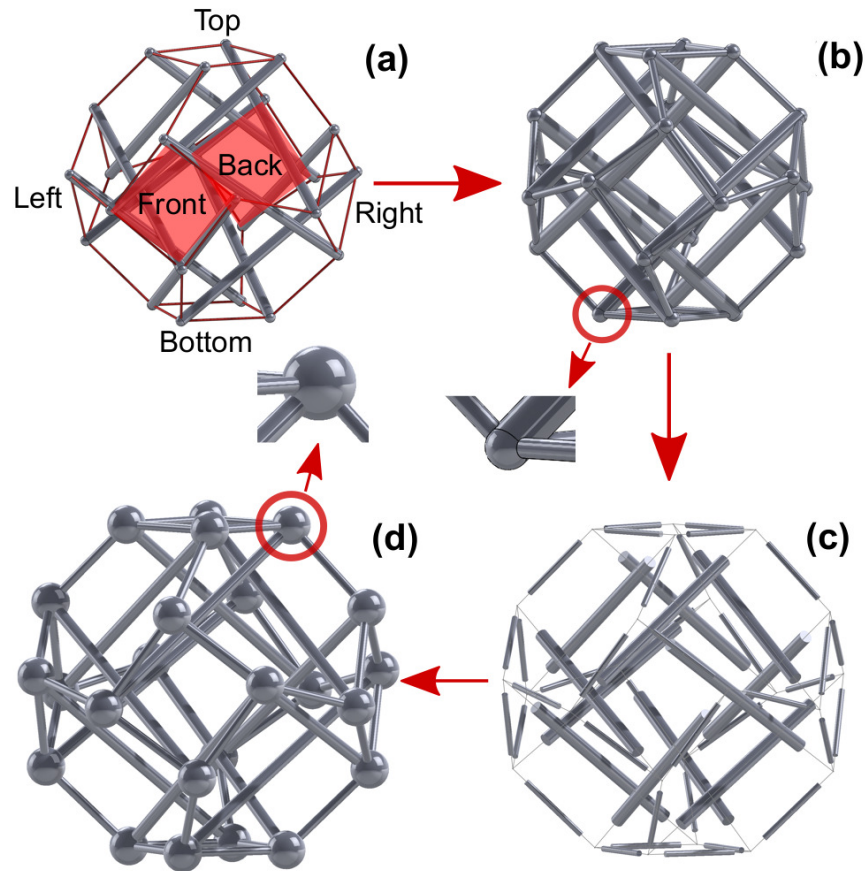


Figure 3.3: (a) Pin-jointed truncated octahedron tensegrity with 6 faces. (b) 3D-printable, fixed-jointed structure with overlapping members. In the updated design, nodal locations and cable lengths are maintained by (c) scaling up the structure while keeping cable lengths constant and (d) inserting spheres at the nodes.

maintained and such that the members do not intersect with each other. Note that the entire structure, including the spheres, is fabricated in a single print with the same material. With this design, all the cables are the same length and all the struts are the same length, and each intersects normal to the sphere. With this change, the compressive response changes dramatically. The structure's stiffness is greatly reduced, as are the maximum local strains from stress concentrations.

We performed compression tests on the spherically-jointed structure. Comparing the deformation of the compressed structure (Figure 3.4(a)) with the results obtained with ABAQUS 3D simulations (Figure 3.4(b)), we notice that each member in the structure behaves like a beam: it undergoes bending, axial loading, and torsion (Figure 3.4(c)). Each has a constant cross section and connects perpendicularly to the spheres. Because of these characteristics, we developed a simpler finite element

model using beam elements. A beam element model allows easy modification of the member diameters for geometric iterations and analysis. Timoshenko beam elements, which allow for transverse shear deformation and large strains, are used rather than Euler-Bernoulli elements. The type of element used is B32, which is the 3-node quadratic Timoshenko beam.

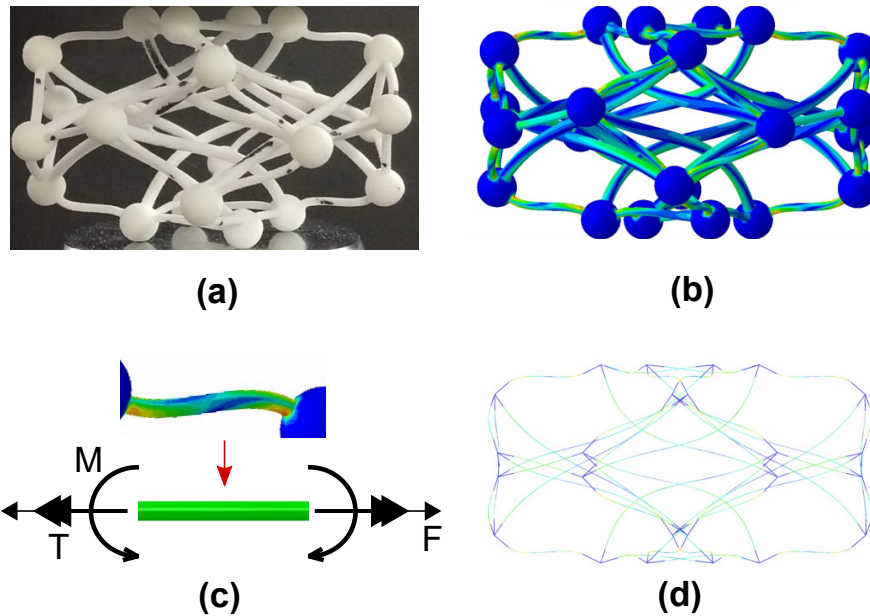


Figure 3.4: (a) Spherically-jointed structure compressed during an experiment. (b) ABAQUS rendering of compression of the spherically-jointed structure. (c) Representation of the mechanical deformation modes exerted on the members of the spherically-jointed structure. (d) ABAQUS beam element rendering of the compression of the spherically-jointed structure.

In the spherically-jointed configuration, each node connects four members. To model the spheres using beam elements, a single element with the length of the radius of the sphere connects the end of each member to the node. This element is given a very large stiffness and appropriately sized cross section and density values, as fully described in Chapter 2. The top and bottom reference points and coupling with the top and bottom face nodes are the same as in the 3D stress simulation. The compressed structure with the beam element simulation is shown in Figure 3.4(d).

Recall that a key objective is that the 3D-printable structure is to be used as a building block for impact absorbing periodic lattices. Although our objective for this work is not to optimize the structure for energy absorption capacity, we needed to adjust the member diameters of the spherically-jointed structure to obtain a longitudinal stress-strain curve and elastic energy capacity that would be useful

for dynamic analyses. We increased the cable diameter to raise the stiffness of the structure, and increased the strut diameter to raise the buckling load and reduce the global buckling strain.

The final 3D-printable, spherically-jointed design has a strut diameter of 2.6 mm and a cable diameter of 1.8 mm for the 1.5 scaled structure, giving a d_s/d_c of 1.44. We define this d_s/d_c as Geometry #2. A complete explanation of the reasoning behind these final member diameters is given in Appendix B. For the purposes of 3D-printing, we size the structure as 48.3 mm in height again, scaling the structure back down by 2/3.

The corresponding spherically-jointed structure longitudinal stress-strain curve (ABAQUS beam element simulation) is seen in Figure 3.5 as the dashed purple line. The initial stiffness increased to 48 kPa. The structure has no distinct buckling point, but asymptotically approaches the buckling stress. Thus, the structure exhibits load limitation at the structure's buckling load. The strain energy density is the area under the longitudinal stress-strain curve. By 0.4 strain, this structure absorbs 3.1 times greater strain energy than the original tensegrity structure (dashed-dotted line in Figure 3.2).

The full ABAQUS 3D stress element simulation response is shown as the purple dotted line in Figure 3.5. The beam element simulation presents a slightly stiffer response, with a final stress 5.6% higher than the full 3D stress simulation. This difference is likely because beam elements present a simplified model of deformation, not taking into account sources of deformation that the 3D stress model is able to capture. The beam element simulation also assumes very slender beams and has sharp transitions connecting the edge elements (representing the spheres) to the cable/strut members. These assumptions cause the beam element simulation to exhibit higher stiffness. The beam element simulation has several advantages, however, over the 3D stress model. The runtime with 8 CPUs for the beam element model is about 6 minutes, where as for the full 3D stress model it is around 20 times longer. It should be noted that this runtime difference significantly compounds with dynamic simulations (Section 3) and with forthcoming lattice simulations. Easy member diameter modification also makes geometry iterations much more straightforward with the beam element model.

At this point, it is important to observe where areas of high local strain occur and the levels of local strain within the structure during compression. Local strain distribution is obtained using the ABAQUS 3D stress element simulation. Maximum

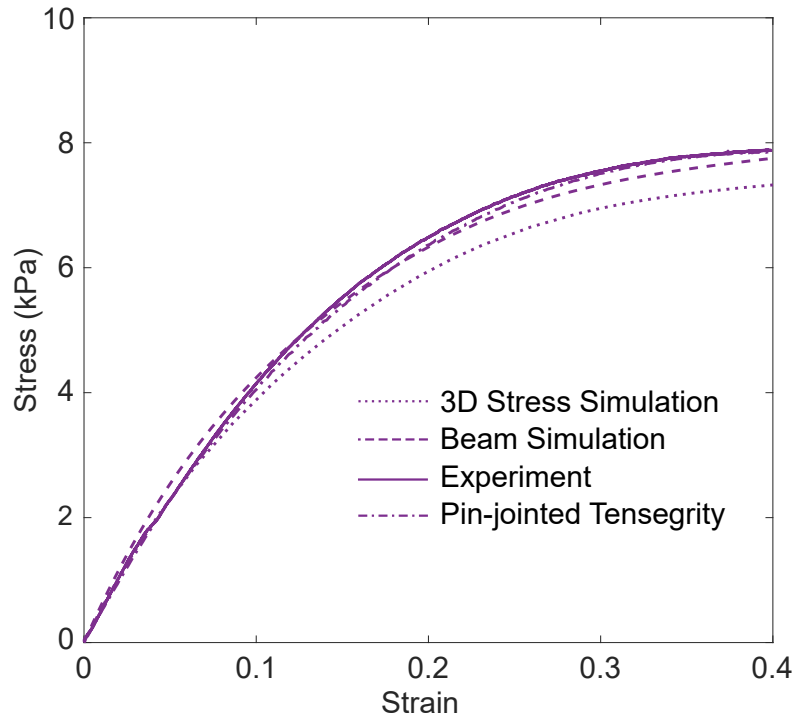


Figure 3.5: Global compressive stress-strain curves showing responses of the 3D stress simulation, beam simulation, corresponding pin-jointed tensegrity simulation, and representative experiment. All four show comparable behavior, indicating the spherically-jointed structure's equivalence to a corresponding pin-jointed tensegrity structure. *This is the final geometry design chosen for the studies in this thesis.*

principal elastic strain within the structure at a global compression level of 0.4 is shown in Figure 3.6. The blue-to-red rainbow colorplot ranges from the lowest strains in blue to the highest strains in red. The highest local strains occur at the intersection points between the cables and the spheres for the 8 cables that connect the top/bottom faces to the side faces. Due to the sharp corner at each intersection from member to sphere, high stress concentrations are produced at these locations. Because the 8 cables connecting the top/bottom faces to the side faces undergo the largest deformation of all the members, the stress concentrations produced at their cable/sphere intersections produce the highest strains in the entire structure.

A magnification of one of these locations is shown in the inset image in the red box in Figure 3.6. We can see that the highest strain is highly localized. The maximum strain produced here is about 0.2. Although theoretically this strain level could cause the structure to rupture (the material's rupture point is around 0.2 strain), this does not occur in our experiments. There are a few reasons for this. First, in a 3D-printed structure, the corners always will be fabricated with some amount of

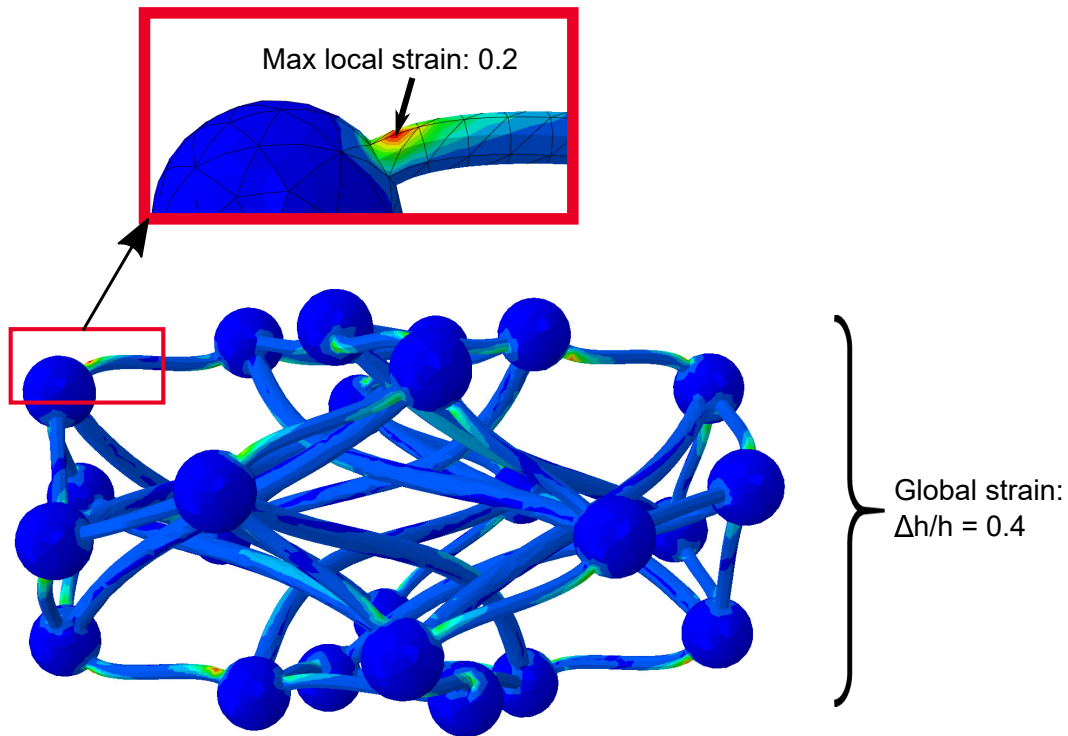


Figure 3.6: Maximum principal elastic strain within the structure at a global strain level of 0.4. The blue-to-red rainbow colorplot ranges from the lowest strains in blue to the highest strains in red. A magnification of one of the the highest local strain locations is shown in the inset red box.

filleting. Even a small fillet introduced at a sharp corner can dramatically reduce the stress concentration there. Thus, the stress concentrations in the printed structure are likely lower than in the ABAQUS simulations. Second, the level of local strain and area of concentration of the highest strain changes significantly with mesh size. With a very fine mesh, the local strain approaches extremely high values over a very small area right at the intersection of cable and sphere, approaching the analytical solution of infinite strain for a sharp transition. This indicates that without the sharp transition, like in the experiments, the local strains at these points could be significantly lower than the rupture point for the material.

Overall, most of the structure shows low local strains, largely below 0.05 strain. In the following chapters, we explore the dynamics of this structure. In those cases, the structure undergoes high and repeated global strain and remains highly elastic. This indicates that overall the strains remain low enough in the structure to not only prevent rupture but also remain elastic (indicating the validity of choosing a hyperelastic material model). In this thesis we do not set out to optimize the structure

for low local strains, but this could be an area of interest for furthering this research.

Next, we turn our focus to obtaining a corresponding pin-jointed tensegrity structure with similar stress-strain response and strain energy capacity as the spherically-jointed tensegrity-inspired structure. The pin-jointed and spherically-jointed structures have different deformation modes. In the spherically-jointed geometry, both the cables and the struts simultaneously affect both the stiffness and buckling load of the structure because they are both bending-dominated. The pin-jointed structure, on the other hand, has purely axially-loaded members. However, when the struts buckle, they undergo pure bending whereas the cables remain at the same axial stress as they were just before the struts buckled. Thus, in the pin-jointed case, the structure's buckling load strictly depends on the strut diameter, whereas the initial stiffness depends on both the cable and strut diameters. So, to find the pin-jointed diameters needed to obtain a similar response to our spherically-jointed structure, we keep the cable diameter the same as that for the spherically-jointed structure, but solve for the strut diameter using a simple force balance.

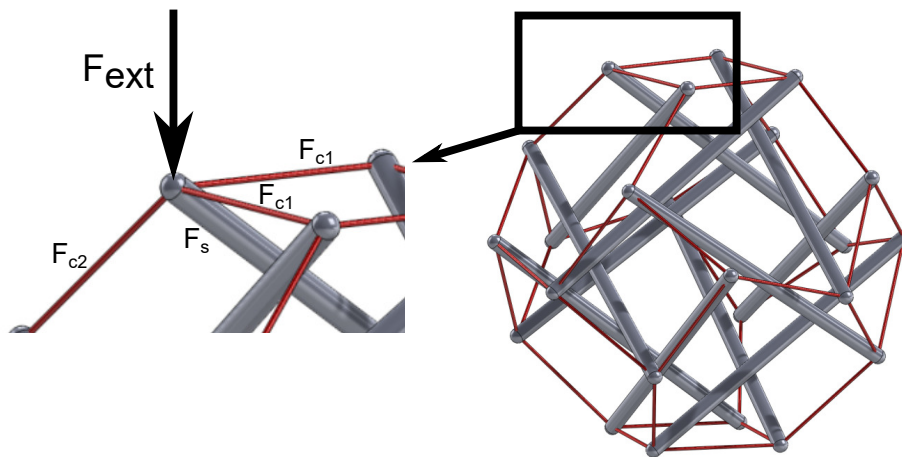


Figure 3.7: Pin-jointed tensegrity structure, zoomed in at the top face leftmost node. Here, we show the forces acting on this node. This enables us to solve for the diameter of the strut needed to achieve a buckling load equal to that of the spherically-jointed tensegrity-inspired structure.

We do this by taking a free body diagram of one of the top face nodes, as seen in Figure 3.7. Zooming in on the left-most top face node in the image, we can see that the node connects three cables and one strut. The top face cables all carry the same load. So we label the force in the strut as F_s , the force in the two face cables as F_{c1} , and the force in the other cable as F_{c2} . We apply a total load on the top face nodes equal to that of the buckling load we observe in the spherically-jointed 48.3

mm tall structure (about 18.1 N). The force balance at this node is a linear system of 3 equations (forces in *x*, *y*, and *z*) and 3 unknowns (F_s , F_{c1} , and F_{c2}). We solve for the unknown forces. Then, since we define the applied load (18.1 N) as the buckling load of the structure, we solve for the diameter of the strut, d_s such that F_s is equal to the buckling load:

$$F_s = \frac{\pi^2 EI}{L_s^2} \quad (3.2)$$

where $I = \pi d_s^4/64$ is the strut's moment of inertia. We found d_s to be 3.32 *mm*.

Thus, the pin-jointed tensegrity has a cable diameter of 1.8 *mm* and a strut diameter of 3.32 *mm*, for a d_s/d_c of 1.84. (We define this as Geometry #3.) We add just enough prestress (2%) so that the structure is load-bearing and the struts just begin to bend at the onset of loading. The pin-jointed response for this structure is shown in Figure 3.5 as the dashed-dotted line. Remarkably, the pin-jointed tensegrity structure response matches very closely with the spherically-jointed tensegrity-inspired structure, achieving the same strain energy capacity and stress-strain curve.

As stated, we add just enough prestress to the pin-jointed structure that the struts just buckle and begin to bend on the onset of loading. This creates a global response that qualitatively mirrors that of the fixed-jointed structure, due to the following reason. If a column is eccentrically loaded or if there is an initial bend in the column, the transverse deflection will be nonzero. Because of this, the increase in the load is gradual and asymptotically approaches the critical buckling load at a rate dependent on the degree of eccentricity/initial bending [111]. In the spherically-jointed structure, since the joints are fixed and the “faces” rotate, the struts bend immediately upon loading. The resulting response asymptotically approaches the critical load of the structure. A similar response occurs with a prestressed pin-jointed structure with struts dimensioned for elastic buckling. At a certain prestress, the struts buckle. Thus when an external load is applied, the response of the structure asymptotically approaches the structure's critical load instead of having a sharp buckling point. Thus, both the pin-jointed structure with just-buckled struts and the fixed-jointed structure immediately undergo bending upon loading and asymptotically approach their buckling loads. This results in both structures having the same response.

A representative experimental compressive response of a 3D-printed tensegrity-inspired structure (with the final Geometry #2) is shown in Figure 3.5 as the purple

solid line. Several samples were tested, and as can be expected, slight variations in the response result from differences in manufacturing. We explore these differences in manufacturing thoroughly in subsequent dynamic studies. In the experiments, the structures can be compressed to 0.48 strain when the struts begin to touch (densification). Both experimental and numerical results agree favorably with the pin-jointed response. With a structure height of 48.3 mm , the spherically-jointed structure has a mass of 3.75 g , which is less than the pin-jointed structure's mass of 5.75 g . The normalized strain energy by mass of the spherically-jointed structure is therefore about 1.5 times greater than the counterpart pin-jointed structure.

3.1.3 Examples of the Design With Alternate Materials and Length Scales

We explored a few examples which indicate that our design method (correlating a pin-jointed structure with a spherically-jointed tensegrity-inspired structure) applies for other strut/cable diameters, materials, and length scales.

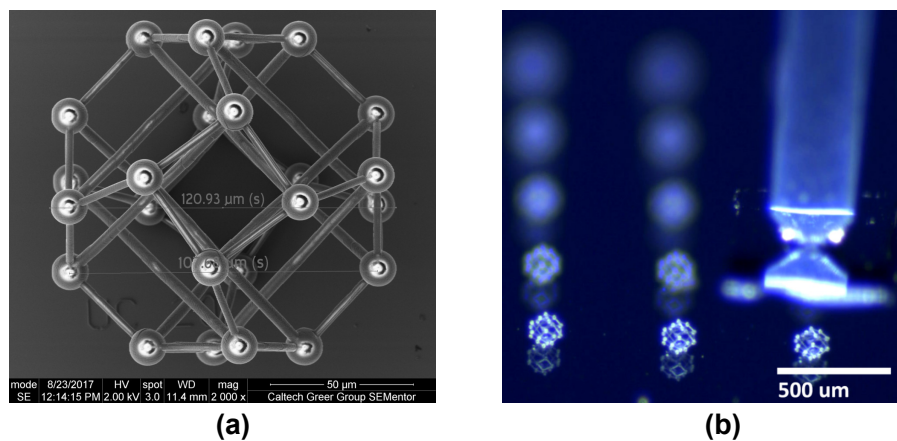


Figure 3.8: Microscale samples with a height of $120\ \mu\text{m}$ were fabricated with the Nanoscribe[®] printing system. (a) A scanning electron microscope photograph of a sample is shown. (b) Photograph of a compression test on a sample using the FemtoTools[™] testing system. The sample on the lower right is being compressed by the force sensor tip, which is lowered by displacement control.

We successfully printed Geometry #2 (d_s/d_c of 1.44) with a height of $120\ \mu\text{m}$ using the Nanoscribe[®] 3D laser lithography printing system. A standard material used by this printer, IP-Dip[™], has been experimentally studied in [112, 113]. In those studies, both a long-term and instantaneous elastic modulus were extracted due to the pronounced viscoelastic behavior of the material. The material's pertinent properties are a long-term modulus of 2.22 GPa , instantaneous modulus of 2.90 GPa , Poisson's ratio of 0.49, and yield stress of 60 MPa . Figure 3.8(a) shows a

scanning electron microscope photograph of the printed structure.

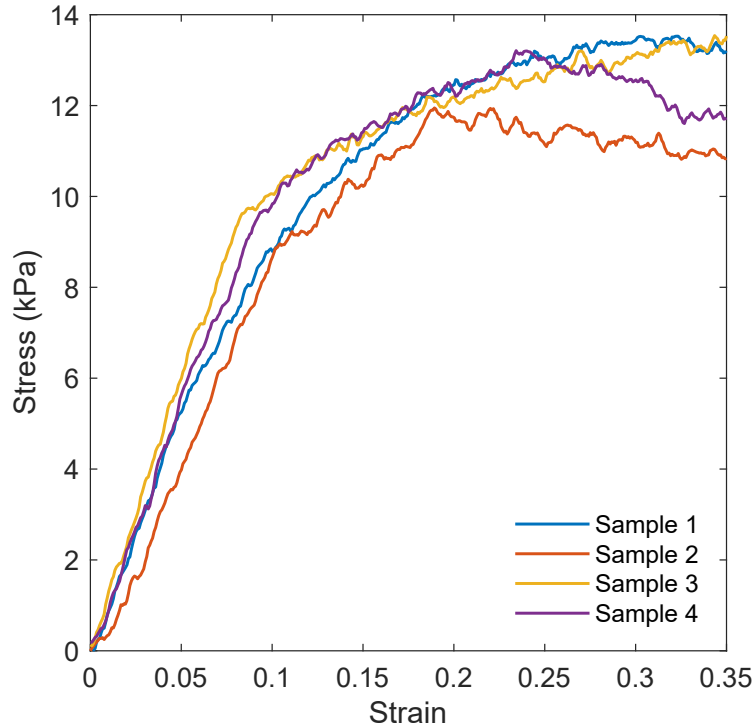


Figure 3.9: Global compressive stress-strain results of compression tests on microscale samples with a height of $120 \mu\text{m}$ and d_s/d_c of 1.44. The results of four samples are shown. The results show behavior similar to the 48.3 mm samples printed with the Shapeways PA2200 material and same d_s/d_c value.

We performed quasistatic compression tests on these structures using the commercial FemtoToolsTM setup. A photograph of a compression test is given in Figure 3.8(b). The results of the compression tests for four samples is given in Figure 3.9. We can see that the response is comparable to what we see for the macroscale samples (Figure 3.5). There is an initial linear region followed by a region of buckling. The buckling produces a plateau in the stress response. The stress levels and buckling load are higher for this case than for the macroscale samples because this material has a higher modulus. Also, the onset of buckling occurs distinctly around 0.1 strain, which is sooner than for the macroscale samples.

Next we give an example of a numerical simulation we ran of a macroscale sample with a different d_s/d_c ratio and linear elastic material properties. We ran the beam element ABAQUS simulation with a linear elastic material ($E = 1.291 \text{ GPa}$, $\nu = 0.3$, and $\rho = 930 \text{ kg/m}^3$), a cable diameter of 1.8 mm , and a strut diameter of 1.2 mm . This gives $d_s/d_c = 0.67$. The result is shown in Figure 3.10 as the solid blue

line. Again, the sample buckles distinctly, producing a plateau in the stress-strain

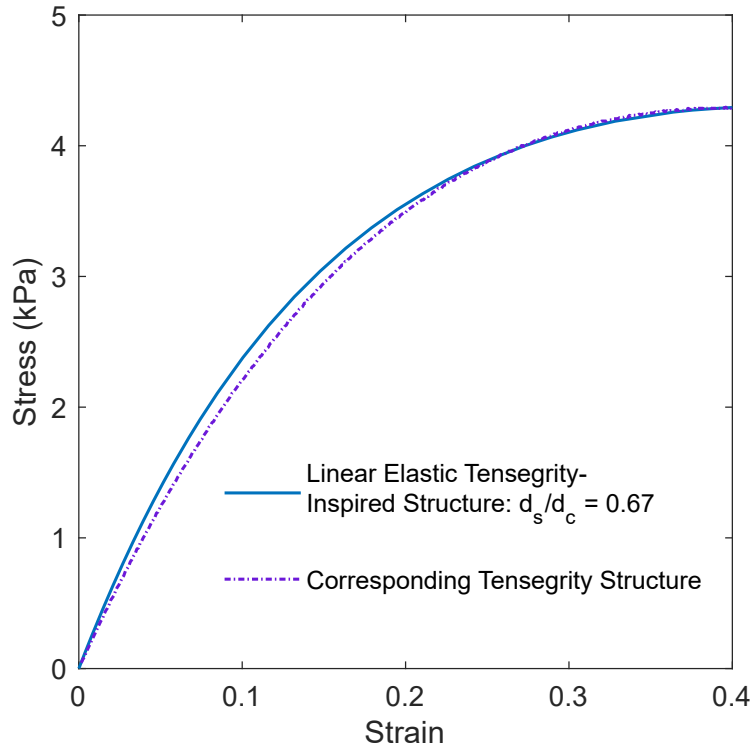


Figure 3.10: Global compressive stress-strain responses of a linear elastic spherically-jointed structure and its corresponding pin-jointed tensegrity structure found using our design method.

response. This indicates that this behavior can occur with our spherically-jointed design even if the material is linear elastic. Using the force balance method for the pin-jointed tensegrity as described earlier in this chapter, we find the pin-jointed strut diameter to be 2.85 mm . We keep the cable diameter at 1.8 mm . The resulting pin-jointed tensegrity response is shown in Figure 3.10 as the dashed-dotted purple line. Again, the responses match very well. Thus, we have demonstrated that our design method to correlate buckling tensegrity structures with a 3D-printable, fixed-jointed structure can be implemented for a range of geometries, materials, and length scales.

3.2 Fundamental Comparison of the Fixed and Pin-Jointed Structures

Although the pin-jointed structure and the 3D-printable, spherically-jointed structure have similar constitutive responses, they are governed by different properties: the pin-jointed structure is stretch-dominated and prestressed, whereas the spherically-jointed structure is bending-dominated and not prestressed. Thus, the

spherically-jointed structure does not have traditional tensegrity traits, such as pre-stress tunability. However, the pin-jointed and spherically-jointed structures share some useful similarities: (i) The faces rotate during compression, producing low local strains. (ii) The slender struts undergo elastic buckling. As a note, the struts in the final designed spherically-jointed structure also satisfy the elastic buckling requirement of Equation 3.1. These traits allow the structure to withstand high deformations while remaining elastic, like a tensegrity. (iii) Strain energy is distributed evenly throughout the structural members. (iv) The nonlinear buckling response is load-limiting. (v) Finally, both types of structures have very low relative density, allowing formation of extremely lightweight lattices.

Relative density is given by the density of the structure divided by the density of the constituent material. The density of the structure is the mass located within a representative volume element (RVE) that is used for tessellating in space, divided by the volume of the RVE. The RVE for the baseline spherically-jointed structure is given in Figure 3.11. The RVE is found by slicing the structure through the

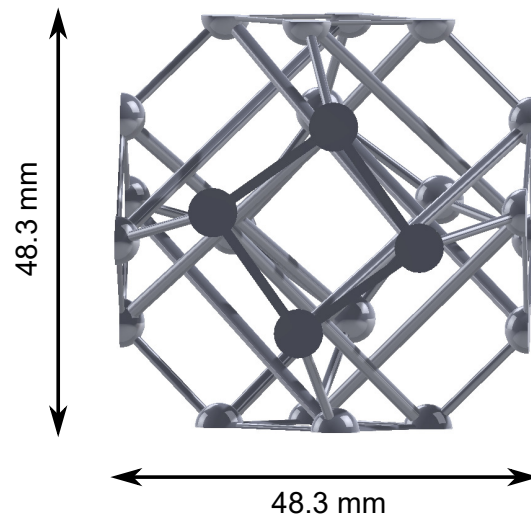


Figure 3.11: Representative volume element of the baseline spherically-jointed, tensegrity-inspired structure. This is used for calculating the relative density of our structure and subsequent lattices.

center of the spheres and cables on the top, bottom, right, left, front, and back faces. The relative density of the final designed structure (Geometry #2) is 2.5%, and the relative density of the corresponding pin-jointed tensegrity is 4.9%. The structure is, therefore, very lightweight, even more so than the pin-jointed tensegrity structure.

Although the spherically-jointed structure is not pin-jointed, it remains elastic

under high deformation (up to 0.48 strain). This is due to a few reasons. First, it achieves low local strains at the intersections between the spheres and members. This is because the faces rotate during compression, but also because elastic buckling occurs. Elastic buckling allows high deformation without plasticity. Second, the cross section of the members remains constant along their length, keeping stress concentrations low at the joints. Third, the beams are slender ($d/L < 10\%$ for cables and $< 5\%$ for struts), which, for a certain applied deformation, produce lower stresses than for a thicker beam. Thus, the structure's elasticity is comparable to a tensegrity structure while remaining easily fabricatable with standard 3D-printing.

Finally, we demonstrate that the struts in the spherically-jointed structure indeed undergo axial buckling and not solely bending and torsion. We do this by showing the axial force along the beam axis of a strut in the spherically-jointed structure. In Figure 3.12, we show the force in the strut normalized by its buckling load for

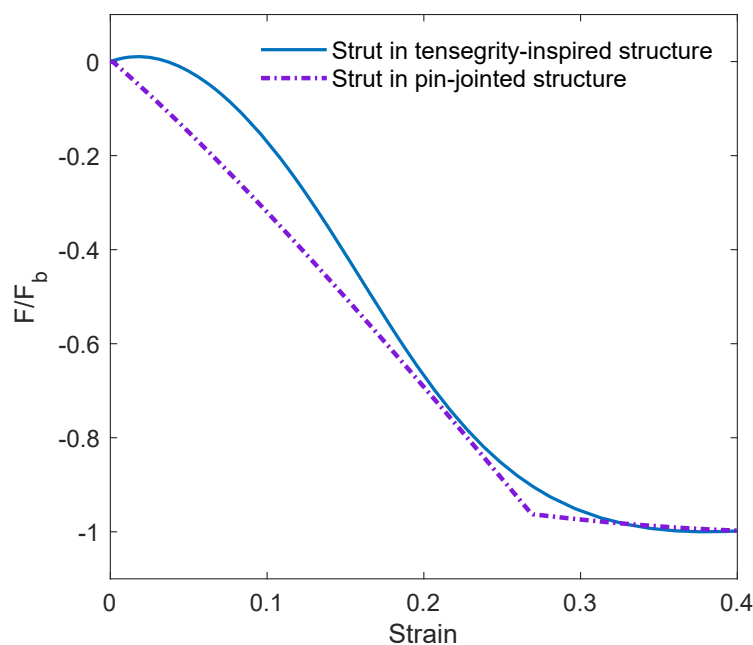


Figure 3.12: The force in a representative strut (F) normalized by its buckling load (F_b) for both the spherically-jointed tensegrity-inspired structure and the corresponding pin-jointed structure, as a function of global compressive strain.

both the spherically-jointed tensegrity-inspired structure and the corresponding pin-jointed structure, as a function of global compressive strain. We show the force in the strut for the un-prestressed pin-jointed structure to illustrate the onset of the buckling load in the strut. What we see is that the axial load in both struts are negative, implying compression. Also, the tensegrity-inspired structure's strut

clearly undergoes buckling between 0.2-0.3 strain. The two curves show the same behavior, indicating that the tensegrity-inspired structure indeed undergoes axial buckling in the struts. In fact, F_b for the tensegrity-inspired structure's strut is extracted as 4.44 N from ABAQUS. Using Euler's buckling criteria, the buckling load for a beam with its dimensions and properties is found to be 3.81 N for perfectly pinned ends and 7.62 N for fixed ends. Interestingly, the strut exhibits a buckling load much nearer to that of perfectly pinned than perfectly fixed ends. This perhaps also contributes to our designed structure's ability to mimic the behavior of a tensegrity.

For the remainder of this thesis, we henceforth call the designed spherically-jointed structure the "tensegrity-inspired structure." The un-tessellated designed structure is referred to as the baseline tensegrity-inspired structure.

3.3 Representative Volume Elements for Tensegrity-Inspired Lattices

Since the baseline tensegrity-inspired structure has six orthogonal faces, it can be tessellated into 3 dimensions to form tensegrity-inspired lattices. However, a series of reflection operations must be performed to do this. These operations are performed on the pin-jointed tensegrity structures in [71] to obtain multi-dimensional lattices, and are fully described there.

The baseline structure cannot be directly tessellated because the faces are initially rotated along their respective axes. Thus, the baseline structure has two configurations: a left-handed and a right-handed configuration. This is seen in Figure 3.13. The left-handed cell has face nodes rotated counterclockwise, whereas the right-handed cell has face nodes rotated clockwise. Thus, both the right-handed and left-handed cells must be used to tessellate the structure to achieve periodicity between faces. The 1D representative volume element (RVE) contains a right- and left-handed cell. The 2D RVE contains two 1D RVEs, or 4 baseline cells. The 3D RVE contains two 2D RVEs, or 8 baseline cells. In this thesis, we study 1D lattices and 3D lattices formed with 1D RVEs and 3D RVEs, respectively. The 3D lattices we study are what we term 3D1D and 3D bulk lattices. The 3D1D lattices are simply lattices of 3D RVEs, but only tessellated in one dimension. This is essentially a 1D lattice. The 3D bulk lattices are lattices of 3D RVEs tessellated in all three dimensions.

Finally, we give the ABAQUS beam element stress-strain responses for the baseline, 1D RVE, and 3D RVE in Figure 3.14. These are for the final design configuration given by Geometry #2. They differ only slightly, with the baseline structure

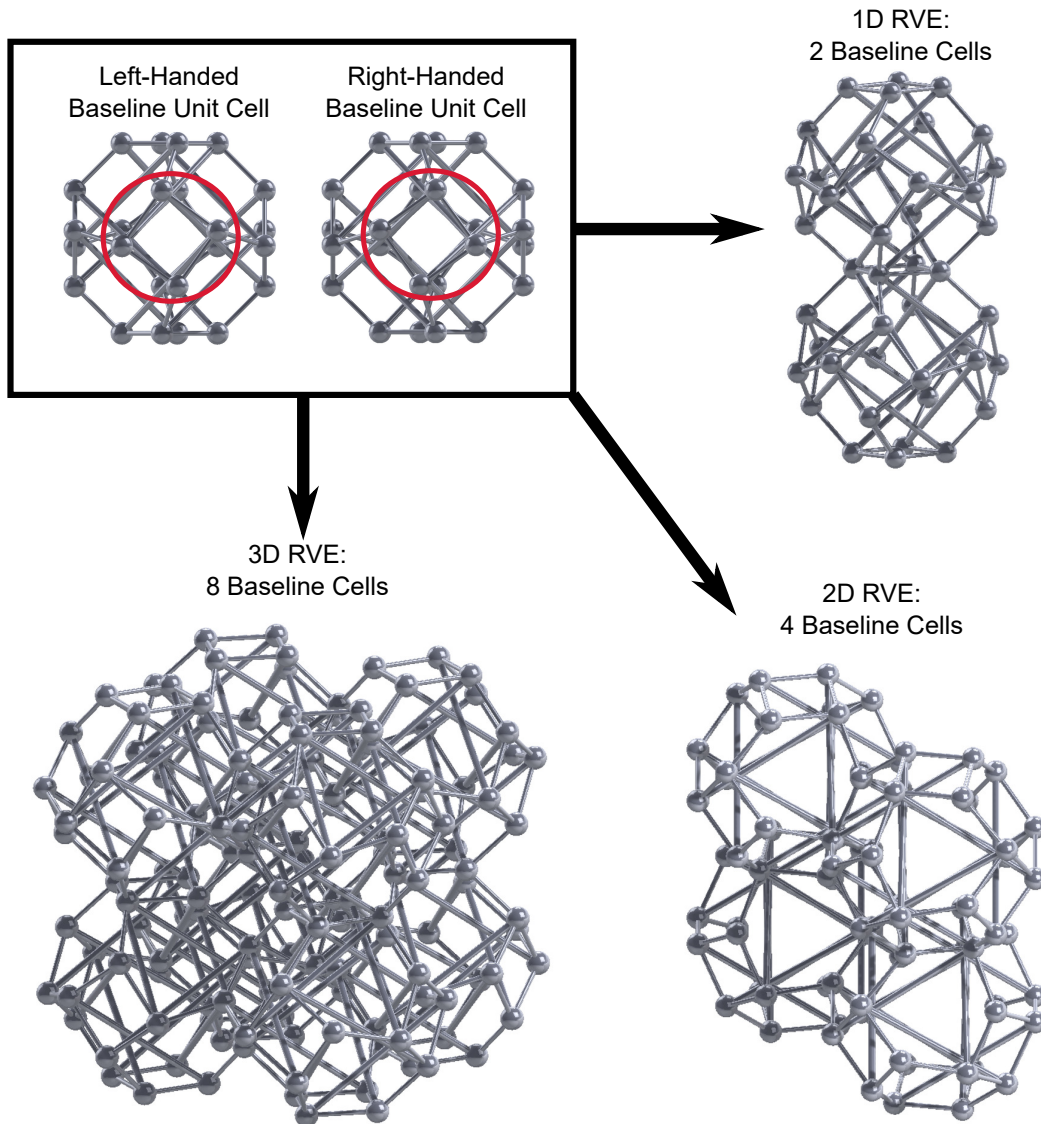


Figure 3.13: The baseline tensegrity-inspired structure has a left-handed and right-handed configuration, and both must be used to tessellate the structure into multidimensional lattices. The representative volume elements and their number of baseline cells are shown.

being the softest and the 3D RVE being the stiffest. The stiffness increase from baseline to 3D is intuitive. This is because as the structure is tessellated, faces (spheres and cables) are “shared” between neighboring baseline cells. This makes the faces unable to rotate as naturally, so there is an additional component of stiffness.

For completeness, we found the effective Poisson’s ratio for each of the 3 RVEs shown in Figure 3.14. This is the axial strain (the compressive strain in Figure 3.14) divided by the transverse strain (how much the RVE expands laterally). The initial

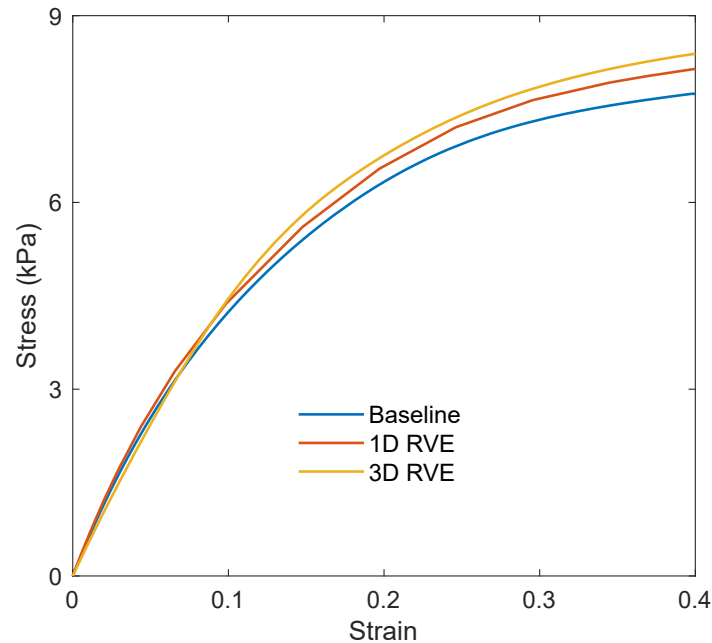


Figure 3.14: Global compressive stress-strain curves from ABAQUS beam element simulations of the baseline, 1D, and 3D RVEs.

Poisson's ratio in the linear region of the stress-strain curves is very close to 2 for all three RVEs. The Poisson's ratio increases significantly as the strain increases to the nonlinear region, reaching almost 5 by densification. A large Poisson's ratio such as this implies higher axial deformation than transverse deformation. The axial deformation greatly exceeds the transverse deformation as the struts buckle. An effective Poisson's ratio larger than 1 has also been exhibited for other types of architected lattices [114, 115]. As we will see, this large Poisson's ratio has a significant effect on the dynamics of these tensegrity-inspired structures.

3.4 Chapter Summary

We have presented a method to overcome manufacturing limitations of tensegrity structures by designing a 3D-printable structure with analogous strain energy capacity and compressive global stress-strain response as a pin-jointed tensegrity structure. The structure design uses spherical joints to separate structural members in a way that maintains certain tensegrity characteristics, allowing the compressive and dynamic responses to behave similarly to a counterpart prestressed buckling tensegrity. The structure is fabricated with a single material, allowing it to be printed with a variety of currently available 3D-printing methods. Without the need for pin-joints or prestress, the structure presented in this paper uses geometry to

produce tensegrity-like characteristics. Such characteristics include stability post-buckling, resilience to severe deformation, very low density, and load-limitation. Simple modification of the member diameters allows straightforward tunability of the structure's mechanical response and strain energy capacity, as the design method is applicable for a range of materials and geometry configurations. Starting with the baseline structure, we showed the process to form representative volume elements that tessellate the structure in space. In the following two chapters, we study the dynamic response of baseline unit cells and tessellated lattices designed with the final geometry defined in this chapter.

*Chapter 4***DYNAMICS: FREQUENCY RESPONSE****4.1 Introduction to Dynamic Frequency Analysis**

In Chapter 3, we presented a method for creating lightweight tensegrity-inspired structures with unique nonlinear buckling characteristics. These structures behave similarly to tensegrity structures in which the struts buckle elastically [23, 71]. Our tensegrity-inspired structure has many advantages, such as low density, high elastic deformation, minimal local strains, high energy capacity, and load limitation. It is also printed with a single material, so it can be fabricated with multiple 3D-printing methods at multiple length scales. This opens the door for creating new types of tensegrity-inspired materials with unique properties.

The quasistatic characteristics we examined in the previous chapter hold promise for the dynamic regime. Particularly of interest is the dynamic behavior of the structure when tessellated into lattices of multiple dimensions. In general, structural lattices can be engineered to propagate elastic waves at desired direction-dependent wave speeds [48–52], and they can be designed to feature bandgaps, i.e., frequency ranges of strong wave attenuation [48, 49, 53–55]. bandgaps are often due to Bragg scattering in these lattices [48]. However, once the lattices are manufactured, the wave properties are often set in stone. There are ways to make the wave response tunable, but it is often a discrete degree of tunability such as arising from bistable mechanisms [116] or an external stimulus [65, 67, 69]. Also, tunable lattices often use very soft materials whose dynamic response is dominated by damping, making practical applications challenging. Tensegrity lattices have been shown to possess exciting dynamic characteristics for both low amplitude frequency excitation [72, 73, 85–87, 117] and impact loading [71, 74–77, 118]. They also display Bragg bandgaps, but present continuous tunability by adjusting prestrain in the cables and/or global compression. This tunability has the potential for creating systems with wave-guiding/lensing attributes. It is also useful for applications where certain levels of wave attenuation, wave speed, or other characteristics are needed at different times without having to replace the entire lattice. However, fabrication of tensegrity lattices beyond a few unit cells has remained elusive due to assembly technicalities, especially at smaller length scales.

In this chapter, we begin to examine how our tensegrity-inspired structure behaves in the dynamic regime by looking at its response to low amplitude frequency excitation. Our structure is of interest in this area. It has tensegrity-like characteristics that produce dynamic attributes such as continuous tunability of bandgaps and wave speeds and rare properties not found in natural materials (e.g., faster shear wave speeds than longitudinal). In this chapter, we provide an experimental demonstration of dynamic properties only previously discovered by numerical and theoretical studies on tensegrity lattices. This analysis also lays a groundwork for understanding subsequent dynamic impact studies on these lattices (Chapter 5). First, we examine the frequency response of an unstrained 1D lattice. Then, we apply global compression to the 1D lattice to study its tunability attributes. Finally, we perform a dispersion analysis on a 3D unit cell to give insight into the dynamics of 3D lattices and compare this to the response of buckling tensegrities [87].

Some content of this chapter has been partially adapted from:

K. Pajunen, P. Celli, and C. Daraio. “Experimental evidence of analog prestrain-induced bandgap tuning in 3D-printed tensegrity-inspired lattices”. In: *Extreme Mechanics Letters* (2020). In Press.

4.2 Unstrained Lattice

4.2.1 Dispersion Results

First, we performed numerical COMSOL simulations on a 1D representative volume element (RVE) with a strut-to-cable diameter ratio of 1.44 using an eigenfrequency step as described in Chapter 2. This analysis provided an estimate of the range of frequencies and characteristics of the dispersion curve for our tensegrity-inspired lattice before performing experiments. Two baseline unit cells comprise a 1D RVE, thus allowing periodic tessellation of the RVE into a 1D lattice. Periodic Bloch boundary conditions are applied on the top and bottom faces of the RVE, as shown in Figure 4.1, so an infinite 1D lattice is simulated. The RVE has a total height of 96.6 mm, which is the height of two baseline unit cells. A linear elastic model for the PA 2200 nylon is implemented, and the part is meshed with quadratic tetrahedral elements. A parametric sweep is performed in the eigenfrequency step which sweeps over values of the wavenumber, k , from 0 to π/a and calculates 20 eigenfrequencies at each k value.

The resulting dispersion curve is shown in Figure 4.2. The dispersion relation

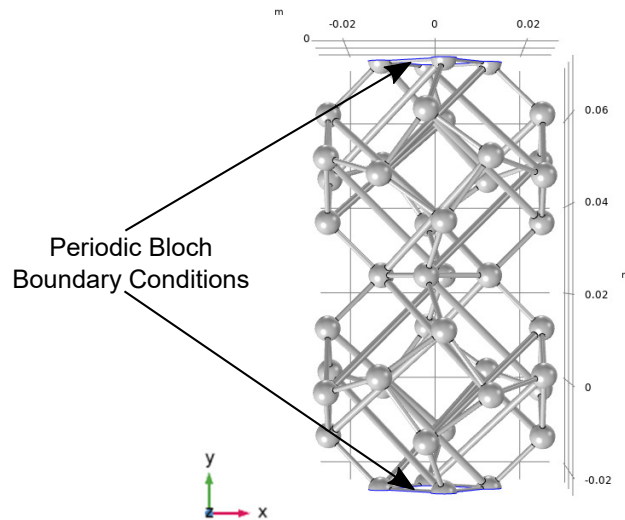


Figure 4.1: Setup of the 1D RVE in COMSOL for eigenfrequency analysis of an infinite 1D lattice. Periodic Bloch boundary conditions are applied on the top and bottom faces.

is plotted in real space, from $k = 0$ to $1/(2a) m^{-1}$, where $a = 0.0966m$. The wavenumber is converted from rad/m to m^{-1} with dividing by 2π . Longitudinal modes are shown as red circles, purple circles are rotational modes, green circles are combined rotational and longitudinal modes, and blue stars are flexural and all other combined modes. The output frequency and wavenumber values from COMSOL do not distinguish between the different mode shapes, so we devised a method to do this. We extracted the displacement magnitude in the vertical (y) direction at three locations in the RVE, and the curl magnitude around the y -axis volume averaged for the whole RVE. These locations are given by the light blue regions in Figure 4.3(a)-(d). Then we establish quantitative thresholds based on the ratios of these values to their maximum over all eigenvalues. (The MATLAB code with the thresholds are given in Appendix A.) These thresholds give the wavenumber and frequency values where vertical displacement and curl have a large percentage of the total displacement. Where vertical displacement is dominant, the mode is longitudinal; where curl is dominant, the mode is rotational; and where curl and vertical displacement are both significant, the mode is combined longitudinal and rotational. All other eigenvalues are flexural or other combined modes.

We needed to establish three locations for extracting the vertical displacement. This is because if we only look at the displacement at the middle of the RVE, we miss the cases where the vertical displacement is high, but the middle stays stationary

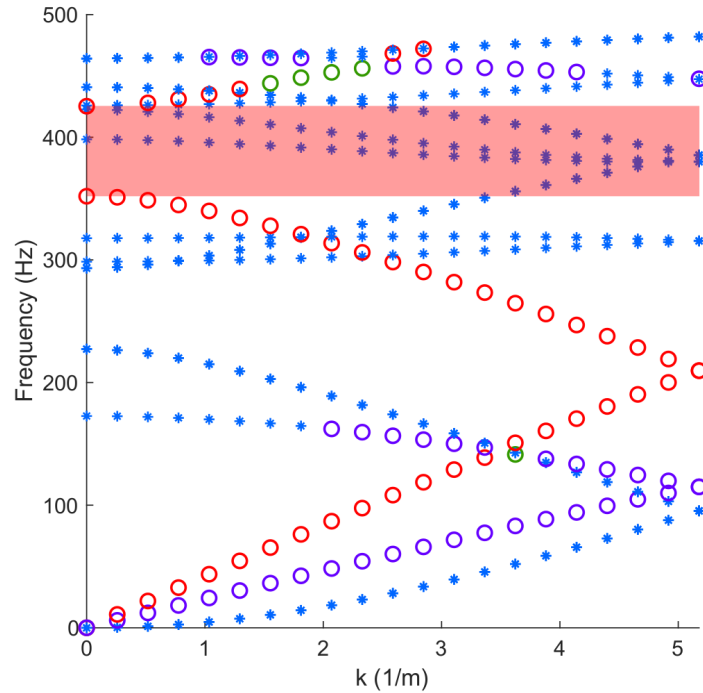


Figure 4.2: Numerical dispersion relation for the unstrained 1D lattice response. The dispersion relation is plotted in real space, from $k = 0$ to $1/(2a) m^{-1}$, where $a = 0.0966m$. The red circular markers are longitudinal modes, the green ones are combined longitudinal and rotational modes, the purple ones are rotational modes, and the blue stars indicate flexural modes and modes that do not clearly belong to any of the above categories. The red shaded region indicates a frequency region where there are no longitudinal modes present; this is a longitudinal bandgap.

(Figure 4.3(e)). Also, if we only look at the displacement at the middle and top of the RVE, we miss the cases where the displacement of the middle of the baseline cells is high, but the middle and top of the RVE remain stationary (Figure 4.3(f)). Finally, we color the eigenvalue markers according to these thresholds in Figure 4.2, as done in [119]. The method is quantitative but slightly arbitrary; however, it gives very good approximations for the distinction of the different mode shapes. Examples of the different mode shapes are given in Figure 4.4. For the purposes of the experiments, we focus on the longitudinal modes.

Looking again at the dispersion curve in Figure 4.2, we can see that there are instances of combined rotational and longitudinal modes at the intersection of the lower longitudinal and rotational branches, as well as above around 425 Hz . For our tensegrity-inspired structure, we expect longitudinal and rotational modes to occur.

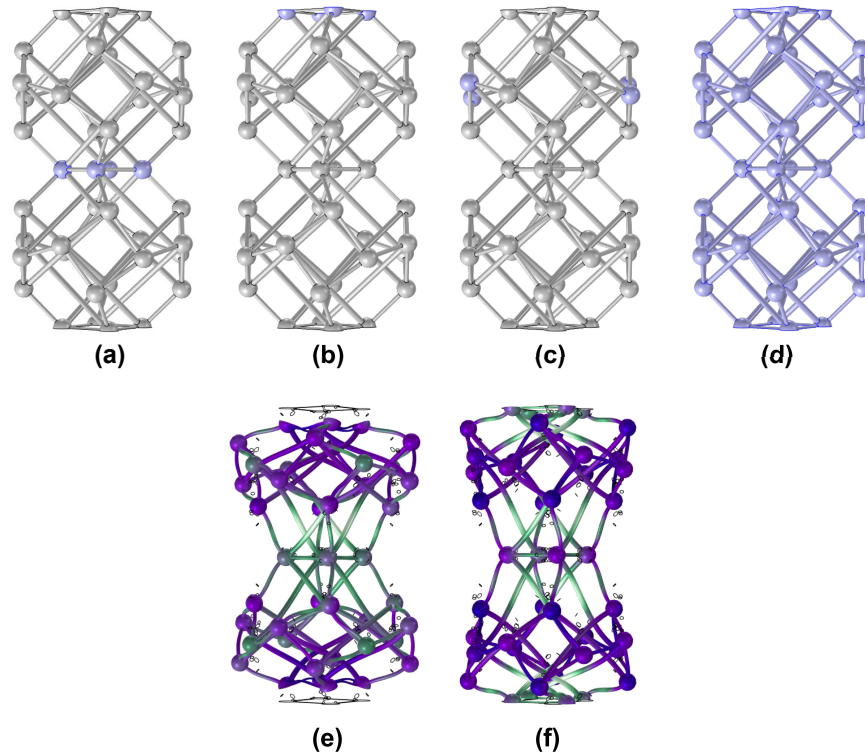


Figure 4.3: The vertical displacement magnitudes are extracted from locations (a), (b), and (c), and the curl magnitude around the vertical axis is extracted for the volume average of the RVE (d). From these magnitudes, we establish quantitative thresholds of these values to distinguish between mode shapes of the dispersion curve. We also show two examples of longitudinal modes where (e) the middle of the RVE stays stationary, but the vertical displacement is large, and (f) the middle and top of the RVE stay stationary, but the vertical displacement of the baseline mid-cell locations is large.

This is because as the structure is compressed vertically, vertical deformation is inherently coupled with rotation of the faces, as described in Chapter 3 and [120]. Thus, it makes sense that the green coupling modes occur at the intersections of the longitudinal and rotational modes in the dispersion curve. As we apply global compression to the lattice, we will see how this coupling evolves. The longitudinal (red) branches follow an unambiguous path, and clearly show a bandgap from 351 to 425 Hz , which is shown by the shaded region in Figure 4.2.

Next, we experimentally reconstructed the dispersion characteristics of the unstrained lattice. To do this, we excited the bottom plate (fabricated through the four spherical nodes on the bottom face) of the 5-RVE 1D lattice specimen with a one-cycle burst. The burst has a carrier frequency of 200 Hz and a wide frequency

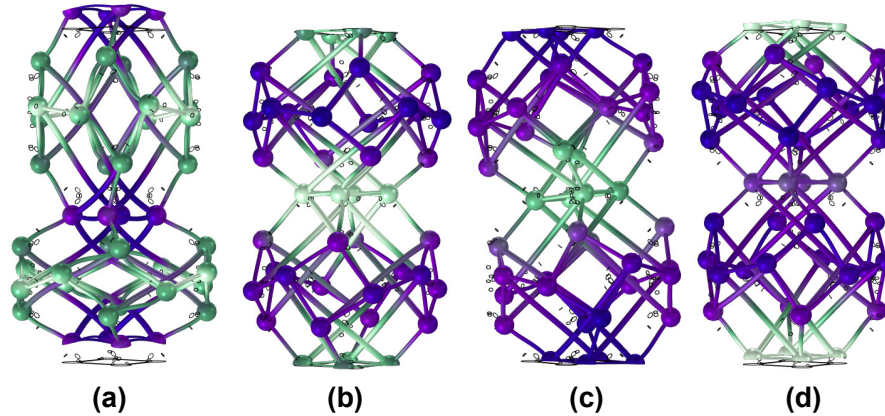


Figure 4.4: Mode shapes for the 1D RVE are shown. (a) Longitudinal, (b) rotational, (c) flexural, (d) combined rotational and longitudinal, where both rotation along the vertical axis and motion vertically are prevalent.

bandwidth, which tests a large frequency range with a compact signal. The laser vibrometer recorded the velocity time history at each of the reflective tape locations, repeating the measurement 128 times at each location and averaging to improve the signal-to-noise ratio. The reflective tapes were placed at the intersection of each baseline unit cell, as well as on the bottom plate, for a total of 10 measurement points. We also employed a high-pass filter to eliminate all ambient noise at frequencies lower than 100 Hz . This filtering step was required since the waves imparted by the transducer onto the specimen are weak, owing to the fact that we are operating the transducer very far from its peak frequency (100 kHz). Once we collected the measured data into a time-space matrix, we obtained a frequency-wavenumber data matrix by using a 2D discrete Fourier transform (2D-DFT). We performed a zero-padding operation to the data prior to performing the 2D-DFT operation. This interpolates along the wavenumber direction and improves visualization of the results despite having only few spatial samples. The experimental dispersion curve is given by the grayscale colormap of Figure 4.5.

The dispersion branches of the experimental results are expected to connect the locations of high velocity amplitude; those locations correspond to structural resonances of the finite specimen [121]. Since we have two measurement points per RVE, one every $a/2$, the plot extends to $k = 1/a$ instead of $1/(2a)$. Thus, prior to overlapping the numerical longitudinal dispersion points onto the experimental data, we “unwrap” the numerical curve about $1/(2a)$ [122], obtaining the red markers of Figure 4.5. The experimental and numerical results agree, with the numerical dispersion following the maxima of the colormap (dark grey/black regions). In

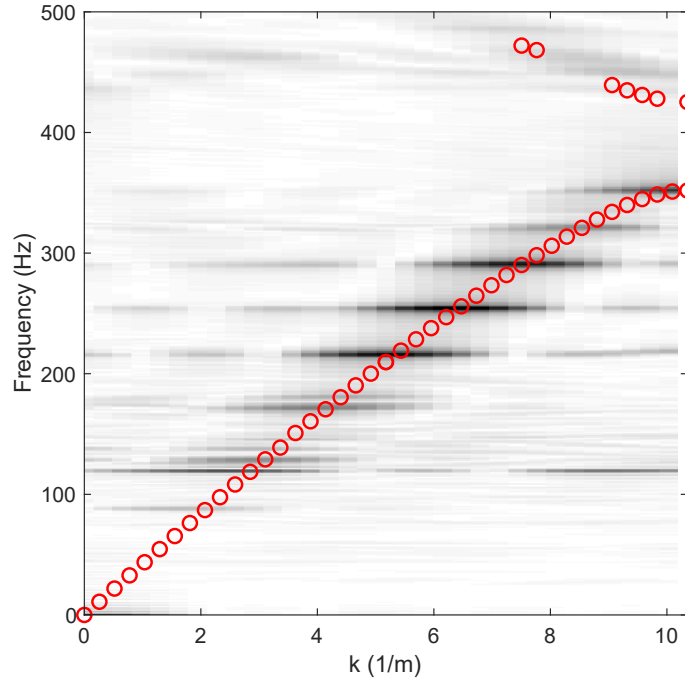


Figure 4.5: The colormap shows the experimentally-reconstructed dispersion plot for longitudinal wave motion of the 5-RVE 1D lattice. We expect the dispersion branches to follow the maxima of the colormap [121]. We see a frequency region of very low amplitude on the colormap from about 350 to 430 Hz , indicating a bandgap. The red circles indicate the “unwrapped” longitudinal wave mode locations from the numerical COMSOL simulations.

particular, the slopes of the lower branch coincide. The bandgap region, highlighted in the experimental plot by the absence of dark regions for vast frequency ranges, fall in a similar range of frequencies. Note that the low velocity amplitude region below 100 Hz is affected by high-pass filtering, and thus a clear trend is not seen in this region.

The morphology of the modes before and after the gap highlight that the bandgap is due to Bragg scattering effects [123]: (i) the branch below the gap veers to zero slope near a characteristic point of the Brillouin zone, and (ii) the two branches delimiting the gap have opposite slopes. Bragg scattering produces bandgaps in periodic systems when the wavelength approaches multiples of twice the size of a characteristic repeating unit cell (i.e., RVE) [124]. This occurs due to the fact that two neighboring RVEs act as two identical scatterers in the lattice at a distance a from each other. As an incoming wave with a certain frequency interacts with two identical scatterers a distance a , the radiated waves from the scatterers interfere destructively at certain wavelengths. The Bragg condition indicates when this is the

case [124]:

$$n\lambda = 2a. \quad (4.1)$$

Here, n is an integer. Thus, in our case, the Bragg bandgap appears at a wavelength the same size as the RVE ($\lambda = 0.0966m$, or $k = 10.352m^{-1}$), where $n = 2$.

4.2.2 Wave Speed Analysis and Comparison with Other Lattices

The longitudinal low-frequency wave speed of the 1D lattice can be readily determined from both the experimental and numerical results. The numerical wave speed is calculated by taking the slope of the dispersion curve in the low frequency region where the curve is linear. Here, the group velocity is equal to the phase velocity. The group velocity is the velocity of the wave packet of superimposed propagating waves with different values of k , and is the slope of the dispersion curve at any point. The phase velocity is the velocity of the phase of the wave with the ω and k of a point on the dispersion curve, and is calculated as $\Delta\omega/\Delta k$. We calculate the phase velocity, which is the longitudinal wave speed, at $k = 2.588m^{-1}$ and $\omega = 108.19Hz$ as $41.8 m/s$.

The experimental (phase) velocity is measured from the velocity time histories recorded at the first and last measurement locations on the lattice; we divide the spatial distance between those locations by the difference between time of occurrence of the same feature of the wave packet (in this case, a peak). Since the packet is centered at $200 Hz$, and since Figure 4.2 shows that dispersive features appear around $300 Hz$, we expect this speed to be characteristic of the non-dispersive part of the branch. An illustration of this calculation is shown in the x-t diagram of the wave propagation in Figure 4.6. In this case, x indicates the spatial location of the measurement points. The 10 measurement points are given on the horizontal axis, and time is recorded on the vertical axis. The colormap shows the amplitude of the laser vibrometer measurements. We zoom in on the first propagated wave on the inset plot. Next, we find the times at the first and last locations where the same feature of the wave packet has a maximum (red lines). From this, we calculate the wave speed as $41.8 m/s$. Hence, the simulation and experimental wave speeds are extremely close in value. Considering that the numerical simulation models an infinite lattice and the experiment uses a finite lattice, both the dispersion and wave speed results match very well. Effects from the experimental setup are likely minimal, and viscoelastic effects from the material do not contribute significantly, which would manifest as observable energy loss in the waves [125].

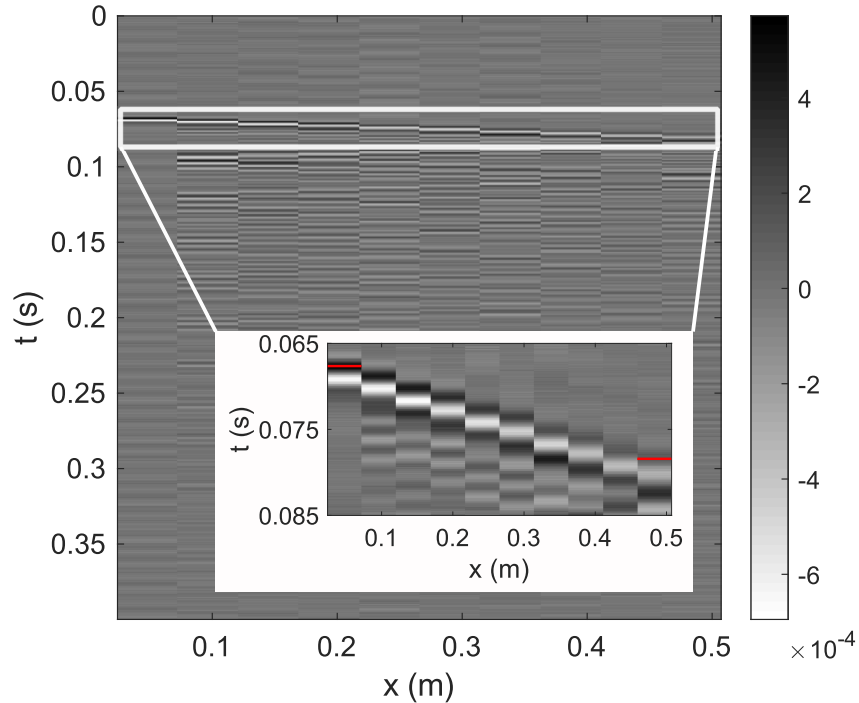


Figure 4.6: A position-time (x - t) diagram showing how the velocity amplitude measurements from the laser vibrometer (given by the grayscale colormap) vary with measurement location and time. This provides an experimental estimate of the long-wavelength, low frequency wave speed. The inset plot zooms in on the first propagated wave through the lattice, where we find the times at the first and last locations where the same feature of the wave packet has a maximum (red lines). The physical distance between these locations divided by the time difference gives the wave speed.

It is useful to compare how this longitudinal wave speed compares with other lattices with the same relative density and material properties as our tensegrity-inspired lattice. Values for the longitudinal wave speed for a simple cubic, body-centered cubic, face-centered cubic, octet, and Kelvin lattice with a relative density of 2.5% and the same material properties as our structure are given in Table 4.1 [126, 127]. All but the Kelvin lattice wave speeds are calculated from dispersion diagrams [127] in the same way we do in this work. The bulk wave speed in an isotropic, linear elastic material is given by [128]:

$$c_0 = \sqrt{\frac{E}{\rho}} \quad (4.2)$$

where E is the modulus of elasticity and ρ is the density of the material. For lattice materials, this is a good approximation of the longitudinal wave speed at low

Lattice Type	Longitudinal Wave Speed (m/s)
Simple Cubic	943.8
Body-Centered Cubic	736.3
Face-Centered Cubic	654.1
Octet	437.5
Kelvin	195.0
Tensegrity-Inspired Structure	41.8

Table 4.1: Longitudinal low frequency wave speeds for other lattice types with the same relative density and material properties as our tensegrity-inspired lattice. All but the Kelvin lattice wave speeds are calculated from dispersion diagrams [127], and the Kelvin wave speed is calculated from Equation 4.2 [126].

frequencies where dispersive effects are negligible and the material behaves linear elastically. This is used to calculate the wave speed of the Kelvin lattice in Table 4.1, whose relationship between density and modulus is given in [126]. As a simple check, the value of the wave speed for our tensegrity-inspired lattice calculated from Equation 4.2 is $46.4 m/s$. This is comparable to the value of $41.8 m/s$ we extracted from the experiment.

As we can see, the wave speed for our tensegrity-inspired structure is considerably lower than the other lattices identified. It is only 3.5% of the constitutive material wave speed (around $1180 m/s$). The first four lattice types in Table 4.1 are stretch-dominated lattices, in that the members undergo stretch-dominated deformation. The Kelvin lattice and our lattice are bending-dominated lattices. It is the case that wave speeds are slower in bending-dominated lattices than stretch-dominated ones for the same density. This is because the stiffness is higher for stretch-dominated lattices, which is for a few reasons. First, in the stretch-dominated cases, the structural members are aligned close to parallel to the longitudinal loading direction. In the bending-dominated cases (Kelvin and ours), all of the members are at a steep angle to the longitudinal direction. This produces a greater stiffness in the longitudinal direction for the stretch-dominated cases. Second, the stiffness of a stretch dominated lattice varies linearly with density for small densities (less than 10%); this is because they can be approximated as trusses with no moments at the joints where Young's modulus and density vary linearly [129]. If a structure is bending-dominated, there are moments at the joints, so Young's modulus varies with a higher power than 1, n , with respect to the density. So, when calculating the low frequency wave speed, Equation 4.2 is a constant for stretch-dominated structures, but is a constant times

density to the power n for bending dominated structures [129]. This makes the wave speeds considerably faster in stretch-dominated than in bending-dominated lattices for the same low density.

The tensegrity-inspired structure wave speed is still lower than for a Kelvin lattice. This is likely because the tensegrity-inspired structure also exhibits rotation of the faces as is it compressed longitudinally, which creates a softening mechanism. It still maintains stiffness, however, even with this softening, because it has the inclusion of the struts under compression running through the interior of the unit cell. A slow wave speed for lattices is desirable for dynamic applications because a slowly propagating wave allows more time for dissipation to occur in the structure, due to material and/or nonlinear effects. In impact cases, for example, the slow wave speed allows more time for impacting accelerations and energy to be mitigated.

4.3 Tunability with Compression

The tensegrity-inspired lattice holds potential for continuous tunability of the dispersion characteristics with global compression. The baseline structure exhibits a non-linear, load-limiting response as it is compressed. The baseline unit cell response varies slightly from the 1D RVE response, so in Figure 4.7 we give the global compressive stress-strain response of the 1D RVE with 3D stress elements in ABAQUS. This best indicates how the lattice we are working with in this section behaves under compression. With increasing compression, the structure deforms dramatically, the struts buckle, and the stiffness of the structure plateaus to almost zero. Thus, we expect the dispersion characteristics of the 1D lattice to change with increasing axial compression.

To perform experiments with varying global compression, we needed to switch to a 3-RVE lattice and support it with anti-buckling strings as described in Chapter 2. The 1D lattice effectively behaves as a slender beam ($L/D = 10$) with low stiffness, corresponding to a low elastic buckling load and buckling strain. We performed a simple linear perturbation on the 5-RVE lattice with the ABAQUS beam element model to see this more clearly, as seen in Figure 4.8. With fixed top and bottom nodes (as in the experiment), the buckling load for the first mode is 6.9 N , corresponding to a buckling strain of 5.3% (Figure 4.8(a)). When attempting to compress the physical 5-RVE lattice, it visibly buckled before 5% strain. The 3D-printed structure inherently has imperfections, inducing buckling before the theoretical load. The 2nd buckling mode (i.e., the first possible buckling mode

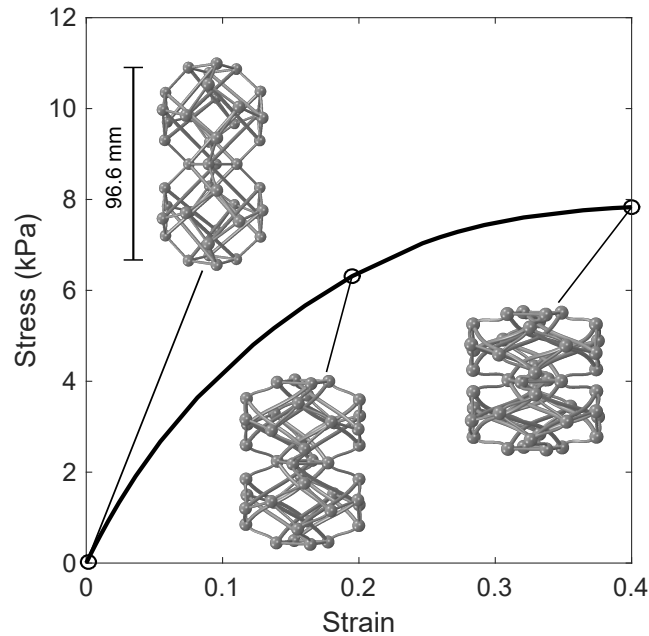


Figure 4.7: The global compressive stress-strain curve of the 1D RVE under compression, as outputted from the ABAQUS 3D stress element simulation. This best indicates how the lattice we are working with in this section behaves under compression. A visual depiction of the deformation in the structure is shown at 0, 0.2, and 0.4 global compressive strain.

when the support strings are added at the center), has a theoretical buckling load of 12.1 N , corresponding to a strain of 12% (Figure 4.8(b)). Again, the 3D-printed structure with support strings would likely enter the 2nd buckling mode before 12% strain due to manufacturing imperfections. Since our goal was to compress the structure to 20% strain, we needed to reduce the size of the lattice.

Thus, we use a lattice with 3 RVEs and add strings at the center that connect to four vertical, rigid rods. Both of these operations prevent the global buckling of the lattice with compression. The strings prevent out-of-axis deformation, but do not prevent movement in the longitudinal direction. They only prevent the first buckling mode; the second buckling mode, the “s-shape” mode, occurs after significant compression with the strings.

We performed the experiments at 0%, 5%, 10%, 15%, and 20% global compressive prestrains. Above 20%, the structure globally visibly deforms into its second buckling mode. Note that for future studies, second mode buckling could be prevented by adding additional support strings. Another valuable metric for the response of the lattice with tuning is transmissibility. The transmissibility is the

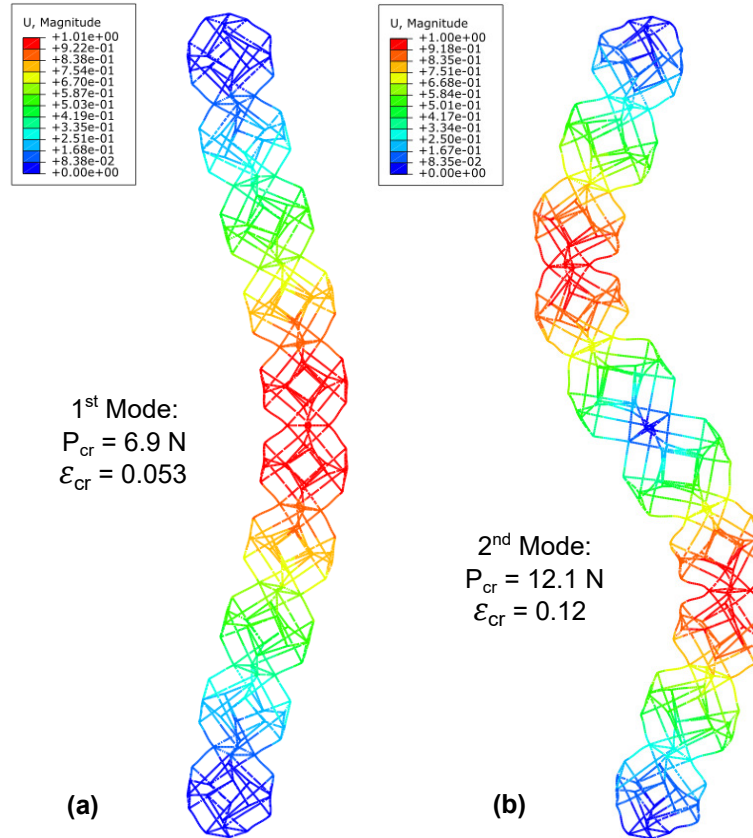


Figure 4.8: Linear perturbation buckling analysis of the 5-RVE lattice in ABAQUS to show the loads and global strains for the (a) first and (b) second buckling modes.

ratio of the velocity amplitude at the output (last) measurement point to the velocity amplitude at the input (first) measurement point for each frequency. When the input and output have the same amplitude, the transmissibility is 1. For regions of high amplitude attenuation, the transmissibility dips significantly below 1. The transmissibility plots are a better comparison between simulation and experiment for a 3-RVE lattice; they both compare finite lattices, rather than an infinite and a finite lattice like for the dispersion plots. The experimental and numerical dispersion curves and transmissibility plots are shown in Figure 4.9 for (a) 0%, (b) 5%, and (c) 10% strain. Numerical results are shown in red, and the experimental results in black.

Looking at the numerical dispersion we clearly see that, with increased compressive strain, the bandgap width reduces and the slope of the acoustic branch decreases, lowering the onset of the bandgap. The signature of bandgap closure that can be read from the experimentally-reconstructed dispersion is the narrowing of

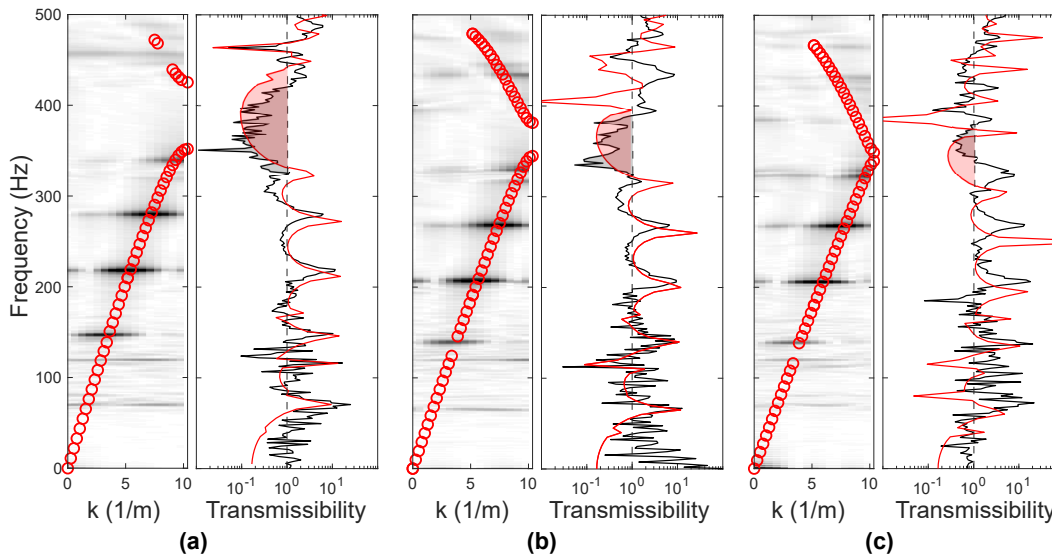


Figure 4.9: Precompression-induced tunability. The left panel of each subfigure represents the experimentally-reconstructed dispersion curve (gray colormap), with overlapped circular markers corresponding to the numerical dispersion relation. The right panel is the transmissibility plot, where the experimental curves are black and the numerical ones are red. The dashed vertical line indicates a transmissibility of 1. The shaded gray and red regions serve as a guide to the eye and indicate what we identify as bandgaps for the experimental and numerical curves, respectively. (a) Lattice compressed to 0% global strain, (b) 5% global strain, and (c) 10% global strain.

the peakless frequency region that extended from 340 to 440 Hz in Figure 4.9(a) for 0% strain. Keep in mind that a perfect match is not attainable here, owing to the fact that the numerics represent the response of an infinite lattice. A 3-RVE lattice particularly produces noise in the experimental response; because of interference from the close boundaries, multiple wave packets interfere with each other, making distinguishing between them difficult and affecting the wave attenuation region. It is clear that the longer, 5-RVE lattice produces a better match with the simulation for 0% prestrain than the 3-RVE lattice, when comparing Figure 4.9(a) with Figure 4.5.

The transmissibility plots, being representative of a finite-lattice response, show an even better match between numerics and experiments. We first analyze the 0% strain case of Figure 4.9(a), where we can see that the structural resonance peaks between black and red curves almost coincide (with a minimal shift of 8 Hz). The experimental response appears to be stiffer, likely due to differences in manufacturing from the nominal geometry and material properties. The noisy nature of the

experimental response below 100 Hz is again due to high-pass filtering. A strong anti-resonance is visible for both numerics and experiments at around 450 Hz , and we claim this to be a feature of the finite structure and not indicative of a bandgap. From the curves, we define as bandgap the wide peakless region from about 340 Hz for the experiment and 450 Hz for the numerics where the transmission dips below 10^0 . This attenuation region, shaded in red for the numerics and in gray for the experiments, is in the vicinity of the numerical dispersion bandgap, yet slightly wider, due to the finite nature of the lattice.

As we increase the strain to 5% and 10%, as shown in Figure 4.9(b) and (c), respectively, anti-resonances and resonance peaks shift towards lower frequencies, highlighting a global softening of the structure. Both the numerical and experimental curves show increased resonance peak density and amplitude near the bandgap. The valley identified as a bandgap in Figure 4.9(a) becomes increasingly narrow and shallow for both simulation and experiment (see the evolution of the shaded regions). The experimental bandgap most significantly shallows and narrows by 10% strain. This confirms that global prestrain indeed causes the bandgap to diminish in size.

We can also note that, as global prestrain increases, the shift between numerical and experimental resonances increases (reaching 19 Hz in Figure 4.9(c)). This is not surprising, as the difference between numerics and experiments is bound to increase for larger prestrains, for several reasons. First, the material model used in COMSOL is linear elastic, rather than hyperelastic, which affects the stiffness values at higher strain levels in the lattice. At these levels, local strains may exceed the region of negligible deviance from the linear elastic region. Second, buckling of the structure could affect the response even before any buckling is visually apparent. In fact, it is likely that buckling affects the structure's response earlier than expected, because even small imperfections from the fabrication process could induce out-of-axis deformation. However, even though these differences exist, the numerical and experimental results are quite comparable.

Figure 4.10 shows the full evolution of the dispersion properties from 0% to 20% strain for numerics and experiments. The bandgap nearly closes, but then opens again at 20% strain for the numerics. We can see the slope of the lower branch of the dispersion curve reducing in both cases (shown by the lowering of frequency of the dark grey regions in the experimental case). This indicates a reduction of the wave speed. As expected, at the higher strain values of 15% and 20%, the experiments

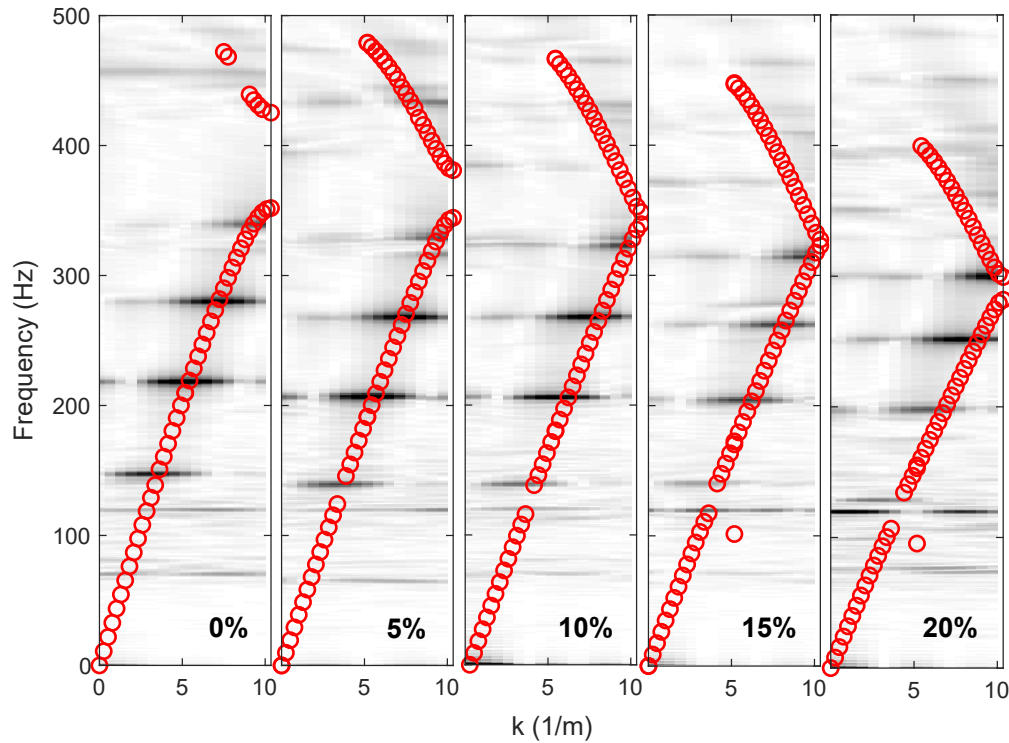


Figure 4.10: The longitudinal dispersion plots of both numerics and experiments for prestrain levels from 0% to 20%. The prestrain levels are given in the lower right-hand corner of each plot.

deviate most significantly from the numerics. At these levels of prestrain, identifying the bandgap is increasingly difficult. For this reason, we consider the consistency of numerics and experiments by tracking the evolution of the longitudinal wave speed with prestrain, as shown in Figure 4.11(a). Both numerical and experimental results show a 16% reduction of wave speed from 0% strain to 10% strain. As compression is increased, the experimental results again show a stiffer response with respect to the numerics, resulting in higher wave speeds. From 0% to 20% strain, the numerical wave speed reduces by 27%, and the experimental wave speed reduces by 19%. The already very low original wave speed of 42 m/s can be reduced about a quarter, even before the structure enters its most significant nonlinear region (seen after 0.2 strain in Figure 4.7). Despite the quantitative discrepancies, our experimental results qualitatively confirm that wave speed and bandgap can be continuously and significantly tuned with prestrain in these tensegrity-inspired lattices.

Due to difficulties in bandgap identification for finite-size systems, we visualize the bandgap evolution from only the numerical dispersion curve in Figure 4.11(b). Upper and lower bounds of the bandgap width, in Hz , are provided for 0%, 5%,

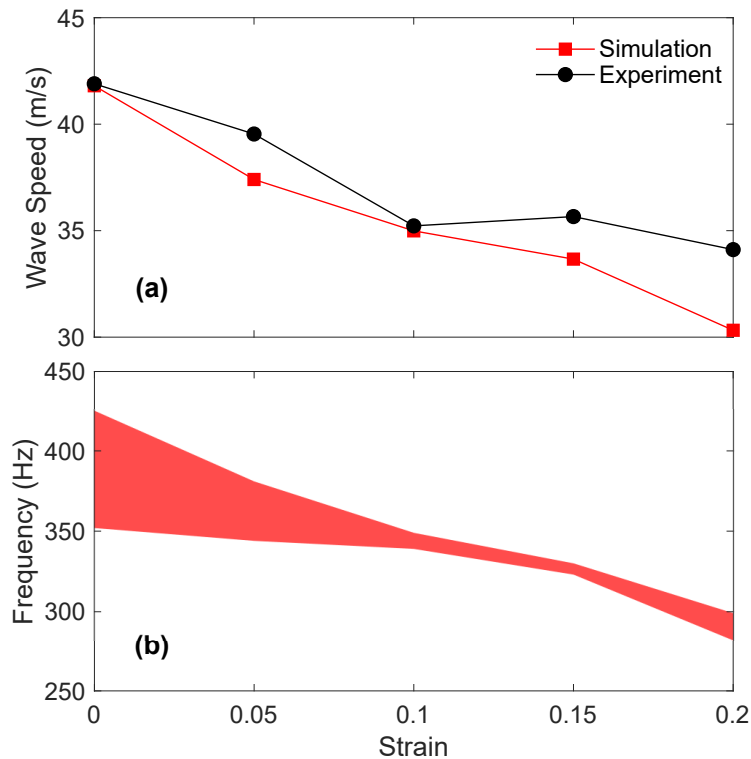


Figure 4.11: (a) Experimental and numerical longitudinal wave speeds at varying levels of global precompression. (b) Evolution of the bandgap width, in Hz , based on the numerical dispersion curve. The bandgap region is shaded for strains up to 0.2.

10%, 15%, and 20% global strain, with the in-between sections shaded in red to visualize the progression of the width. At no global precompression, the gap is relatively large, from 352 to 425 Hz . As precompression is applied, the bandgap narrows significantly and shifts to lower frequencies. Interestingly, at 15% strain, the bandgap nearly closes and is only 7 Hz wide, from 323 to 330 Hz . The bandgap then slightly opens again at 20% strain. This lattice shows that the Bragg scattering bandgap can be significantly altered, again even before the structure reaches the plateau of its stress-strain curve (after 0.2 strain in Figure 4.7).

At this point it is valuable to note how these tunability characteristics can be applied in a practical application. Acoustic lenses formed with periodic chains like our 1D lattices have been shown to exhibit dramatic energy focusing effects [77, 130] due to tunable wave speeds. The focusing effect arises from varying levels of precompression or prestress in parallel chains of periodic elements and applying an impacting wave to the strings of chains perpendicularly. Because the chains have varying levels of precompression or prestress, they have different wave speeds; as

they are compressed by the impacting wave, waves with different phase velocities are generated in the chains, and the wave coalesce to a focal point in the adjacent host medium [77, 130]. An illustration of this is shown for a case of tensegrity chains with varying prestrain in Figure 4.12 [77]. In our case, these tensegrity-inspired, 3D-printable lattices could be used to control waves in similar manners by continuously varying precompression on parallel chains.

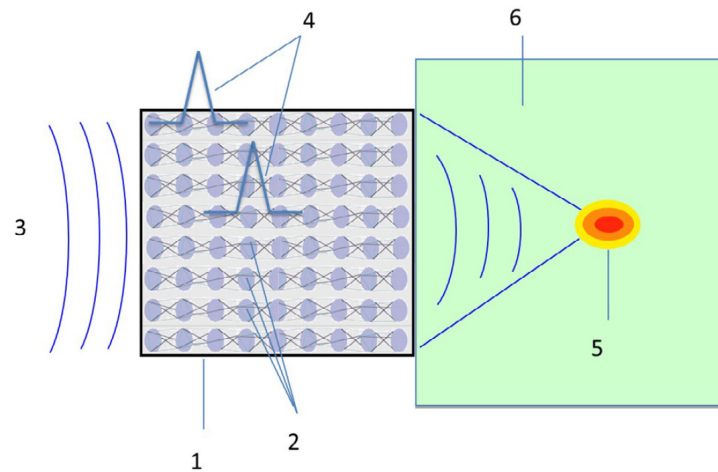


Figure 4.12: F. Fabbrocino and G. Carpentieri demonstrated this example of a tensegrity focusing lens [77]. The acoustic lens (1) consists of an array of tensegrity and lumped mass chains, each subject to different prestress levels (2). The incident wave signal (3) creates multiple waves with different phase velocities (4) within the array. These waves come together at a focal point (5) in the adjacent medium (6) [77]. A similar concept could be applied to the tensegrity-inspired lattices in this thesis.

Another observation we made from this analysis was how the remaining mode shapes, other than longitudinal, changed with increasing global prestrain. This was observable in the numerical COMSOL simulations. The complete dispersion curves for all modes and compression levels up to 20% strain are shown in Figure 4.13. Again, red circles are longitudinal modes, purple circles are rotational modes, green circles are combined rotational and longitudinal modes, and the blue stars are flexural and all other mode types. Each panel shows the level of compression in the bottom right-hand corner.

We see several interesting attributes. From 0% strain to 5% strain, the upper branch of the longitudinal curve becomes fully unambiguous because the rotational mode distances from it. Also, the initial flexural mode flattens out and does not increase from zero frequency until $k = 2$. The flexural mode continues to flatten

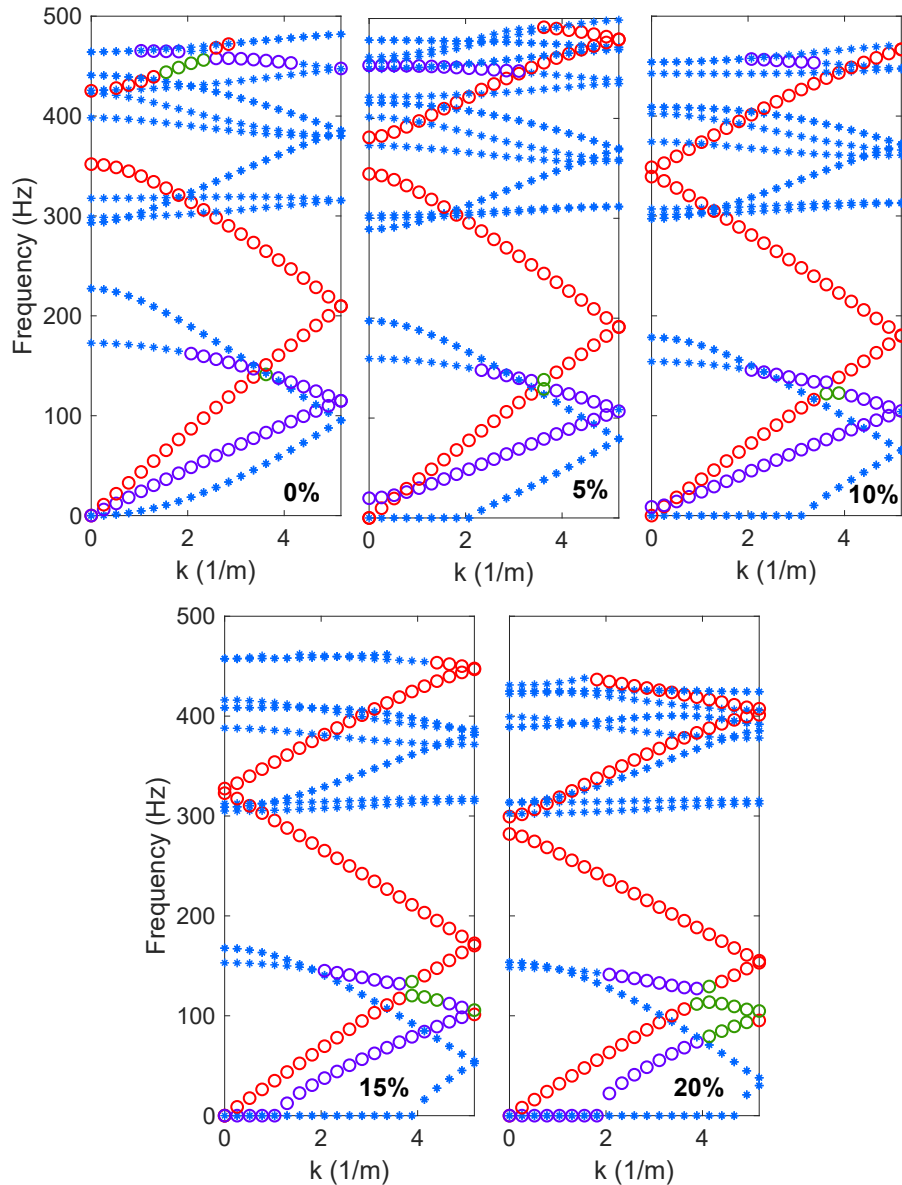


Figure 4.13: Complete COMSOL dispersion results for each level of compressive prestrain (shown in bottom right-hand corner of each panel). Again, red circles are longitudinal modes, purple circles are rotational modes, green circles are combined rotational and longitudinal modes, and the blue stars are flexural and all other mode types.

through 20% strain. The rotational mode also flattens starting at 15% strain and continues flattening through 20% strain. These are zero energy modes, and they indicate that there exist low frequency wave numbers where it is not possible for anything but longitudinal waves to propagate at these compression levels. Interestingly, the same kind of behavior has been seen in tensegrity lattices with buckling

struts [87]. In that case, as prestrain is increased in the cables (analogous to the application of global prestrain in our case), zero energy flat modes appear. This is due to the fact that the struts have buckled in the lattice, leading them to become “floppy” at low frequencies [87]. It is possible that the same concept applies for our tensegrity-inspired lattices: as the compression level increases, the struts approach their buckling load and encounter less resistance, becoming “floppy” and contributing to zero energy modes.

A second observation we make from Figure 4.13 is that as compression increases, the combined modes (green circles) become much more prevalent at the lower frequency intersection of the rotational and longitudinal branches. The branches themselves look as if they begin melding together. That is, instead of following a clear path through the longitudinal branch, as compression is increased, the rotational branch “jumps” from a lower frequency to higher after combining for a few modes with the longitudinal branch (seen from 5% to 15% strain). Then, at 20% strain, the pure rotational mode itself undergoes a large jump from about 74 Hz to 127 Hz . The rotational modes in between those frequency values have a significant longitudinal contribution. It makes sense that there would be such coupling. As stated previously, as the structure is compressed, the faces rotate, so there is automatically some coupling between longitudinal motion and rotational motion. Then, as the structure is compressed, this coupling in the frequency regime is increased because the compression constricts how freely the structure is able to move. The structure “wants” to move in a certain way, but the prestrain forces it to move differently. We have observed in several ways how our tensegrity-inspired structure is continuously and significantly tunable with compression, making it desirable for dynamic applications where such tuning is required.

4.4 3D RVE Dispersion Characteristics

So far in this chapter, we have looked at only one-dimensional lattices and their dispersion characteristics. This information is useful to understand the dynamics of the tensegrity-inspired structure in a basic periodic arrangement, but in many applications 3D lattices are required. They are more practical, especially for impact applications, and they provide room for more heterogeneous wave propagation attributes to manifest. The dispersion characteristics of 3D RVEs are therefore of interest.

To find the dispersion curve of a 3D RVE, we build a model in COMSOL as

described in Chapter 2. Recall that the 3D RVE of the tensegrity-inspired structure is comprised of 8 baseline unit cells. Periodic Bloch boundary conditions are applied on all x, y, and z faces (total of 24 faces) of the periodic RVE. Sweeping the wavenumber (now the full wave vector, \vec{k}) is more complex in the 3D case than the 1D case. Next, we give an overview of the general derivation of the wave vector, \vec{k} .

The lattice vector in real space is:

$$\vec{R} = n_1\vec{a}_1 + n_2\vec{a}_2 + n_3\vec{a}_3 \quad (4.3)$$

where $\vec{a}_1 = a_1\hat{x}$, $\vec{a}_2 = a_2\hat{y}$, and $\vec{a}_3 = a_3\hat{z}$. The reciprocal lattice vector is given by:

$$\vec{G} = m_1\vec{b}_1 + m_2\vec{b}_2 + m_3\vec{b}_3 \quad (4.4)$$

where the basis vectors are shown in Equations 4.5, 4.6, and 4.7.

$$\vec{b}_1 = 2\pi \frac{\vec{a}_2 \times \vec{a}_3}{\vec{a}_1 \cdot (\vec{a}_2 \times \vec{a}_3)} \quad (4.5)$$

$$\vec{b}_2 = 2\pi \frac{\vec{a}_3 \times \vec{a}_1}{\vec{a}_2 \cdot (\vec{a}_3 \times \vec{a}_1)} \quad (4.6)$$

$$\vec{b}_3 = 2\pi \frac{\vec{a}_1 \times \vec{a}_2}{\vec{a}_3 \cdot (\vec{a}_1 \times \vec{a}_2)} \quad (4.7)$$

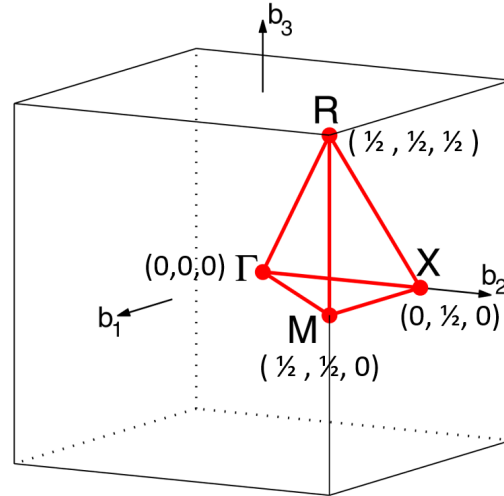
Finally, the Bloch wave vector, \vec{k} , is related to the reciprocal lattice vector by:

$$\vec{k} = u\vec{b}_1 + v\vec{b}_2 + w\vec{b}_3. \quad (4.8)$$

The periodicity of our 3D RVE is simple cubic. Thus, its first Brillouin zone (the uniquely defined primitive RVE in reciprocal space) is given in Figure 4.14 [131], and the reciprocal coordinates at each of the symmetry points, Γ , M , X , and R are shown. For the simple cubic lattice, the basis vectors for \vec{k} and \vec{b} are related by:

$$\vec{b}_1 = \frac{2\pi}{a}\hat{k}_x, \quad \vec{b}_2 = \frac{2\pi}{a}\hat{k}_y, \quad \vec{b}_3 = \frac{2\pi}{a}\hat{k}_z. \quad (4.9)$$

Thus, following the path of the first Brillouin zone shown in Figure 4.14, in COMSOL we sweep \vec{k} as follows for the 7 regions of the first Brillouin zone. We find 20 eigenvalues for each value of the sweep.



CUB path: Γ -X-M- Γ -R-X|M-R

Figure 4.14: The first Brillouin zone of a simple cubic 3D RVE is shown in reciprocal space. The path is given below the diagram. [131]

$$\Gamma \text{ to } X: k_x = 0, k_y = 0 \text{ to } \frac{\pi}{a}, k_z = 0$$

$$X \text{ to } M: k_x = 0 \text{ to } \frac{\pi}{a}, k_y = \frac{\pi}{a}, k_z = 0$$

$$M \text{ to } \Gamma: k_x = \frac{\pi}{a} \text{ to } 0, k_y = \frac{\pi}{a} \text{ to } 0, k_z = 0$$

$$\Gamma \text{ to } R: k_x = 0 \text{ to } \frac{\pi}{a}, k_y = 0 \text{ to } \frac{\pi}{a}, k_z = 0 \text{ to } \frac{\pi}{a}$$

$$R \text{ to } X: k_x = \frac{\pi}{a} \text{ to } 0, k_y = \frac{\pi}{a}, k_z = \frac{\pi}{a} \text{ to } 0$$

$$X \text{ to } M: k_x = 0 \text{ to } \frac{\pi}{a}, k_y = \frac{\pi}{a}, k_z = 0$$

$$M \text{ to } R: k_x = \frac{\pi}{a}, k_y = \frac{\pi}{a}, k_z = 0 \text{ to } \frac{\pi}{a}$$

As done in [87], we normalize the frequencies of the dispersion relation in the following way. We obtain the longitudinal wave speed in the bulk material by the relation $c_0 = \sqrt{E/\rho}$. For our material, $E = 1.291\text{GPa}$ and $\rho = 930\text{kg/m}^3$, giving $c_0 = 1178\text{m/s}$. Then, we obtain a reference frequency, ω_r , by the relation $\omega_r = c_0/a$, where a is the characteristic length of the RVE. For $a = 0.0966\text{m}$ and $c_0 = 1178\text{m/s}$, this gives $\omega_r = 12194.6\text{Hz}$. Then, the normalized frequency is the

frequency divided by the reference frequency, or $\Omega = \omega/\omega_r$. This was done in [87] for the dispersion relation of a prestressed buckling tensegrity 3D RVE. In that case, the normalization ensures validity of the dispersion relation for a range of tensegrity truncated octahedron lattices, with a linear elastic material and the same geometric cable and bar diameters with respect to the unit cell length, a . We do this here for the same reason and to compare our results with the results from [87].

The numerical dispersion relation for the 3D RVE is given in Figure 4.15. The red dotted lines denote longitudinal pressure modes, and blue stars denote all other modes. We see several interesting traits from the dispersion curve. First, the

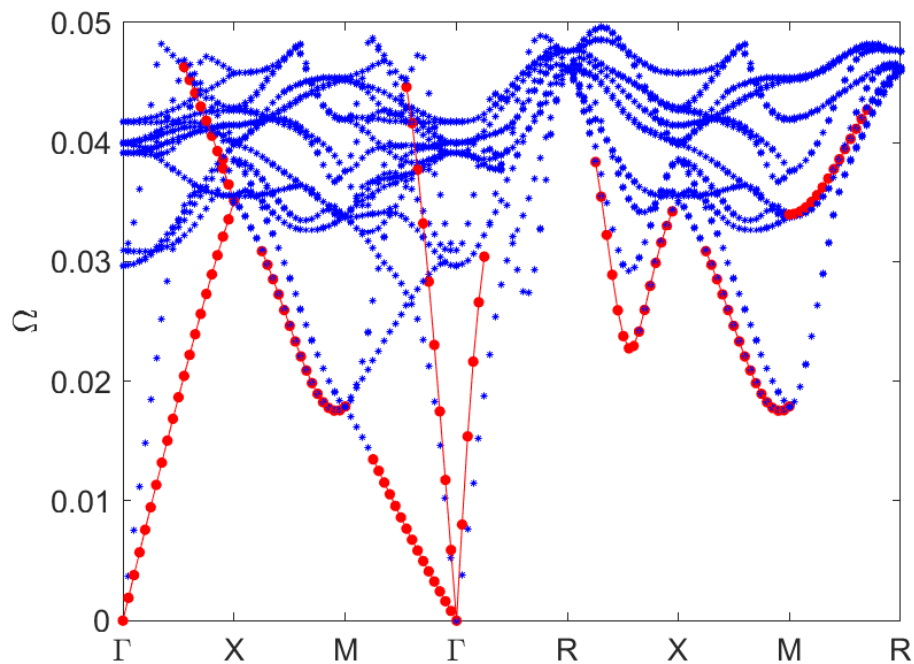


Figure 4.15: The 3D RVE dispersion relation is shown for all 7 regions of the first Brillouin zone. Red dotted lines are longitudinal pressure modes and blue stars are all other modes, including shear modes. The frequencies are normalized as described in the text. We see that in the first longitudinal region, ΓX , the low frequency shear mode has a speed of 176 m/s , which is about twice as fast as the longitudinal speed (89.6 m/s), unlike in natural solid materials. Also, the diagonal wave speed in region ΓR (334 m/s) is about twice that of the shear speed in region ΓX .

low frequency shear wave speed in the first region, ΓX , is in fact faster than the longitudinal wave speed. This region is analogous to the direction studied in the 1D RVE analysis in the previous sections of this chapter. A faster shear speed than

longitudinal speed is very rarely observed in natural materials [132], but has been observed in dilational metamaterials [133] as well as 3D tensegrity lattices [87] analogous to our own lattice.

Second, the steep longitudinal modes in regions $M\Gamma$ and ΓR are diagonal pressure modes. These branches have a speed twice as fast as the shear speed in region ΓX . They have a speed of 334 m/s , the shear speed in region ΓX is 176 m/s and the longitudinal speed in ΓX is 89.6 m/s . The longitudinal ΓX speed is about twice the longitudinal speed in the 1D lattice (41.9 m/s); this was also observed for buckling tensegrity lattices in [87]. It is possible that the large Poisson's ratio (initially 2) contributes to the shear and diagonal speeds being faster than the longitudinal speeds. A Poisson's ratio greater than 1 means that the transverse motion essentially is "stiffer" than the longitudinal motion, leading to faster wave speeds in the transverse directions. Faster shear and diagonal speeds than longitudinal speeds indicate that this type of lattice will exhibit unique waveguiding and/or lensing characteristics in impact applications, even without the application of prestress.

Third, the low frequency rotational modes entirely disappear. This is likely because rotation of the faces is significantly constrained in the 3D case, due to all faces of each baseline cell being connected to an adjacent cell face.

For comparison, we show the 3D RVE dispersion relation for a buckling truncated octahedron tensegrity lattice in Figure 4.16, as given in [87]. In this case, they look at an RVE with $a = 1.26\text{ m}$, strut and cable diameters of 2.3 cm and 1.15 cm , respectively, and made of titanium ($E = 100\text{ GPa}$ and $\rho = 4480\text{ kg/m}^3$). The lattice is slightly prestressed, but the struts are not fully buckled.

The dispersion relation looks remarkably similar to the dispersion relation for our lattice (Figure 4.15). The scaling of frequency varies between the two, but this is due to the fact that our lattice has different cable and strut diameter ratios with respect to the RVE length. In both cases, the shear wave speed (steep low frequency branch in the ΓX region of Figure 4.16) is faster than the longitudinal wave speed (shallower low frequency branch in the ΓX region of Figure 4.16). The longitudinal wave speed also is twice that of the 1D lattice for both our structure and the tensegrity structure. Also, the overall shapes of the dispersion curves are quite similar for all 7 regions, with no low frequency modes in the last 3 regions in both cases. It is intriguing that even for a 3D lattice in the dynamic regime, the response of our tensegrity-inspired lattice behaves so similarly to a tensegrity lattice. This indicates that our lattice is a readily fabricatable option (unlike true tensegrity lattices) that

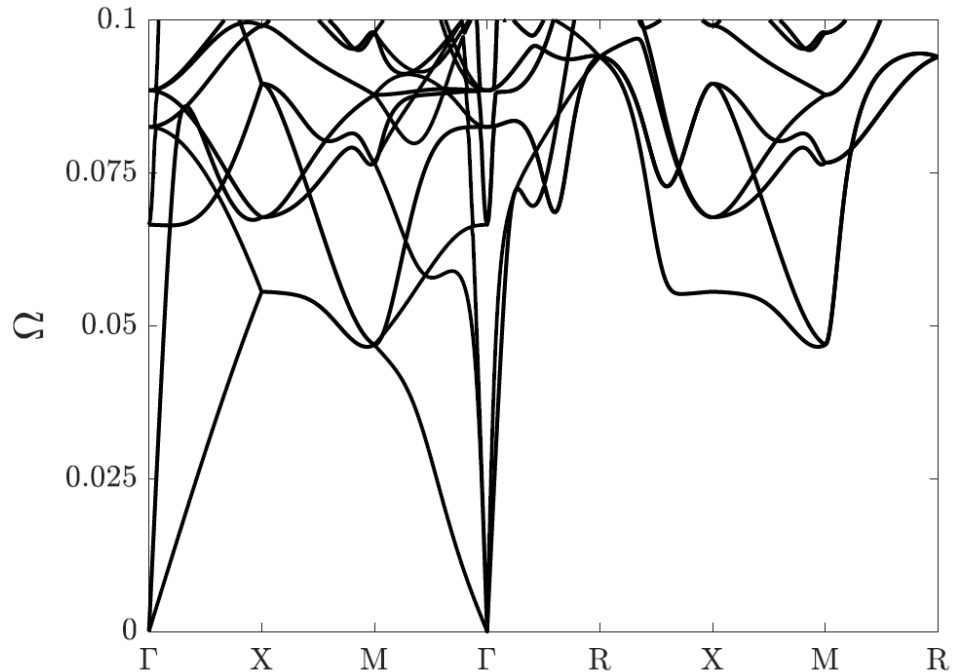


Figure 4.16: The 3D RVE dispersion relation for a buckling truncated octahedron tensegrity lattice as given in [87].

achieves the same desirable and unique characteristics that tensegrity lattices have thus far only theoretically exhibited.

4.5 Chapter Summary

We have investigated the response of nonlinear tensegrity-inspired lattices subject to low amplitude frequency excitation. We first examined 1D lattices, both experimentally and numerically. At no precompression, the longitudinal dispersion curve shows a Bragg scattering bandgap with a width of about 70 Hz and a very low wave speed of around 40 m/s . This wave speed is compared to other lattices with the same relative density and constitutive material, and our structure attains the lowest wave speed by far, making it desirable for dynamic applications. Experiments and simulations match very well at no precompression, but they stray from each other increasingly with higher precompression due to global buckling effects, material property differences, and manufacturing defects. However, both experiments and simulations show significant and continuous tunability of dispersion properties with global precompression. Since the deformation remains elastic even at large strains, repeatable and active tuning of the lattice response is potentially achievable. Wave speed reduces by about 25% by a strain level of 20%, and the bandgap shifts down

and its width reduces dramatically. This high level of tunability makes the lattice a good candidate for energy focusing or waveguiding applications, like in Figure 4.12, due to different wave speeds attainable in the lattice with varying levels of precompression.

The 3D dispersion characteristics also show unique behaviors. The most significant finding is that the shear wave speed is twice as fast as the longitudinal wave speed at low frequencies, which is rarely observed in natural materials. The diagonal wave speed is twice as fast as the shear speed as well. Faster diagonal and shear speeds than longitudinal speeds indicate the potential of even the unstrained lattice to exhibit energy redirection of impact pulses. We will explore this in the next chapter. Fascinatingly, our tensegrity-inspired lattice exhibits very similar dispersion patterns as buckling tensegrity lattices [87]. Even in this dynamic regime, our structure, which has fundamentally different deformation modes than a pin-jointed tensegrity, attains similar desirable behaviors as real tensegrity structures, with the added advantage of being easily fabricatable and testable. Although we have explored one geometric configuration in this chapter, we believe these principles can be extended to other configurations to enhance the attainable dispersion attributes. Two examples would be: (i) using these RVEs as springs connecting larger masses, to create phononic systems with richer wave attributes [86], and (ii) creating alternate RVE configurations, such as those which tessellate in space with spatial gaps, that can open more unique and extensive bandgap systems [72].

*Chapter 5***DYNAMICS: IMPACT****5.1 Introduction of Impact Studies**

In the previous chapter, we studied the response of these tensegrity-inspired structures under low amplitude wave excitation. We saw that they exhibit unique dynamic characteristics, such as low wave speeds and tunable wave attenuation with global compression. In this chapter, we examine the response of tensegrity-inspired structures under impact loading. Lightweight, reusable materials are often needed for many engineering impact applications, such as shielding for air and spacecraft, electronic device protection, and wearables such as helmets. Often, the mechanism used for energy dissipation in impact is plastic deformation [40, 134–136]. However, this renders the material largely unusable for subsequent impacts. We show in this chapter that tensegrity-inspired structures and periodic lattices exhibit high energy absorption, elastic deformation under impact, and unique wave propagation characteristics. This also corroborates recent theoretical and numerical work in the area of tensegrity structures and lattices [16, 17, 23, 71, 74, 76].

Three types of impact conditions are studied, each giving unique insight into the structure's behavior. In the first scenario, a long-duration pulse is exerted on the structure by a heavy, falling mass. With drop weight experiments and simulations, fundamental characteristics of the baseline unit cell and 1D lattices are observed, such as load limitation, wave speeds, and elastic deformation. In the second scenario, the specimen is dropped from a height such that it impacts a rigid surface at an initial impact velocity, v_0 . In the third scenario, a short-duration, high energy pulse is exerted on the top of the structure by a small falling mass and the energy transmission characteristics are studied. In the second and third scenarios, we study 1D, 3D1D, and 3D lattices. The extension to higher dimension lattices gives insight into how energy propagates in transverse directions as well as additional energy dissipation properties that cannot be observed in 1D lattices. Sample drop experiments are performed on 1D and 3D1D lattices, and numerical simulations are performed for the remaining studies.

The strain rates we study range from approximately 40 s^{-1} for the long pulse (drop weight) analyses, to 260 s^{-1} for the short duration pulse analyses. This work

therefore sits in the intermediate strain rate dynamic regime between quasistatic and high strain rate dynamic situations, according to the table in Figure 5.1. Inertial forces are important to consider, as well as the effects of the test setup. In this region, we study the propagation of elastic waves in the lattice structures.

STRAIN RATE, s^{-1}	COMMON TESTING METHODS	DYNAMIC CONSIDERATIONS	
10^7	HIGH VELOCITY IMPACT -Explosives -Normal plate impact -Pulsed laser -Exploding foil -Incl. plate impact (pressure-shear)	SHOCK-WAVE PROPAGATION	INERTIAL FORCES IMPORTANT
10^6		SHEAR-WAVE PROPAGATION	
10^5		PLASTIC-WAVE PROPAGATION	
10^4	DYNAMIC-HIGH -Taylor anvil tests -Hopkinson Bar -Expanding ring		
10^3	DYNAMIC-LOW High-velocity hydraulic, or pneumatic machines; cam plastometer	MECHANICAL RESONANCE IN SPECIMEN AND MACHINE IS IMPORTANT	
10^2			INERTIAL FORCES NEGLIGIBLE
10^1			
10^0	QUASI-STATIC Hydraulic, servo-hydraulic or screw-driven testing machines	TESTS WITH CONSTANT CROSS- HEAD VELOCITY STRESS THE SAME THROUGHOUT LENGTH OF SPECIMEN	
10^{-1}			
10^{-2}			
10^{-3}			
10^{-4}			
10^{-5}			
10^{-6}	CREEP AND STRESS- RELAXATION -Conventional testing machines -Creep testers	VISCO-PLASTIC RESPONSE OF METALS	
10^{-7}			
10^{-8}			
10^{-9}			

Figure 5.1: Classification of mechanical specimen testing according to strain rate. [137]

Some content of this chapter has been partially adapted from:

K. Pajunen et al. "Design and impact response of 3D-printable tensegrity-inspired structures". In: *Materials & Design* 182 (2019), p. 107966.

5.2 Drop Weight: Long-Duration Impact

As shown in Chapter 3, tensegrity structures with buckling struts have a nonlinear compressive response that exhibits load limitation. This characteristic applies to their dynamic impact response, as shown in [23]. Forces within the structure plateau as the struts reach their buckling load. Our tensegrity-inspired unit cell corresponds to an equivalent tensegrity unit cell. Because our structure exhibits this load limiting attribute as well, we expect the dynamic loads to not exceed that of the buckling load of the structure (around 18.6 N). Drop weight experiments and simulations are performed first on the baseline unit cell to demonstrate this and examine the basic dynamics. We also assess the effect of the test setup and choice of material in the experimental results and validate our dynamic simulations. Then, we study 1D lattices comprised of 5 baseline unit cells to see how the characteristics translate beyond single unit cells. The drop weight tests are done with a large falling mass at a low impact speed. The resulting long duration impact produces low strain rates, allowing straightforward observation of the basic dynamic deformation of the structure.

5.2.1 Baseline Unit Cell

Force Response and Observation of Load Limitation

We fabricated multiple baseline unit cell samples with a total height of 54.1 *mm*, and a height of 48.3 *mm* from the top face nodes to the bottom face nodes. Due to variation in manufacturing, several samples had member diameters significantly lower or higher than the nominal diameters of 1.2 *mm* cables and 1.73 *mm* struts. So, using a caliper, we took measurements of the cables and strut diameters for many samples. For testing, we chose 4 samples that had average member diameter measurements within 4% of the nominal member diameters and had no visible defects.

Two masses of 100 *g* and 200 *g* were manufactured for the drop weight tests. As explained in Chapter 2, ABAQUS dynamic implicit simulations were performed to complement the experiments. As a preliminary analysis before validation, we ran simulations to narrow down a range of velocities that would achieve sufficient compression of the sample to at least 0.4 strain. Since the 100 *g* mass would require very large drop heights to achieve the velocities needed, experiments were performed with the 200 *g* mass. The 200 *g* mass also gave more repeatable impact velocities for a given height.

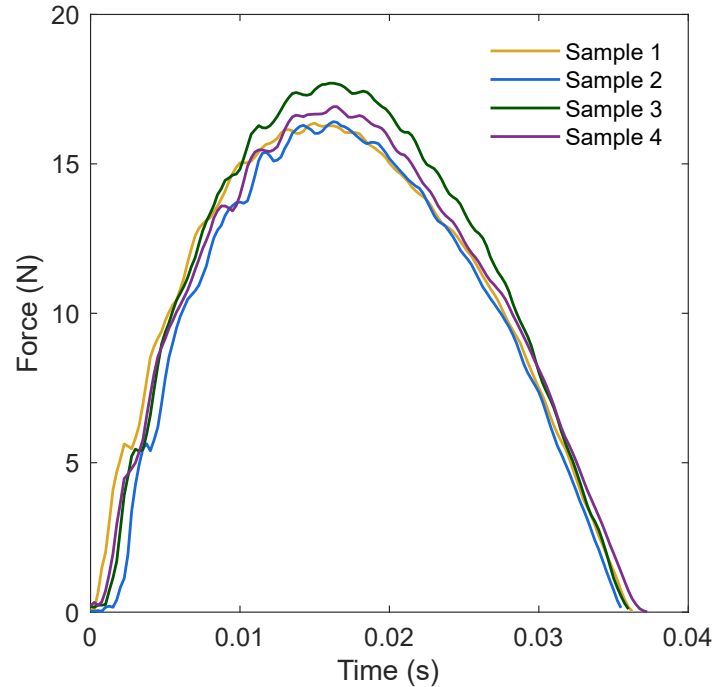


Figure 5.2: Force-time curves for the four baseline unit cell samples at an impact velocity of 1.15 m/s , corresponding to an impact energy ratio, E_i/E_m , of 0.4. This shows the variance in the sample responses due to manufacturing differences.

The four samples were impacted with a 200 g mass three times at each impact velocity. The impact velocity corresponds to an impact energy (E_i), which is a fraction of the maximum strain energy of the structure (E_m) before densification (320 mJ). The impact energy is given by the kinetic energy of the falling mass:

$$E_i = \frac{1}{2} m_i v_i^2 \quad (5.1)$$

where m_i is the impacting mass and v_i is the impacting velocity.

To illustrate the variation in the 4 samples for a given velocity, the force-time curves for an impact velocity of 1.15 m/s (E_i/E_m of 0.4) is shown in Figure 5.2. The samples give comparable results, with some variation in peak force and impact duration. Sample 3 is the stiffest, achieving the highest force during impact. Wave speed shows a larger variance between samples. There is a short lag time before the force increases from zero; this is the transmission time for the wave to travel through the structure, and thus it determines the wave speed.

For the experiments, the lag time is determined by the time between when the mass touches the structure and when the force sensor reading begins to increase. The time when the mass touches the structure is a bit ambiguous due to significant

Impact Speed	0.8	1.05	1.4
Sample 1	45.1	40.3	48.3
Sample 2	48.3	38.6	50.5
Sample 3	40.6	56.4	45.1
Sample 4	42.9	45.1	43.5
Average Wave Speed	44.2	44.4	47.1
Standard Deviation	9.2	9.1	7.2

Table 5.1: Wave speed measurements for each sample from baseline unit cell drop weight tests. For each sample and impact speed, the average wave speed from 3 tests is given. The wave speeds are averaged for all samples at each impact speed, and the standard deviation of the values is given. All units are m/s .

noise in the accelerometer data. This noise, combined with the short distance to travel and short lag time, make the wave speed difficult to accurately report for single unit cells. Average wave speed measurements for the 4 samples at selected impact speeds are shown in Table 5.1. The standard deviation of the measurements for each impact speed is also given. From this, we see that the spread of values is significant.

We also see in Table 5.1 the interesting result that the wave speed does not clearly increase or decrease with increasing impact speed. This is explained by considering the duration of the impact. For these drop weight tests, the impacting mass is very large (58 times more than the structure), and the impacting velocity subsequently low. Because of this, the impacting pulse is a long-duration pulse, lasting the entire time span of the compression of the sample.

To illustrate this, the result of a test on Sample 3 at an impact velocity of 0.8 m/s is shown in Figure 5.3(a). The applied force as derived from the accelerometer data is shown by the dashed-dotted line, and the transmitted force as measured by the force sensor on the bottom of the structure is shown by the solid line. We can see that the impacting pulse lasts for the duration of sample compression. Because of this, the applied force is approximately the same as the transmitted force, by conservation of momentum. The Fourier transform of the applied force signal is shown in Figure 5.3(b). Because of the long-duration, low amplitude pulse, the pulse contains predominantly a small range of very low frequencies below 100 Hz . Since the frequency components of the signal are below 100 Hz , they all travel without dispersion in the linear region of the longitudinal mode of the dispersion curve. As such, the wave speed remains consistent for a wide range of impacting velocities due to the long-duration pulse. This is the case for the baseline unit cell

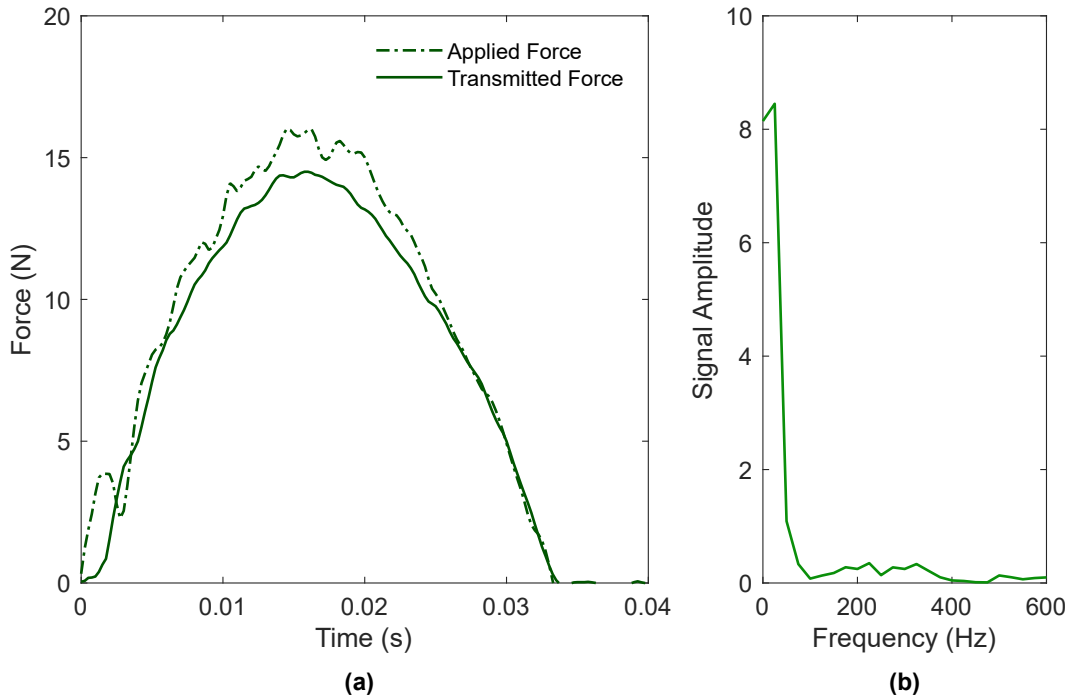


Figure 5.3: An experimental result for Sample 3 at an impact velocity of 0.8 m/s , corresponding to an impact energy ratio, E_i/E_m , of 0.18. (a) The applied force on the top of unit cell derived from accelerometer measurements is shown by the dashed-dotted line, and transmitted force measured by the force sensor on the bottom of the unit cell is shown by the solid line. (b) The discrete Fourier transform of the applied force.

experiments as well as the 1D lattice experiments with the long-duration pulse. The wave speeds found in Table 5.1 are also consistent with the wave speed of 40 m/s from the dispersion curve.

ABAQUS dynamic implicit simulations were performed to complement the experiments. Also, validation of the dynamic simulations allows them to be used in studying the behavior of higher dimensional lattices with different loading cases. First, we compared the results of the beam element and the 3D stress tetrahedral element ABAQUS models. Figure 5.4 shows the result of each simulation for a 0.8 m/s impact. The responses differ slightly, most markedly in the amplitude of oscillation. Inertial effects come into play in the dynamic case. The spherical joints are modeled as rigid beam elements with the same moment of inertia as the spheres, but there will be some differences inherent by the contrasting modeling methods. This likely plays a role in the amplitude of oscillation of the response. Also, the impact time is shorter for the beam element simulation. As seen in Chapter 3, the

beam element model is slightly stiffer than the 3D tetrahedral element model, so the shorter impact time is expected.

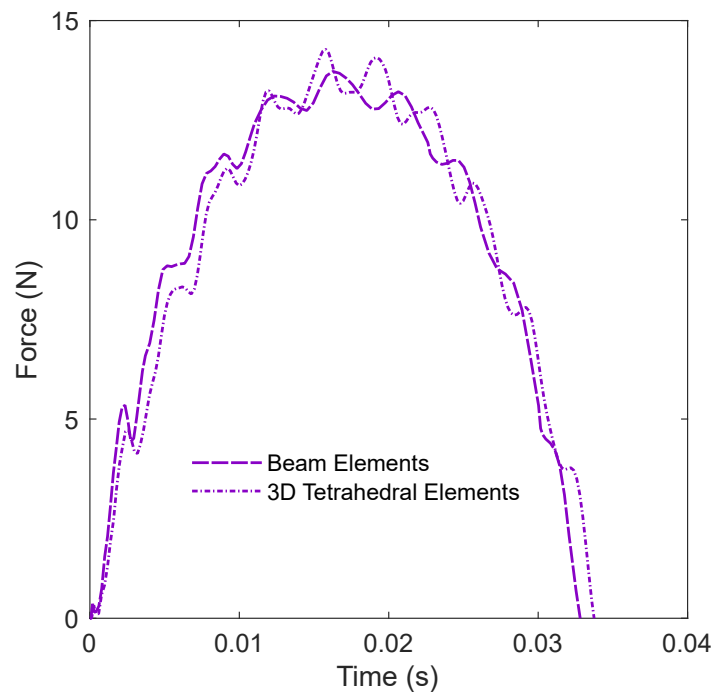


Figure 5.4: Beam element and 3D tetrahedral element ABAQUS dynamic implicit simulation results, which show the force-time response on the bottom of the structure for an impact velocity of 0.8 m/s ($E_i/E_m = 0.18$). The lag time, the time for the wave to pass through the structure initially, is the same for both simulations.

The lag time is the same for both simulations, with a corresponding wave speed of 78 m/s . During the first wave transmission, the structure has not had time to deform significantly, and as such, the structure's density and initial linear elasticity generate the wave speed. Also, the numerical initial conditions possibly influence the numerical wave speed; this and dissipation in the experiments likely account for the higher wave speeds for the numerics. Since these characteristics are the same for both simulations, it makes sense that the tetrahedral elements and beam element simulations show the same lag time.

The beam element simulation produces results in significantly less runtime than the 3D tetrahedral element simulation. Since the results for both simulations, both quasistatic and dynamic, are comparable, all dynamic simulations are performed using beam elements moving forward. This allows straightforward and computationally feasible numerical modeling of multidimensional lattices.

Next, we examine the evolution of the force-time response with increasing impact energy. The force-time results (at the bottom of the unit cell) for experiments on Sample 4 and ABAQUS simulations at four impact energies are shown in Figure 5.5. ABAQUS beam element dynamic implicit simulation results are given by the dashed lines and the experimental results are given by the solid lines. For the sake of visual clarity due to differences in lag time, we set $t = 0$ to when the force begins to increase for each curve.

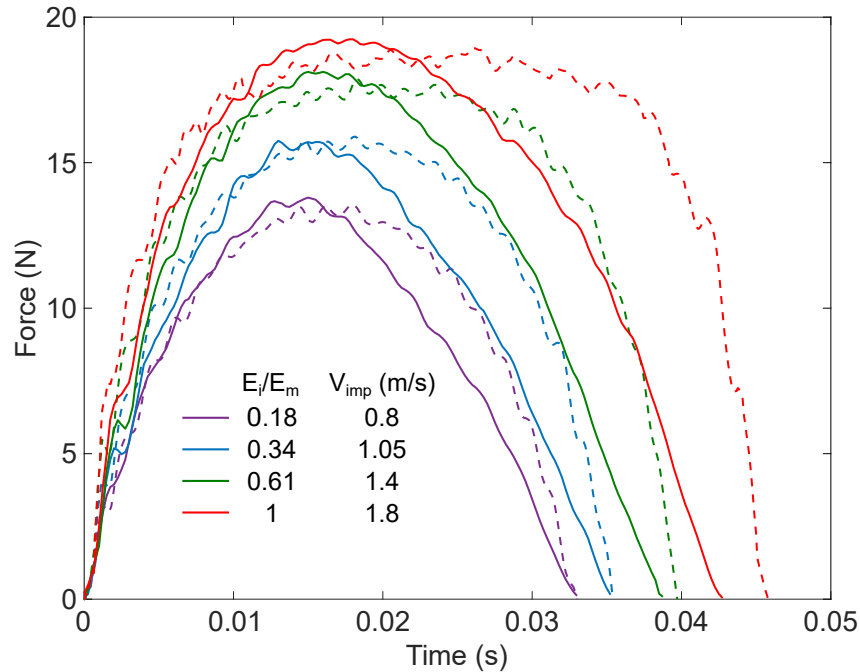


Figure 5.5: The force-time response of the structure (Sample 4) at varying impact energies, as a ratio of the impact energy to the maximum strain energy of the structure before densification. Impacting velocities are also shown, corresponding to the impact energy ratios. The solid lines are experimental curves and the dashed lines are results of the ABAQUS beam element simulation. The force plateaus to the structure's buckling force as the impact energy increases.

There are oscillations in the force response, both during loading and unloading, but more distinct during loading. These oscillations are due to the stress wave travelling back and forth within the structure, vibration of the struts, and rotation of the structure's faces during compression. Videos of the experiments show that the structure's top and bottom faces do not smoothly rotate with time, but rotate in distinct stages, contributing to oscillations in the reaction force.

At the lower impact energies, the structure does not compress enough to enter the buckling region, so the response does not plateau from buckling. At higher

impact energies, most noticeably at an impact energy ratio of 1, there is a significant plateau in the force response, as the strain approaches over 40%. The structure's dynamic response thus exhibits load-limiting: the maximum forces do not exceed the buckling load of the structure (about 18.6 N).

In general, the simulation and experiments agree favorably, showing similar behaviors, such as impact duration and maximum forces. However, there are differences between the simulations and experiments in Figure 5.5. The curves match well during the loading phase, but during unloading the experimental curves drop quickly while the simulation curves mirror their loading phase. In the experiments, energy is dissipated due to internal friction (hysteresis). Due to this, the response is less oscillatory, and the unloading curve loses energy. We examine the loss of energy in the experiments later in this section. The beam element simulation in ABAQUS does not consider hysteresis or plasticity in the material, so the loading and unloading sections do not differ significantly. Thus, the plateau is more readily observed in the simulation. We do not apply hysteresis in the simulation because hysteresis is not implementable with beam elements within ABAQUS. Addition of the hysteresis term would be possible with the full 3D stress simulation. However, beam elements are required for lattice simulations, where the model size would become significantly larger, and full 3D stress simulations would become impractical. Although the simulations are a good representation of the response of the structure, we recognize that experiments are necessary in order to obtain behavior that the simulation cannot provide. Also, it is valuable to note that experimental samples can vary significantly, so a comparison of several samples with the numerical results is important.

Before comparing the results of samples at increasing impact energy, first we examine how the quasistatically equivalent pin-jointed structure compares in the dynamic regime. We found the dynamic response of the pin-jointed structure using the approach developed in [23]. The results of the pin-jointed tensegrity simulation for two impact energies are shown in Figure 5.6(a) in dotted lines, along with the ABAQUS beam element simulation results in dashed lines. We can see that the pin-jointed response agrees favorably with the spherically-jointed structure response. They correspond very well at the low impact energy, when the structures' stiffnesses are linear. However, at the high impact energy, the pin-jointed response has a slightly higher force and shorter impact time than the ABAQUS simulation. Overall, the structures behave similarly with nonlinearity due to buckling in the struts, and they

both exhibit load limitation.

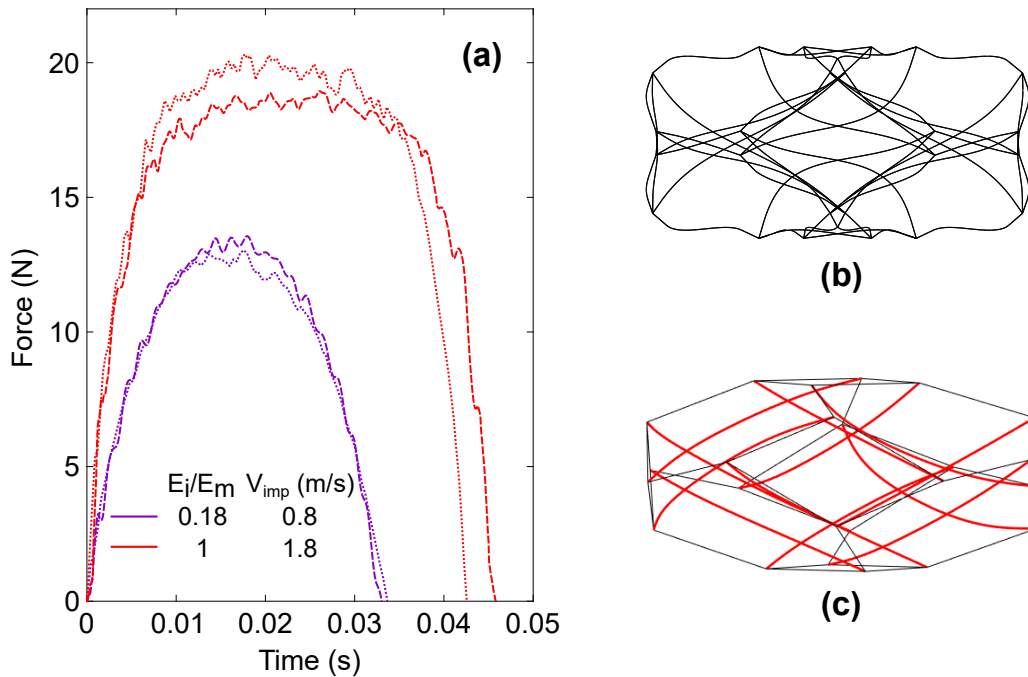


Figure 5.6: Dynamic results of the quasistatically equivalent pin-jointed baseline unit cell and the beam element simulation of the spherically-jointed structure. (a) Comparison of the pin-jointed structure simulation (dotted lines) and the spherically-jointed ABAQUS beam element simulation (dashed lines) for two impact energies. (b) Deformation of the structure from the beam element simulation at maximum compression during a 1.8 m/s impact. (c) Deformation of the structure from the pin-jointed simulation at maximum compression during a 1.8 m/s impact.

It is fascinating that the pin-jointed and spherically-jointed structures behave similarly even in the dynamic regime. Figure 5.6(b) and (c) show the shape of the deformation at maximum compression during the 1.8 m/s impact for the beam element and pin-jointed simulations, respectively. It is clear that the struts bend significantly in both cases, but the entire structure is bending dominated in the beam element case. Also, the spherically-jointed structure has significant inertia contributions at the nodes due to the spheres, which do not exist in the pin-jointed case. Aside from the difference in deformation mechanisms, the lower maximum force (and longer impact time) for the 1.8 m/s impact of the beam element case could be partly due to the added inertia from the spheres. The similarity of the two structures again shows that our tensegrity-inspired structure is an easily manufacturable structure that exhibits the same unique and desirable characteristics of tensegrities.

Now we compare the results of the four experimental samples with increasing

impact energy. Figure 5.7 shows results of the 4 tested samples along with the ABAQUS and pin-jointed simulations. Each sample was tested 3 times at most impact energies, and the maximum force was recorded for each test. Error bars are shown for impact energies that were tested 3 times. The maximum force increases

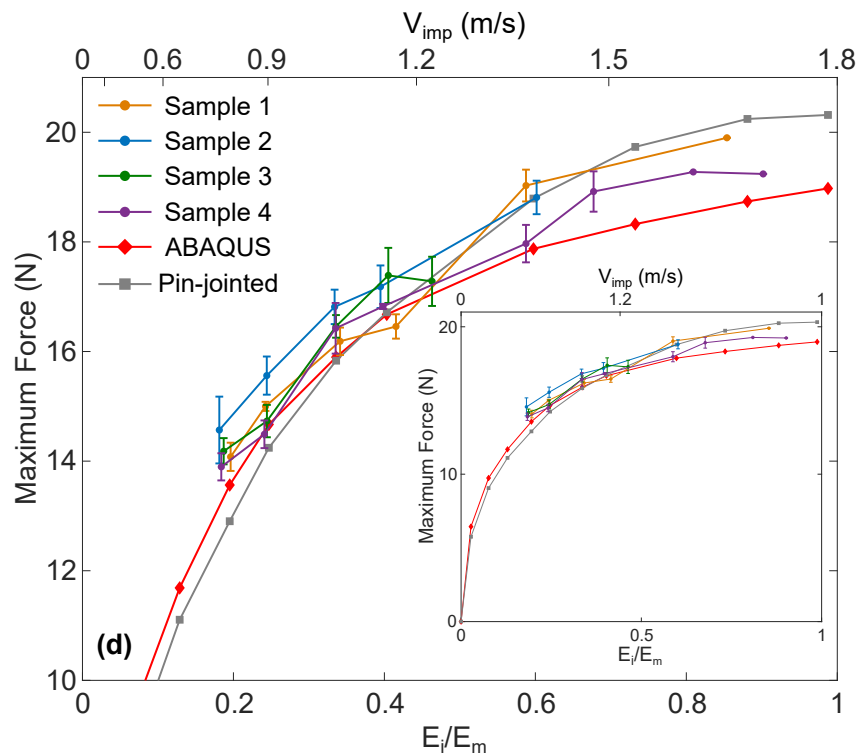


Figure 5.7: The maximum force exhibited by the tensegrity-inspired structure as a function of both the impact energy ratio and impacting velocity. The experimental results of 4 samples are shown with error bars. The ABAQUS beam element simulation results and the pin-jointed simulation results are also shown for comparison. In the inset plot, the force and impact energy ratio are given to the origin in order to observe the significant plateau of the maximum force. The plateau begins at energies well below the maximum energy capacity of the structure ($E_i/E_m = 1$).

with the impact energy ratio, but a distinct plateau is observed. The plateau is markedly seen in the inset plot, which shows the curves to an impact ratio of 0. This shows that the desired load-limiting characteristic not only is present, but is exhibited beginning at impact energies significantly lower than the maximum energy capacity of the structure ($E_i/E_m = 1$). Also, the experimental results for all 4 samples agree favorably with the simulation results. Variation between the samples is acceptable. This plateau behavior is analogous to the behavior of the maximum force with impact energy for the pin-jointed buckling tensegrity structure described in [23].

Analysis of Energy Loss During Impact

Next, it is important to consider energy loss during impact of the baseline unit cell. In Figure 5.8, the experimental global longitudinal stress-strain curves for varying impact energy ratios are shown. E_d is the dissipated energy as a percentage of the impact energy, and is the area within the stress-strain curve loop. If there was no dissipation during impact, for example, the loading and unloading curves would be identical, and the stress-strain loop area would be zero. It is clear that energy dissipation is substantial even at low impact energies. This dissipation could be due to factors such as internal friction (hysteresis), plastic deformation, and friction/damping in the test setup.

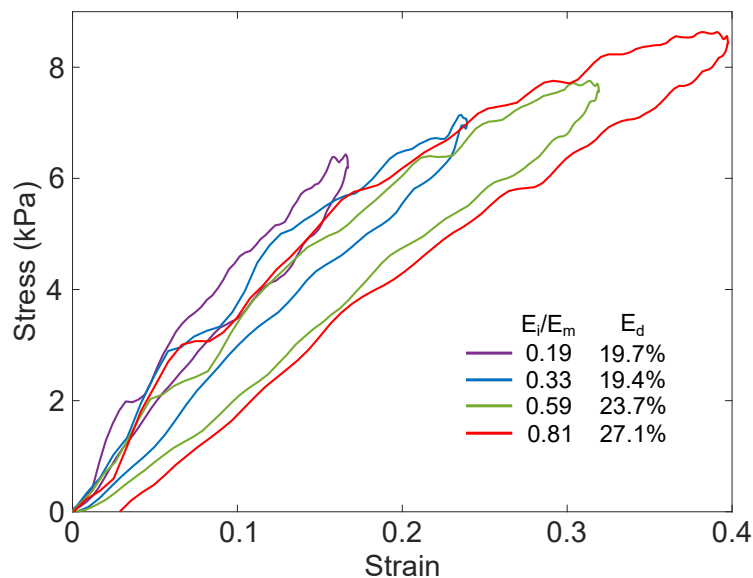


Figure 5.8: Experimental dynamic stress-strain curve during impact of the test structure (Sample 4). Stress and strain here are the effective global stress and strain in the direction of vertical impact. The energy dissipated as a percentage of the impact energy is listed for each impact energy ratio.

By comparing the loss of momentum in experiments with two different impacting masses, we can evaluate the effect of the test setup in energy loss. The same impacting momentum can be achieved with different impacting masses by appropriately changing the impacting velocity, as given by the equation:

$$p_i = m_i v_i \quad (5.2)$$

where m_i is the impacting mass and v_i is the impacting momentum. We ran several experiments keeping both momentum and energy constant for two impacting masses.

An example is shown in Figure 5.9. In this case, impacting momentum is held constant at $0.23Ns$. The force-time curves for Sample 3 for the 100 g and 200 g masses are shown. The area under this curve gives the total momentum absorbed during impact. For no dissipation, the area under the curve would be $2p_i$. For the 100 g mass, the absorbed momentum is $0.386Ns$, and for the 200 g mass, it is $0.376Ns$, for a percent difference of 2.6%. Both cases dissipate about 17% of the momentum from the impact. Because two masses are used, forces such as friction and drag inherently differ between the two tests. However, these forces appear to be negligible, since momentum absorption is approximately the same for both masses. We found this behavior to be consistent for other samples and impacting energies as well. The agreement between the two experiments indicate that the test setup does not contribute significantly to energy loss during impact.

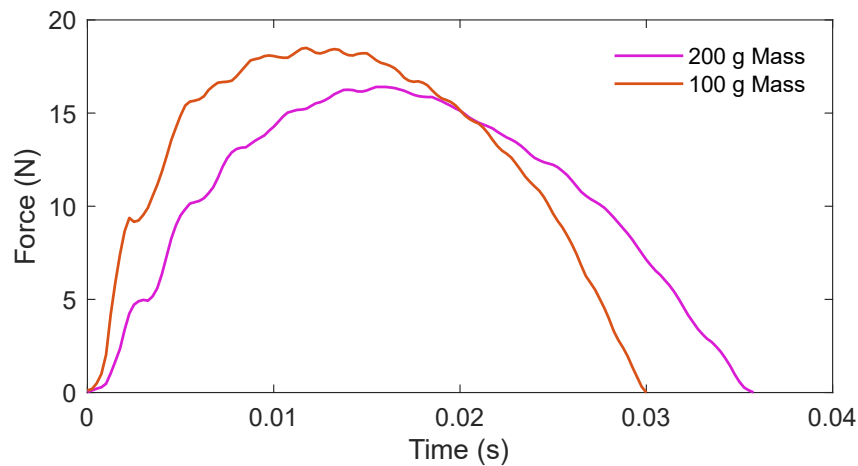


Figure 5.9: To evaluate the effect of the test setup on energy loss, the force-time results of two experiments with a constant impacting momentum of $0.23Ns$ are given. The area under the curves gives the total momentum absorbed during impact.

Another possible source of energy loss is plastic deformation. For repeated impact applications, one desirable characteristic of tensegrity structures is that they remain elastic even under high deformations. Since an objective for our tensegrity-inspired structure is to be reusable even under high deformation, plastic deformation should be kept to a minimum. As seen in Figure 5.8, for the lower three impact energies, strain after unloading is effectively zero. For $E_i/E_m = 0.81$, there is about 3% remaining strain, but this is immediately after the mass separates from the structure. When the remaining strain is measured one minute later, the remaining strain is significantly less than 1%. This lag in strain is due to the material's viscoelasticity.

In Table 5.2, the remaining strain after 24 impacts and after each impact for a wide

	Total After 24 Impacts	Average After Each Impact
Sample 1	1.76%	0.06%
Sample 2	1.66%	0.11%
Sample 3	3.18%	0.15%
Sample 4	2.52%	0.11%
Average	2.28%	0.11%

Table 5.2: The total remaining strain after 24 impacts for each sample, and the average remaining strain after each impact. The structure undergoes little plastic deformation, even after many impacts, showing the resilience and reusability of the structure.

variety of impact energies is shown for the four samples. After each impact, the remaining strain averages less than 0.2%, showing very little plastic deformation. Even after 24 impacts, the remaining strain is, on average, 2.28%. This shows that the structure is reusable and quite resilient to repeated loading, even at increasing impact energies. As an illustration of the elasticity of the structure, a series of images from a drop weight test with an E_i/E_m of 1 is shown in Figure 5.10. The 5 images are taken at increasing times up to t_{imp} , which is the total time of impact. The structure compresses to about 0.5 strain at the time of maximum compression ($t = 0.5t_{imp}$). At t_{imp} , when the mass separates from the structure, the structure very nearly recovers its initial height. As described in Chapter 3, rotation of the faces with compression, constant cross section in the members, elastic buckling in the struts, and the slender beams produce low local strains in the structure. We have shown that this property translates into the dynamic regime, giving our tensegrity-inspired structure the unique capability of remaining elastic under high and repeated dynamic deformation.

The structure maintains the tensegrity characteristic of an elastic response under high deformation. Because there is little plastic deformation, the dissipated energy during the impact is almost entirely due to hysteresis in the material. This indicates that for materials with different viscoelasticity and hysteric properties, energy dissipation could be significantly reduced.

Energy Absorption Comparison

Although the designed spherically-jointed structure has not been optimized for energy absorption performance, a comparison of its energy performance with several

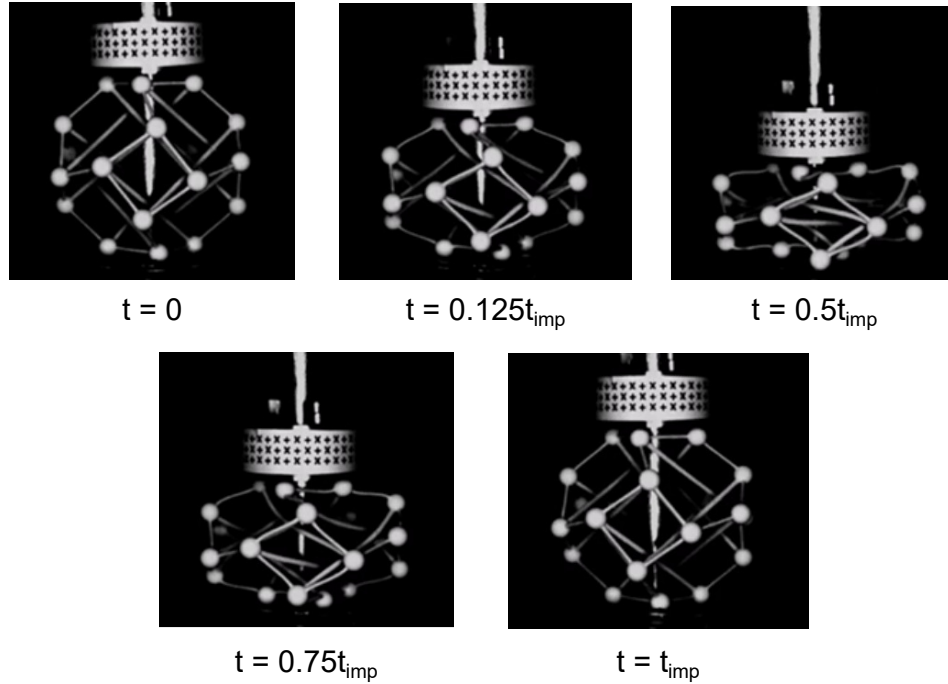


Figure 5.10: A series of images from a drop weight test with an E_i/E_m of 1. The images are shown at increasing times, from 0 to t_{imp} , which is the total impact time of the structure. The initial height of the structure is nearly recovered after impact.

types of manufacturable lattice materials is useful. This comparison is shown in Figure 5.11. Here, the energy absorption efficiency, W_{min} , is defined as [40]:

$$W_{min} = C_{min} \rho_r \quad (5.3)$$

where ρ_r is the relative density and C_{min} is the minimum cushion factor. The minimum cushion factor is given by [40]:

$$C_{min} = \frac{\sigma}{Q} \quad (5.4)$$

where σ is the maximum stress of the material's stress strain-curve until failure (e.g., densification, yield, or rupture), and Q is the area under the stress-strain curve up to σ . The minimum value of the cushion factor, C_{min} , represents the maximum impact absorption efficiency of the material, and theoretical limit of C_{min} for a material is 1. Cushion factor (or its inverse) is often used to assess the energy absorption of porous materials, such as lattices [138–141]. W_{min} is also a useful quantity because, like C_{min} , a design with lower W_{min} indicates better energy absorption. For instance, if two materials have the same C_{min} and one has a lower W_{min} , the material with lower W_{min} absorbs the same energy at a given stress, but uses less material. This means that it offers the lowest mass for equivalent impact absorption.

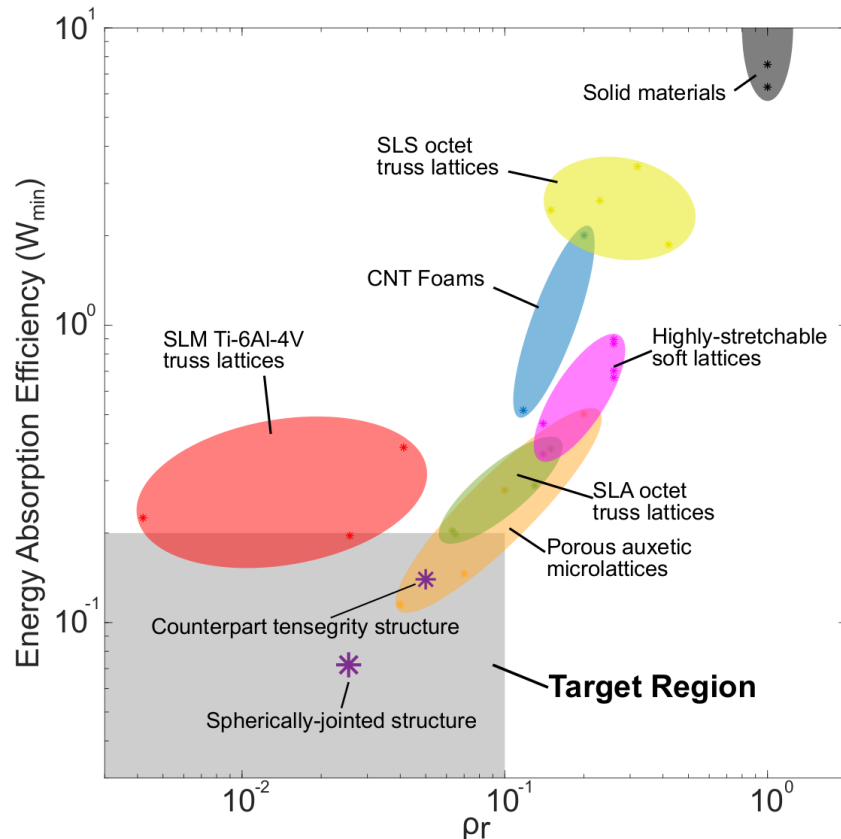


Figure 5.11: Energy absorption efficiency (W_{min}) by relative density for the spherically-jointed structure and counterpart pin-jointed structure, as well as for several lattice, foam, and solid materials. The energy absorption efficiency is given by the cushion factor multiplied by the relative density of the material. The target region is defined by a W_{min} less than 0.21 and relative density less than 0.1 (reasons explained in the text). Solid materials all have a relative density of 1 and their W_{min} extend well beyond the range of this plot, as indicated by the truncated gray oval. The structures presented in this work lie within the target region, with the spherically-jointed structure exhibiting the best energy absorption efficiency of all presented materials, along with a very low relative density. The lattice, foam, and solid material data was obtained from the following sources: solid materials [40], CNT Foams [40], porous auxetic microlattices [40], SLS octet truss lattices [142], highly-stretchable soft lattices [138], SLA octet truss lattices [139], SLM Ti-6Al-4V truss lattices [143].

In Figure 5.11, we plot W_{min} against relative density for several lattices, foams, and solid materials. We define a target region, which is given by a relative density lower than 0.1 and a W_{min} lower than 0.21. This is chosen for the following reasons. Often, non-metal lattices require higher relative densities due to manufacturing constraints and thus commonly have relative densities above 10%. Also, the best

available lattice foams have C_{min} values as low as 2.1 [40]. Multiplying C_{min} of 2.1 by a relative density of 0.1 gives a target region limit of $W_{min} = 0.21$. For both our spherically-jointed structure and the counterpart pin-jointed structure, $C_{min} = 2.82$. For the spherically-jointed structure, $W_{min} = 0.07$, and for the pin-jointed structure, $W_{min} = 0.14$. Thus, the structures in this work lie within the target region, exhibiting remarkable energy efficiency and very low relative densities for polymer structures. Interestingly, the spherically-jointed structure exhibits the lowest W_{min} of all shown structures and the lowest polymer relative density, even compared to its counterpart pin-jointed tensegrity structure.

Also, several of the other lattices in Figure 5.11 do not elastically deform under impact, but plastically deform, making them non-reusable. The structures designed in this work elastically deform and are reusable under multiple impacts. This shows that, even without optimization of energy absorption, our design shows novel characteristics, making it promising for use in ultra-lightweight, energy absorbing metamaterials.

5.2.2 1D Lattices

Baseline unit cell tests provided insight into the basic dynamic behavior of the tensegrity-inspired structure. They also showed how variability in 3D-printing and the chosen material affect the structure's response in experiments. These studies showed the promise of the unit cell as a building block for unique energy absorbing metamaterials with very low mass. Next, we examine the response of 1D lattices under long-duration drop weight impact. We choose a lattice with 5 baseline cells. More cells would have made achieving sufficient compression of the sample difficult, and 5-cell lattices were readily fabricated. Longer chains of cells would not have provided significantly more information on the impact characteristics for a long-duration pulse. For short-duration pulses where force reduction through the lattice is a consideration, we examine longer strings of unit cells later in this chapter.

This section will demonstrate how the characteristics observed in the baseline cell translate to 1D lattices. In addition, we will begin to understand how elastic waves propagate in these lattices.

Force Response

We fabricated 1D lattices using 5 baseline unit cells, each with a height of 48.3 mm, producing a nominal total height of 24.15 cm. As expected, we found significant

variation in the samples. Member diameters varied significantly between samples and within each lattice. Also, because the lattices are larger and have more members than the baseline unit cells, most samples had visible defects, such as pre-bent struts, elongated unit cells, and broken members. Again, we chose a sample for experiments that had member diameter measurements within 4% of the nominal member diameters. However, every sample showed visible defects; the chosen sample had the least defects of the printed samples, but still had pre-bent cables and struts.

Using the same drop weight testing system used for the baseline unit cells, we performed drop weight tests on the sample with the 200 g mass at varying impact velocities, with 3 tests at each velocity to ensure repeatability. To present the repeatability of the tests, Figure 5.12 shows the results of the three tests performed on the lattice at an impact velocity of about 0.7 m/s. The force given is the force measured by the force sensor on the bottom of the lattice, and the transmission lag time is zeroed out. The experiment is extremely repeatable. The impact velocity, impact time, slopes, oscillations, etc. are strikingly similar between experiments. This again indicates the reusability of the structure.

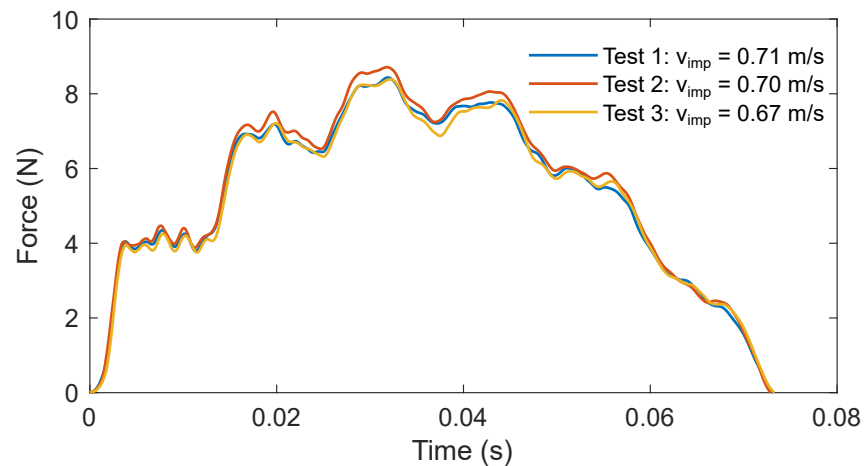


Figure 5.12: The reaction force measured by the force sensor from three experimental tests on the lattice structure with the impacting mass falling from the same drop height. The transmission time is zeroed out. The impacting velocity for each test is shown in the legend. The results agree considerably, showing high repeatability for the experiments.

Figure 5.13 shows the force-time response at the bottom of the lattice at various impacting velocities for both simulation and experiment. The transmission time is zeroed out for visual clarity due to differences in wave speed. A discussion of

wave speeds will be given later in this section on 1D long-duration impact. For the current purpose, we look at the behavior of the force response. Figure 5.13(a) shows the reaction force measured by the force sensor for 4 impacting velocities, Figure 5.13(b) shows the results of the simulation for 5 impacting velocities, and Figure 5.13(c) compares the results of the experiments and simulations for two impacting velocities.

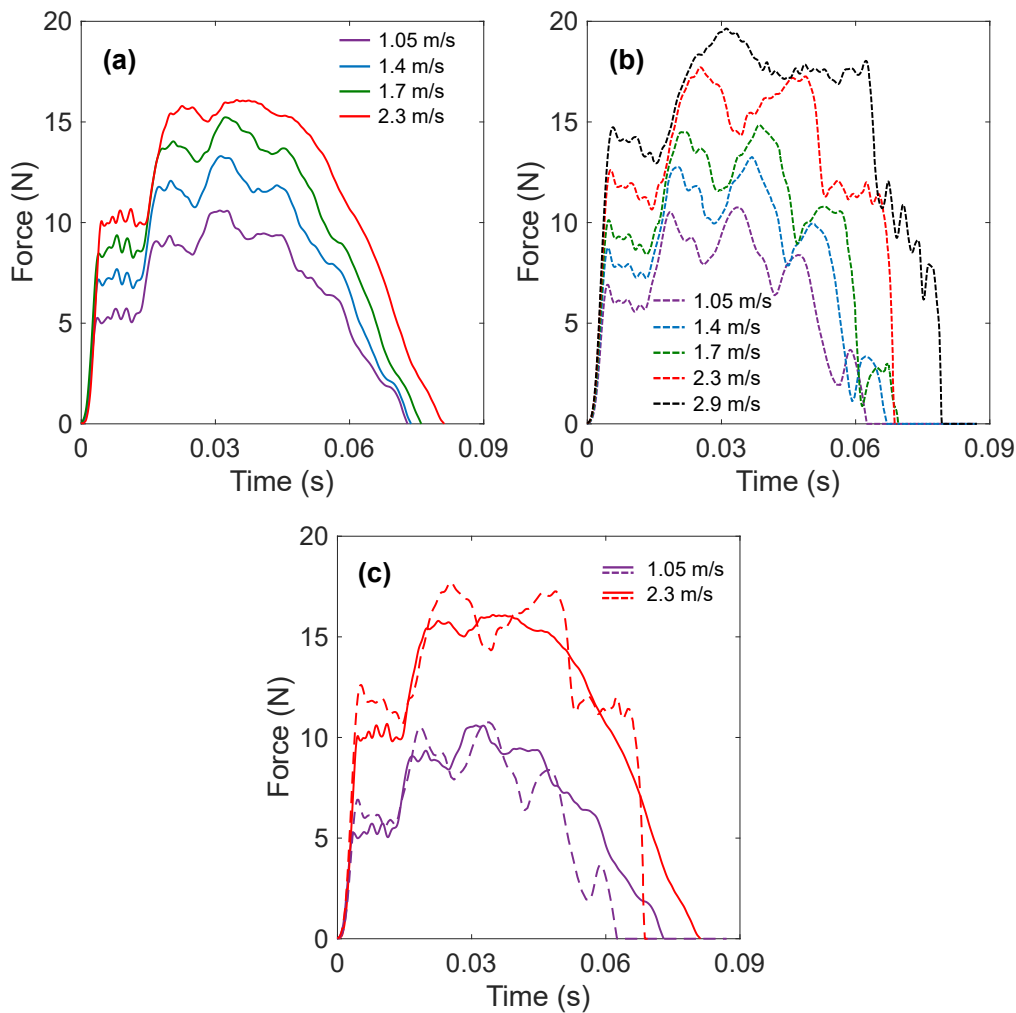


Figure 5.13: Reaction force of the rigid plate at the bottom of the lattice over time for several impacting velocities. (a) Experimental response for four impacting velocities. (b) ABAQUS beam element simulation results for five impacting velocities. The plateau in the force is seen clearly in the 2.9 m/s response. (c) Comparison of response of the numerical and experimental results for two impacting velocities.

We observe several key similarities between simulations and experiments. First, at each velocity, the initial rise in force from the first transmitted wave has the same slope. This is so consistent because the initial wave is linear and depends only on the

structure's initial stiffness and density. These tests are for a long-duration loading pulse with the same duration time as the compression of the lattice. Therefore, for the first wave transmission, there is only slight compression of the structure, which falls within the linear region of the force-displacement curve. As such, the structure itself has not deformed enough for variations due to hysteresis, modeling assumptions, etc. to produce significant differences between numerics and experiments. Second, there are "stages" apparent in the response, where a significant increase/decrease in force is followed by a plateau. This occurs several times during compression. By watching the videos of the experiments and simulations, it is clear why this occurs. We can see that the structure compresses sequentially, as waves travel back and forth through the lattice. Qualitatively, the unit cells seem to successively compress to a relatively constant level, but the large impacting mass then initiates another compressive pulse, causing the cycle to repeat. This behavior clearly translates into the force response. The "rise and plateau" behavior appears to be characteristic of long-duration drop weight experiments on periodic crystals [144].

Since the force capacity of each unit cell is the structure's buckling load, the forces are all below this value (around 18.6 N). We see the behavior of load limitation in the lattice, just like was observed for the unit cell. We begin to see this in the experiment in the 2.3 m/s test; the maximum compression plateau begins to spread out over time, without a clear peak like in the 1.7 m/s test. We see the force plateau most markedly in the simulation 2.9 m/s response. The maximum peak spreads out over time. The third peak disappears entirely, and instead plateaus to just under the buckling load for a span of 21.4 ms , which is over 25% of the total impact time. These results indicate that no matter the size or length of one of these tensegrity-inspired lattices, the maximum reaction force will always be less than the force capacity (buckling load) of the bottom unit cells. This property will be important in reducing transmitted forces and mitigating waves in short-duration impulses.

We show the experimental force response up to 2.3 m/s , but show an additional impact velocity of 2.9 m/s for the simulation (Figure 5.13(b)). This is because the sample had already been tested 36 times at the 2.3 m/s impact shown, and in the 37th test, a cable in the sample broke. This cable had been visibly bent before the first test, so it was a weak location in the lattice. In order to show more clearly the load limitation characteristic, we ran another simulation at 2.9 m/s .

The experiments show the same type of difference between loading and unloading that was observed in the baseline unit cell in Figure 5.5. In Figure 5.13(a), we can

see a clear difference between loading and unloading. During unloading, the force drops at a relatively constant rate until the structure fully decompresses. This is due to energy loss during impact, which we examined for the baseline unit cell. This is a material response. In the simulations (Figure 5.13(b)), however, this energy loss does not occur, as internal friction is not accounted for. The marked difference in the experiment and simulation is seen in what can be attributed to this energy loss in the material. The simulated force is significantly more oscillatory. For each of the compression “rises and plateaus,” the simulation is more of a sequence of “peaks and valleys.” Without damping, an oscillatory response like this is expected. The final unloading at the end of the impact is also a sharp decrease, rather than a smooth slope to zero force. In Figure 5.13(c), we can clearly see these differences between numerics and experiment. The total impact time is longer for the experiments because of the smooth unloading characteristic. In general, the behavior agrees well between the experiments and simulations for various impact velocities.

Deformation Behavior and Wave Characteristics

Next, we investigate the deformation behavior of the lattice during compression. Recall the global compressive stress-strain behavior of the baseline unit cell from Chapter 3; the experimental curve is given again here in Figure 5.14. We can approximate two regions: a linear region from 0 to 0.15 strain, and a nonlinear/buckling region from 0.15 to 0.48 (densification) strain. Load limitation in the baseline unit cell and also in 1D lattices is due to sufficient deformation of the structure such that the nonlinear buckling region is reached. Considering the lattice as a chain of masses and springs, each unit cell effectively acts as a nonlinear spring, thus affecting the dispersion properties, wave speeds, and other wave propagation characteristics.

For long-duration impact, we see some interesting attributes of the deformation and how this linear to nonlinear/buckling affects the response. In Figure 5.15, we show the effective longitudinal strain of each unit cell in the lattice over time for various impacts. Figure 5.15(a) gives a picture of the lattice, with colored numbers referring to each of the five baseline unit cells. The falling mass impacts cell number 1. In the subsequent plots, the colored curves give the longitudinal strain of each of those unit cells. The result of a 1.05 m/s impact is given in (b)-(c), a 2.3 m/s impact in (d)-(e), and a 2.9 m/s impact in (f); (b) and (d) are experimental results, and (c), (e), and (f) are numerical results. We can see that for all impacts, the compression of each cell occurs in stages, just as we saw for the force response. During the

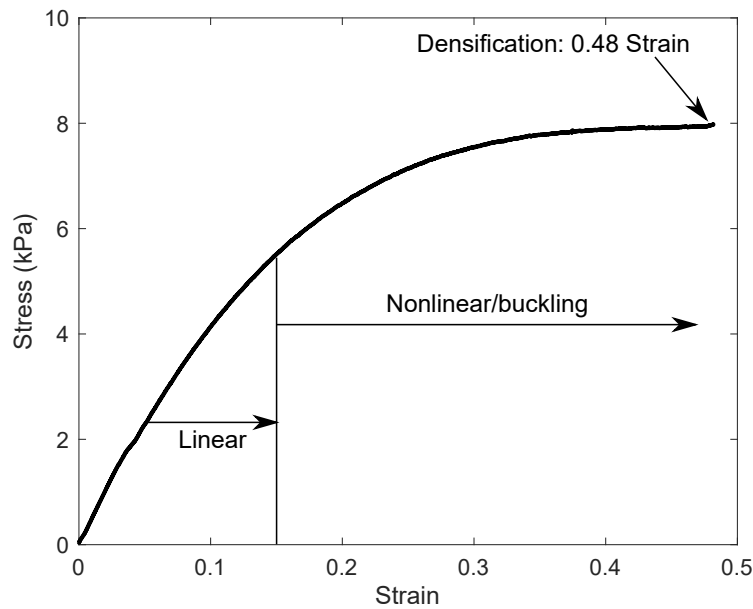


Figure 5.14: The global compressive stress-strain curve of the quasistatic compression experiment on the baseline unit cell. We identify two regions: a linear region from 0 to 0.15 strain, and a nonlinear/buckling region from 0.15 to 0.48 strain. Densification, where contact begins between the struts, occurs at 0.48 strain.

first transmitted wave (from 0 s to around 0.004 s), the cells only compress a small amount (about a fifth) of their total compression. The cells' deformations then increase and decrease in sequence, and are compressed during the entire impact time. The simulations have a shorter impact time than the experiments, as seen in the force response.

For the 1.05 m/s impact ((b) and (c)), the cells only compress to about 0.1 strain, which is in the linear region of Figure 5.14. As such, both simulation and experiment are oscillatory through the whole impact. Particularly in the numerical results, the wave response is very linear: the compression stages occur in equal time spans, for a total of 10 stages. With no damping, this consistency is expected. The experimental result has a less oscillatory response during unloading than loading, which is expected from energy loss in the material. Cell number 1 and cell number 5 compress the most for both simulation and experiment, which is consistent with the fact that they are the boundary cells. Both interface with a rigid surface, and when the wave reaches the boundary, the deformation is doubled compared to the previous cell due to conservation of momentum at the rigid wall. The intermediate cells have less oscillation.

For the 2.3 m/s impact ((d) and (e)), the cells compress much more, to about

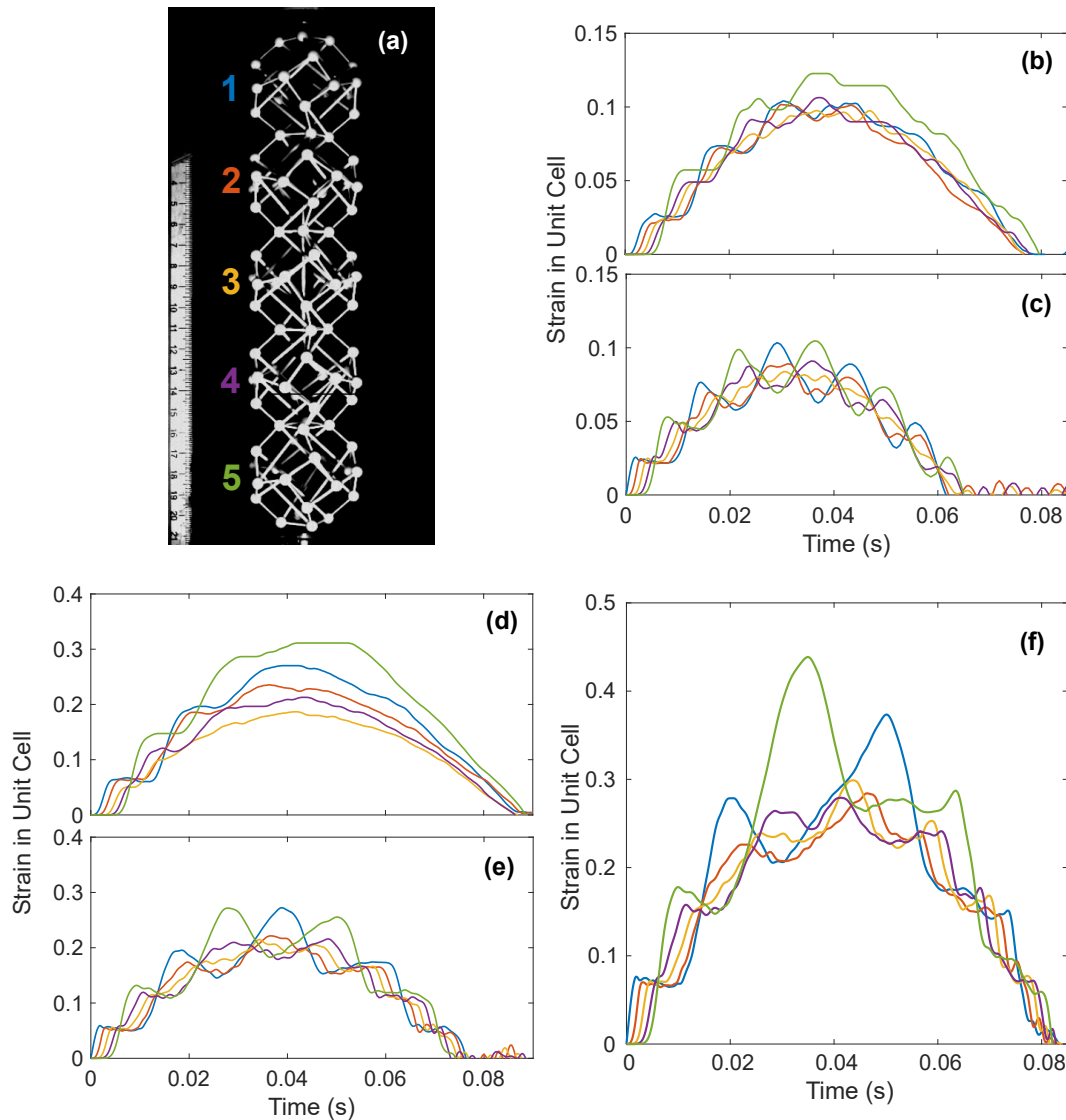


Figure 5.15: (a) The 5 unit cells in the lattice are labeled with colored numbers, with the color corresponding to its effective longitudinal strain-time curve in (b)-(f). The longitudinal strain of each unit cell over time for a 1.05 m/s impact is shown for experiment (b) and ABAQUS simulation (c). The strain of each unit cell over time for a 2.3 m/s impact is shown for experiment (d) and ABAQUS simulation (e). (f) The ABAQUS simulation result of unit cell strain over time for a 2.9 m/s impact.

0.3 strain, thus entering the nonlinear region in Figure 5.14. The response begins mostly linearly, but once the cells reach about 0.15 strain, we start seeing a marked difference from the 1.05 m/s impact. In the simulation, the compression waves begin to spread out more over time, reducing the slope amplitudes and reducing the number of stages (now only 9). This is most clearly seen in the intermediate cells. The boundary cells also show this; the slope of compression in cell number 5 from

0.04 s to 0.05 s is significantly spread. In the experiment (d), once the compression reaches about 0.15 strain, we see a total disappearance of the compression stages. The dispersion from hysteresis as well as the high levels of compression in the nonlinear region smooth out the response significantly, and all the cells compress smoothly together. Both experimental curves show slightly higher compression levels than the numerical curves. Also, cell number 3 compresses the least. Cell 3 had higher member diameters than the other cells, and so it was the stiffest of the cells. Thus, it does not compress as it would ideally. These differences in compression from the numerical simulations is due to deviations from the nominal geometry measurements in manufacturing. Some deviation is unavoidable.

For the 2.9 m/s impact numerical result (f), the compression levels go deep into the nonlinear region up to almost 0.45 strain. We see a drastic change in the response due to this. Again after 0.15 strain, the compression stages become less distinct and muddled. The boundary cells attain dramatic levels of compression. Looking at cell 5, there is a large peak in compression at about 0.035 s followed by a stark plateau lasting one quarter of the impact time. The intermediate cells also exhibit these flat plateaus over much of the impact time. The stages of compression become interwoven and wave speeds significantly affected due to dispersion from the nonlinear response in the unit cells.

Figure 5.16 shows snippets of the compression during impact for an experiment at 2.3 m/s impacting velocity. The red line was placed at the top nodes of the lattice at $t = 0$ and stretched across to $t = t_{imp}$. Remarkably, the lattice visibly recovers its original height entirely immediately at the end of impact. We saw again for these lattice experiments that the lattice had very low remaining strain (well under 1%) after each impact. After 24 impacts, the total remaining strain was only 1.1%. We tested this lattice 36 times. The resilience of the structure over multiple impacts is thus seen also in lattices as well as baseline unit cells. In each frame, we can see that the center cell does not compress as much as its neighboring cells, because it is the stiffest cell. This corroborates Figure 5.15(d). At $t = 0.25t_{imp}$, which is about 0.021 s , the top cell is compressed the most, as seen from Figure 5.15(d). After the time of maximum compression, the lattice smoothly uncompresses to $t = 0.25t_{imp}$. It is important to note that in these long-duration pulse experiments, we see very little vibration in the individual members of the unit cells. The impacting pulse contains only low frequencies as previously explained. In turn, higher frequency resonances within individual members are not excited in this regime. We will see later in this

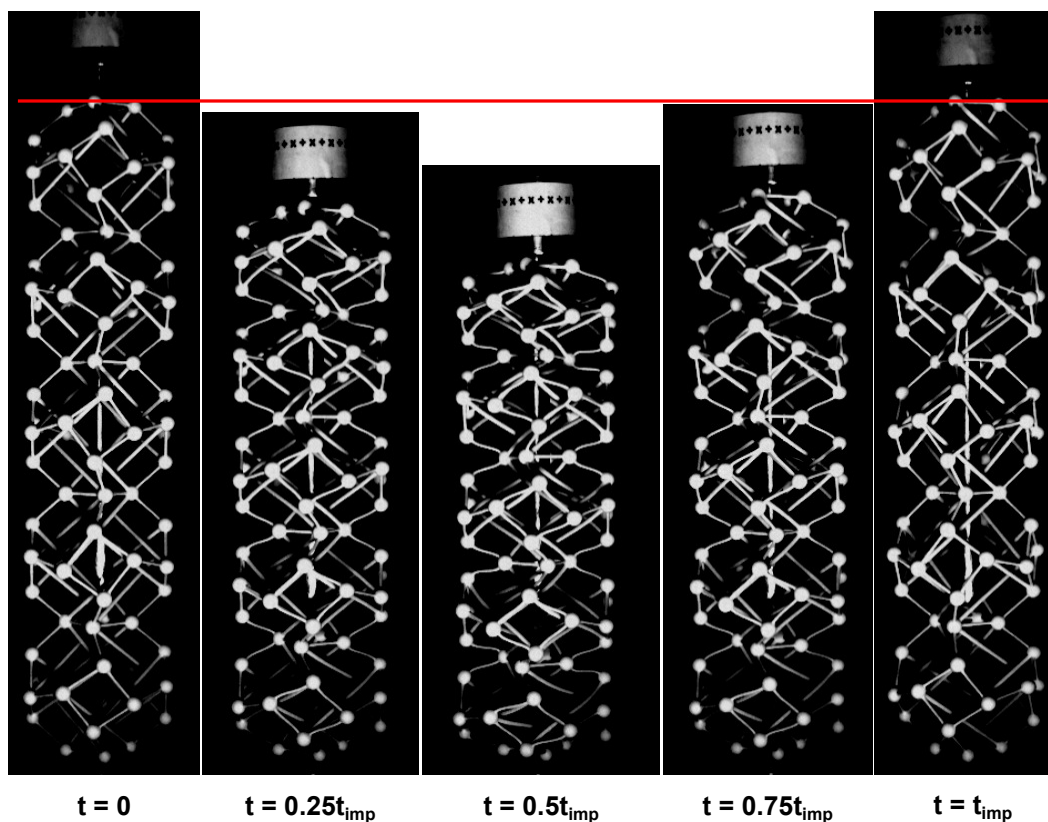


Figure 5.16: Frames from an experimental video of the lattice compression for a 2.3 m/s impact velocity. The frames are given at various stages of compression up to total impact time, $t = t_{imp}$. The red line is placed on the top nodes of the structure in the $t = 0$ image. The red line extends to $t = t_{imp}$, showing that the structure visibly fully recovers its original height after impact.

chapter how short-duration pulses excite vibration in the members. Vibration in the members is a mechanism to trap energy within the lattice, reducing accelerations, spreading pulses over time, and mitigating impact forces. This type of behavior is observed in [134].

Next, we look at the leading wave speeds for these tests. The accelerometer was not needed for these tests because finding the leading wave speed through the structure is much more straightforward with a lattice. The transmission time for the wave to traverse through the structure is longer than with the baseline unit cell. Also, we measure the displacement of the structure at 5 points: at the top of the structure, and at the nodes at each intersection point between unit cells. Because of this, we calculate the transmission time for the wave front as the time from when the top nodes of the lattice begin to move to when the top nodes of the bottom unit cell reach a velocity that is 1% of the impact velocity. We call this the “1% rule.” The

Impact Speed	Experiment Average	ABAQUS Simulation
0.75	58.0	72.6
1.05	54.7	70.9
1.4	51.1	71.1
1.7	51.7	72.2
2.3	53.1	70.8

Table 5.3: Leading wave speed measurements for 1D lattice long-duration impact experiments and simulations for multiple impact speeds. All values are in m/s . The experimental values are averaged for multiple tests at each impact speed. We calculate the transmission time for the wave front as the time from when the top nodes of the lattice begin to move to when the top nodes of the bottom unit cell reach a velocity that is 1% of the impact velocity.

wave speed is the length of four baseline unit cells divided by the transmission time. There are many different methods to define wave speed for impact experiments; this is a method used in [134]. It will be useful for the sample drop experiments where there is no reaction force measured at the free end of the structure.

The initial wave speeds from the experiments and simulations are shown in Table 5.3. We again see that the leading wave speeds are quite consistent with varying impact velocity, as expected for a long-duration impact pulse. The simulations have a higher wave speed than the experiments, as was seen with the baseline unit cell. The wave speed is about the same as that of the baseline unit cell ($73 m/s$). However, the experimental wave speeds are slightly higher than for the baseline unit cell, where the wave speed was about $45 m/s$. This difference could be due to a few things. The stiffness of the lattice is slightly higher than a single baseline cell simply because rotation of the faces at the intersections between cells is somewhat constrained. This leads to an increase in wave speed. Also, variations in manufacturing could easily affect the wave speed. We have seen that even in the lattice itself there is variation in stiffness. Finally, finding the wave speed from unit cell experiments was difficult due to the short distance traveled by the wave and a short transmission time. This combined with the noise in the accelerometer created high variance in wave speed between tests. The lattice wave speed is much more readily calculated and consistent.

Looking at the velocity propagation through the lattice gives insight into how the wave propagates and evolves with varying impact velocity. This is shown in Figure 5.17. Figure 5.17(a) shows where the velocity measurements are taken and are given

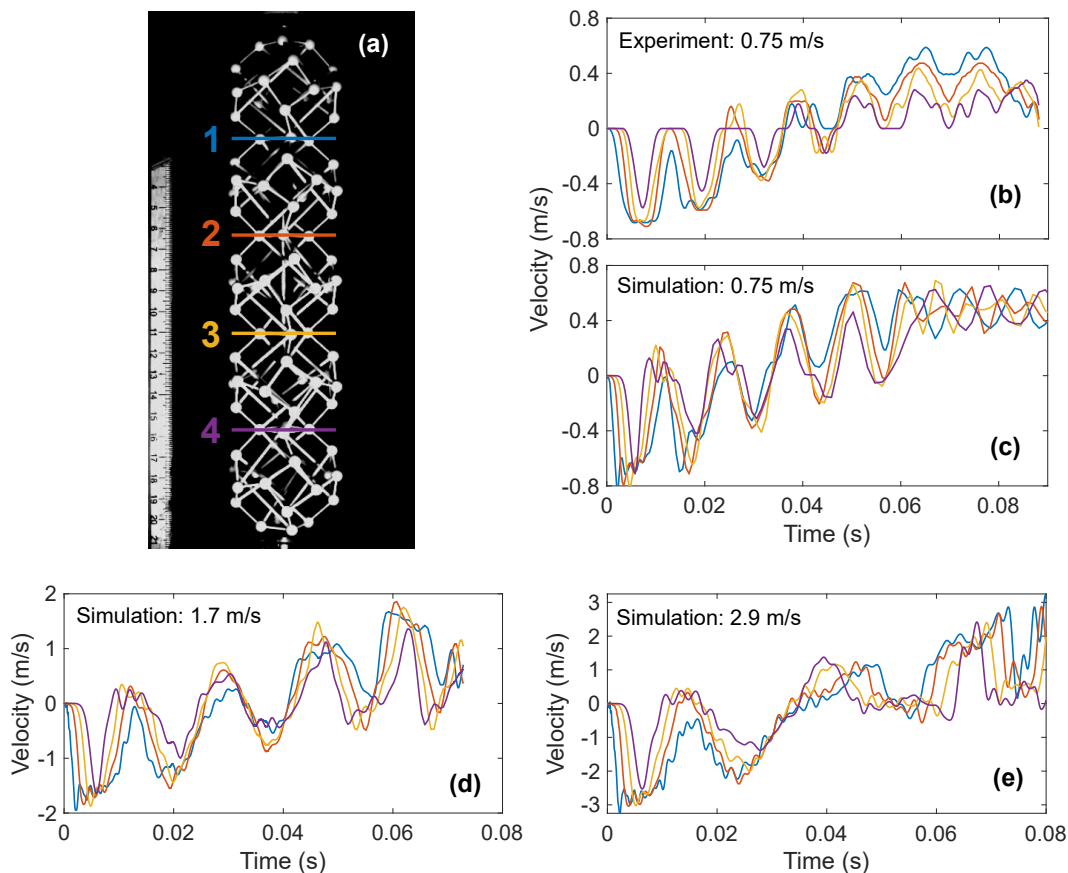


Figure 5.17: (a) An image of the lattice is given, with velocity measurement locations labeled by number and by color. The colors correspond to the appropriate curve in the plots. (b) Experimental velocity results at unit cell intersection points for an impact of 0.75 m/s . Numerical ABAQUS velocity results at unit cell intersection points for an impact of (c) 0.75 m/s , (d) 1.7 m/s , and (e) 2.9 m/s .

a color and a number. The top of the lattice is also measured, but it follows the same velocity path as the impacting mass, so it is not shown in the following plots for clarity. In Figure 5.17(b) and (c), the results for a 0.75 m/s impact are given. For the experiment, the maximum frame rate we could achieve was 3000 frames per second, so the resolution was not high enough to fully capture some of the peaks and valleys. The behavior can still be easily seen, however. Comparing (b) and (c), we can see that the behavior is in agreement between experiment and simulation. There are 5 clear valleys and 4 clear peaks occurring at approximately the same points. Again, the simulation is more oscillatory with higher amplitudes, including after release of the impacting mass (about 0.065 s). The individual cell compression levels are in the linear region of the displacement curve, so the velocity propagation is very linear. For both experiment and simulation, the wave speed remains constant

through the entire impact, as shown by the constant time lag between peaks and valleys.

To clearly show how the wave propagation changes with dramatically increasing deformation levels (and thus impacting velocity), we show two more results for the simulation in Figure 5.17(d) and (e). In (d), the maximum strain reached in the bottom unit cell is about 0.2. So, this is just entering the nonlinear region of the displacement curve. The initial wave speed is the same as for other impact velocities, but as time progresses, the wave speed slows. This is seen by the increasingly longer distances between successive valleys in the velocity. Other than this, the response remains mostly linear, with several significant peaks and valleys. However, at a high level of impacting velocity and thus cell compression (maximum of 0.45 strain), we see significant influence from the structure's nonlinearity. In Figure 5.17(e), the results for a 2.9 *m/s* impact are shown. Again, the initial wave speed is the same as for other velocities. However, when the cells compress to 0.15 strain and above (between 0.015 and 0.065 *s*, as seen in Figure 5.15(f)), the response does not resemble a linear response at all. The wave front dramatically widens and the sharp peaks and valleys disappear almost entirely. All the velocities smoothly increase together. The peak begins to appear again after 0.06 *s* because the compression levels are low, but it is significantly widened. The response becomes highly dispersive at high levels of compression.

5.3 Sample Drop Tests

In the previous sections, we observed several unique characteristics from long-duration impact analyses on our tensegrity-inspired structures. Load limitation, dispersive wave properties, resilience to increasing and repeated deformation, low wave speeds, high energy absorption for low mass, etc. are all attributes of these structures. For the subsequent impact studies, we enter a region of higher strain rates with higher frequency pulses. By doing this, we see how the structure's dynamic properties can reduce force transmission/accelerations and affect the transmission of energy through not only 1D, but also 3D lattices.

In this section, we show results of sample drop tests where a lattice sample is dropped from a height such that it impacts the ground at a certain velocity. This type of test is often used to show the ability of a lattice or material to mitigate forces from impact, such as to protect a fragile payload (e.g., an egg) [71, 145, 146]. Here, we extend beyond 1D lattices and perform tests on 1D, 3D1D, and bulk 3D lattices. The 1D and 3D1D lattices have 3 RVEs each, and the 3D bulk lattice is tessellated in all 3 dimensions such that it is $4 \times 4 \times 4$ RVEs (total of 512 baseline unit cells). Experiments were performed on the 1D and 3D1D lattices, but not the 3D bulk lattice.

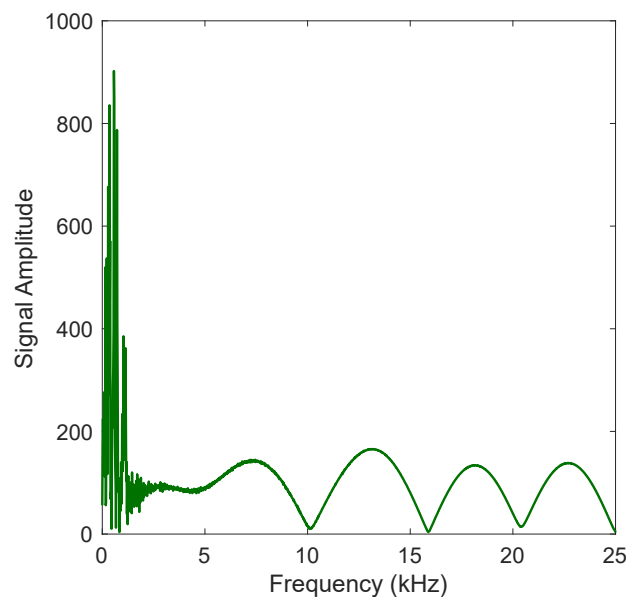


Figure 5.18: The discrete Fourier transform of the applied force pulse on the lattice's bottom nodes in a sample drop test of a 3D1D 3 RVE lattice.

Unlike the long-duration impacts for the drop weight tests, the impacting pulse for the sample drop experiments lasts for a small percentage of the total impact time

(less than 7%). Thus, frequencies contained in the impacting pulse varies greatly from what we saw for the long-duration impact in Figure 5.3(b). For the sample drop of a 3D1D lattice, a representative sample of the Fourier transform of the applied force signal is shown in Figure 5.18. Because the force signal is a high-amplitude, short-duration pulse, the pulse contains a large range of frequencies up to 25 kHz , and a very high amplitude signal up to around 1400 Hz . The non-dispersive region in the dispersion curve lies below around 200 Hz . So, we expect the impacting pulse to produce frequency components in the dispersive region, creating dispersion in the response throughout impact. This dispersion produces unique capabilities for the mitigation of impact forces, as we will see in this and the following section.

5.3.1 Experimental Results

We performed sample drop experiments on 1D and 3D1D lattices, each with 3 RVEs. We varied the impact velocity of the sample onto the rigid plate by adjusting the drop height. We performed 3 tests at each impact velocity, which varied from 2.8 m/s to approximately 6.5 m/s . We compared the results with ABAQUS dynamic implicit simulations at the corresponding impact velocities. Because observing the wave propagation attributes was the goal for these tests, the variables of interest were velocity at the intersection of each baseline unit cell, longitudinal strain of each baseline unit cell, and initial wave speed. For the following figures that discuss these variables, the curves are colored according to Figure 5.19. Although the 3D1D lattice is shown, the same locations apply for the 1D lattice. The velocity measurement locations are shown by the colored lines at cell intersections. The cells within the colored shaded boxes indicate the longitudinal strain measurement locations. For example, the green curves on the strain plots show the longitudinal strain of the unit cells at cell location #2. These strains are defined as:

$$\epsilon_i = \Delta h_i / h_i, \quad (5.5)$$

where h_i is the original height of cell i and Δh_i is the change in the height of the cell with compression.

Figure 5.20 shows the strain development within the 1D lattice for various impact velocities. A maximum impact velocity of only 6.5 m/s was achievable in the experiments due to drop height limitations. The solid lines are experimental curves and the dashed lines for locations 1 and 6 are the ABAQUS simulation results. We make several observations from these results. The simulations and experiments match fairly well for all impact velocities, but match best for the lower impact

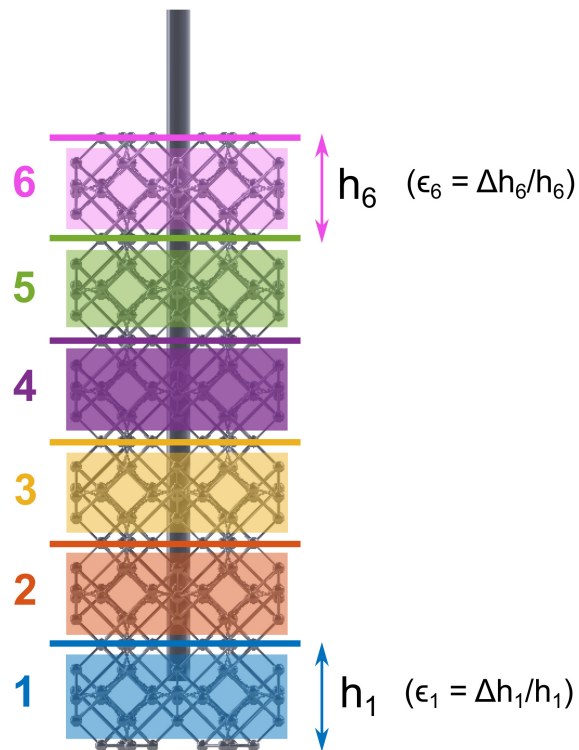


Figure 5.19: A 3D1D lattice is shown with measurement locations for wave propagation analysis. The colored lines at the cell intersections indicate where velocity measurements are taken, and the shaded cells are where cell longitudinal strain measurements are taken. The longitudinal strains are defined as indicated by the inset equations. The colored numbers are a numerical reference to each corresponding measurement location.

velocities. This is analogous to the behavior we observed for baseline unit cell drop weight tests in Figure 5.5. At the lower impact energies, the differences due to hysteresis do not play as significant a role as at the higher impact energies. The total impact time (ending where location 6 strain goes to 0 strain) is very similar between experiments and numerics, with them matching best at 3.6 m/s and 4.5 m/s . The numerical results have a longer impact time for the higher impact velocities. In the simulations (although not shown for clarity), the maximum strain in each location reduces from the previous location. For the experiment, in general the strain reduces from location 1 to location 6, but we see that locations 2 and 4 particularly do not follow this pattern. This is observed most clearly in Figure 5.20(b) and (c). Since this behavior is consistent with varying impact velocity, it is due to manufacturing defects in the sample. That is, the cells at locations 2 and 4 are less stiff than

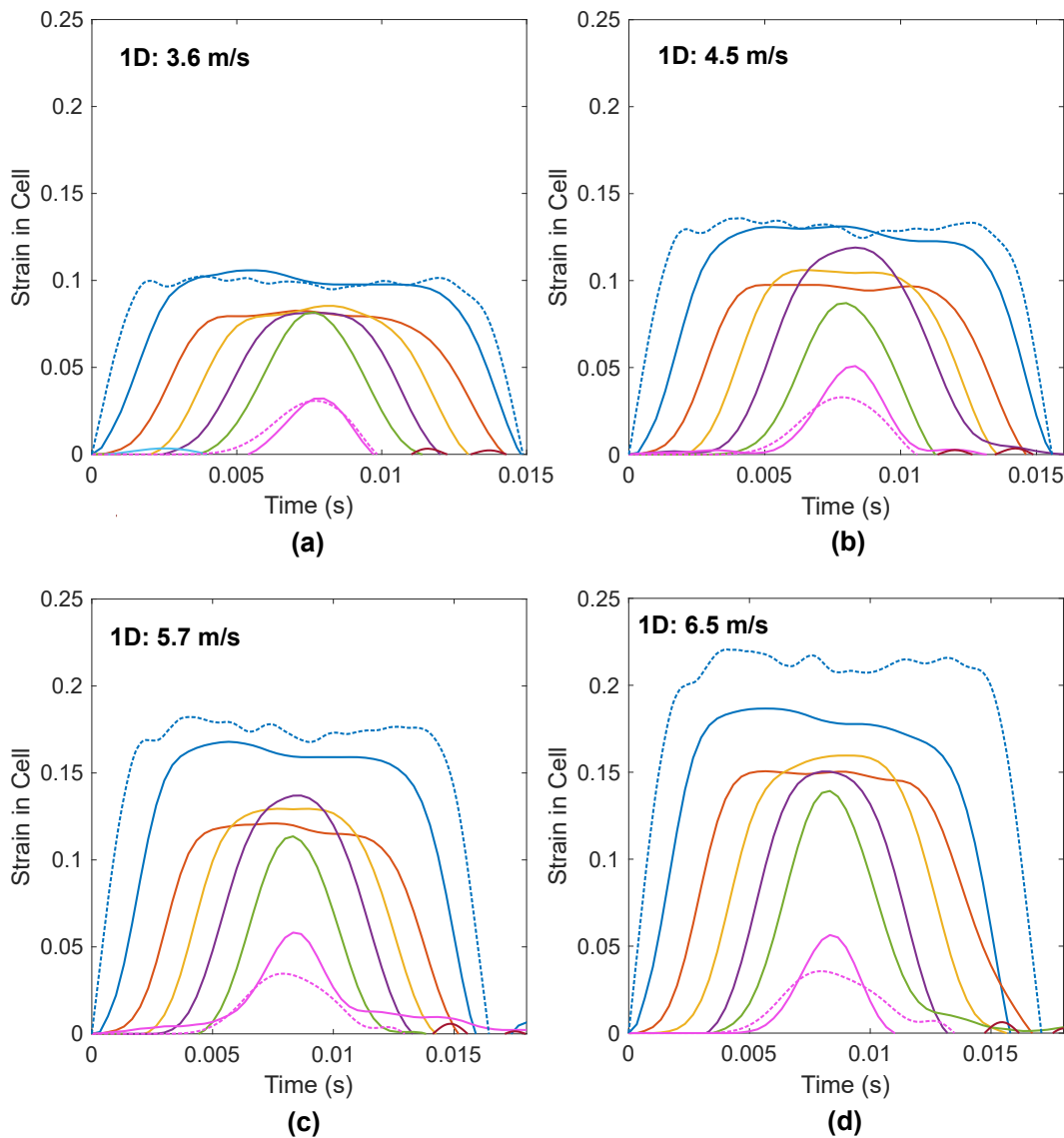


Figure 5.20: Strain development in a 1D lattice drop test for various impact velocities. The colors of the curves correspond to the cell locations in Figure 5.19. The dashed lines for locations 1 and 6 are ABAQUS simulation results, and the solid lines for all locations are the experimental results.

the surrounding cells likely due to member diameters deviating from the nominal values. Another likely source of error in the experiments is that the guiding rod was not perfectly rigid. Although we tried to reduce sway, it was unavoidable that it deviated slightly from vertical during drop and impact.

A key observation made from Figure 5.20 is that the local cell strains in the lattice reduce significantly from location 1 to location 6. The top unit cell compresses markedly less than the bottom unit cell. In a lattice with a linear stress-strain

response, each unit cell would compress approximately the same amount for a sample drop test such as this. That is, the top cell would compress as much as the bottom cell. However, for the tensegrity-inspired lattice, we see a very different response. In every case, even before reaching nonlinear strain levels, the reduction in strain from location 1 to 6 is significant (at least 60% reduction). This is indicative of high dispersion in the lattice response created by the short impulse. We will study the wave propagation characteristics later in this section where we will explore this more.

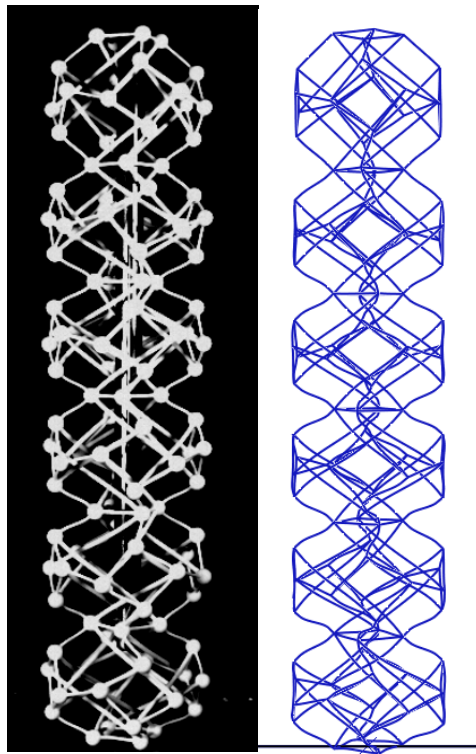


Figure 5.21: Snapshots of the experimental (left photo) and numerical ABAQUS (right snapshot) deformation of the lattice for a 6.5 m/s sample drop test. The bottom unit cell compresses the most, and the top unit cell compresses significantly less.

Images of the lattice at maximum compression for the 6.5 m/s impact are shown in Figure 5.21. The left panel is a photo of the high speed experiment, and the right is a snapshot of the deformation in ABAQUS. We can see that the deformation is similar in both, and that the bottom unit cell compresses the most, and the top unit cell compresses by far the least. This reduction in unit cell strain levels corresponds to a reduction in force seen by each unit cell. Thus, forces are reduced significantly in the lattice by the time the wave reaches the top of the lattices.

Next, we show the response of the 3D1D lattice for two drop velocities in Figure 5.22. The experimental results are again shown with solid lines, and the simulation with dashed lines. The strains are shown for a 2.8 m/s and 5.4 m/s impact in panels

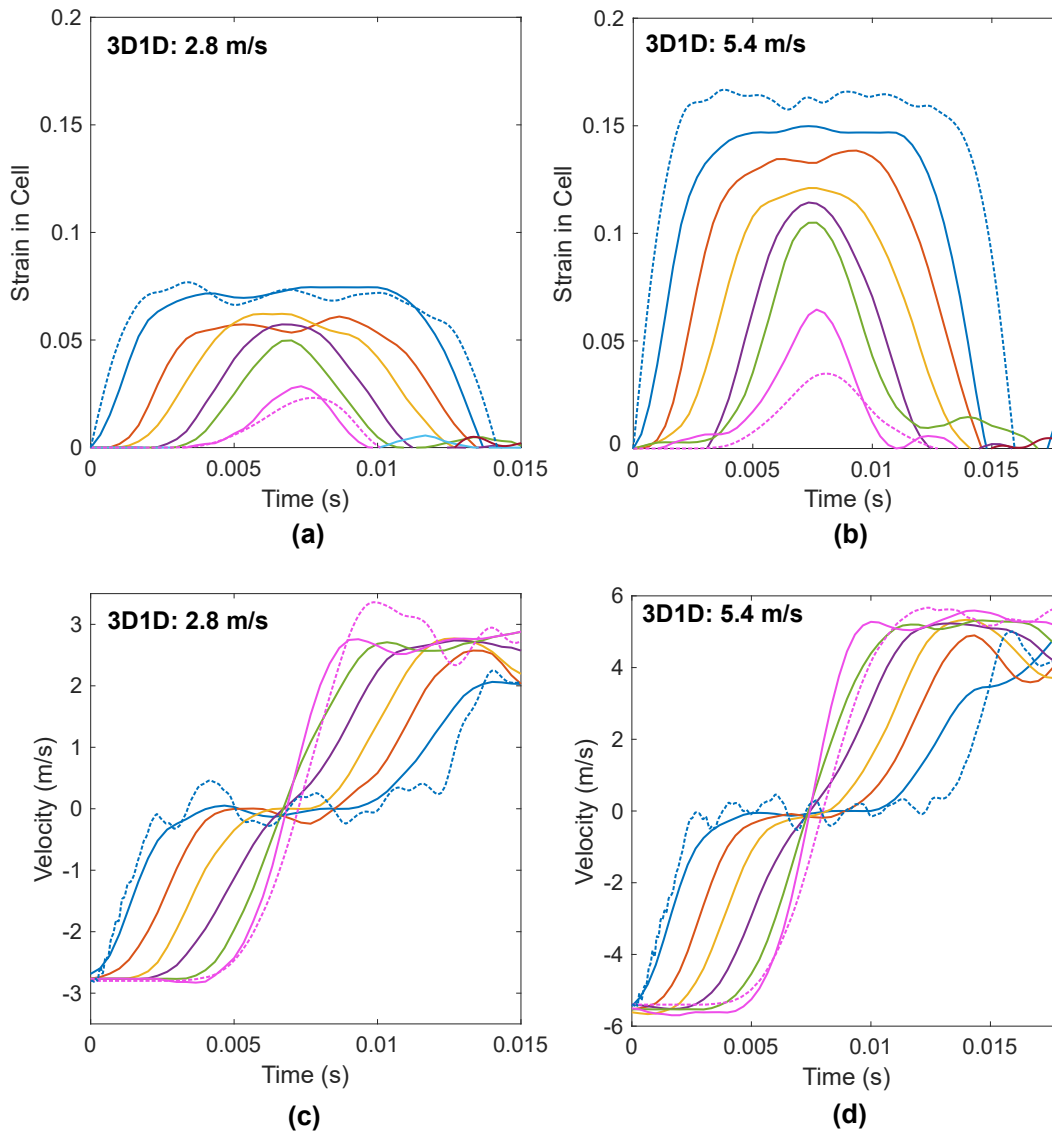


Figure 5.22: The sample drop results are shown for a 3D1D lattice. The dashed lines are simulations and the solid lines are experiments. The strains in each cell location are shown for a 2.8 m/s impact in (a) and a 5.4 m/s impact in (b). The velocities at each location are shown for a 2.8 m/s impact in (c) and a 5.4 m/s impact in (d).

(a) and (b). We see similar behavior to the 1D lattice results. The simulations and experiments match better for the lower impact speed. Panel (b) clearly shows that each successive unit cell location compresses less than the previous, like seen in the simulations. The 3D1D sample thus likely had more uniform fabrication with

no cell location being significantly less or more stiff than the others. In addition, since each cell location in the 3D1D case has 4 baseline cells, if one of the cells is less stiff than the other three, the differences are effectively “averaged out” by all 4 cells. Thus, it is useful to note that with these tensegrity-inspired lattices, higher dimensional lattices are more robust to manufacturing errors than 1D lattices. In fact, since only one 3D1D sample was manufactured for our tests, we observed that one of the cables in cell location 6 (top) was broken before any tests were performed. However, since the top saw little deformation and defects effectively average out at each cell location, this had little influence on the response and the sample survived over 12 tests. In most applications, higher dimensional lattices would need to be used, so this resilience for higher dimensional lattices is a significant advantage.

The velocity profiles for the 2.8 m/s and 5.4 m/s impacts are shown in Figure 5.22(c) and (d). The simulation results closely match those of the experiments for both impact velocities. The main difference is that the simulation shows significant oscillation in the response at cell location 1 (the bottom of the lattice). This oscillation reduces dramatically by the time the wave reaches cell location 6, where the response is smooth. The oscillations are not observed in the experiments. This is due to the lack of temporal resolution from the high speed camera. The frame rate is 3000 fps , but the total impact time is less than 0.02 s for all tests (one quarter of the impact time of the drop weight experiments). This means that a maximum of 60 frames are captured during the impact; thus, the experimental result captures very little oscillation that occurs in the lattice. The oscillations have an influence on the lattice response, which we will describe later in this section.

We also see in 5.22(c) and (d) that the rebound velocity is very close to the impact velocity in both cases. This was seen for both 1D and 3D1D lattices at all speeds. This indicates that the tensegrity-inspired lattice exhibits a significantly elastic impact response. Conservation of momentum requires that with no dissipation, the rebound velocity be equal and opposite to the impact velocity. We do have dissipation in our 3D-printed structure, but the response remains significantly elastic. A quantitative representation of this was found using the coefficient of restitution (e), a common measure of the elasticity of objects under impact. It is given by:

$$e = \sqrt{\frac{h_{rebound}}{h_{drop}}}. \quad (5.6)$$

For the experiments, we took high speed videos, but also took videos from further away with a phone camera, where we captured the drop and rebound heights using

a measuring tape. The camera lost resolution for the higher impact speeds, but for impacts below 4 m/s , the coefficient of restitution was found on average to be 0.84. A comparison of this with other objects is given in Table 5.4. Our tensegrity-

Coefficient of Restitution, e	
Superball	0.9
Table-tennis ball	0.89
Basketball	0.87
<i>This Work</i>	<i>0.84</i>
Tennis ball	0.79
Baseball	0.55
Foam rubber ball	0.3
Beanbag	0.05

Table 5.4: Coefficients of restitution for common objects under impact. [147, 148]

inspired lattice falls between a basketball and a tennis ball in its restitution ability. This implies that it preserves a significant portion of energy from impact, thus allowing it to bounce several times before coming to a stop. Its dissipation is due to friction, drag, and structural damping, not to plasticity. Tensegrity structures have been studied as candidates for planetary landers due to this type of elasticity characteristic [23, 30, 32–35]. Because the kinetic energy from impact is stored as elastic strain energy, instead of inducing plasticity or damage, a tensegrity with a high coefficient of restitution is desirable. Our tensegrity-inspired lattices display this characteristic.

We document the leading wave speeds observed as an average of all tests for the 1D and 3D1D experiments and simulations in Table 5.5. Again, we calculate this based on when the velocity in the final cell (location 6) changes by 1% of the impact velocity. Again, we see that the simulations give higher wave speeds than the experiments due to numerical initial conditions and dissipation in the experiment. Both the simulation and experiment show higher wave speeds for the 3D1D lattice than the 1D lattice. An increase like this is expected due to the 3D RVE dispersion results given in Chapter 4, where the longitudinal wave speed approximately doubled from about 45 m/s to 88 m/s from 1D to 3D. We do not see a doubling of the wave speed here, but that is because we are not looking at a 3D lattice tessellated in all 3 dimensions like in the dispersion analysis. Essentially, the 3D1D lattice is still a 1D lattice, as it is periodic in only y . Therefore, its wave speed is slower than in a full 3D bulk lattice. An example of this is how a slender rod made of a solid isotropic

material has a slower longitudinal wave speed than the bulk material; this is due to effects from the Poisson's ratio [149]. Since the Poisson's ratio is very large in our case (around 2 initially), it has a large effect on the bulk wave speed.

Lattice Type	Experiment	Simulation
1D	55.1	64.5
3D1D	62.1	74.2

Table 5.5: Observed leading wave speeds in 1D and 3D1D lattices for both experiments and simulations. The results are averaged for all sample drop tests. All units are in m/s .

Finally, we performed a few experiments with a glass ornament on top of the lattice to observe its protective capabilities. We cut a hole through the bottom of the ornament parallel with its top opening such that it could slide through and along the guiding rod during impact. We performed the ornament drop tests for a 1D lattice at $3.6 m/s$ impact and the 3D1D lattice at $5.4 m/s$. The ornament survived with no fractures in both cases. Images from the 3D1D test at $5.4 m/s$ impact are shown in Figure 5.23. The sample with the ornament before the test and the sample at maximum compression during impact are shown on the left. The ornament after the test is shown on the top right. It shows no fractures of any kind and survived the test. As a comparison, we performed a drop at $3.3 m/s$ of solely the ornament onto the rigid surface, and the ornament ruptured (seen in lower right). The lattice drop of $5.4 m/s$ corresponded to a drop height of 7.3 feet (2.3 meters). The simulation for a $5.4 m/s$ drop of a 3D1D lattice shows a 76.8% reduction in acceleration (and thus force) from location 1 to location 6. The ornament survives due to these greatly reduced accelerations, thus showing the impact mitigating capabilities of our tensegrity-inspired lattices.

5.3.2 Wave Characteristics

Energy Localization

As we have seen, the tensegrity-inspired structure has the capability of mitigating energy significantly from the bottom to the top of the structure in a sample drop test. This is due to two main reasons: (i) nonlinearity in the baseline unit cell stress-strain response, and (ii) energy trapping in the struts.

In the experimental videos, it is clear that the struts in the first and second cell locations vibrate extensively through impact, but the upper cells' struts vibrate very

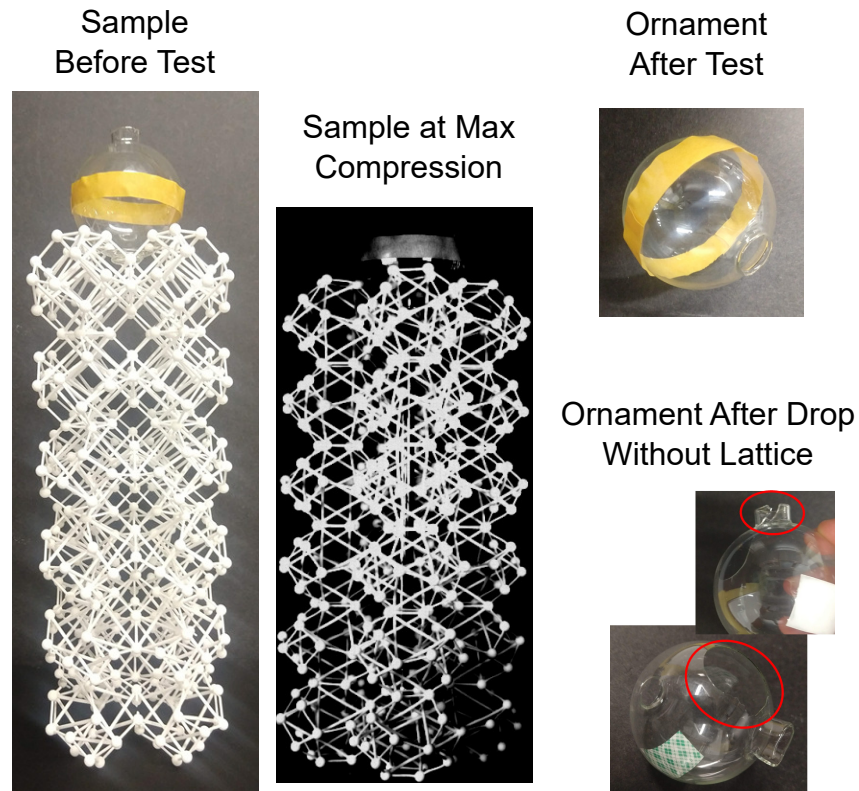


Figure 5.23: Images of sample drop test with a glass ornament sitting on top of the lattice. Sample best for the test with the ornament is shown on the left. A high speed video image of the sample and ornament at maximum compression during a 5.4 m/s impact is shown in the center. The ornament after this test is shown on the top right, and an ornament after a drop test without a lattice is shown on the bottom right (broken areas circled in red).

little. This is the case for both 1D and 3D1D impacts. The lower cells' struts vibrate at a high frequency induced by the high frequency pulse at the bottom. The quantitative experimental data does not capture this oscillation because the frame rate was not high enough (although we can visibly see the vibration in the videos). However, the simulations provide this, as we have seen already by the velocity profiles in Figure 5.22(c) and (d). To demonstrate this more clearly, in Figure 5.24 we extract the 3D1D lattice velocity profiles for an 8.5 m/s impact, at a single point at each intersection (instead of averaged over all horizontal points). By looking at a single point, we can observe more clearly the oscillations from vibration. What we can see is that the velocity at the first location (bottom) exhibits a highly noisy and oscillatory response. Going up the lattice, the oscillations begin to die down very quickly, and by the last two cell locations, the response is mostly smooth. The majority of the energy from the pulse seems to localize near the impact due to these

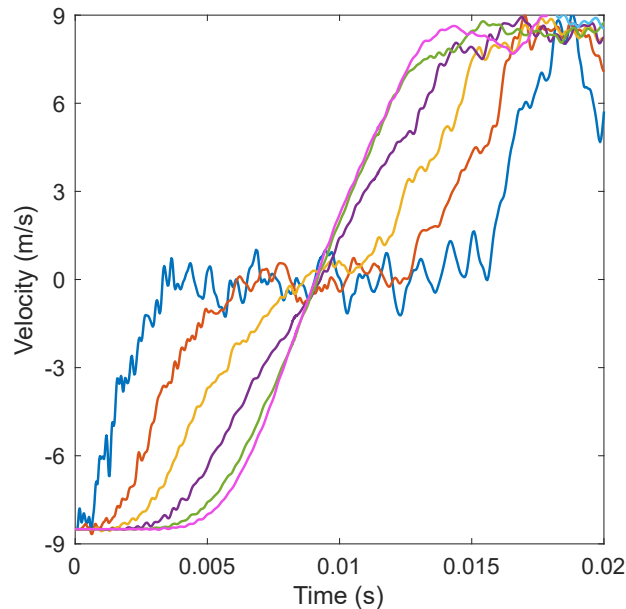


Figure 5.24: ABAQUS velocity profiles for a single point at each cell location in the 3D1D lattice for an impact speed of 8.5 m/s .

vibrations.

Next, we show the results for a 3D bulk lattice which we simulate in ABAQUS, where we see this localization phenomena, but also observe the dynamics of the bulk lattice under impact. Bulk lattices are useful to study because in most dynamic applications, a lattice tessellated in 3D dimensions would need to be used for practical reasons. Also, if fabricated at very small length scales, a bulk lattice effectively can be used as a new type of material [40, 150–153]. Also, a 3D bulk lattice eliminates any global buckling issues.

We ran simulations of a sample drop test for a 3D bulk lattice with 4 RVEs in each dimension ($4 \times 4 \times 4$ RVEs, or $8 \times 8 \times 8$ baseline unit cells), for a total of 512 baseline unit cells. The impact velocities studied were 2.8 m/s , 5 m/s , 7.5 m/s , and 8.5 m/s . In Figure 5.25, we show the time progression of the 3D bulk lattice for an impact of 8.5 m/s . The colormap shows the vertical component of the velocity, with deep blue indicating the impact velocity and red indicating the opposite of the impact velocity. We observe several interesting characteristics. The deformation of the structure again shows that the unit cells on the bottom of the structure deform the most and the top unit cells deform the least. The video of this impact shows most clearly how the structure deformation fluctuates significantly throughout impact; the gradient in deformation from bottom to top brings about a significant effect from

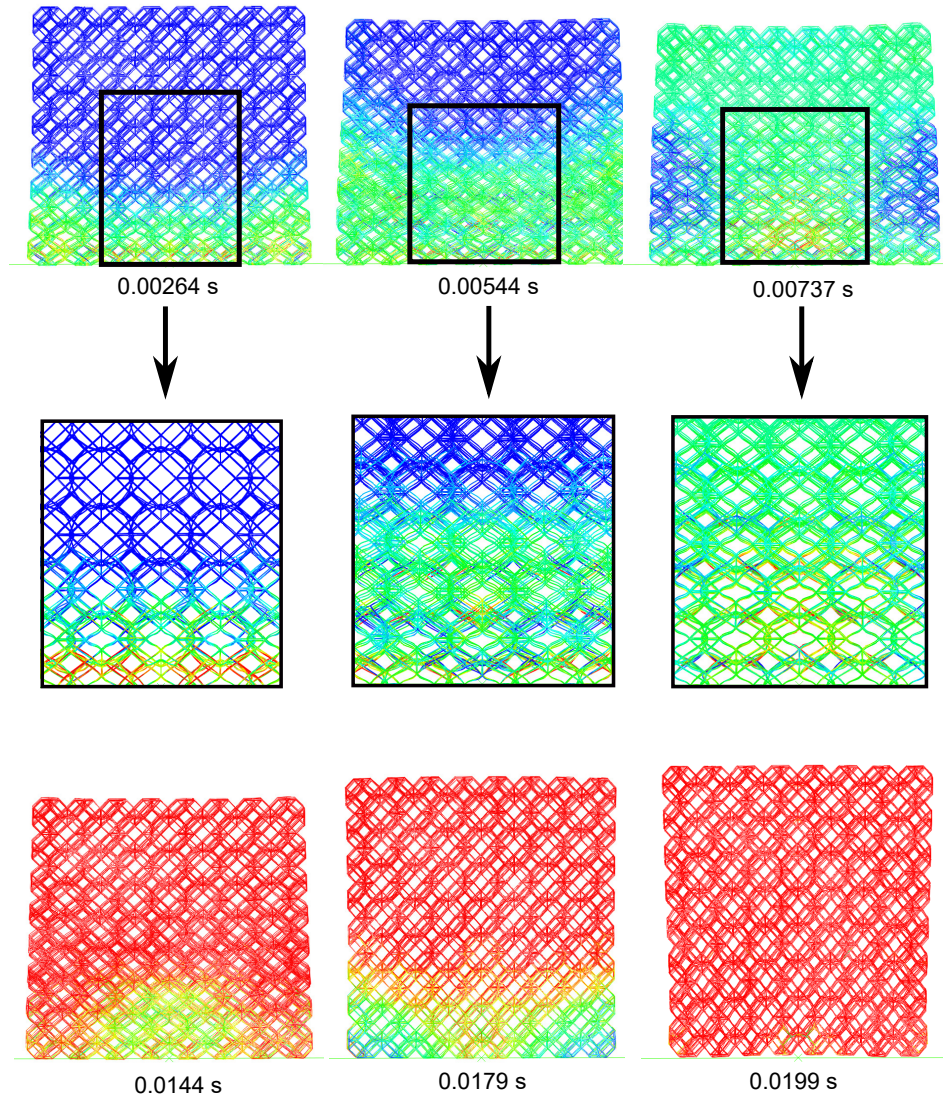


Figure 5.25: The time evolution of the 8.5 m/s impact of a 3D bulk lattice ($4 \times 4 \times 4$ RVEs). The colormap shows the vertical component of the velocity, with deep blue indicating the impact velocity and red indicating the opposite of the impact velocity. We zoom in on the regions in black boxes for the first three timestamps to show localization within the struts.

the large Poisson's ratio, contributing to this fluctuation.

We also see that the velocity propagation exhibits unique directionality. At 0.00264 s , the wave is propagating relatively evenly in the vertical direction. At 0.00544 s , the wave begins to form a “U” shape which shows faster wave propagation on the edges. At 0.00737 s , the fastest regions are on the sides in the vertical center of the structure. As the structure begins moving upward, localized velocity regions remain in the lower half of the structure, in the bottom center at 0.0144 s and bottom

edges at 0.0179 *s*. The entire structure uniformly travels upward after impact ($t = 0.0199$ *s*). What we see from this is that the travelling waves become heavily directional. Since the structure is tessellated in 3 dimensions, shear and diagonal waves propagate, rather than just the longitudinal wave. This is consistent with the results of the 3D dispersion curves obtained in Chapter 4. The heavily directional waves we observe in Figure 5.25 are due to the shear and diagonal wave speeds being faster than the longitudinal wave. That is, energy goes much more quickly to the edges than to the top of the lattice.

We calculated both the longitudinal wave speed and diagonal wave speeds (using the 1% rule) to compare with the results from the dispersion curve. It is not simple to calculate the shear wave speed, since the diagonal wave speed is faster than the shear speed. The vertical component of the diagonal wave speed was found by taking the vertical distance from the bottom to the center of the lattice and dividing that distance by the time the wave took to reach the leftmost center point. The diagonal wave speed is readily calculated from this as 349 *m/s*. The longitudinal wave speed was found to be 112 *m/s*. As seen in the dispersion results from Chapter 4, the longitudinal wave speed in this case is about twice that of the 1D lattice speed (112 *m/s* vs. 64.5 *m/s*, from Table 5.5). Also, the dispersion results in Chapter 4 gave a diagonal wave speed of 334 *m/s*, which is comparable to what we calculate here (349 *m/s*). The heavy directionality in the diagonal directions focuses energy to the side/edge regions and thus slows the energy transfer to the top of the lattice.

At the first three timestamps in Figure 5.25, we zoom in on the regions indicated by the black boxes to observe how the struts behave. At 0.00264 *s*, we see that heavy localization of velocity occurs in the struts in the bottom layer. Cables show relatively small velocities (green regions) compared to the struts. At 0.00544 *s*, the struts in the first two vertical cell layers show heavy oscillation, and slightly less oscillation is seen in the third layer. At 0.00737 *s*, the longitudinal wave has traversed all the way to the top of the lattice, but only the struts in the lowest 3-4 vertical layers show oscillation. This indicates that energy is “trapped” in the buckled struts, such that oscillation heavily dies down with increasing vertical distance from the location of impact.

A quantitative visualization of this trapping is seen in Figure 5.26. Here, we show the velocity magnitude at the center of two struts, shown by the locations in the inset image of the lattice. One is at the bottom of the lattice near the impact site, and the other is 5 cell lengths from the bottom. The velocity of the strut at cell

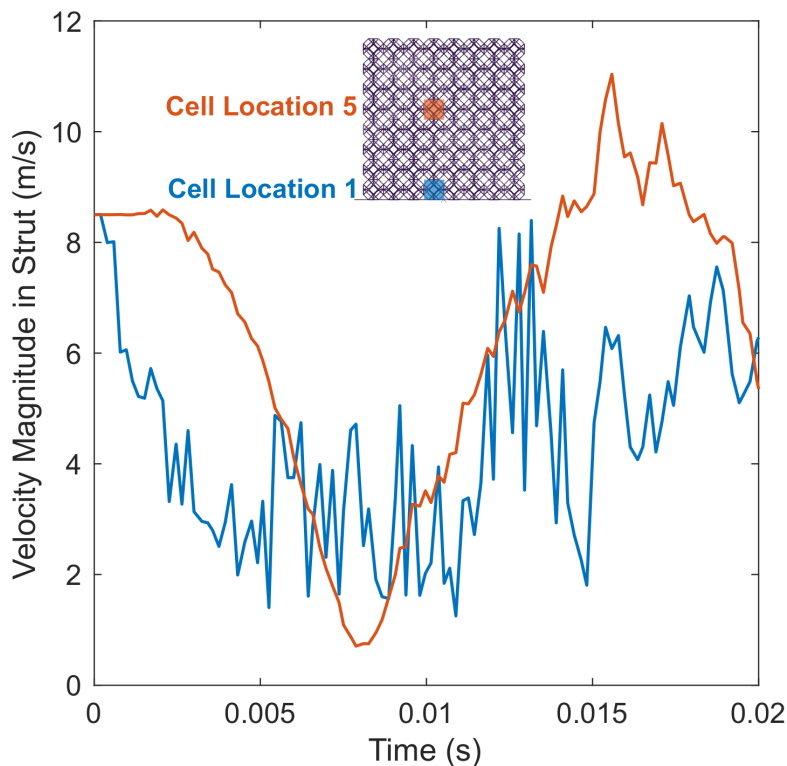


Figure 5.26: For an 8.5 m/s impact, the velocity magnitude at the center of two struts is shown. The inset indicates the locations in the lattice where the strut velocities are measured.

location 1 shows a highly oscillatory response and the velocity at cell location 5 is a comparatively very smooth response. This shows that the strut at the bottom of the lattice undergoes dramatic local vibrations for nearly the entire impact time of 0.02 s . The vibrations die out almost entirely by about halfway through the lattice, well before reaching the top. Sharp, high amplitude accelerations die out by reaching the top of the lattice due to this energy trapping. This is also observed for the lower impact speeds and for the 1D and 3D1D lattices.

Dispersive and Asymmetric Wave Propagation

Another indication of the unique characteristics of these lattices is the dispersive and asymmetric propagation of waves from impact loading. This characteristic was observed in buckling tensegrity lattices in [71] for the case of a 3D bulk lattice falling onto a rigid surface. We show the velocity propagation through the lattice by vertical propagation for the 3D bulk 8.5 m/s impact in Figure 5.27. Instead of a clear, nearly constant wavefront propagating from left to right like in a linear lattice, we see that

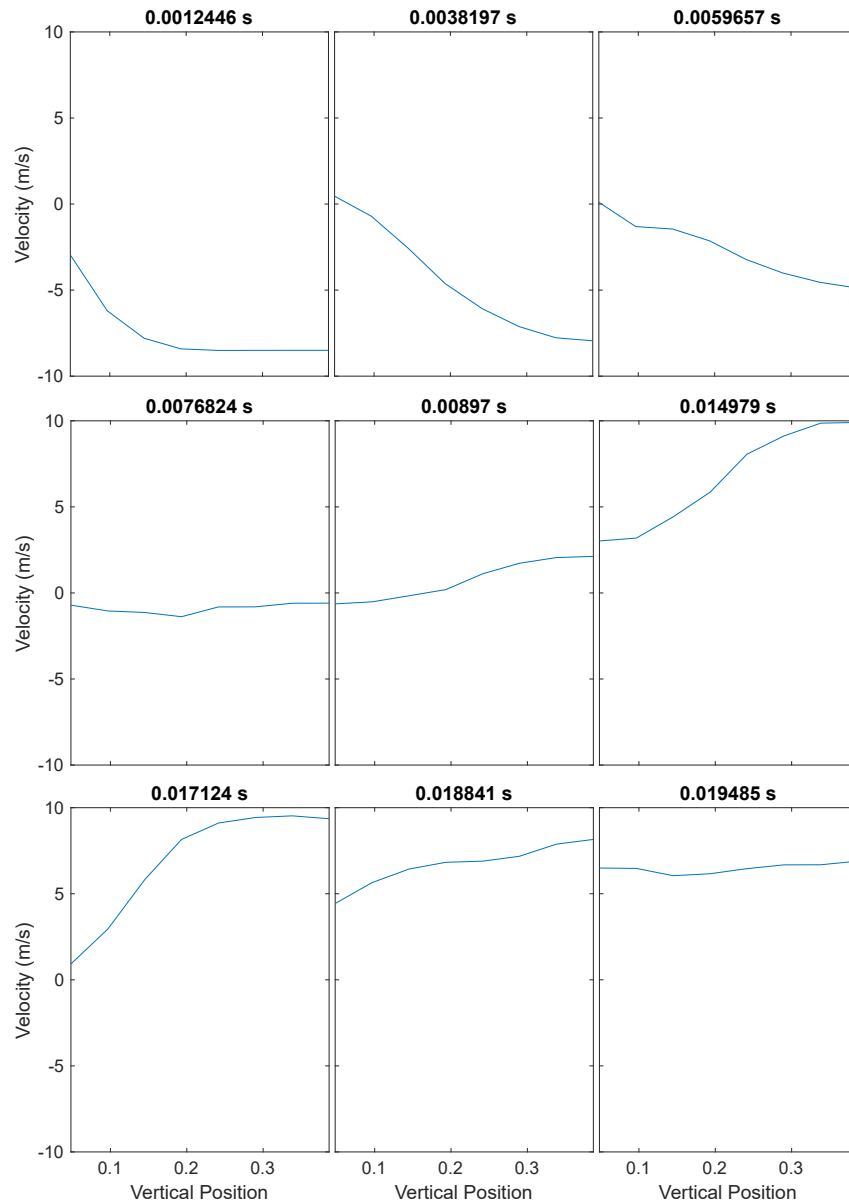


Figure 5.27: Vertical velocity propagation through the lattice by vertical position for the 3D bulk 8.5 m/s impact. The velocity profiles for 9 timestamps are shown. The impact begins on the left of the velocity-position plot at 8.5 m/s .

the wavefront very early begins spreading significantly. The first three timestamps show that the wave reaches the top of the lattice without a clear wavefront. This compressive wavefront is more dispersive than in the case of the pin-jointed 3D tensegrity lattice [71]. The reflected wave begins forming very slowly and expands slowly, differing highly from the sharp reflection of waves in non-dispersive media. This attribute of dispersive wave propagation is yet another appealing characteristic of our tensegrity-inspired lattices for dynamic applications.

Comparison Between Lattice Types

Finally, we present a quantitative comparison between the 1D, 3D1D, and 3D bulk lattices under sample drop impact. As we have seen, all three types exhibit rich dynamic properties. One significant characteristic is their impact mitigation ability. This is easily seen by the reduction in unit cell strains from the impact location to the top of the lattice, where a payload might need to be protected. This reduction in strain corresponds to a reduction in impact accelerations, which are damaging to a payload. A simple comparison between lattices, then, is this reduction in strains. We define the normalized parameter, ϵ_6/ϵ_1 , as the maximum longitudinal strain of the top cell location divided by the maximum longitudinal strain of the bottom cell location in the lattice. The values ϵ_6 and ϵ_1 are defined in Figure 5.19 and Equation 5.5. For example, a value of 0.4 for the parameter ϵ_6/ϵ_1 means that the top cell location reaches a 60% lower maximum strain value than the bottom cell. Lower values mean higher impact mitigation ability of the lattice.

We show a plot of ϵ_6/ϵ_1 versus impact velocity for the 1D, 3D1D, and bulk 3D lattice simulations in Figure 5.28. We see that in all cases, the tensegrity-inspired

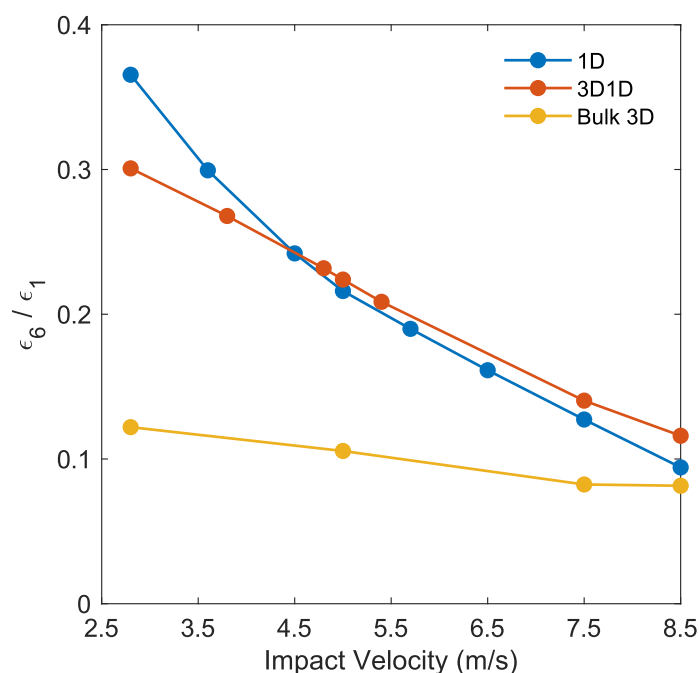


Figure 5.28: ϵ_6/ϵ_1 is the maximum strain at the top cell location divided by the maximum strain at the bottom cell location in a lattice. Here, we show simulation results of ϵ_6/ϵ_1 as a function of impact velocity for 1D, 3D1D, and bulk 3D tensegrity-inspired lattices.

lattices are very good at reducing impact energy. The top location strain is always at least 60% less than the bottom strain. Also, in all cases ϵ_6/ϵ_1 reduces with impact velocity. Interestingly, the 1D and 3D1D lattices show a similar trend and values of ϵ_6/ϵ_1 . This is likely because both are effectively 1D lattices without the ability to transfer energy in transverse directions. The 1D lattice actually shows better strain mitigation by the highest impact velocities than the 3D1D lattice.

In comparison, the 3D bulk lattice far outperforms the 1D and 3D1D lattices. Even at low impact speeds, the strain mitigation is 88%, and is lower than the other two lattices for all impact velocities. The bulk lattice performs the best because it not only shows dispersion and energy trapping in the struts (like the 1D and 3D1D lattices also do), but also has directionality in its wave propagation. Faster shear and diagonal wave speeds redirect energy to the lower edges of the lattice before the wave reaches the top. This is also why ϵ_6/ϵ_1 only reduces slightly over the entire range of impact velocity: diagonal and shear speeds are always faster than longitudinal, and thus the lattice does not need high deformation to exhibit this behavior.

Not only does the bulk lattice perform the best, but it has the lowest maximum strain value as well. At 8.5 *m/s*, the 1D lattice bottom cell reached 40% strain (close to maximum before densification) and the bottom of the 3D1D lattice reached 32% strain. However, at 8.5 *m/s* the the bulk lattice bottom cells only reached 24% strain. This means that the 1D lattice cannot be impacted at higher speeds than 8.5 *m/s*, and the 3D1D lattice would not withstand much higher speeds. But the 3D bulk lattice would be able to withstand significantly higher impact velocities than 8.5 *m/s* before reaching its maximum strain capacity.

5.4 Flatten the Curve: Short Duration Impulse by a Falling Mass

Lastly, we provide a brief overview of the last type of impact test: a short duration pulse exerted on the lattice from a small falling mass. This differs from the previous impact tests we have examined in the following ways. First, it differs from the drop weight tests at the beginning of this chapter in that the impact velocity is very high and the falling mass is very small. This produces a high energy pulse with a short duration, equivalent to applying a force pulse with a high magnitude over a short period of time. Second, this contrasts from the sample drop tests in that the impacting mass separates from the lattice after the pulse has been applied. Because of this, the unit cell hit by the impacting pulse does not stay compressed during the entire deformation, like in the sample drop tests, but a bell-shaped travelling displacement wave traverses through the structure.

Finally, this configuration best represents the type of impacts in typical real-world applications. That is, instead of the architected lattice material itself falling onto a rigid surface (like in the sample drop case), the lattice material remains stationary as an impactor hits the lattice. An example of this is a helmet: the protective helmet material stays stationary, an impactor hits it, the wave traverses through the helmet, and the protected object (i.e., the head) remains safe. Essentially, the helmet material “spreads” the impacting momentum over time, thus reducing the forces and increasing the reaction pulse duration by conservation of momentum.

This type of impact best indicates the ability of the tensegrity-inspired lattice to reduce impact forces. It is important to note that this type of impact has several overlapping features that we observed in the sample drop case (e.g., high frequency pulse, energy trapping, strut vibration).

Only simulations are performed in this section using the same ABAQUS dynamic implicit simulation as in the rest of this chapter. Experiments were not able to be performed due to technical difficulties with accelerating a very small mass to a high impact velocity onto a 3D-printed lattice. We perform these simulations on 1D, 3D1D, and 3D bulk lattices. For the 1D and 3D1D cases, we simulate 5-RVE and 10-RVE lattices (10 and 20 baseline cells) to understand how waves propagate over long distances in these lattices and how force reduction varies between lattice lengths.

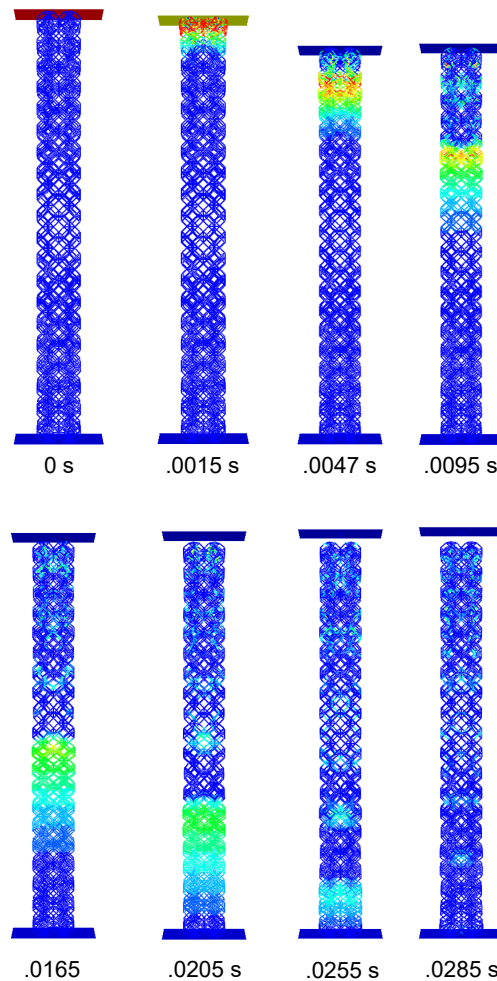


Figure 5.29: Vertical velocity propagation over time for a 3D1D lattice with 10 RVEs, 18 m/s impact. The colormap ranges from 0 (blue) to v_{imp} (red). The mass separates at 0.0047s.

5.4.1 Wave Propagation

We ran iterative simulations to find a mass of the impactor such that the impulse duration was less than one-third of the duration of impact. This allowed us to observe a reduction of force through the structures. To keep strain rates low enough (without entering a ballistic range) and deformation levels approximately the same between each type of lattice, we kept the velocity range constant, but changed the mass for each type of lattice. The masses for the 1D, 3D1D, and 3D bulk lattices were 2.5 g, 10 g, and 160 g, respectively. The 3D1D lattice has 4 times the mass of the 1D lattice because its impacting surface is 4 times larger, and the 3D bulk lattice has 64 times the mass of the 1D lattice because its impacting surface is 64 times larger. We found that by choosing these masses, we achieved similar deformation

levels and impacting pulse durations between lattices for the same impact velocities. Henceforth, when stating impact conditions for each simulation, we do not refer to the impacting mass but only the impact velocity. The impacting mass is assumed to be as stated here.

We ran simulations for each lattice type with impactor velocities of 6 m/s , 12 m/s , and 18 m/s . For the 18 m/s case, the 1D and 3D1D lattices achieved baseline cell deformations close to densification. At 6 m/s , the cell deformations were all in the linear region of Figure 5.14. Thus, we achieved both linear and nonlinear ranges of deformation levels.

To visualize the propagation of waves for this type of impact, we show the vertical velocity propagation within the 3D1D lattice with 10 RVEs for an 18 m/s impact over time in Figure 5.29. The colormap ranges from 0 (blue) to v_{imp} (red). In this type of impact, we see a distinct travelling wave indicated by a “packet” of color traveling through the structure. The mass separates at 0.0047 s , well before the wave reaches the bottom of the structure. The wave begins as a localized high velocity region, indicated by the red at the top at 0.0015 s . The wave begins traversing and immediately begins to widen, thus reducing velocities within the wave packet, as seen at 0.0047 s and 0.0095 s . This is due to high dispersion in the structure. By 0.0095 s , the red impact velocity nearly disappears as the pulse widens to about 3 baseline cell lengths. At 0.0165 s , the velocity is significantly reduced (red is gone), and by 0.0205 s the pulse has spread to about 5.5 baseline cell lengths. The wave reaches the bottom of the structure at very low velocity. This type of behavior is seen for all lattice types and is most pronounced for the highest impact velocities.

To illustrate this behavior more quantitatively, we show space-time (x - t) diagrams of the kinetic energy through a 1D 10-RVE lattice for the three impact energies in Figure 5.30. The kinetic energy is normalized by the maximum kinetic energy at the first cell location (location of impact). In the top three panels, we scale the colorbar from 0 to 1. At 6 m/s , the propagating wave is distinct and clearly traverses the length of the lattice and a clear reflected wave propagates. The highest kinetic energy (red) is only observed in the first 4 cells, and KE/KE_{max} quickly reduces to 0.5 or less. The rate of reduction of kinetic energy is not nearly as great as it is for 12 m/s and 18 m/s , however. At 12 and 18 m/s , the time taken to traverse through the structure increases (i.e., wave speed decreases), and by 18 m/s there is no clear reflected wave. The response is much more dispersive, induced by high nonlinear deformations in the first few unit cells and vibration in the struts (energy trapping).

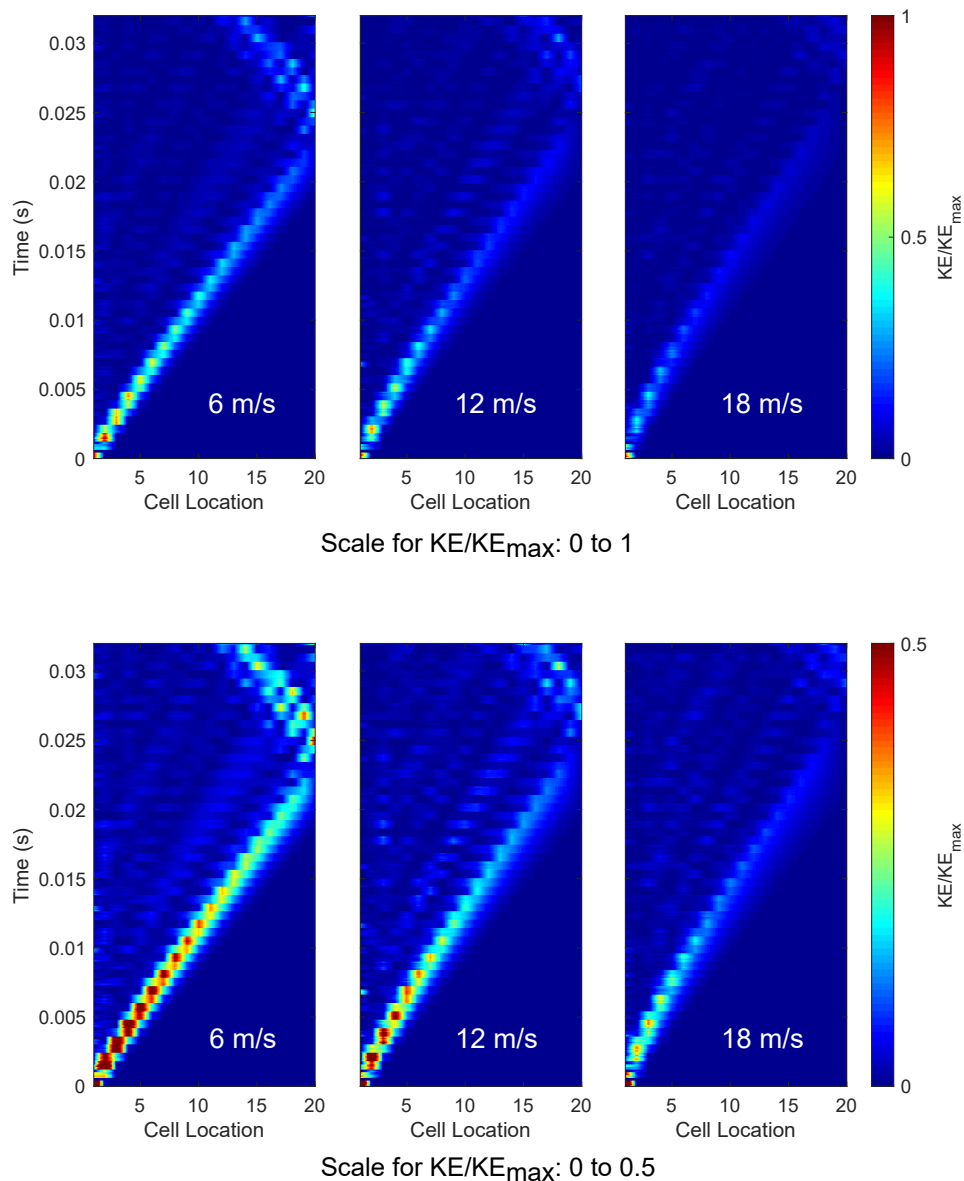


Figure 5.30: Space-time (x-t) diagrams for a 10 RVE (20 baseline cell locations) 1D lattice. The colorbar plots the normalized Kinetic Energy, KE/KE_{max} , where KE_{max} is the maximum kinetic energy at the first cell location (location of impact). The top three panels show this for a colorbar scale from 0 to 1, and the bottom three show this for a scale from 0 to 0.5.

In fact, at 18 m/s , high kinetic energy regions (red) are only seen at the location of impact. The kinetic energy immediately reduces to around 0.6 by the second cell location.

To see this more clearly, we plot the x-t diagram again, but for a colorbar range of 0 to 0.5, in the lower three panels. The 6 m/s case more clearly shows the

reflected wave and other characteristics stand out more significantly. But for 18 m/s , the wave is so dispersive that by cell location 5, KE/KE_{max} is less than 0.3, and almost all kinetic energy is mitigated by the end of the lattice. There is still no clear reflected wave. This indicates the extreme energy mitigation capability of our tensegrity-inspired lattices.

In this case, we looked at the kinetic energy distribution within a lattice over time under a short duration impact. To form a more complete picture of how energy is distributed in these lattices under impact, we provide in Appendix C an impact example showing the distribution of strain and kinetic energy in the two member types. This information is useful for informing future directions of this research, as we explain there.

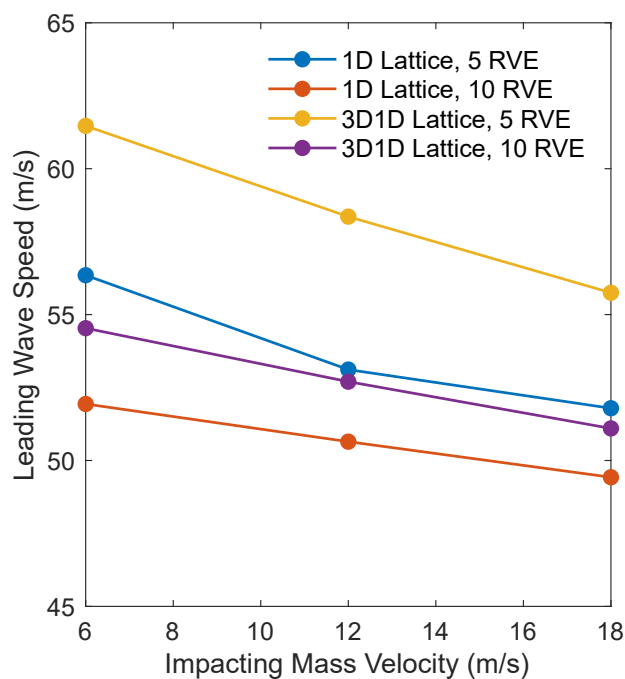


Figure 5.31: Leading wave speeds as a function of impact velocity for 1D and 3D1D lattices, both 5 and 10 RVEs long.

As we saw in Figure 5.30, the wave speed decreased as impact energy increased. In Figure 5.31, we show the wave speed as a function of impact velocity for 1D and 3D1D lattices, both 5 and 10 RVEs long. As a reminder, the leading wave speed is calculated by the distance from the impact to the last cell location divided by the time it takes for the wave to reach 1% of the impact velocity at that location. First, we see that the longer lattices have lower wave speeds than the shorter lattices. This is because in the longer lattices, the wave is able to spread out more from

dispersion, and more energy is trapped higher in the lattice. This brings the wave speed down. For all lattices, the wave speed also decreases as impact velocity is increased. Higher impact velocities increase the deformation of the first unit cell, thus inducing the nonlinear response of the structure. The structure's nonlinearity from buckling is a mechanism that suddenly spreads out the impacting forces, and along with dispersion and energy trapping, the wave speed is reduced.

Next, we examine the response of a 3D bulk lattice under this short duration impact. In Figure 5.32, we show the impact response of a 3D bulk (4x4x4 RVE) lattice under a 12 m/s impact. The colorbar in all plots indicates the vertical velocity normalized by the impacting velocity, on a scale of 0 to 0.5 so color gradients can be more clearly observed. On the left, we show the bulk lattice at three steps in time, when the wave reaches a peak at the three locations indicated by the black cut regions. On the right, for each timestamp, we show a plot of the normalized velocity over the horizontal cut region in the transverse directions (X and Z). At about 0.0015 s , the wave begins to propagate and is localized at the top of the structure. The propagation looks fairly linear, with the entire top layer uniformly achieving similar velocities. This is seen on the right-hand plot. There are no localized regions transversely; all locations have a very high velocity near the impact velocity.

At 0.0037 s , the wave has reached the center of the lattice. The high velocity regions, instead of propagating uniformly downward, get redirected starkly to the diagonal edges. This is seen in the right-hand plot most clearly. The diagonal outermost edges have very high velocity localization, whereas the center has very low velocity. This produces a sharp gradient in velocity on the X-Z plane. As seen also in the sample drop tests, the diagonal wave speed is about 4 times as fast as the longitudinal wave speed. The diagonal wave speed “wins out” over the longitudinal wave we saw at 0.0015 s . Energy gets redirected to the side regions instead of moving downwards. This prevents large amounts of energy from reaching the bottom of the lattice, as seen at 0.0053 s . The plot of the cut plane on the right shows that the diagonal regions of high velocity at 0.0037 s in the lattice center do not propagate to the diagonal regions on the bottom of the lattice. The highest velocities are at the center, but these velocities are very low, with a v/v_{imp} of less than 0.2. This shows the bulk lattice's desirable capability of redirecting energy away from the bottom surface, which may be an object that needs to be protected from impact.

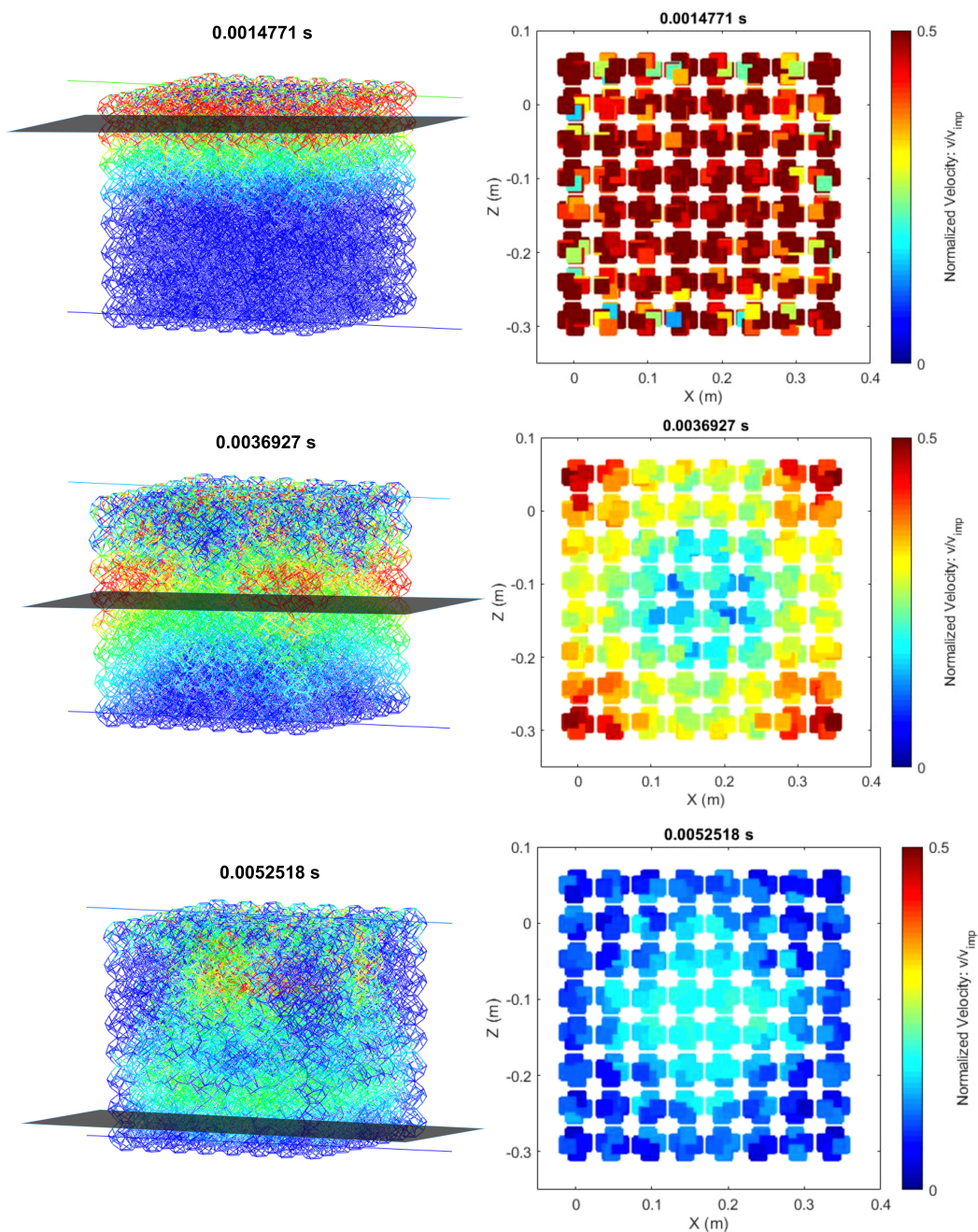


Figure 5.32: The impact response of a 3D bulk (4x4x4 RVE) lattice under a 12 m/s impact. The colorbar in all plots indicates the vertical velocity normalized by the impacting velocity, on a scale of 0 to 0.5. On the left, we show the bulk lattice at three steps in time, when the wave reaches a peak at the three locations indicated by the black cut regions. On the right, for each timestamp, we show a plot of the normalized velocity over the horizontal cut region indicated in the transverse directions (X and Z).

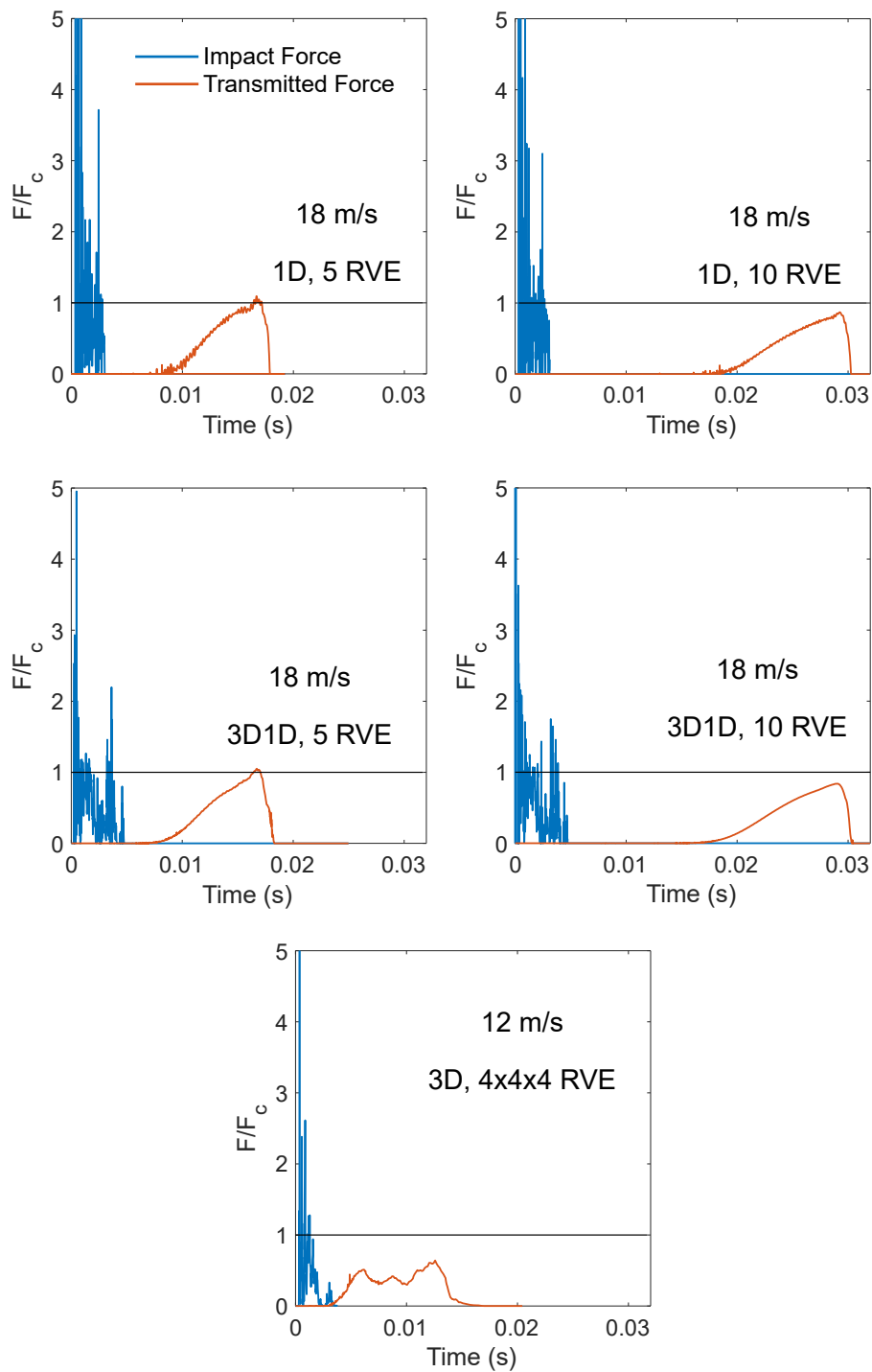


Figure 5.33: The force of impact and the transmitted reaction force for various lattices and impact velocities, as indicated on the plots. F/F_c is the force normalized by F_c , which is the force capacity of the bottom layer unit cells. The black line indicates where $F/F_c = 1$.

5.4.2 Force Transmission Reduction

Finally, we look at the reduction of impact forces through these lattices. The impact force is the pulse exerted by the impacting mass on the lattice. The transmitted force is the reaction force measured on the bottom plate under the lattice. For impact applications, if an object needs to be protected, a material such as a foam or lattice is desired to “spread” the impacting pulse over time through it, so that by the time it reaches the object, the forces are lowered and the impulse on the protected object lasts a longer time. This can be termed “flattening the curve,” and is simply conservation of momentum. The area under the impacting pulse force-time curve must be equal to the area under the force-time curve at each subsequent location in the lattice, so if time increases, force decreases. Note that the reaction force profile on the bottom plate is twice the area of the impacting pulse, as the wave is not only transmitted but also reflected at this location.

We plot the force of the impact and the transmitted reaction force for various lattices and impact velocities in Figure 5.33. F/F_c is the force normalized by F_c , which is the force capacity of the bottom layer unit cells. That is, the reaction force will never exceed that of the buckling load of the combined bottom unit cells. For the 1D lattice, F_c is 18.6 N, for 3D1D, it is four times that, and for 3D bulk, it is 64 times that. We choose this normalization to not only show clearly the difference between impact and transmitted forces, but also to show that the lattices retain the load limiting property we see in the baseline unit cell.

For all cases, we see that the impact force is a noisy, high amplitude force pulse with a duration around 0.004 s long. At 18 m/s impact velocity, the 3D1D and 1D 5-RVE lattices (two left panels), achieve very high strains in their top unit cells. Thus, it is not surprising to see that F/F_c reaches nearly 1. We can see that the force profile is about doubled in time from the impact pulse and the maximum forces are reduced significantly. However, as the length of the lattices increase to 10 RVEs (right two panels), the force pulse is spread further over time and the forces are reduced below $F/F_c = 1$. Longer lattices have more opportunity for energy trapping and dispersion to spread out waves. Thus, even though the top cells reach very high strains, the reaction force can be brought to forces lower than the force capacity. We also show the response for the 3D bulk lattice at 12 m/s. The impacting pulse is similar in amplitude and length, but the transmitted force reaches only about $F/F_c = 0.5$. Although convergence issues did not allow us to find the response of the lattice at 18 m/s, we conjecture that the 3D bulk lattice is particularly capable of mitigating

impact forces due to its added ability to redirect waves.

5.5 Chapter Summary

In this chapter, we have explored the dynamics of our tensegrity-inspired structures and lattices under impact loading. Baseline unit cell drop weight tests demonstrated the reusability of the structure for multiple impacts and demonstrated its energy capacity and load limitation behavior. These tests also showed that our tensegrity-inspired structure again behaves like its pin-jointed tensegrity counterpart structure. Compared to other lattice materials, our structure exhibits remarkable energy absorption efficiency with a very low relative density. Short-duration impacts of these lattices exhibited their remarkable ability to mitigate impact forces. This mitigation is due to the nonlinear response of the unit cells, dispersive wave propagation, and energy trapping in the vibrating struts. Localized non-uniform trapping of kinetic energy creates the same effect as energy dissipation in lattices with mechanisms such as plasticity. However, the tensegrity-inspired structures remain highly elastic, with a coefficient of restitution similar to a tennis ball, making them advantageous over one-use architected materials for impact protection.

CONCLUSIONS AND FUTURE DIRECTIONS

6.1 Summary

In this thesis, we presented a foundational study for a new type of metamaterial, which we term “tensegrity-inspired” metamaterials. They are extremely lightweight ($\rho_r = 2.5\%$) periodic lattices of building block structures that exhibit tensegrity-like characteristics in both the static and dynamic regime, such as load limitation, resilience to severe deformation, high elastic strain energy absorption, tunability with precompression, and impact mitigation. We designed this 3D-printable building block structure in order to overcome manufacturing limitations of pin-jointed tensegrity structures, while maintaining an equivalent strain energy capacity and compressive response. As explained in Chapter 3, the structure design uses spherical joints to separate structural members in a way that maintains certain tensegrity characteristics, allowing the compressive and dynamic responses to behave similarly to a counterpart prestressed buckling tensegrity. The structure is fabricated with a single material, allowing it to be printed with a variety of currently available 3D-printing methods. Without the need for pin-joints or prestress, the structure uses geometry to produce tensegrity-like characteristics. The designed structure provides a way to exploit many useful characteristics of a tensegrity structure without needing cumbersome manufacturing.

Using the tensegrity-inspired building block structure, we constructed multidimensional lattices and studied their dynamic behavior. In Chapter 4, we performed dispersion analyses on 1D and 3D lattices. The nonlinearity of the structure’s compressive response produces a dramatic evolution of the lattice’s dynamic characteristics. Continuous tunability of the bandgap and wave speeds is obtained by increasing the level of global precompression, making these lattices a candidate for acoustic lenses with energy focusing. Since the deformation remains elastic even at large strains, repeatable and active tuning of the lattice response is potentially achievable. Results for 3D lattices showed very similar characteristics as for a pin-jointed tensegrity 3D lattice [87], such as zero energy modes and higher shear speeds than longitudinal speeds. This chapter provided a foundation for understanding the subsequent dynamic impact analyses.

In Chapter 5, we delved into a range of impact studies on these tensegrity-inspired lattices. Long-duration drop weight tests on baseline unit cells and 1D lattices showed their high elasticity under impact: they produced only low levels of plastic strain even after dozens of impacts. These tests showed the structures' load limitation characteristic; i.e., their maximum loads are governed by the buckling load of the baseline structure. The structures exhibit extremely good energy absorption efficiency compared to a range of similar lattice materials. Short duration impulse tests, including sample drop tests and tests with a small impacting mass, showed remarkable dynamic traits. Dispersion due to the nonlinearity of the structure rapidly spreads out impacting momentum and traveling waves, reducing damaging accelerations and lowering velocities. A sample drop test exhibited the lattices' capability to protect a fragile object from breakage (i.e., a glass ornament). In addition to the nonlinear response producing dispersion, we observe significant energy trapping near the location of impact by high vibration in the struts. The struts oscillate rapidly, keeping kinetic energy from the impulse localized near the impact site. Finally, simulations on 3D bulk lattices showed their unique capability of redirecting waves. Since the diagonal wave speed is faster than the longitudinal wave speed, impact energy redirects toward the edges and prevents most energy from propagating toward the bottom of the lattice, where a protected object might be located. Although these lattices were inspired by tensegrity structures, these tensegrity-inspired lattices are a new type of lightweight, readily 3D-printable metamaterial with remarkable dynamic properties.

6.2 Future Directions

A range of future directions of 3D-printable tensegrity-inspired metamaterials can be taken beyond the fundamental study presented in this thesis. Even without optimization of energy absorption or dispersion characteristics, the tensegrity-inspired lattices show remarkable properties that are appealing for a range of dynamic applications. However, the member diameters can readily be changed, and richer wave attributes can be achieved by optimizing for energy performance, alternating unit cells with different member diameters, or placing "holes" in the lattice by periodically removing unit cells (this has been done in [72]). Material limitations certainly presented themselves with the polymer used in this thesis (e.g., hysteresis, viscoelasticity, relatively low material strength, etc.). These limitations can be overcome by using other materials. Metals are likely a desirable choice due to their high strength; however, a quick preliminary analysis of steel used in this lattice showed that local

strains at the cable joints would easily enter the plasticity region for a metal. This could be overcome by redesigning the cable geometry to reduce these strains (e.g., a spiral shape).

Another design possibility to achieve better performance would be to pursue other tensegrity configurations than a truncated octahedron. A disadvantage of the octahedron is that since the struts run through the interior of the lattice, densification occurs at strains below 50%. Strain energy could be increased by change to a configuration where densification occurs much later in the compression, such as if the struts run mostly near the exterior of the lattice.

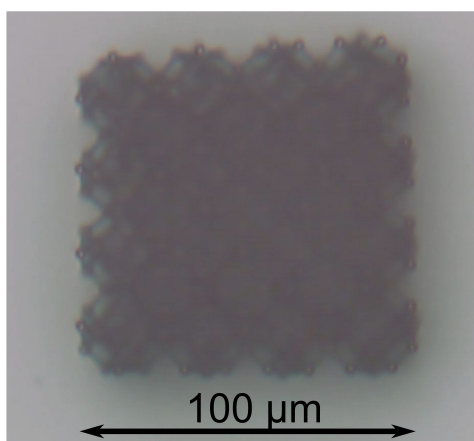


Figure 6.1: Tensegrity-inspired 3D lattice printed with the Nanoscribe printer.

Our tensegrity-inspired lattices are good candidates for new types of effective materials, such as for foam in a helmet or shielding devices for electronics or space applications. The readily manufacturable nature of our tensegrity-inspired structures allow them to be printed at multiple length scales with a variety of printers. We successfully printed a 2x2x2 RVE 3D lattice of our design using the Nanoscribe system, as shown in Figure 6.1. A static/dynamic analysis of these types of metamaterials at small length scales would dramatically open up their potential for a variety of applications.

Finally, when we began this research, we started with the idea of “tensegrity sands.” That is, printing several unit cells at a very small length scale and combining them together in a random, granular configuration. The appeal behind this is that the energy absorption of tensegrity structures might be higher for random than for periodically arranged combinations of unit cells. Since our tensegrity-inspired lattices are 3D-printable at a small length scale such as sand, this might be an

interesting avenue to pursue. The tensegrity-inspired metamaterials presented in this thesis open up a new family of lightweight metamaterials that possess dynamically rich attributes.

BIBLIOGRAPHY

- [1] R. L. Swanson. “Biotensegrity: a unifying theory of biological architecture with applications to osteopathic practice, education, and research—a review and analysis”. In: *The Journal of the American Osteopathic Association* 113.1 (2013), pp. 34–52.
- [2] S. Pellegrino. “Deployable structures”. In: Springer, 2001, pp. 179–198.
- [3] J. Zhang and M. Ohsaki. “Tensegrity Structures”. In: Springer, 2015, pp. v–vii.
- [4] J. M. Busch. *A Decade of Sculpture: The New Media in the 1960s*. Associated Univ Press, 1974.
- [5] C. Reilly and D. E. Ingber. “Art advancing science: filmmaking leads to molecular insights at the nanoscale”. In: *ACS nano* 11.12 (2017), pp. 12156–12166.
- [6] C. B. Reilly and D. E. Ingber. “Multi-scale modeling reveals use of hierarchical tensegrity principles at the molecular, multi-molecular, and cellular levels”. In: *Extreme Mechanics Letters* 20 (2018), pp. 21–28.
- [7] D. E. Ingber. “Tensegrity I. Cell structure and hierarchical systems biology”. In: *Journal of cell science* 116.7 (2003), pp. 1157–1173.
- [8] D. E. Ingber. “The architecture of life”. In: *Scientific American* 278.1 (1998), pp. 48–57.
- [9] R. E. Skelton et al. “An introduction to the mechanics of tensegrity structures”. In: *Proceedings of the 40th IEEE Conference on Decision and Control*. Vol. 5. IEEE. 2001, pp. 4254–4259.
- [10] M. Masic, R. E. Skelton, and P. E. Gill. “Optimization of tensegrity structures”. In: *International Journal of Solids and Structures* 43.16 (2006), pp. 4687–4703. doi: 10.1016/j.ijsolstr.2005.07.046.
- [11] R. E. Skelton et al. “Minimum mass design of tensegrity bridges with parametric architecture and multiscale complexity”. In: *Mechanics Research Communications* 58 (2014), pp. 124–132. doi: 10.1016/j.mechrescom.2013.10.017.
- [12] K. Nagase and R. E. Skelton. “Minimal mass tensegrity structures”. In: *Journal of The International Association for Shell and Spatial Structures* 55.1 (2014), pp. 37–48.
- [13] I. Oppenheim and W. Williams. “Mechanics of tensegrity prisms”. In: *Proceedings of the 14th international symposium on automation & robotics in construction*. 1997.

- [14] A. G. Tibert and S. Pellegrino. “Review of form-finding methods for tensegrity structures”. In: *International Journal of Space Structures* 18.4 (2003), pp. 209–223. DOI: 10.1260/026635103322987940.
- [15] A. G. Tibert and S. Pellegrino. “Deployable tensegrity reflectors for small satellites”. In: *Journal of Spacecraft and Rockets* 39.5 (2002), pp. 701–709. DOI: 10.2514/2.3867.
- [16] F. Fraternali, G. Carpentieri, and A. Amendola. “On the mechanical modeling of the extreme softening/stiffening response of axially loaded tensegrity prisms”. In: *Journal of the Mechanics and Physics of Solids* 74 (2015), pp. 136–157. DOI: 10.1016/j.jmps.2014.10.010.
- [17] A. Amendola et al. “Experimental investigation of the softening–stiffening response of tensegrity prisms under compressive loading”. In: *Composite Structures* 117 (2014), pp. 234–243. DOI: 10.1016/j.compstruct.2014.06.022.
- [18] I. Mascolo et al. “On the Geometrically Nonlinear Elastic Response of Class $\theta=1$ Tensegrity Prisms”. In: *Frontiers in Materials* 5 (2018), p. 16. DOI: 10.3389/fmats.2018.00016.
- [19] H. Furuya. “Concept of deployable tensegrity structures in space application”. In: *International Journal of Space Structures* 7.2 (1992), pp. 143–151. DOI: 10.1177/026635119200700207.
- [20] C. Sultan. “Modeling, design, and control of tensegrity structures with applications”. PhD thesis. 1999.
- [21] C. H. Juan and J. M. Mirats-Tur. “Tensegrity frameworks: static analysis review”. In: *Mechanism and Machine Theory* 43.7 (2008), pp. 859–881. DOI: 10.1016/j.mechmachtheory.2007.06.010.
- [22] R. Motro. *Tensegrity: structural systems for the future*. Elsevier, 2003.
- [23] J. J. Rimoli. “A reduced-order model for the dynamic and post-buckling behavior of tensegrity structures”. In: *Mechanics of Materials* 116 (2018), pp. 146–157. DOI: 10.1016/j.mechmat.2017.01.009.
- [24] Z. Littlefield et al. “From quasi-static to kinodynamic planning for spherical tensegrity locomotion”. In: *Robotics Research*. Springer, 2020, pp. 947–966.
- [25] K. Y. Volokh, O. Vilnay, and M. Belsky. “Tensegrity architecture explains linear stiffening and predicts softening of living cells”. In: *Journal of biomechanics* 33.12 (2000), pp. 1543–1549.
- [26] H. Murakami. “Static and dynamic analyses of tensegrity structures. Part II. Quasi-static analysis”. In: *International Journal of Solids and Structures* 38.20 (2001), pp. 3615–3629.

- [27] A. Amendola et al. “On the additive manufacturing, post-tensioning and testing of bi-material tensegrity structures”. In: *Composite Structures* 131 (2015), pp. 66–71.
- [28] H. C. Tran and J. Lee. “Geometric and material nonlinear analysis of tensegrity structures”. In: *Acta Mechanica Sinica* 27.6 (2011), pp. 938–949.
- [29] C. Paul, F. J. Valero-Cuevas, and H. Lipson. “Design and control of tensegrity robots for locomotion”. In: *IEEE Transactions on Robotics* 22.5 (2006), pp. 944–957.
- [30] J. J. Rimoli. “On the impact tolerance of tensegrity-based planetary landers”. In: *57th AIAA/ASCE/AHS/ASC Structures, Structural Dynamics, and Materials Conference*. 2016, p. 1511.
- [31] K. Wang et al. “Distributed System of Mobile Passive Tensegrity Structures”. In: *AIAA Scitech 2020 Forum*. 2020, p. 0076.
- [32] C. A. Gebara, K. C. Carpenter, and A. Woodmansee. “Tensegrity Ocean World Landers”. In: *AIAA Scitech 2019 Forum*. 2019, p. 0868.
- [33] E. A. Peraza Hernandez, R. Goyal, and R. E. Skelton. “Tensegrity Structures for Mass-Efficient Planetary Landers”. In: *Proceedings of IASS Annual Symposia*. Vol. 2018. 27. International Association for Shell and Spatial Structures (IASS). 2018, pp. 1–8.
- [34] J. Bruce et al. “SUPERball: Exploring tensegrities for planetary probes”. In: (2014).
- [35] V. SunSpiral et al. “Tensegrity based probes for planetary exploration: Entry, descent and landing (EDL) and surface mobility analysis”. In: *International Journal of Planetary Probes* 7 (2013), p. 13.
- [36] C. A. Gebara. “Tensegrity Ultra-Lightweight Probe”. In: *JPL SLAMS Early Career Forum 2018*. 2018.
- [37] N. A. Fleck, V. S. Deshpande, and M. F. Ashby. “Micro-architected materials: past, present and future”. In: *Proceedings of the Royal Society A* 466.2121 (2010), pp. 2495–2516. DOI: 10.1098/rspa.2010.0215.
- [38] K. T. Tan, H. H. Huang, and C. T. Sun. “Blast-wave impact mitigation using negative effective mass density concept of elastic metamaterials”. In: *International Journal of Impact Engineering* 64 (2014), pp. 20–29. DOI: 10.1016/j.ijimpeng.2013.09.003.
- [39] S. Cui et al. “Mechanical metamaterials foams with tunable negative poisson’s ratio for enhanced energy absorption and damage resistance”. In: *Materials* 11.10 (2018), p. 1869. DOI: 10.3390/ma11101869.
- [40] C. Q. Lai and C. Daraio. “Highly Porous Microlattices as Ultrathin and Efficient Impact Absorbers”. In: *International Journal of Impact Engineering* 120 (2018), pp. 138–149. DOI: 10.1016/j.ijimpeng.2018.05.014.

- [41] S. Gaitanaros and S. Kyriakides. “On the effect of relative density on the crushing and energy absorption of open-cell foams under impact”. In: *International Journal of Impact Engineering* 82 (2015), pp. 3–13.
- [42] R. V. Craster and S. Guenneau. *Acoustic metamaterials: Negative refraction, imaging, lensing and cloaking*. Vol. 166. Springer Science & Business Media, 2012.
- [43] G. Theocharis, N. Boechler, and C. Daraio. “Nonlinear phononic structures and metamaterials”. In: *Acoustic metamaterials and phononic crystals, Springer series in solid state sciences* 173 (2013).
- [44] M. Lu, L. Feng, and Y. Chen. “Phononic crystals and acoustic metamaterials”. In: *Materials today* 12.12 (2009), pp. 34–42.
- [45] M. I. Hussein, M. J. Leamy, and M. Ruzzene. “Dynamics of phononic materials and structures: Historical origins, recent progress, and future outlook”. In: *Applied Mechanics Reviews* 66.4 (2014).
- [46] A. Leonard, L. Ponsón, and C. Daraio. “Exponential stress mitigation in structured granular composites”. In: *Extreme Mechanics Letters* 1 (2014), pp. 23–28.
- [47] M. Miniaci et al. “Experimental observation of a large low-frequency band gap in a polymer waveguide”. In: *Frontiers in Materials* 5 (2018), p. 8.
- [48] A. S. Phani, J. Woodhouse, and N. A. Fleck. “Wave propagation in two-dimensional periodic lattices”. In: *The Journal of the Acoustical Society of America* 119.4 (2006), pp. 1995–2005. DOI: 10.1121/1.2179748.
- [49] S. Gonella and M. Ruzzene. “Analysis of in-plane wave propagation in hexagonal and re-entrant lattices”. In: *Journal of Sound and Vibration* 312.1 (2008), pp. 125–139. DOI: 10.1016/j.jsv.2007.10.033.
- [50] F. Casadei and J.J. Rimoli. “Anisotropy-induced broadband stress wave steering in periodic lattices”. In: *International Journal of Solids and Structures* 50.9 (2013), pp. 1402–1414. ISSN: 0020-7683. DOI: 10.1016/j.ijsolstr.2013.01.015.
- [51] A. Bayat and S. Gaitanaros. “Wave Directionality in Three-Dimensional Periodic Lattices”. In: *Journal of Applied Mechanics* 85.1 (Nov. 2017). DOI: 10.1115/1.4038287.
- [52] A. Bacigalupo and M. Lepidi. “Acoustic wave polarization and energy flow in periodic beam lattice materials”. In: *International Journal of Solids and Structures* 147 (2017), pp. 183–203. DOI: 10.1016/j.ijsolstr.2018.05.025.
- [53] Y. Liebold-Ribeiro and C. Körner. “Phononic Band Gaps in Periodic Cellular Materials”. In: *Advanced Engineering Materials* 16.3 (2014), pp. 328–334. DOI: 10.1002/adem.201300064.

- [54] S. Krödel et al. “3D Auxetic Microlattices with Independently Controllable Acoustic Band Gaps and Quasi-Static Elastic Moduli”. In: *Advanced Engineering Materials* 16.4 (2014), pp. 357–363. doi: 10.1002/adem.201300264.
- [55] P. Wang et al. “Locally resonant band gaps in periodic beam lattices by tuning connectivity”. In: *Physical Review B* 91 (2 2015), p. 020103. doi: 10.1103/PhysRevB.91.020103.
- [56] S. Gonella, A. C. To, and W. K. Liu. “Interplay between phononic bandgaps and piezoelectric microstructures for energy harvesting”. In: *Journal of the Mechanics and Physics of Solids* 57.3 (2009), pp. 621–633. doi: 10.1016/j.jmps.2008.11.002.
- [57] D. Tallarico et al. “Tilted resonators in a triangular elastic lattice: Chirality, Bloch waves and negative refraction”. In: *Journal of the Mechanics and Physics of Solids* 103 (2017), pp. 236–256. doi: 10.1016/j.jmps.2017.03.007.
- [58] K. Bertoldi and M. C. Boyce. “Mechanically triggered transformations of phononic band gaps in periodic elastomeric structures”. In: *Physical Review B* 77 (2008), p. 052105. doi: 10.1103/PhysRevB.77.052105.
- [59] L. Wang and K. Bertoldi. “Mechanically tunable phononic band gaps in three-dimensional periodic elastomeric structures”. In: *International Journal of Solids and Structures* 49.19 (2012), pp. 2881–2885. doi: 10.1016/j.ijsolstr.2012.05.008.
- [60] P. Wang et al. “Harnessing Buckling to Design Tunable Locally Resonant Acoustic Metamaterials”. In: *Physical Review Letters* 113 (2014), p. 014301. doi: 10.1103/PhysRevLett.113.014301.
- [61] S. Shan et al. “Harnessing Multiple Folding Mechanisms in Soft Periodic Structures for Tunable Control of Elastic Waves”. In: *Advanced Functional Materials* 24.31 (2014), pp. 4935–4942. doi: 10.1002/adfm.201400665.
- [62] J. Li, V. Slesarenko, and S. Rudykh. “Auxetic multiphase soft composite material design through instabilities with application for acoustic metamaterials”. In: *Soft Matter* 14 (30 2018), pp. 6171–6180. doi: 10.1039/C8SM00874D.
- [63] J. R. Raney et al. “Stable propagation of mechanical signals in soft media using stored elastic energy”. In: *Proceedings of the National Academy of Sciences of the United States of America* 113.35 (2016), p. 052105. doi: 10.1073/pnas.1604838113.
- [64] Y. Chen et al. “Lattice Metamaterials with Mechanically Tunable Poisson’s Ratio for Vibration Control”. In: *Physical Review Applied* 7.2 (2017), p. 024012. doi: 10.1103/PhysRevApplied.7.024012.

- [65] M. A. Nouh, O. J. Aldraihem, and A. Baz. “Periodic metamaterial plates with smart tunable local resonators”. In: *Journal of Intelligent Material Systems and Structures* 27 (2016), pp. 1829–1845. DOI: 10.1177/1045389X15615965.
- [66] P. Celli et al. “Wave control through soft microstructural curling: bandgap shifting, reconfigurable anisotropy and switchable chirality”. In: *Smart Materials and Structures* 26 (2017), p. 035001. DOI: 10.1088/1361-665X/aa59ea.
- [67] Q. Zhang, K. Zhang, and G. Hu. “Smart three-dimensional lightweight structure triggered from a thin composite sheet via 3D printing technique”. In: *Scientific Reports* 6 (2016), p. 22431. DOI: 10.1038/srep22431.
- [68] C. Nimmagadda and K. H. Matlack. “Thermally tunable band gaps in architected metamaterial structures”. In: *Journal of Sound and Vibration* 439 (2019), pp. 29–42. DOI: 10.1016/j.jsv.2018.09.053.
- [69] A. Bayat and F. Gordaninejad. “Band-Gap of a Soft Magnetorheological Phononic Crystal”. In: *Journal of Vibration and Acoustics* 137.1 (2015), p. 011011. DOI: 10.1115/1.4028556.
- [70] Z. Wang et al. “Tunable Digital Metamaterial for Broadband Vibration Isolation at Low Frequency”. In: *Advanced Materials* 28.44 (2016), pp. 9857–9861. DOI: 10.1002/adma.201604009.
- [71] J. J. Rimoli and R. K. Pal. “Mechanical response of 3-dimensional tensegrity lattices”. In: *Composites Part B: Engineering* 115 (2017), pp. 30–42. DOI: 10.1016/j.compositesb.2016.10.046.
- [72] K. Liu et al. “Unraveling tensegrity tessellations for metamaterials with tunable stiffness and bandgaps”. In: *Journal of the Mechanics and Physics of Solids* 131 (2019), pp. 147–166. DOI: 10.1016/j.jmps.2019.05.006.
- [73] L. Zhao and E. A. Peraza Hernandez. “Theoretical study of tensegrity systems with tunable energy dissipation”. In: *Extreme Mechanics Letters* 32 (2019), p. 100567. DOI: 10.1016/j.eml.2019.100567.
- [74] F. Fraternali, L. Senatore, and C. Daraio. “Solitary waves on tensegrity lattices”. In: *Journal of the Mechanics and Physics of Solids* 60.6 (2012), pp. 1137–1144. DOI: 10.1016/j.jmps.2012.02.007.
- [75] F. Fraternali et al. “Multiscale tunability of solitary wave dynamics in tensegrity metamaterials”. In: *Applied Physics Letters* 105.20 (2014), p. 201903. DOI: 10.1063/1.4902071.
- [76] C. Davini, A. Micheletti, and P. Podio-Guidugli. “On the impulsive dynamics of T3 tensegrity chains”. In: *Meccanica* 51.11 (2016), pp. 2763–2776. DOI: 10.1007/s11012-016-0495-y.
- [77] F. Fabbrocino and G. Carpentieri. “Three-dimensional modeling of the wave dynamics of tensegrity lattices”. In: *Composite Structures* 173 (2017), pp. 9–16.

- [78] A. Zhang, B. Cera, and A. Agogino. “Characterization of six-bar spherical tensegrity lattice topologies”. In: *Proceedings of the IASS Symposium 2018: Creativity in Structural Design*. 2018.
- [79] J. M. Mirats-Tur and S. H. Juan. “Tensegrity frameworks: Dynamic analysis review and open problems”. In: *Mechanism and Machine Theory* 44.1 (2009), pp. 1–18. DOI: [10.1016/j.mechmachtheory.2008.06.008](https://doi.org/10.1016/j.mechmachtheory.2008.06.008).
- [80] J. Michielsen, R. H. B. Fey, and H. Nijmeijer. “Steady-state dynamics of a 3D tensegrity structure: simulations and experiments”. In: *International Journal of Solids and Structures* 49.7-8 (2012), pp. 973–988. DOI: [10.1016/j.ijsolstr.2011.12.011](https://doi.org/10.1016/j.ijsolstr.2011.12.011).
- [81] C. Sultan. “Designing structures for dynamical properties via natural frequencies separation: Application to tensegrity structures design”. In: *Mechanical Systems and Signal Processing* 23.4 (2009), pp. 1112–1122. DOI: [10.1016/j.ymsp.2008.08.014](https://doi.org/10.1016/j.ymsp.2008.08.014).
- [82] S. Faroughi, H. H. Khodaparast, and M. I. Friswell. “Non-linear dynamic analysis of tensegrity structures using a co-rotational method”. In: *International Journal of Non-Linear Mechanics* 69 (2015), pp. 55–65. DOI: [10.1016/j.ijnonlinmec.2014.11.021](https://doi.org/10.1016/j.ijnonlinmec.2014.11.021).
- [83] I. J. Oppenheim and W. O. Williams. “Vibration of an elastic tensegrity structure”. In: *European Journal of Mechanics-A/Solids* 20.6 (2001), pp. 1023–1031. DOI: [10.1016/S0997-7538\(01\)01181-0](https://doi.org/10.1016/S0997-7538(01)01181-0).
- [84] I. J. Oppenheim and W. O. Williams. “Vibrations and design of tensegrity structures”. In: *Revue française de génie civil* 7.3 (2003), pp. 377–389. DOI: [10.1080/12795119.2003.9692501](https://doi.org/10.1080/12795119.2003.9692501).
- [85] A. O. Krushynska et al. “Accordion-like metamaterials with tunable ultra-wide low-frequency band gaps”. In: *New Journal of Physics* 20.7 (2018), p. 073051. DOI: [10.1088/1367-2630/aad354](https://doi.org/10.1088/1367-2630/aad354).
- [86] A. Amendola et al. “Tuning frequency band gaps of tensegrity mass-spring chains with local and global prestress”. In: *International Journal of Solids and Structures* 155 (2018), pp. 47–56. DOI: [10.1016/j.ijsolstr.2018.07.002](https://doi.org/10.1016/j.ijsolstr.2018.07.002).
- [87] R. K. Pal, M. Ruzzene, and J. J. Rimoli. “Tunable wave propagation by varying prestrain in tensegrity-based periodic media”. In: *Extreme Mechanics Letters* 22 (2018), pp. 149–156. DOI: [10.1016/j.eml.2018.06.005](https://doi.org/10.1016/j.eml.2018.06.005).
- [88] K. Caluwaerts et al. “Design and control of compliant tensegrity robots through simulation and hardware validation”. In: *Journal of the royal society interface* 11.98 (2014), p. 20140520.
- [89] R. Connelly and M. Terrell. “Globally rigid symmetric tensegrities”. In: *Structural Topology* 1995 núm 21 (1995).

- [90] N. Vassart and R. Motro. “Multiparametered formfinding method: application to tensegrity systems”. In: *International journal of space structures* 14.2 (1999), pp. 147–154.
- [91] C. Sultan, M. Corless, and R. Skelton. “Reduced prestressability conditions for tensegrity structures”. In: *40th Structures, Structural Dynamics, and Materials Conference and Exhibit*. 1999, p. 1478.
- [92] K. Kebiche, M. N. Kazi-Aoual, and R. Motro. “Geometrical non-linear analysis of tensegrity systems”. In: *Engineering structures* 21.9 (1999), pp. 864–876.
- [93] N. B. Kahla and K. Kebiche. “Nonlinear elastoplastic analysis of tensegrity systems”. In: *Engineering Structures* 22.11 (2000), pp. 1552–1566.
- [94] L. Zhang et al. “Geometrically nonlinear elasto-plastic analysis of clustered tensegrity based on the co-rotational approach”. In: *International Journal of Mechanical Sciences* 93 (2015), pp. 154–165.
- [95] R. Skelton. “Dynamics and control of tensegrity systems”. In: *IUTAM symposium on vibration control of nonlinear mechanisms and structures*. Springer. 2005, pp. 309–318.
- [96] A. Campesato. “Unprecedented Structural Skins. Experiments towards an Intelligent Tensegrity Skin”. In: *Procedia Engineering* 155 (2016), pp. 183–194. DOI: 10.1016/j.proeng.2016.08.019.
- [97] K. Liu et al. “Programmable deployment of tensegrity structures by stimulus-responsive polymers”. In: *Scientific reports* 7.1 (2017), p. 3511. DOI: 10.1038/s41598-017-03412-6.
- [98] H. Xu and D. Pasini. “Structurally efficient three-dimensional metamaterials with controllable thermal expansion”. In: *Scientific reports* 6 (2016), p. 34924. DOI: 10.1038/srep34924.
- [99] A. A. Bauhofer et al. “Harnessing Photochemical Shrinkage in Direct Laser Writing for Shape Morphing of Polymer Sheets”. In: *Advanced Materials* 29.42 (2017), p. 1703024. DOI: 10.1002/adma.201703024.
- [100] “ABAQUS 6.14 Documentation”. In: *Dassault Systemes Simulia Corporation* 651 (2014).
- [101] *Material Data Sheet PA 2200*. URL: http://www.shapeways.com/topics/udesign/materials/white_strong_flexible/pa2200_material_data_sheet_12_08_en_.pdf.
- [102] A. F. Epee et al. “Constitutive model for a semi-crystalline polymer under dynamic loading”. In: *International Journal of Solids and Structures* 48.10 (2011), pp. 1590–1599.
- [103] M. Kutz. *Applied plastics engineering handbook: processing, materials, and applications*. William Andrew, 2016, pp. 517–532.

- [104] J. J. Rimoli. *Tensegrity Structures And Methods of Constructing Tensegrity Structures*. US Patent App. 16/339,864. Aug. 2019.
- [105] Y. Li et al. “Constructing tensegrity structures from one-bar elementary cells”. In: *Proceedings of the Royal Society A: Mathematical, Physical and Engineering Sciences* 466.2113 (2010), pp. 45–61.
- [106] F. J. Owens. *Physics of magnetic nanostructures*. Wiley Online Library, 2015.
- [107] Y. Li et al. “Constructing tensegrity structures from one-bar elementary cells”. In: *Proceedings of the Royal Society A: Mathematical, Physical and Engineering Sciences* 466.2113 (2009), pp. 45–61. DOI: 10.1098/rspa.2009.0260.
- [108] R. E. Skelton and M. C. de Oliveira. “Tensegrity systems”. In: Springer, 2009, p. 3.
- [109] R. Budynas and K. Nisbett. *Shigley’s Mechanical Engineering Design*. McGraw-Hill Education, 2010. Chap. Chapter 4: Deflection and Stiffness.
- [110] W. D. Callister and D. G. Rethwisch. *Materials science and engineering*. Vol. 5. John wiley & sons NY, 2011.
- [111] J. M. Gere and B. J. Goodno. *Mechanics of Materials*. Cengage Learning, USA, 2012.
- [112] S. Krödel et al. “Stress relaxation in polymeric microlattice materials”. In: *Materials & Design* 130 (2017), pp. 433–441.
- [113] J. Bauer et al. “Push-to-pull tensile testing of ultra-strong nanoscale ceramic–polymer composites made by additive manufacturing”. In: *Extreme Mechanics Letters* 3 (2015), pp. 105–112.
- [114] M. Abdelhamid. “Effective Mechanical Properties of 3D Structural Metamaterials”. MA thesis. York University, 2017.
- [115] P. Chopra. “Effective mechanical properties of lattice materials”. PhD thesis. University of British Columbia, 2011.
- [116] N. Nadkarni, C. Daraio, and D. M. Kochmann. “Dynamics of periodic mechanical structures containing bistable elastic elements: From elastic to solitary wave propagation”. In: *Physical Review E* 90.2 (2014), p. 023204.
- [117] A. Amendola et al. “Tuning frequency band gaps of tensegrity mass-spring chains with local and global prestress”. In: *International Journal of Solids and Structures* 155 (2018), pp. 47–56. DOI: 10.1016/j.ijstr.2018.07.002.
- [118] A. Micheletti, G. Ruscica, and F. Fraternali. “On the compact wave dynamics of tensegrity beams in multiple dimensions”. In: *Nonlinear Dynamics* (2019). DOI: 10.1007/s11071-019-04986-8.

- [119] S. Krödel, A. Palermo, and C. Daraio. “Acoustic properties of porous microlattices from effective medium to scattering dominated regimes”. In: *The Journal of the Acoustical Society of America* 144.1 (2018), pp. 319–329. DOI: 10.1121/1.5046068.
- [120] K. Pajunen et al. “Design and impact response of 3D-printable tensegrity-inspired structures”. In: *Materials & Design* 182 (2019), p. 107966. DOI: 10.1016/j.matdes.2019.107966.
- [121] P. Celli et al. “Bandgap widening by disorder in rainbow metamaterials”. In: *Applied Physics Letters* 114.9 (2019), p. 091903. DOI: 10.1063/1.5081916.
- [122] E. V. Dontsov, R. D. Tokmashev, and B. B. Guzina. “A physical perspective of the length scales in gradient elasticity through the prism of wave dispersion”. In: *International Journal of Solids and Structures* 50.22 (2013), pp. 3674–3684. DOI: 10.1016/j.ijsolstr.2013.07.012.
- [123] L. Brillouin. *Wave propagation in periodic structures*. Second. Dover, 1953.
- [124] H. P. Myers. *Introductory solid state physics*. CRC press, 1997.
- [125] M. Oudich et al. “Experimental evidence of locally resonant sonic band gap in two-dimensional phononic stubbed plates”. In: *Physical Review B* 84.16 (2011), p. 165136.
- [126] I. Arretche and K. H. Matlack. “On the interrelationship between static and vibration mitigation properties of architected metastructures”. In: *Frontiers in Materials* 5 (2018), p. 68.
- [127] S. S. Injeti et al. “Architected lattices with optimized elastic wave speeds”. In: *Journal of the Mechanics and Physics of Solids* (2020). In press.
- [128] A. F. Bower. *Applied mechanics of solids*. CRC press, 2009.
- [129] W. Chen et al. “Stiff isotropic lattices beyond the Maxwell criterion”. In: *Science advances* 5.9 (2019), eaaw1937.
- [130] A. Spadoni and C. Daraio. “Generation and control of sound bullets with a nonlinear acoustic lens”. In: *Proceedings of the National Academy of Sciences* 107.16 (2010), pp. 7230–7234.
- [131] W. Setyawan and S. Curtarolo. “High-throughput electronic band structure calculations: Challenges and tools”. In: *Computational materials science* 49.2 (2010), pp. 299–312.
- [132] J. Achenbach. *Wave propagation in elastic solids*. Elsevier, 2012.
- [133] T. Bückmann et al. “On three-dimensional dilational elastic metamaterials”. In: *New journal of physics* 16.3 (2014), p. 033032.
- [134] H. A. Burgoyne and C. Daraio. “Elastic–plastic wave propagation in uniform and periodic granular chains”. In: *Journal of Applied Mechanics* 82.8 (2015).

- [135] F. Sun et al. “Crushing mechanism of hierarchical lattice structure”. In: *Mechanics of Materials* 97 (2016), pp. 164–183.
- [136] A. Ghaedizadeh et al. “Tuning the performance of metallic auxetic metamaterials by using buckling and plasticity”. In: *Materials* 9.1 (2016), p. 54.
- [137] M. A. Meyers. *Dynamic behavior of materials*. John Wiley & Sons, 1994, p. 299.
- [138] Y. Jiang and Q. Wang. “Highly-stretchable 3D-architected mechanical metamaterials”. In: *Scientific reports* 6 (2016), p. 34147. doi: 10.1038/srep34147.
- [139] M. Mohsenizadeh et al. “Additively-manufactured lightweight Metamaterials for energy absorption”. In: *Materials & Design* 139 (2018), pp. 521–530. doi: 10.1016/j.matdes.2017.11.037.
- [140] L. J. Gibson and M. F. Ashby. *Cellular solids: structure and properties*. Cambridge university press, 1999.
- [141] N. C. Nayak and D. K. Tripathy. “Deformation and energy absorption characteristics of microcellular ethylene-octene copolymer vulcanizates”. In: *Polymer Engineering & Science* 42.6 (2002), pp. 1274–1285. doi: 10.1002/pen.11030.
- [142] Y. Sha et al. “Design and strengthening mechanisms in hierarchical architected materials processed using additive manufacturing”. In: *International Journal of Mechanical Sciences* 149 (2018), pp. 150–163. doi: 10.1016/j.ijmecsci.2018.09.038.
- [143] I. Ullah, M. Brandt, and S. Feih. “Failure and energy absorption characteristics of advanced 3D truss core structures”. In: *Materials & Design* 92 (2016), pp. 937–948. doi: 10.1016/j.matdes.2015.12.058.
- [144] H. A. Burgoyne et al. “Guided impact mitigation in 2D and 3D granular crystals”. In: *Procedia Engineering* 103 (2015), pp. 52–59.
- [145] S. Shan et al. “Multistable architected materials for trapping elastic strain energy”. In: *Advanced Materials* 27.29 (2015), pp. 4296–4301.
- [146] R. Thevamaran, E. R. Meshot, and C. Daraio. “Shock formation and rate effects in impacted carbon nanotube foams”. In: *Carbon* 84 (2015), pp. 390–398.
- [147] The University of Hong Kong Department of Physics. *Chapter 5 The Science of Soccer*. 2013. URL: <https://www.physics.hku.hk/~phys0607/lectures/chap05.html> (visited on 03/12/2020).
- [148] J. Persson. “Measure the coefficient of restitution for sports balls”. In: *Physics Education* 47.6 (2012), p. 662.
- [149] M. Harrison. *Vehicle refinement: controlling noise and vibration in road vehicles*. Elsevier, 2004.

- [150] L. R. Meza et al. “Resilient 3D hierarchical architected metamaterials”. In: *Proceedings of the National Academy of Sciences* 112.37 (2015), pp. 11502–11507.
- [151] X. Wendy Gu and J. R. Greer. “Ultra-strong architected Cu meso-lattices”. In: *Extreme Mechanics Letters* 2 (2015), pp. 7–14.
- [152] M. Pham et al. “Damage-tolerant architected materials inspired by crystal microstructure”. In: *Nature* 565.7739 (2019), pp. 305–311.
- [153] T. Baldacchini. *Three-dimensional microfabrication using two-photon polymerization: fundamentals, technology, and applications*. William Andrew, 2015.

Appendix A

APPENDICES FOR CHAPTER 2

A.1 MATLAB Codes for Dispersion Experiments

MATLAB Files to Generate the Burst Signal and Input Signal

```

1 %% BURST GENERATION FILE
2
3 close all
4 clear all
5 clc
6
7 %% CONTROL PARAMETERS FOR THE BURST ...
  ===== %%
8
9 % CARRIER FREQUENCY OF THE BURST
10 nnu=200; %[Hz]
11
12 % NUMBER OF CYCLES IN THE BURST (5)
13 Nc=1;
14
15 % NUMBER OF SAMPLES IN THE BURST+RELAXATION TIME WINDOW (2500)
16 nsteps=63999;
17
18 % LENGTH OF THE RELAXATION TIME = (ratiotime-1)*(length burst) ...
  (70)
19 ratiotime=150;
20
21 % SAVE THE BURST?
22 burstexport='no';
23
24 %% BURST GENERATION ...
  ===== %%
25
26 % SIGNAL GENERATION
27 [time,TT,tmax,dt,wtot,Wf,fx,pos_fx]=input_signal_generation(nnu,Nc, ...
  ...
28     nsteps,ratiotime);
29

```

```

30 % EXPORTING THE SIGNAL
31 if isequal(burstexport,'yes')
32     dlmwrite('burst.txt',wtot,'precision','%5f')
33 end
34
35 % PLOTS OF THE SIGNAL
36 figure; subplot(2,1,1); hold all; plot(time*10^3,wtot,'rx-'); ...
    box on
37 % title('Generated burst - Time domain')
38 xlabel('Time [ms]')
39 ylabel('Amplitude [-]')
40 set(gca,'FontSize',18,'FontName','Times','fontWeight','normal');
41 set(findall(gcf,'type','text'),'FontSize',18,'FontName','Times', ...
    ...
42     'fontWeight','normal')
43
44 subplot(2,1,2);
45 plot(fx(pos_fx),abs(Wf(pos_fx))/max(abs(Wf(pos_fx))),'-','LineWidth',2)
46 % title('Generated burst - Frequency spectrum')
47 xlabel('Frequency, f [Hz]')
48 ylabel('Amplitude [-]')
49 set(gca,'FontSize',18,'FontName','Times','fontWeight','normal');
50 set(findall(gcf,'type','text'),'FontSize',18,'FontName','Times', ...
    ...
51     'fontWeight','normal')
52 hold all; grid on; box on; axis tight

1 function ...
    [time,TT,tmax,dt,wtot,Wf,fx,pos_fx]=input_signal_generation( ...
    ...
2     nnu,Nc,nsteps,ratiotime)
3
4 % function ...
    [time,wtot,Wf,fx,pos_fx]=input_signal_generation(nnu,Nc,nsteps)
5 % generates a narrow-band sine burst with prescribed ...
    characteristic
6 % frequency and number of cycles by using a sinusoidal ...
    function as the
7 % smoothing function and calculates its frequency spectrum
8 %-----INPUT-----%
9 %     -nnu
10 %         (scalar) Frequency in Hz (cycles per second)

```

```

11 %   -Nc
12 %       (scalar) N. of oscillation cycles in the burst
13 %   -nsteps
14 %       (scalar) N. of intervals in the burst time window
15 %   -ratiotime
16 %       (scalar) multiplying it times the length of the ...
        sinusoidal burst,
17 %       we get the length of the relaxation time interval
18 %-----OUTPUT-----%
19 %   -time
20 %       (1 x nsteps+1) Time domain array
21 %   -wtot
22 %       (1 x nsteps+1) Signal time history
23 %   -fx
24 %       (1 x nsteps+1) Frequency domain array
25 %   -Wf
26 %       (1 x nsteps+1) Signal frequency spectrum
27 %   -pos_fx
28 %       (1 x nsteps/2) Positive frequencies
29
30 %-----%
31 %-----BEGIN ROUTINE-----%
32 %-----%
33 TT=1/nnu;
34 t1max=Nc/nnu;
35 %ratiotime=1;
36 tmax=t1max*ratiotime;
37 dt=tmax/nsteps;
38 time=0:dt:tmax;
39 t1=0:dt:t1max;
40 %%%%%%%%%%%%%%%%%%%%%%%%%%%%%%%%%%%%%%%%%%%%%%%%%%%%%%%%%%%%%%%%%%%%%%%%%
41 we=2*pi*nnu;
42 %w1=sin(we*t1/(2*Nc)); %w1=ones(1,length(t1));
43 w1=hann(length(t1))'; %Window function
44 w2=sin(we*t1);
45 wtemp=w1.*w2;
46 wtot=zeros(size(time));
47 wtot(1,1:length(t1))=wtemp';
48 % figure (11), hold on, plot(time,wtot,'ro-');
49 %%%%%%%%%%%%%%%%%%%%%%%%%%%%%%%%%%%%%%%%%%%%%%%%%%%%%%%%%%%%%%%%%%%%%%%%%
50
51 %% PUT ratiotime=5 dt=tmax/1000 for smooth Fourier transform
52 fsamp=1/(time(2)-time(1));

```

```

53 % fsamp=1/(t1(2)-t1(1));
54 fx=fsamp*(-length(time)/2:length(time)/2-1)/length(time);
55 pos_fx=find(fx>=0);
56 % fx=fsamp*(-length(t1)/2:length(t1)/2-1)/length(t1);
57 % pos_fx=find(fx>=0);
58 Wf=fft(wtot); Wf=fftshift(Wf); % Wf=find(Wf>=0); % w2
59 % figure, ...
    semilogx(fx(pos_fx),abs(Wf(pos_fx))/max(abs(Wf(pos_fx))), ...
60 %'LineWidth',2)
61 % axis tight; grid on
62 %-----%
63 %-----END ROUTINE-----%
64 %-----%

```

MATLAB File to Reconstruct Dispersion Curve

```

1 %% DISPERSION RELATION RECONSTRUCTION FOR SURFACE WAVE EXPERIMENTS
2 % 2018/10 -- Caltech -- Antonio Palmero, Paolo Celli, Lorenzo ...
    Affentranger
3
4 clear
5 close all
6 clc
7
8 %% LOAD DATA
9
10 % QUANTITIES TO UPDATE EVERY TIME
11 n_points=10;
12
13
14 % Choose the data file. Email pajunen2010@gmail.com for data ...
    files.
15 stringstart='Tensegrity_Frequency_Tests_Data/20191111_TensegrityA_' ...
    ...
16 '0Pre_Burst1cycle200Hz850mV_Inner_Point'; %10 unit cells,
17 %0 compression
18 %stringstart='Tensegrity_Frequency_Tests_Data/
19 %20191111_Tensegrity6D_'
20 %'0Pre_Burst1cycle200Hz850mV_Inner_Point';
21 %6 Unit Cells, 0 compression
22 %stringstart='Tensegrity_Frequency_Tests_Data/
23 %20191111_Tensegrity6D_'
24 %'0d05Pre_Burst1cycle200Hz850mV_Inner_Point';

```

```

25     %6 unit cells, 0.05 comp.
26 % stringstart='Tensegrity_Frequency_Tests_Data/
27     %20191111_TensegrityA6Cells_'
28     %'0d1Pre_Burst1cycle200Hz850mV_Inner_Point';
29     %6 unit cells, 0.1 comp.
30 % stringstart='Tensegrity_Frequency_Tests_Data/
31     %20191111_TensegrityA6Cells_'
32     %'0d15Pre_Burst1cycle200Hz850mV_Inner_Point';
33     %6 unit cells, 0.15 comp.
34 % stringstart='Tensegrity_Frequency_Tests_Data/
35     %20191111_TensegrityA6Cells_'
36     %'_0d2Pre_Burst1cycle200Hz850mV_Inner_Point';
37     %6 unit cells, 0.2 comp.
38
39 for ii=1:n_points
40     load([stringstart num2str(ii) '.mat']);
41     A(:,ii)=Y1;
42 end
43 T=X1;
44 dx=0.0483; %m, spatial distance between measurement points
45 a = 2*dx; %unit cell height
46
47 % USEFUL QUANTITIES
48 T=T-T(1); %shift time vector
49 L=length(T); %number of time instants
50 X=dx*(1:n_points); %vector of measurement locations
51
52 % % SPACE-TIME EVOLUTION PLOT (SEISMOGRAM)
53 figure;
54 imagesc(X,T(1:20:end),A(1:20:end,:));
55 set(gca,'Ydir','reverse')
56 colormap gray; colormap(flipud(colormap));
57 colorbar
58 ylabel('t (s)')
59 xlabel('x (m)')
60 set(gca,'FontSize',18)
61 set(gca,'FontName','Arial')
62 pbaspect([1 0.5 1]) %0.66*.4
63 ylim([0.065 0.085])
64 yticks(0.065:0.01:0.085)
65 %caxis([0 0.0004])
66
67

```

```

68 %% 2DFFT
69
70 % WAVENUMBER VECTOR
71 ZPk=2^(nextpow2(length(X))+2);
72 kx=1/(X(2)-X(1))*(-length(X)/2:length(X)/2-1)/length(X);
73 kxZP=1/(X(2)-X(1))*(-ZPk/2:ZPk/2-1)/ZPk;
74
75 % TIME VECTOR
76 ZPf=2^(nextpow2(length(T))+1);
77 f=1/(T(2)-T(1))*(-length(T)/2:length(T)/2-1)/length(T);
78 fZP=1/(T(2)-T(1))*(-ZPf/2:ZPf/2-1)/ZPf;
79 FF=length(f);
80
81 % DFT OPERATION
82 FA(:, :) = abs(fftshift(fft2(A, ZPf, ZPk)));
83
84 % DISPERSION PLOT
85 figure
86 imagesc(kxZP, fZP, FA/max(max(FA)));
87 % imagesc(k(1:K), f(1:FF)/1000, FA(2:FF, 1:K));
88 set(gca, 'ydir', 'normal');
89 set(gca, 'FontSize', 9)
90 set(gca, 'FontName', 'Arial')
91
92 pbaspect([1 1 1]) %0.66*.4
93 colormap gray; colormap(flipud(colormap));
94 %colorbar
95 %title('6 Cells: 20% Compression')
96 xlabel('k (1/m)')
97 ylabel('Frequency (Hz)')
98 ylim([0 500])
99 yticks([0 100 200 300 400 500])
100 %xlim([0 1/(2*0.0483)])
101 xlim([0 1/a])
102 caxis([0 0.7])
103
104 % Uncomment the following section to add simulation results
105 %to the plot.
106 % Again, email pajunen2010@gmail.com for data files.
107
108 % %Add simulation
109 %
110 % hold on

```

```

111 % load d_0d2
112 % data_ky = d_0d2;
113 % turn_point = 155.1; %171.65; %209.72; %180.6; %191.03; %
114 %
115 % LW = 0.7*1.5;
116 % size_ky = length(data_ky(:,1));
117 % if size_ky < 530
118 %     for i = 1:size_ky
119 %         if data_ky(i,5) < 0.3 && (data_ky(i,3) > .35 || ...
120 %             data_ky(i,4)
121 %                 > 0.35 || data_ky(i,6) > 0.8)
122 %                     %plot(data_ky(i,1),data_ky(i,2), 'o', 'color', ...
123 %                         'red')
124 %                     if data_ky(i,2) > turn_point
125 %                         if data_ky(i,2) < 450
126 %                             data_ky_mirrored=-data_ky(i,1) +
127 %                                 %2*max(data_ky(:,1));
128 %                                 ...
129 %                             plot(data_ky_mirrored./(2*pi),data_ky(i,2), 'o',
130 %                                 'color', 'red','LineWidth',LW)
131 %                         end
132 %                     else
133 %                         plot(data_ky(i,1)./(2*pi),data_ky(i,2), 'o', ...
134 %                             'color',
135 %                             'red','LineWidth',LW)
136 %                         end
137 %                     end
138 %                 else
139 %                     for i = 1:(size_ky/2)
140 %                         if data_ky(i,5) < 0.3 && (data_ky(i,3) > .35 || ...
141 %                             data_ky(i,4) >
142 %                             %0.35 || data_ky(i,6) > 0.8)
143 %                                 %plot(data_ky(i,1),data_ky(i,2), 'o', 'color', ...
144 %                                     'red')
145 %                                 if data_ky(i,2) > turn_point
146 %                                     if data_ky(i,2) < 470
147 %                                         data_ky_mirrored = -data_ky(i,1)
148 %                                             %+ max(data_ky(:,1));
149 %                                         ...
150 %                                         plot(data_ky_mirrored./(2*pi),data_ky(i,2), 'o',
151 %                                             'color', 'red', 'LineWidth',LW)
152 %                                         end
153 %                                     end
154 %                                 end
155 %                             end
156 %                         end
157 %                     end
158 %                 end
159 %             end
160 %         end
161 %     end

```

```

147 %             else
148 %                 plot(data_ky(i,1)/(2*pi),data_ky(i,2), 'o', ...
    'color',
149 %'red', 'LineWidth',LW)
150 %             end
151 %         end
152 %     end
153 % end
154 %
155 %
156
157 %scatter(data_ky_mirrored(:,1)/(2*pi),data_ky_mirrored(:,2))
158 % figure
159 % scatter(data_ky_mirrored(:,1),data_ky_mirrored(:,2))
160
161
162
163 %Calculate wave speed from experiment.
164 [maxxxx, index_start]=max(A(1:17310, 1)); %t = 0.0692s
165 [maxx, index_end]=max(A(1:18922,6)); %t = 0.0757s
166 wave_speed = (.0483-.2898)/(T(index_start)-T(index_end))

```

MATLAB File to Sort COMSOL Dispersion Data into Mode Shapes

```

1
2 % Kirsti Pajunen
3
4 % data_ky: First column is the
5 %wave number, ky, second column is frequency in Hz.
6 % Email pajunen2010@gmail.com if you would like data tables.
7
8 %This file sorts the frequency data from COMSOL into longitudinal,
9 %rotational, combined longitudinal and rotational, and other ...
    (including
10 %flexural) modes, and indicates this in the plot used ...
    differently colored
11 %and shaped markers.
12
13 clear
14 close all
15
16 a = 0.0966; %unit cell length, m
17

```

```

18
19 load d_0d2
20 data_ky = d_0d2;
21 %turn_point = 209.72;
22
23 size_ky = length(data_ky(:,1));
24 figure
25 set(gca,'FontSize',12)
26 set(gca, 'FontName', 'Arial')
27 pbaspect([0.5 1 1]) %0.66
28 box on
29 hold on
30 LW = 0.7;
31 for i = 1:size_ky
32
33     if data_ky(i,1) <= 33 && data_ky(i,2) < 500
34
35         %Longitudinal
36         if data_ky(i,5) < 0.3 && (data_ky(i,3) > .35 || ...
37             data_ky(i,4) > ...
38                 0.35 || data_ky(i,6) > 0.8)
39             % if data_ky(i,3) > .35 || ...
40                 data_ky(i,4)>0.35||data_ky(i,6) > 0.8
41                 plot(data_ky(i,1),data_ky(i,2), 'o', 'color', ...
42                     'red', 'LineWidth',LW*1.5) %Red./(2*pi)
43         %end
44
45         %Longitudinal and rotational combined
46         elseif data_ky(i,5) > 0.3 && (data_ky(i,3) > .35 || ...
47             data_ky(i,4) > 0.35 || data_ky(i,6) > 0.8)
48             %if data_ky(i,5) > 0.3
49                 plot(data_ky(i,1),data_ky(i,2), 'o', 'color', ...
50                     [51/255 ...
51                     153/255 0/255], 'LineWidth',LW*1.5)
52         %end
53
54         %Rotational
55         elseif data_ky(i,3) < .35 && data_ky(i,4) < 0.35 && ...
56             ata_ky(i,5) > 0.3 && data_ky(i,6) < 0.8
57             plot(data_ky(i,1),data_ky(i,2), 'o', 'color', ...
58                 [102/255 ...
59                 0/255 255/255], 'LineWidth',LW*1.5)

```

```

57     %Flexural and other
58     else
59         plot(data_ky(i,1),data_ky(i,2), '*', ...
60             'MarkerSize',4, ...
61             'color', [0/255 102/255 255/255], ...
62             'LineWidth',LW/4)
63
64     end
65 end
66
67 xlabel('k (1/m)')
68 ylabel('Frequency (Hz)')
69 xlim([0 2*pi/(2*a)])
70 ylim([0 500])
71 %xticks([0 0.5*(1/(2*a)) 1/(2*a)])
72 %xticklabels({'0', '1/(4*a)', '1/(2*a)'})
73 yticks([0 100 200 300 400 500])

```

A.2 MATLAB Code for Drop Weight Experiments

```

1 %This code processes the data from drop weight tests on a ...
   single unit cell.
2 %This can be modified to process data from drop weight lattice ...
   tests and
3 %also lattice drop tests. Please email pajunen2010@gmail.com ...
   for data files
4 %and also code for the lattice drop and fall tests.
5
6 clear all;
7 close all;
8 clc;
9
10
11 Delta_Plate_BottomWeight = 0.3;
12
13 SampleHeightOriginal = 0.0483;
14 SampleHeightInitial = 0.0483;
15 SampleHeightAfter5min = 0.0483;
16
17 DropHeight = Delta_Plate_BottomWeight - SampleHeightInitial;

```

```

18
19 mass = 0.197536 + 0.003; %Weight mass + sample mass
20 SensitivityPCB = 11241; %Force sensor 200B02: 11241 mV/kN
21 SensitivityAcc = 0.47;
22 %Sensitivity of Accelerometer model 356A01: 0.47 mV/(m/s )
23
24 %% import oscilloscope data
25
26 FilenameOscill = 'force';
27 ColRange = 'A:D';
28 Oscill = xlsread(FilenameOscill,ColRange);
29
30 startOscill = 200;
31 endOscill = 1100;
32 TimePCB = Oscill(startOscill:endOscill,1);
33 VoltageBottom = Oscill(startOscill:endOscill,2);
34 VoltageTop = Oscill(startOscill:endOscill,4);
35
36 %take voltage difference in order to eliminate voltage/force,
37 %that is due to mass of structure and glass plate
38 BottomForce = (VoltageBottom - VoltageBottom(1))*1e6 / ...
    SensitivityPCB;
39 BottomForce = smooth(BottomForce);
40
41 TopForce = - mass * (VoltageTop - VoltageTop(1))*1e3 / ...
    SensitivityAcc;
42
43 [MaxBottomForce,locs_BottomForce] = max(BottomForce);
44 MaxBottomForce = MaxBottomForce
45
46
47 %% Apply butterworth Filter
48
49 f_cutoff =1000; % cutoff frequency for filter
50 f=1/(TimePCB(2)-TimePCB(1)); % sampling frequency
51 fnorm =f_cutoff/(f/2); % normalized cut off frequency
52
53 [b,a] = butter(3,fnorm,'low'); % Low pass Butterworth filter ...
    of order 3
54 LP_TopForce = filtfilt(b,a,TopForce); % filtering
55 LP_MA_TopForce = smooth(LP_TopForce); %moving average
56
57 freqz(b,a,128,f), title('low pass filter characteristics')

```

```

58
59 figure(1)
60 subplot(3,1,1)
61 plot(TopForce), title('Unfiltered Data')
62 subplot(3,1,2)
63 plot(LP_TopForce), title('Lowpass Filtered Data')
64 subplot(3,1,3)
65 plot(LP_MA_TopForce), title('Lowpass Filtered and Smoothed Data')
66
67 [MaxTopForce,locs_TopForce] = max(LP_MA_TopForce);
68
69 %% get position, speed and acceleration
70
71 FilenameCoord = 'disp';
72 ColRange = 'B:D';
73 Coord = xlsread(FilenameCoord,ColRange);
74 Coord = Coord;
75 PCCStartIndex = 5;%20;
76 PCCEndIndex = length(Coord);%130; %or: length(Coord) if weight ...
    is caught
77 %after 1 impact
78 TimePCCCoord = Coord(PCCStartIndex:PCCEndIndex,1);
79 Y0 = Coord(PCCStartIndex:PCCEndIndex,3);
80
81 SmoothY0 = smooth(Y0);
82
83 %speed of weight needed later for determination of 1st touch
84 TimePCCSpeed_Smooth = TimePCCCoord(1:end-1);
85 Y0SpeedSmooth = smooth(diff(SmoothY0) ./ diff(TimePCCCoord));
86
87 %Acceleration inaccurate (2 differentiations), not used
88 %TimePCCAcc_Smooth = TimePCCCoord(1:end-2);
89 %Y0AccSmooth = smooth(diff(Y0SpeedSmooth) ./ ...
    diff(TimePCCSpeed_Smooth));
90
91 %% find coordinates at maximum compression between sample and ...
    weight
92
93 [min_SmoothY0,locs_SmoothY0] = min(SmoothY0);
94 MaxCompressionTime = TimePCCCoord(locs_SmoothY0);
95 MaxCompressionHeight = min_SmoothY0;
96
97 %% find coordinates and time at first touch between sample and ...

```

```

    weight
98 %using topforce data and determine velocity at first touch time
99
100 found = 0;
101 index = locs_TopForce;
102 while found == 0
103     if LP_MA_TopForce(index) > 1.5
104         %increase value 0 (f.ex. 1)
105         %if acceleration data does not cross 0 immediately
106         index = index - 1;
107     else
108         if LP_MA_TopForce(index - 1) < LP_MA_TopForce(index) ...
109             && ...
110                 LP_MA_TopForce(index - 1) > 0
111             index = index - 1;
112         else
113             found = 1;
114             FirstTouchTime = TimePCB(index);
115             ForceStart = index;
116         end
117     end
118
119 %Find impact speed and sample height @ first impact
120 %index of position data is different from index of ...
    oscilloscope data
121 % => find position index i by comparing the times
122 found = 0;
123 i = locs_SmoothY0;
124 while found == 0
125     if TimePCCoord(i) > TimePCB(index)
126         i = i - 1;
127     else
128         found = 1;
129         RefHeight = SmoothY0(i);
130         SpeedAtImpact = Y0SpeedSmooth(i);
131     end
132 end
133
134 %% find coordinates and time when shock wave reaches bottom nodes
135 %using bottomforce data
136 %often not accurate (due to oscillations in force sensor data),
137 %has to be determined manually

```

```

138
139 found = 0;
140 index = locs_BottomForce;
141 while found == 0
142     if BottomForce(index) > 0.5
143         %value 0.5 should eliminate oscillation issue
144         index = index - 1;
145     else
146         if BottomForce(index - 1) < BottomForce(index) && ...
147             BottomForce(index - 1) > 0
148             index = index - 1;
149         else
150             found = 1;
151             WaveArrivalTime = TimePCB(index);
152         end
153     end
154 end
155
156 %% Only gravity acting / release /no force acting between ...
157     sample and weight
158
158 found = 0;
159 index = locs_BottomForce;
160 while found == 0
161     if BottomForce(index) > 0.5
162         %increase value 0 (f.ex. 1)
163         %if weight does not release from test sample (broken ...
164             sample)
165         index = index + 1;
166     else
167         if BottomForce(index + 1) < BottomForce(index) && ...
168             BottomForce(index + 1) > 0
169             index = index + 1;
170         else
171             found = 1;
172             ReleaseTime = TimePCB(index);
173             ForceEnd = index;
174         end
175     end
176
177 %find height of the sample at release
178 %index of position data is different from index of ...

```

```

    oscilloscope data
179 % => find position index i by comparing the times
180 found = 0;
181 i = locs_SmoothY0;
182 while found == 0
183     if TimePCCCoord(i) < TimePCB(index)
184         i = i + 1;
185     else
186         found = 1;
187         ReleaseHeight = SmoothY0(i);
188     end
189 end
190
191 %Duration of impact
192 TotalImpactTime = ReleaseTime - FirstTouchTime;
193
194 %% Maximum strain
195
196 MaxCompressionDelta = abs(MaxCompressionHeight - RefHeight)
197 MaxStrain = MaxCompressionDelta / SampleHeightInitial;
198 MaxStrainOriginal = MaxCompressionDelta / SampleHeightOriginal;
199
200 %% Plotting
201
202 figure(3)
203 subplot(2,1,1)
204
205 yyaxis left
206 hold on
207 plot(TimePCCCoord, SmoothY0)
208 %xlim([TimePCCCoord(1) inf])    %adjusted x-axis range
209
210 ax = gca;
211 ax.XLabel.String = 'Time [s]';
212 ax.XLabel.FontSize = 12;
213 ax = gca;
214 ax.YLabel.String = 'Displacement [m]';
215 ax.YLabel.FontSize = 12;
216
217 yyaxis right
218 plot(TimePCB, BottomForce)
219 plot(TimePCB, LP_MA_TopForce)
220

```

```

221 ax = gca;
222 ax.YLabel.String = 'Force [N]';
223 ax.YLabel.FontSize = 12;
224
225 plot([FirstTouchTime FirstTouchTime],get(gca,'ylim'),'--k')
226
227 plot([MaxCompressionTime MaxCompressionTime],get(gca,'ylim'),'k')
228
229 plot([ReleaseTime ReleaseTime],get(gca,'ylim'),'-.k')
230
231 grid on
232 hold off
233 legend('Y0','Bottom Force','Top Force','FirstTouchTime',...
234        'MaxCompressionTime','ReleaseTime')
235
236 subplot(2,1,2)
237
238 hold on
239 plot(TimePCCSpeed_Smooth,Y0SpeedSmooth,'-')
240
241 plot([FirstTouchTime FirstTouchTime],get(gca,'ylim'),'--k')
242 plot([MaxCompressionTime MaxCompressionTime],get(gca,'ylim'),'k')
243 plot([ReleaseTime ReleaseTime],get(gca,'ylim'),'-.k')
244
245 ax = gca;
246 ax.XLabel.String = 'Time [s]';
247 ax.XLabel.FontSize = 12;
248 ax = gca;
249 ax.YLabel.String = 'Speed [m/s]';
250 ax.YLabel.FontSize = 12;
251 xlim([TimePCCCoord(1) inf])      %adjusted x-axis range
252
253 grid on
254 hold off
255 legend('Y0SpeedSmooth','FirstTouchTime', ...
256        'MaxCompressionTime','ReleaseTime')
257
258 %% Plot stress strain curve and deterring energies, max strain ...
259     etc.
260 TimePCBDuringImpact = TimePCB(ForceStart:ForceEnd);
261
262 %Unit of stressPCB: N/m^2 = Pa

```

```

263 stressPCB = BottomForce(ForceStart:ForceEnd)/(pi() * ...
264     (0.0405739 * 2/3)^2);
265
266 %%%Force on bottom plate for energy calculations.
267 forceBottom = BottomForce(ForceStart:ForceEnd);
268 %%%
269
270 %resampling displacement data to sampling rate of pcb output data:
271 ResampledY0 = interp1(TimePCCoord,SmoothY0,TimePCBDuringImpact)
272
273 %consider strain as positive during compression
274 %shift curve such that stress strain curve starts at 0 strain
275 %This is also the displacement data used to calculate energy.
276 CompressionDelta = -(ResampledY0 - RefHeight);
277
278 strain = CompressionDelta / SampleHeightInitial;
279
280 [max_disp, index_max_disp] = max(CompressionDelta);
281 W_max = ...
        trapz(strain(1:index_max_disp),stressPCB(1:index_max_disp))
282 %maximum stored strain energy, unit: Joules
283
284 W_dissipated = abs(W_max) - abs(trapz(CompressionDelta( ...
285     index_max_disp+1:end),forceBottom(index_max_disp+1:end)))
286 %dissipated strain energy, unit: Joules
287
288 Energy_Ratio = W_dissipated/W_max;
289 stressPCB_max = max(stressPCB)
290 strain_max = max(strain);
291 %for comparison: check if this value is very close to ...
        MaxStrain value
292 %(small variations may be a consequence of resampling ...
        procedure (interp1))
293
294 %Determination of remaining strain
295 RemainingStrainInstantaneous = strain(end)
296
297 RemainingStrain5min = abs((SampleHeightAfter5min - ...
        SampleHeightInitial) ...
298     / SampleHeightInitial)
299
300 %remaining strain compared to untested sample
301 TotalRemainingStrain=abs((SampleHeightAfter5min - ...

```

```

        SampleHeightOriginal)...
302     / SampleHeightOriginal)
303
304 %plot stress strain hysteresis
305 figure(2)
306 plot(CompressionDelta, forceBottom)
307 %plot(strain, stressPCB); %Unit: N/m^2 = Pa
308 hold on
309 xlim([0 inf])      %adjusted x-axis range
310 ylim([0 inf])     %adjusted y-axis range
311 grid on
312 % plot(strain_m, UnloadingFit(1)*strain_m+UnloadingFit(2), 'r')
313 % legend('Cycle1', 'LinearFit')
314 ax = gca;
315 ax.XLabel.String = 'Displacement [m]';
316 %ax.XLabel.String = 'Strain [-]';
317 ax.XLabel.FontSize = 12;
318 ax = gca;
319 ax.YLabel.String = 'Force [N]';
320 %ax.YLabel.String = 'Stress [Pa]';
321 ax.YLabel.FontSize = 12;
322 hold off
323
324 %% Plot effective stiffness over time
325
326 %compute effective stiffness instead of E-modulus as E_module ...
    would be an
327 %approximation (out of stress-strain curve, with approximated
328 %cross-sectional area for stress = Force / Area
329 EffectiveStiffness = ...
    BottomForce(ForceStart:ForceEnd)./CompressionDelta;
330 figure(4)
331 plot(TimePCBDuringImpact, EffectiveStiffness)
332 grid on
333 MaxEffStiffness = max(EffectiveStiffness)
334
335 %% Effective Wave Speed & Wave Propagation
336
337 %determine effective wave speed
338 %this speed is the same in the same media
339 %so with deformation of sample, it will change
340 %not accurate because time at wave arrival is usually not correct
341

```

```

342 WavePropTimeFirst = WaveArrivalTime - FirstTouchTime;
343 EffWaveSpeed = SampleHeightInitial / WavePropTimeFirst;
344
345
346 %determine how many times wave propagates through sample ...
    during loading
347 %phase -> this is not accurate because effective wave speed ...
    could not be
348 %determined correctly
349 Counter = 1;
350 LastBoundaryTime(Counter) = FirstTouchTime;
351 WaveDirection = -1;
352 LastHeight = SampleHeightInitial;
353
354 %Determine Time/Index of max. compression
355 [MaxDisp,EndIndex] = min(ResampledY0);
356
357
358 for i=2:EndIndex
359     VarDisp(i) = SampleHeightInitial - CompressionDelta(i);
360     DeltaTime = TimePCBDuringImpact(i) - ...
        LastBoundaryTime(Counter);
361     if WaveDirection < 0
362         WaveFront(Counter) = LastHeight(Counter) - ...
            EffWaveSpeed*DeltaTime;
363     if WaveFront(Counter) <= 0
364         Counter = Counter + 1 ;
365         Index(Counter) = i;
366         LastBoundaryTime(Counter) = TimePCBDuringImpact(i);
367         WaveDirection = -1 * WaveDirection;
368         LastHeight(Counter) = 0;
369     end
370     else
371         WaveFront(Counter) = LastHeight(Counter) + ...
            EffWaveSpeed * DeltaTime;
372     if WaveFront(Counter) >= VarDisp(i)
373         Counter = Counter + 1 ;
374         Index(Counter) = i;
375         LastBoundaryTime(Counter) = TimePCBDuringImpact(i);
376         WaveDirection = -1 * WaveDirection;
377         LastHeight(Counter) = VarDisp(i);
378     end
379 end
380 end

```

```
381 end
382
383 WavePropCounter = Counter;
384
385 %% parameters
386 %Output parameters
387 par = ...
    [SampleHeightInitial;DropHeight;MaxBottomForce;MaxTopForce;...
388  stressPCB_max;MaxStrain;MaxStrainOriginal;TotalImpactTime; ...
389  SpeedAtImpact;...
390  WavePropTimeFirst;EffWaveSpeed;MaxCompressionDelta;...
391  MaxEffStiffness;W_max;W_dissipated;RemainingStrainInstantaneous;...
392  RemainingStrain5min;TotalRemainingStrain;Energy_Ratio]
```

Appendix B

APPENDICES FOR CHAPTER 3

B.1 Relaxation Tests for Two Materials

We performed relaxation tests on ASTM D638 standard samples using the Instron machine in order to compare the viscoelastic properties of two materials. To perform the tests, we clamped the dogbones in the tensile fixture and applied a strain rate of 1000 mm/s until the samples reached a tensile strain of 0.03. Then, the strain was kept constant for 60 minutes, recording the force and displacement with time. A strain of 0.03 remains in the elastic region for both materials. The results are shown in Figure B.1.

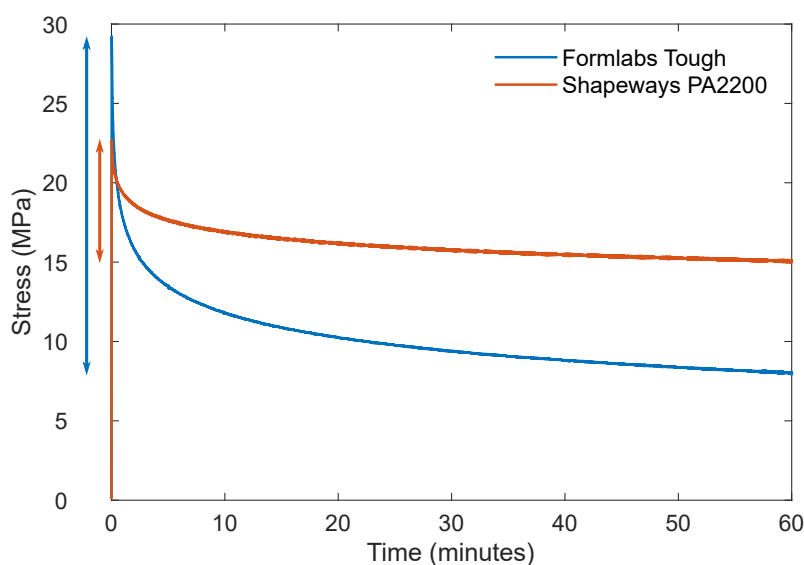


Figure B.1: Relaxation tests performed on the Shapeways PA2200 polyamide nylon material and the Formlabs “Tough” material. ASTM D638 Type IV specimens are loaded in tension, and the strain is held constant at 0.03. The reduction in stress is then measured over time. The magnitude of stress reduction is indicated by the colored arrows next to the vertical axis.

We observe that over the 60 minute time period, the stress in the Formlabs material reduces by over 70%, whereas the stress in the Shapeways material reduces by only 33%. This magnitude of stress reduction is indicated by the colored arrows next to the vertical axis. Thus, the Shapeways material was found to exhibit significantly lower viscoelasticity than the Formlabs material. This was one of the reasons we

chose it for our studies of tensegrity-inspired structures.

B.2 Intermediate Geometry Design Iterations

After obtaining the response of the pin-jointed structure with Geometry #1, it was clear that this geometry was not appealing in terms of energy absorption capacity. Keeping in mind the application of this structure being a building block for impact absorbing periodic lattices, we desired to increase the energy absorption of the structure and obtain a final design for the dynamic experiments.

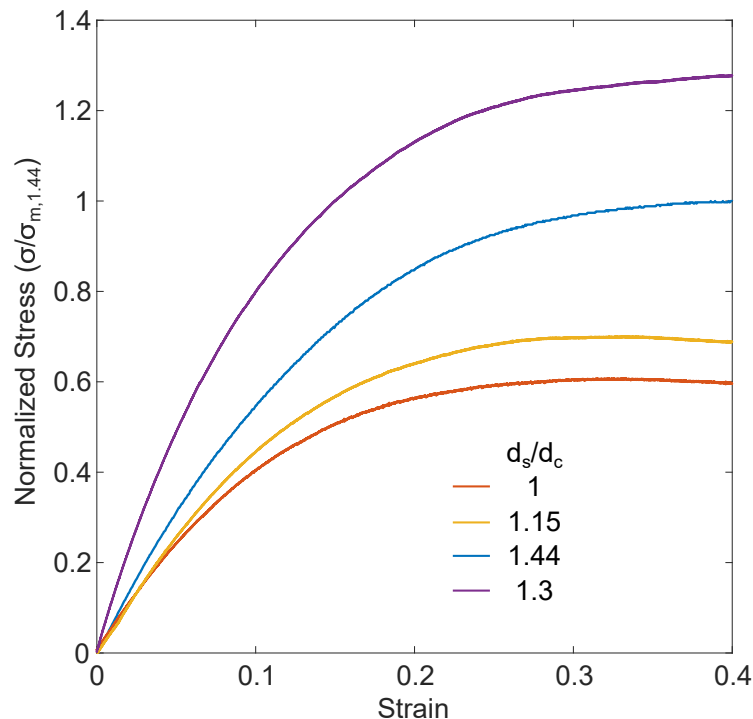


Figure B.2: Experimental stress-strain responses of four member diameter geometries of the spherically-jointed structure. The parameter d_s/d_c is the strut-to-cable diameter ratio. The stress is normalized by the maximum stress of the chosen final design (d_s/d_c of 1.44) for comparison.

The stiffness and buckling load of the structure directly affect the energy absorption, i.e., the area under the stress-strain curve. Changing the member diameters easily affect these parameters. However, we needed to keep in mind the practical aspects of changing the diameters, including manufacturing producibility and stress concentrations at the intersections with the spheres. We desired to keep the stress concentrations low in order to reduce any plastic deformation within the structure.

In Figure B.2, stress-strain curves of 4 experiments are shown according to different values of strut-to-cable diameter ratio (d_s/d_c). The stress is normalized

by the maximum stress of the chosen final design (Geometry #3 with a d_s/d_c of 1.44). All 4 designs were easily printable with the chosen manufacturing method, with both strut and cable diameters large enough for dependable fabrication.

At the lowest d_s/d_c values, the buckling load is lower than the higher d_s/d_c structures, and the stiffness is also lower. This reduces the energy capacity of the structure, making these choices unappealing. Looking, then, between $d_s/d_c = 1.44$ and $d_s/d_c = 1.3$, it might appear that $d_s/d_c = 1.3$ would be the best choice for energy absorption. However, the member diameters play a key role in stress concentrations. The cable diameters are the same for all d_s/d_c , except for $d_s/d_c = 1.44$, which has a thinner cable diameter. This is important because with a fixed amount of deformation (here, 0.4 strain), the structures with thicker cables result in higher stress concentrations. Plastic deformation from the stress concentrations is exhibited clearly by the reduction in force for the two lowest d_s/d_c values. Plastic deformation is not readily seen in the $d_s/d_c = 1.3$ plot, but since this has equal strut and higher cable diameters than the $d_s/d_c = 1.44$ structure, the stress concentrations are lower in the $d_s/d_c = 1.44$ structure. Therefore, $d_s/d_c = 1.44$ was the design that we chose.

APPENDIX FOR CHAPTER 5

C.1 Distribution of Kinetic and Strain Energy in a Lattice Under Impact

In Chapter 5, we examined how our tensegrity-inspired lattices have unique capabilities under impact, such as energy redirection, energy trapping, and dispersion. However, in terms of energy, we only examined the kinetic energy in the lattice. This is useful, since impact forces (and thus transmitted forces) are directly related to kinetic energy. However, the energy input into the lattice from the impactor is transmitted through the lattice via both strain energy and kinetic energy. Here, we examine the strain and kinetic energy distribution in a 10 RVE 3D1D lattice under impact by a 10 g impactor traveling at 18 m/s. Figure C.1 shows the kinetic and strain energy in the cables and the struts for this impact scenario over time.

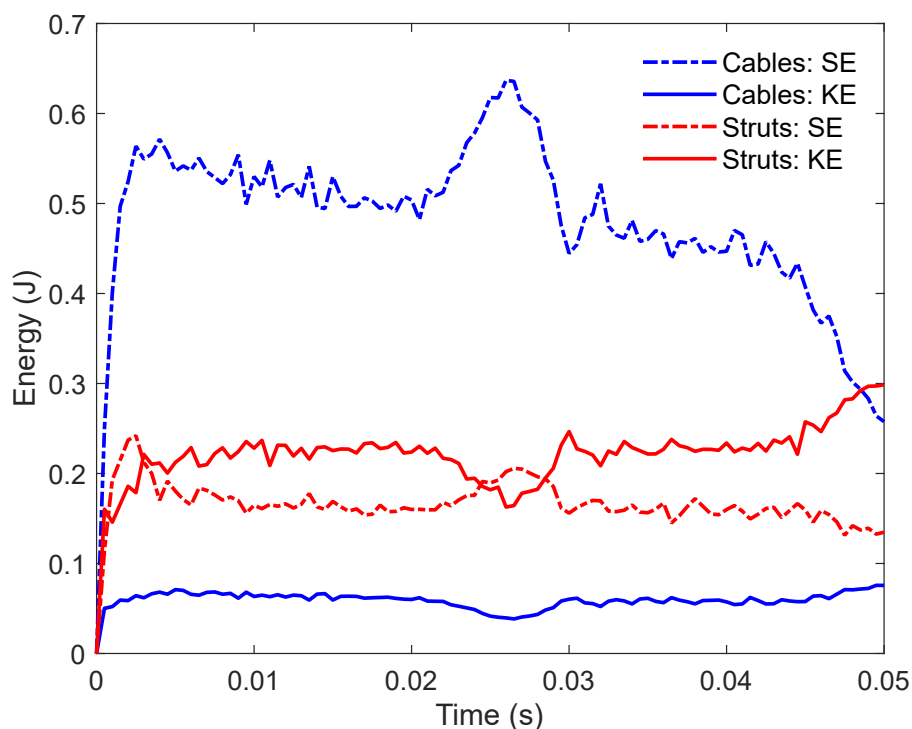


Figure C.1: Strain energy (SE) and kinetic energy (KE) in all cables and all struts in a 10 RVE 3D1D lattice under impact by a 10 g impactor traveling at 18 m/s.

The most striking observation is that the cables carry almost half of the energy in the lattice via strain energy. This means that the cables absorb a large amount

of energy purely through their deformation. (In Chapter 3, we saw that the cables deform the most of all of the members.) The struts carry the second largest amount of energy through kinetic energy. This supports our observation that the struts vibrate significantly during impact, thus trapping a large portion of energy in this vibration mechanism. In this figure, we see that the cables have very low kinetic energy compared to the struts, as expected. The strain energy in the struts, however, is quantitatively comparable to the kinetic energy in the struts, meaning that although the struts trap energy through vibration, they also absorb energy through deformation. The buckling of the struts produces this significant strain energy.

These observations of energy distribution are key to designing these lattices to achieve desired characteristics for applications. For example, it might be desirable to design the structure such that the majority of the energy is partitioned to kinetic energy of strut vibration. This would reduce the dependence of the lattice's impact performance on the material being able to deform significantly while remaining elastic.